Measurement of the Relative Fragmentation Fractions of $\bar{B}$ Hadrons

by

Karen Ruth Gibson

Submitted in partial fulfillment of the
requirements for the degree of
Doctor of Philosophy
at
Carnegie Mellon University
Department of Physics
Pittsburgh, Pennsylvania

Advised by Professor Manfred Paulini

June 9, 2006

Abstract

Measurement of the Relative Fragmentation Fractions of $\bar{B}$ Hadrons

This thesis describes the first Run II measurement of b quark fragmentation into $\bar{B}^0$, B^-, and $\bar{B}_s^0$ mesons and Λ_b^0 baryons using semileptonic B decays. The result is based on 360 pb^{-1} of data collected with the CDF detector in $p\bar{p}$ collisions at $\sqrt{s} = 1,960$ GeV at the Tevatron Collider at Fermilab. The fragmentation fractions are measured for an effective $\bar{B}$ hadron p_T threshold of 7 GeV/c to be $f_u/f_d = 1.054 \pm 0.018\,(stat)^{+0.025}_{-0.045}\,(sys) \pm 0.058\,(\mathcal{BR})$, $f_s/(f_u + f_d) = 0.160 \pm 0.005\,(stat)^{+0.011}_{-0.010}\,(sys)^{+0.057}_{-0.034}\,(\mathcal{BR})$, and $f_{\Lambda_b}/(f_u + f_d) = 0.281 \pm 0.012\,(stat)^{+0.058}_{-0.056}\,(sys)^{+0.128}_{-0.086}\,(\mathcal{BR})$. $f_s/(f_u + f_d)$ agrees both with previous CDF measurements and the world averages, dominated by the LEP measurements, within $\sim 1\,\sigma$. However, $f_{\Lambda_b}/(f_u + f_d)$ is approximately twice the value which has been measured at LEP and in CDF Run I and disagrees with the LEP results by approximately $2\,\sigma$.

To my father, who has always been my inspiration.

Acknowledgments

I would especially like to thank my advisor, Professor Manfred Paulini, for his insight, wisdom, and encouragement throughout my doctoral education. He has consistently supported me and, in my opinion, considerably advanced my development as a scientist. He is the kind of physicist I hope one day to become; one who is able to maintain integrity and resolve in the face of the political storms that often engulf high energy particle physics. I will always be grateful for the time that we spent working together and the level of true scientific collaboration that we achieved by the end of my doctoral work. I also greatly enjoyed getting to know Ann, Emma, and Helen Paulini, whose warmth and fond regard has consistently enlivened the social gatherings through which I've come to know them.

I would also particularly like to thank Professor James Russ for his long influence on my educational career, which stretches back to my junior year as an undergraduate in his Electricity and Magnetism course. He has consistently provided excellent advice about many subjects, physics chief among them. His help and insights into my thesis work have been invaluable and I am immensely grateful for the chance to have known and worked with him. I also appreciate having the chance to get to know Mrs. Carolyn Russ, whose own insights and charm provide a very pleasant counterpoint to that of her husband.

I greatly appreciate the efforts of my thesis committee, Professors Manfred Paulini (chair), James Russ, Frederick Gilman, Richard Holman, and Matthew Herndon for taking the time to (mostly) read my thesis.

I would of course be remiss if I did not properly acknowledge all of the scientists and technicians who contribute in many ways to the operation of the CDF experiment. Without their work and expertise, none of the rest would be possible. I am also terribly grateful to have had the opportunity to meet and get to know so many fascinating physicists who work on the CDF experiment. They have enriched my life and work in innumerable ways, both individually and collectively. I particularly appreciate the members of the B physics group, whose different contributions helped to facilitate my measurement and whose critiques helped to improve it.

My graduate student life has been immensely improved by my association with Dr. Gavril Giurgiu. I will warmly remember the times we spent discussing both physics and life in graduate school. I'm most fond of his natural pessimism, which he balances to great effect with an extremely engaging sense of humor. I feel very lucky to have had the opportunity to get to know him and will long cherish our friendship and all of the good memories we've shared.

I am deeply indebted to Vivek Tiwari for both his professional and personal connection. His dry sense of humor and overall good spirits set him apart from many of the people I

have known, particularly when taken in sum with his generally contrary nature. I have truly enjoyed the friendship we have developed over the past five years and look forward to many more.

I would not be able to achieve any measure of success, as person or as a physicist, without the loving support of my mother, Marlene Gibson, my brother, Joseph Gibson, and my parents-in-law, Yoshiko and Yoshinori Kusumoto. I love them all and I am so very fortunate to have them be a part of my life. I would particularly like to thank my grandmother, Lucille Dallas, for her selflessness, generosity, and love. She has been a model of kindness, strength, and perseverance for our family in so many ways and I know without a doubt that I am a better person for it. I cannot express in words how grateful I am to her for everything she has done for me.

My husband, Ryuji Kusumoto, is one of the very best people that I know and I am continually grateful for his presence in my life. He is funny and clever and thoughtful and kind and frustrating in nearly equal measure. I cannot believe that I met and fell in love with such a wonderful man.

It is unequivocally true that I would not be writing these acknowledgments without the loving and persistent guidance of my father. His strength, determination, and wisdom have been touchpoints for me throughout my life. He is also one of the smartest and most interesting people I know.

I would also like to acknowledge the love and comfort provided to me for the past twenty years by my family's cat, Tiger Gibson, who passed away shortly after my thesis defense, while I was visiting CERN to decide on my future path. He was a dearly loved cat and is dearly missed.

Contents

List of Tables

List of Figures

Chapter 1

Introduction

The bottom quark was first discovered at Fermi National Accelerator Laboratory (Fermilab) in 1977 [1]. It is the second heaviest quark and is significantly heavier than the up, down, and strange quarks, commonly referred to as the "light" quarks. This difference in mass gives hadrons with one bottom quark and one or two light (anti-)quarks special properties, since the light quark degrees of freedom can be decoupled from the heavy quark, much as the electron motion in the Hydrogen atom can be decoupled from the motion of the proton. Bottom quarks produced in hadronic $p\bar{p}$ collisions combine with quarks and gluons to form hadrons in a process called fragmentation [2]. In this process, the color field around the primary $p\bar{p}$ interaction creates additional quark-antiquark pairs, providing quarks which can combine with the bottom quark to create a b flavored hadron, either a $\bar{B}$ meson or b-baryon. Fragmentation is governed by the strong force and cannot be reliably calculated by perturbative QCD [3]-[5]. Consequently, the fragmentation properties of b quarks must be determined empirically.

This thesis describes the measurement of the flavor dependence of the fragmentation process for b quarks produced in hadronic $p\bar{p}$ collisions at $\sqrt{s} = 1.96$ TeV. The probabilities that the fragmentation of a b quark will result in a B^-, $\bar{B}^0$, $\bar{B}^0_s$ meson and Λ^0_b baryon[1], schematically shown in Figure 1.1, are defined as f_u, f_d, f_s and f_{Λ_b} respectively. The contributions from the production of excited $\bar{B}$ hadrons that decay into final states containing a B^-, $\bar{B}^0$, $\bar{B}^0_s$ meson or Λ^0_b baryon are explicitly included in this definition of the fragmentation fractions. In order to reduce systematic uncertainties arising from the poor knowledge of the b quark production cross section in $p\bar{p}$ collisions or absolute determinations of trigger and tracking efficiencies, the b quark fragmentation fractions are measured relative to f_d.

The data used in this measurement represents an integrated luminosity of approximately 360 pb^{-1} collected with the Collider Detector at Fermilab (CDF) experiment [6] between February 2002 and August 2004. Semileptonic decays of $\bar{B}$ hadrons ($\bar{B} \to \ell^- \bar{\nu} D X$) provide high statistics samples for studying the fragmentation properties of b quarks. Five charm signals, $D^0 \to K^-\pi^+$, $D^{*+} \to D^0\pi^+$, $D^+ \to K^-\pi^+\pi^+$, $D^+_s \to \phi(\to K^+K^-)\pi^+$, and $\Lambda^+_c \to pK^-\pi^+$, are reconstructed and combined with a lepton to establish signals which can be related to semileptonic B^-, $\bar{B}^0$, $\bar{B}^0_s$, and Λ^0_b decays, shown in Figure 1.2, through a sample composition. A simple example relating the $\ell^- D^+$ signal to the $\bar{B}^0$ parent, assuming that

[1] Charge conjugates are implied throughout the text.

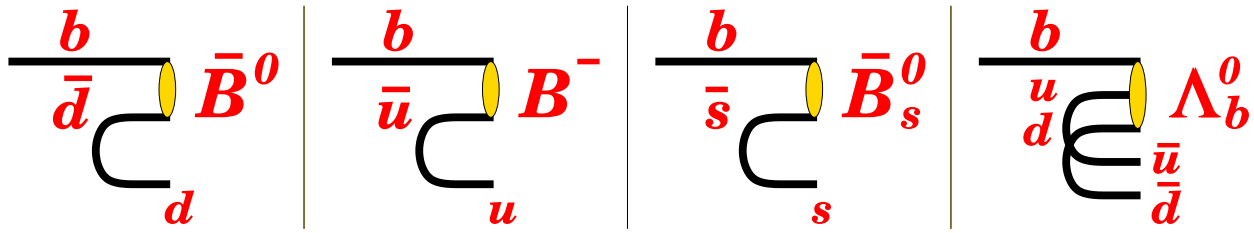

Figure 1.1: Schematic of b quark fragmentation into $\bar{B}$ hadrons.

the only semileptonic decay into that final state was the ground state $\bar{B}^0 \to \ell^- \bar{\nu} D^+$ decay, is

$$\begin{aligned} N(\ell^- D^+) &= N(\bar{B}^0) \times \mathcal{BR}(\bar{B}^0 \to \ell^- \bar{\nu}_\ell D^+) \\ &\quad \times \mathcal{BR}(D^+ \to K^- \pi^+ \pi^+) \times \varepsilon(\bar{B}^0 \to \ell^- \bar{\nu}_\ell D^+). \end{aligned} \tag{1.1}$$

The number of reconstructed $\ell^- D^+$ combination, $N(\ell^- D^+)$, can be related to the number of $\bar{B}^0$ mesons, $N(\bar{B}^0)$, produced in the fragmentation process by the branching ratio of the $\bar{B}^0 \to \ell^- \bar{\nu} D^+$ decay, multiplied by the branching ratio of the $D^+ \to K^- \pi^+ \pi^+$ charm decay, and the efficiencies for the entire decay chain to occur and be detected under operating conditions of the CDF detector. While most of the efficiencies are calculated from Monte Carlo, some efficiencies are not well-described by Monte Carlo and are instead determined from data. The real sample composition for the $\ell^- D^+$ signal is much more complicated than Eq. (1.1), with cross-talk from many excited charm states originating from the B^-, $\bar{B}^0$, and $\bar{B}^0_s$ mesons.

In Run I of the Fermilab Tevatron, the fraction of $\bar{B}^0_s$ mesons produced relative to the number of $\bar{B}^0$ mesons was measured $\sim 2\,\sigma$ higher at CDF [7] than the Large Electron Positron (LEP) e^+e^- collider measurements of this quantity [8]. The second of the Run I measurements, which followed a technique very similar to the one used in this measurement, found $f_s/(f_u+f_d) = 0.213 \pm 0.068$ and $f_{\Lambda_b}/(f_u+f_d) = 0.118 \pm 0.042$, assuming $f_u/f_d = 1$. The world averages of the fragmentation fractions taken from the PDG [9], which are dominated by the LEP results, are $f_u = f_d = (39.8 \pm 1.0)\%$, $f_s = (10.3 \pm 1.5)\%$, and $f_{b-baryon} = (10.0 \pm 1.7)\%$. In addition to the anomalous measurements of the fragmentation fractions at CDF Run I, the time-integrated, flavor averaged mixing parameter, $\bar{\chi} = f_d \chi_d + f_s \chi_s$, where χ_d and χ_s are the time-integrated mixing parameters of the $\bar{B}^0$ and $\bar{B}^0_s$ mesons, was also measured 2-3 σ higher at CDF than at LEP [10, 11]. This discrepancy in the value of $\bar{\chi}$ led to speculation that the value of $\bar{\chi}$ may be higher at the Tevatron because of the presence of new physics [12].

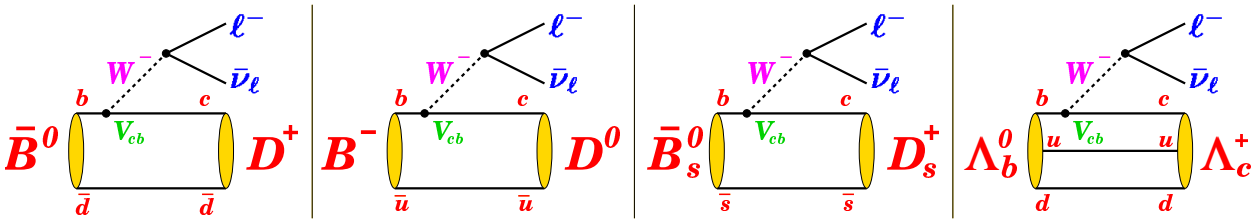

Figure 1.2: Diagram of semileptonic $\bar{B}$ hadron decays.

Another possibility is that the fragmentation fraction of $\bar{B}_s^0$ relative to $\bar{B}^0$ is simply higher at the Tevatron. Since the fragmentation process may be different at hadron colliders and e^+e^- colliders, the measurement of the fragmentation fractions in Run II with significantly improved statistics is clearly of interest.

The structure of this thesis is as follows. The Standard Model of particle physics is discussed in Chapter 2, with special emphasis on $\bar{B}$ hadron production and decays, then the Fermilab accelerator complex and CDF detector is explained in Chapter 3. The Monte Carlo used in the measurement is described in Chapter 4 and the lepton-charm signal reconstruction is discussed in Chapter 5. The sample composition used to relate the parent $\bar{B}$ hadrons to the lepton-charm signals is described in Chapter 6. Efficiencies determined both from data and Monte Carlo are discussed in Chapter 7, with particular attention given to the choice of $\bar{B}$ hadron transverse momentum spectrum in Chapter 8. The fit method used to extract the fragmentation fractions from the sample composition is detailed in Chapter 9, where both toy tests of the fit and fits to data are explained. Systematic uncertainties assigned to the measurement are described in Chapter 10 and the final results with all uncertainties are given in Chapter 11.

Chapter 2

Theoretical Framework

2.1 The Standard Model

The advent of the Standard Model of particle physics occurred with the development of electroweak theory in the early 1970's, which extended the theory of quantum electrodynamics (QED) [13] to include the weak interaction [14]. Following great success in predicting electroweak couplings and decay rates, the Standard Model was extended to include the strong interaction with the development of quantum chromodynamics (QCD) in the mid-1970's. With the inclusion of the color field, the Standard Model has proved remarkably robust. As much as physicists might wish for the contrary, no fundamental problems with the Standard Model have been uncovered in the past thirty years. In the 1990's many electroweak measurements made at LEP [11] confirmed the Standard Model to high precision. One feature of the theory is that it does not predict any of the masses of its three fundamental quark and lepton families or gauge boson masses, which are listed with their Standard Model SU(3)×SU(2)×U(1) gauge group representations in Table 2.1. The SU(3) symmetry is related to the color symmetries of QCD, while the SU(2) symmetry describes the left and right-handedness of the weak interaction and the U(1) symmetry describes the electromagnetic field. Local gauge invariance in field theories is a requirement for the renormalizability (*i.e.* the ability to subtract off the infinities) of the theory.

The large number of free parameters in the Standard Model is both one of its strengths and weaknesses, since a theory which requires so much external information in order to predict relevant numbers is hardly satisfactory as a fundamental explanation of the universe. Interesting recent discoveries like neutrino oscillations [15], while not explicitly included as a part of the Standard Model, do not challenge its underpinnings. The Higgs boson [16], from which all other fundamental particles derive their masses, is the only particle in the Standard Model that has yet to be observed experimentally. The masses of the quarks and gauge bosons are listed in Table 2.2.

Color SU(3) was developed to explain the flavor SU(3) symmetry observed in the meson and baryon mass spectra measured in the late 1960's [17]. The measured half-integral spin of baryons, which are interpreted as three-quark states, necessitated half-integral spin for the quarks as well. Color was introduced because spin-$\frac{3}{2}$ baryons containing three quarks of the same flavor would otherwise be in a completely symmetric state of space, spin, and

Field	SU(3)	SU(2)	U(1)
$\begin{pmatrix} u_L^i \\ d_L^i \end{pmatrix}$	**3**	**2**	$\frac{1}{6}$
u_R^i	**3**	**1**	$\frac{2}{3}$
d_R^i	**3**	**1**	$-\frac{1}{3}$
$\begin{pmatrix} \nu_L^i \\ e_L^i \end{pmatrix}$	**1**	**2**	$-\frac{1}{2}$
e_R^i	**1**	**1**	-1
$\begin{pmatrix} H^+ \\ H^0 \end{pmatrix}$	**1**	**2**	$\frac{1}{2}$

Table 2.1: Gauge group representations of the i^{th} family of quarks and leptons in the Standard Model, where $\psi_L^i = \frac{1}{2}(1-\gamma_5)\psi$ and $\psi_R^i = \frac{1}{2}(1+\gamma_5)\psi$.

Particle	Mass [GeV/c^2]
u	$(1.5-4)\times 10^{-3}$
d	$(4-8)\times 10^{-3}$
s	$0.080-0.130$
c	$1.15-1.35$
b	$4.6-4.9$
t	174.3 ± 5.1
W	80.425 ± 0.038
Z	90.1876 ± 0.0021

Table 2.2: Masses of the quarks and gauge bosons. The masses of the quarks, with the exception of the top quark, have been estimated, while the gauge bosons and the top quark mass have been experimentally measured [9].

$SU(3)_{flavor}$. Since fermions are required by Fermi-Dirac statistics to have a totally anti-symmetric wave function, an additional quantum number called color was introduced. Three colors (*e.g.* red, green, and blue) are carried both by quarks and gluons, the latter of which are the propagators of the strong force. Because gluons also carry color, gluon self-interaction occurs in QCD, shown in Figure 2.1. The self-interaction of field propagators is not a feature of Abelian gauge theories like QED. Another constraint on the color hypothesis is that only color singlets can occur in nature: mesons $q_A\bar{q}^A$ and baryons $\epsilon_{ABC}q^Aq^Bq^C$, where ϵ_{ABC} is the antisymmetric tensor and $A, B, C = 1...8$ run over the eight color degrees of freedom of the gluon field. The QCD Lagrangian for quarks and gluons is [9]

$$\mathcal{L}_{QCD} = -\frac{1}{4}G^A_{\mu\nu}G^{A\mu\nu} + i\sum_q \bar{\psi}^i_q\gamma^\mu(D_\mu)_{ij}\psi^j_q - \sum_q m_q\bar{\psi}^i_q\psi_{qi}, \tag{2.1}$$

where the gluon field strength tensor $G^A_{\mu\nu}$ is

$$G^A_{\mu\nu} = \partial_\mu\mathcal{A}^A_\nu - \partial_\nu\mathcal{A}^A_\mu - g_s f_{ABC}\mathcal{A}^B_\mu\mathcal{A}^C_\nu, \tag{2.2}$$

and the SU(3) color covariant derivative $(D_\mu)_{ij}$ is

$$(D_\mu)_{ij} = \delta_{ij}\partial_\mu + ig_s\sum_A \frac{\lambda^A_{i,j}}{2}\mathcal{A}^A_\mu. \tag{2.3}$$

ψ^i_q are the Dirac spinors associated with the i^{th} color (of three) and q^{th} flavor and the $\mathcal{A}^A_\mu$ are the gluon fields. g_s is the QCD coupling constant and λ_A are the eight Hermitian and traceless Gell-Mann matrices [18]. The third term in the $G^A_{\mu\nu}$ tensor is the non-Abelian term which distinguishes QCD from QED. In an Abelian group, all of the generators of the group commute. In a non-Abelian group, the generators do not commute, and the commutation relations are governed by the structure constants of the group algebra. f_{ABC} are the structure constants of the SU(3) group, defined by the commutation relation of the eight generators of the theory,

$$[\lambda_A, \lambda_B] = 2if_{ABC}\lambda_C. \tag{2.4}$$

The effective QCD coupling strength is given by $\alpha_s(\mu) = g_s^2(\mu)/4\pi$, where μ is the scale introduced by renormalization. The μ dependence of α_s is commonly parameterized in terms of the dimensional quantity Λ_{QCD}, which "represents the scale at which the coupling would diverge if extrapolated outside the perturbative domain" [17]. One of the peculiar features

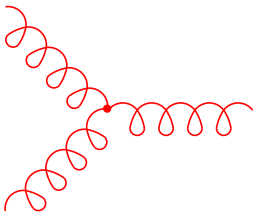

Figure 2.1: Gluon self-interaction.

of QCD is asymptotic freedom [5, 19], where $\alpha_s \to 0$ at infinite energies or infinitesimally small distances, while QCD becomes strongly coupled at energies of $\Lambda_{QCD} \sim 200$ MeV. Consequently, perturbation theory works well at short distances (large momentum transfers), but breaks down for larger distances. Since the u, d, and s quarks have masses $m_q \ll \Lambda_{QCD}$, they can be treated as massless in the theory to a good approximation. Conversely, the c, b, and t quarks have masses $m_Q \gg \Lambda_{QCD}$. In this case it is possible to use an effective theory, where the heavy quarks are integrated out of the theory, to describe processes that occur well below the masses of these quarks. Transitions involving a heavy quark Q can then be included in the effective theory with non-renormalizable operators suppressed by factors of $1/m_Q$.

The electroweak Lagrangian, based on the SU(2)×U(1) gauge group, predicts the electromagnetic and weak interactions of all known particles. The left-handed fermion fields transform as doublets under SU(2), while the right-handed fields form SU(2) singlets. The Lagrangian for the fermion fields, ψ_i, after spontaneous symmetry breaking, which is introduced to give mass to the Gauge bosons and fermions, is [9]

$$\begin{aligned}
\mathcal{L}_{EW,fermions} &= \sum_{i=1..3} \bar{\psi}_i \left(i\partial\!\!\!/ - m_i - \frac{g m_i H}{2M_W} \right) \psi_i \\
&\quad - \frac{g}{2\sqrt{2}} \sum_{i=1..3} \bar{\psi}_i \gamma^\mu (1-\gamma^5)(T^+ W_\mu^+ + T^- W_\mu^-) \psi_i \\
&\quad - e \sum_{i=1..3} \bar{\psi}_i \gamma^\mu \psi_i A_\mu \\
&\quad - \frac{g}{2\cos\theta_W} \sum_{i=1..3} \bar{\psi}_i \gamma^\mu (g_V^i - g_A^i \gamma^5) \psi_i Z_\mu,
\end{aligned} \tag{2.5}$$

where the weak (Weinberg) angle $\theta_W \equiv \tan^{-1}(g'/g)$, the positron electric charge $e = g \sin\theta_W$, the massless photon field $A_\mu \equiv B_\mu \cos\theta_W + W_\mu^3 \sin\theta_W$, and the massive charged $W_\mu^\pm \equiv (W_\mu^1 \mp i W_\mu^2)$ and neutral $Z_\mu \equiv -B_\mu \sin\theta_W + W_\mu^3 \cos\theta_W$ boson fields. T^+ and T^- are the weak isospin raising and lowering operators, while W_μ^i are the SU(2) gauge bosons and B_μ is the gauge boson for the U(1) group. The vector coupling, $g_V^i \equiv t_{3L}(i) - 2q_i \sin^2\theta_W$, depends on the Weinberg angle, the electric charge of the fermion, q_i, in units of e, and the weak isospin of the i^th fermion, $t_{3L}(i)$. The axial vector coupling, $g_A \equiv t_{3L}(i)$, depends only on the weak isospin of the i^{th} fermion. The electroweak Lagrangian governs the semileptonic decays of $\bar{B}$ hadrons which are used in this measurement.

The weak eigenstates of the fermion fields are not the mass eigenstates, so that the fermion fields

$$\psi_i = \begin{pmatrix} u_i \\ d_i' \end{pmatrix} \tag{2.6}$$

of the i^{th} fermion family which appear in the electroweak Lagrangian are related to the mass eigenstates of the QCD Lagrangian by

$$d_i' \equiv \sum_j V_{ij} d_j, \tag{2.7}$$

where V_{ij} for $i, j = 1, 2, 3$ is the Cabibbo-Kobayashi-Masakawa (CKM) [20] matrix. The CKM matrix determines the relative transition rates between "up" type quarks and "down"

type quarks in weak decays. The standard parameterization [9] of the CKM matrix uses three angles θ_{12}, θ_{23}, θ_{13}, and a phase, δ_{13},

$$\begin{aligned} V &= \begin{pmatrix} V_{ud} & V_{us} & V_{ub} \\ V_{cd} & V_{cs} & V_{cb} \\ V_{td} & V_{ts} & V_{tb} \end{pmatrix} \\ &= \begin{pmatrix} c_{12}c_{13} & s_{12}c_{13} & s_{13}e^{-i\delta_{13}} \\ -s_{12}c_{23} - c_{12}s_{23}s_{13}e^{-i\delta_{13}} & c_{12}c_{23} - s_{12}s_{23}s_{13}e^{-i\delta_{13}} & s_{23}c_{13} \\ -s_{12}s_{23} - c_{12}c_{23}s_{13}e^{-i\delta_{13}} & -c_{12}s_{23} - s_{12}c_{23}s_{13}e^{-i\delta_{13}} & c_{23}c_{13} \end{pmatrix}, \end{aligned} \tag{2.8}$$

where $c_{ij} = \cos\theta_{ij}$ and $s_{ij} = \sin\theta_{ij}$. The imaginary terms lead to CP violation. CP violation has been experimentally observed in the K- and B-meson systems and can be parameterized theoretically, but its origin is fundamentally unknown. Although the CKM matrix has been parameterized in several ways, one of the clearest is the so-called Wolfenstein parameterization [21], which expresses the elements as an expansion in the Cabibbo angle (θ_{12}), $\lambda \equiv \sin\theta_{12}$,

$$V = \begin{pmatrix} 1-\lambda^2/2 & \lambda & A\lambda^3(\rho - i\eta) \\ -\lambda & 1-\lambda^2/2 & A\lambda^2 \\ A\lambda^3(1-\rho-i\eta) & -A\lambda^2 & 1 \end{pmatrix} + \mathcal{O}(\lambda^4), \tag{2.9}$$

where A, ρ, and η are real numbers. In the semileptonic decays of $\bar{B}$ hadrons considered in this measurement, the relevant CKM matrix element is V_{cb}, which has been measured to lie within the range $[0.038, 0.044]$ with a 90% confidence level [9].

In $p\bar{p}$ collisions, the b quark production processes (see Section 2.2) are not known at all orders in QCD and must be inferred from QCD models and measurements of the b quark transverse momentum spectrum. Once a b quark is produced, it combines with an anti-quark or with two other quarks through fragmentation processes to form a $\bar{B}$ hadron. Theoretical estimates of these fragmentation processes (see Section 2.3) are also dependent on empirical models. In the past fifteen years, theoretical calculations of the properties of $\bar{B}$ hadrons containing one heavy quark Q and a light anti-quark $\bar{q}$ (or two light quarks qq) have been facilitated with the development of Heavy Quark Effective Theory (HQET) [22]. This effective theory allows the b quark mass to be treated as infinite relative to the light quark masses and greatly simplifies the expansion of the form factors. The spectator model, which assumes that the heavy quark decay is independent of the light quark flavors, is used in this measurement to predict semileptonic $\bar{B}$ mesons decay rates.

2.2 $\bar{B}$ Production

Three categories of b quark production are present in $p\bar{p}$ collisions at $\sqrt{s} = 1.96$ TeV, where a minimum transverse momentum of $p_T(b) > 5$ GeV/c and central b production (rapidity $|y \equiv \frac{E_{||}-p_{||}}{E_{\perp}-p_{\perp}}| \leq 1$) is considered [23]. Feynman diagrams for different production processes involving gluons are shown in Figure 2.2. The dominant mode of b production at high transverse momenta is flavor excitation, which occurs when a gluon scatters off of a quark in

the proton-anti-proton interaction and produces a b quark via subprocesses like $g+b \to g+b$, $q+b \to q+b$, or $\bar{q}+b \to \bar{q}+b$. Flavor creation (see Figure 2.2) via the subprocesses $q+\bar{q} \to b+\bar{b}$ or $g+g \to b+\bar{b}$ likely contributes less than 35% to the total rate of b production and generally results in a softer b quark transverse momentum spectrum than flavor excitation. The third category of b quark production is in parton shower/fragmentation processes, in which only gluons or light quarks participate in the 2-to-2 hard parton scattering subprocess. Predictions for the rates of these shower subprocesses vary considerably depending on the QCD model used, but parton showers/fragmentation might contribute to the total b production at a level comparable to flavor creation. Gluon splitting, in which a gluon is scattered between two partons and then splits to form a $b\bar{b}$ quark pair, is included in this third category of b production. It is a significant mode of b production at low transverse momenta.

2.3 $\bar{B}$ Fragmentation

Theoretical predictions of the fragmentation of heavy quarks have been made by Petersen *et al.* [24] in the early 1980's. These predictions rest upon the assumption that the heavy quark Q and the hadron formed from the heavy quark, $H = Q\bar{q}$ or Qqq (plus gluons and light $q\bar{q}$ pairs), should have nearly the same energy and momentum, since attaching the light degrees of freedom is expected to decelerate the heavy quark Q very little. Considering a hadron $H = Q\bar{q}$ and light quark q produced by the fragmentation of the heavy quark Q, the energy transfer through fragmentation $\Delta E = E_H + E_q - E_Q$ is related to the transition amplitude,

$$\mathcal{A}(Q \to H + q) \propto \frac{1}{\Delta E}. \tag{2.10}$$

Assuming $m_H \simeq m_Q$, the energies can be expanded about the particles masses

$$\begin{aligned} \Delta E &= \sqrt{m_Q^2 + z^2 P^2} + \sqrt{m_q^2 + (1-z)^2 P^2} - \sqrt{m_Q^2 + P^2} \\ &\propto 1 - \frac{1}{z} - \frac{\epsilon_Q}{1-z}, \end{aligned} \tag{2.11}$$

where P is the momentum of the fragmenting heavy quark Q, $z = E_H/E_{max}$ is the fraction of energy carried by the hadron, zP is the fraction of momentum imparted to the hadron by Q, and $\epsilon_Q \approx m_q^2/m_Q^2$. The amplitude in Eq. (2.10) is squared and a factor of z^{-1} is included for longitudinal phase space to obtain the Petersen function for the fragmentation of heavy quarks

$$D_Q^H(z) = \frac{N}{z[1 - (1/z) - \epsilon_Q/(1-z)]^2}. \tag{2.12}$$

A sum over all hadrons containing Q,

$$\sum_{H_Q} \int D_Q^H(z) dz = 1, \tag{2.13}$$

fixes the normalization N. The maximum of fragmentation function occurs at $z \simeq 1 - 2\epsilon_Q$ and the distribution has a width of $\sim \epsilon_Q$. $\epsilon_c = 0.15$ in the original Petersen determination

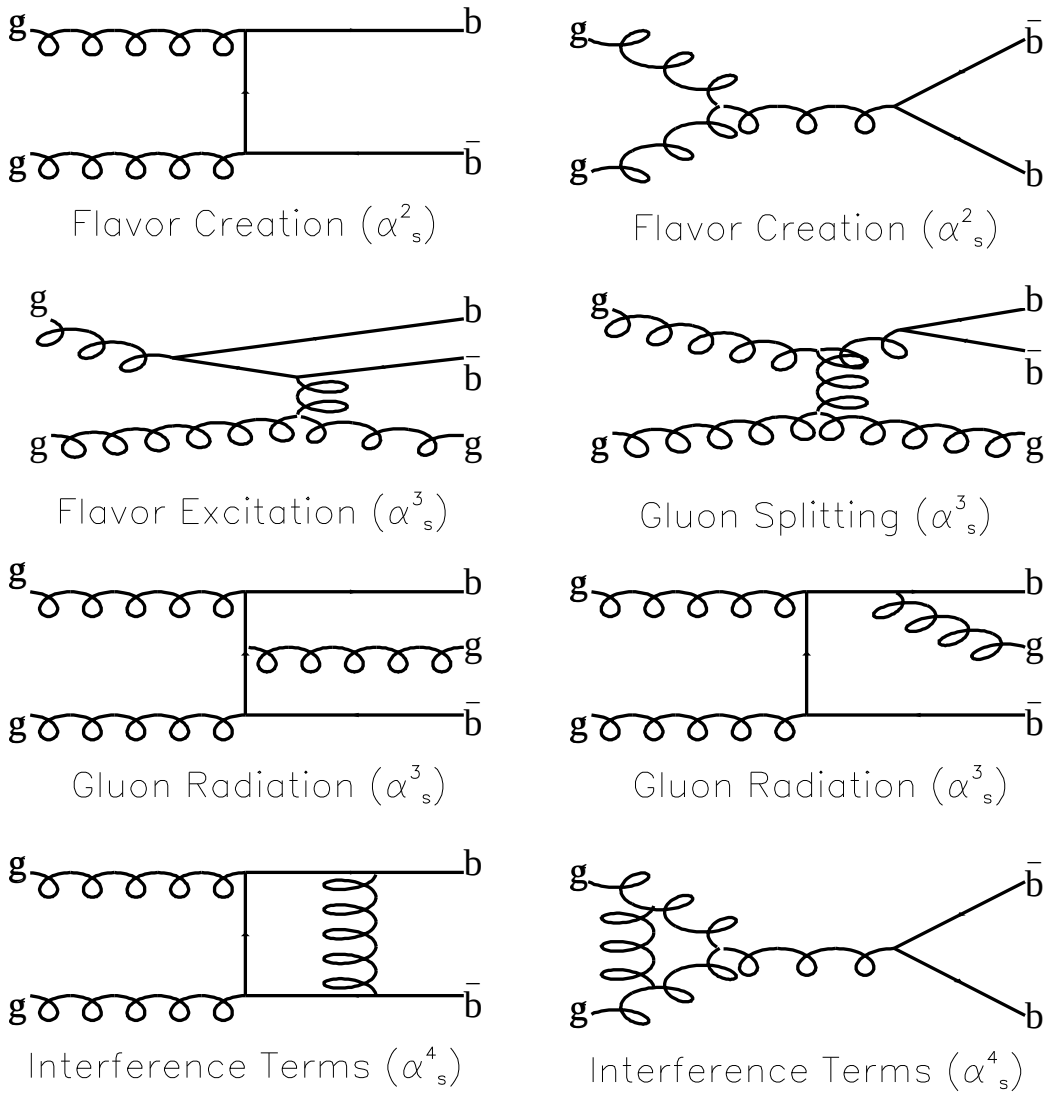

Figure 2.2: $\bar{B}$ production processes via gluons in $p\bar{p}$ collisions, taken from Ref [25].

and $\epsilon_b = (m_c/m_b)^2\epsilon_c$. A value of $\epsilon_b = 0.006$ is commonly chosen as the input Petersen fragmentation value in Monte Carlo simulations used at CDF. This measurement does not use the Petersen fragmentation model, instead relying on a measured p_T spectrum determined from data for the Monte Carlo generation (see Chapter 4).

2.4 $\bar{B}$ Decays

The masses, quark content, and quantum numbers of the bottom and charm hadrons considered in this measurement are listed in Table 2.3. These quantum numbers govern the matrix elements needed to describe the decay rates, angular correlations between daughter particles, polarizations, etc. A number of predictions in good agreement with measurements of $\bar{B}$ meson decay rates have been made within the framework of HQET, most notably by Isgur, Scora, Grinstein, and Wise [26, 27], among others. While this theoretical work is on reasonably solid ground, not as much progress has been made in predicting b-baryon decay rates, partly due to the dearth of Λ_b^0 data available relative to the abundance of $\bar{B}$ meson data. A recent constituent quark model calculation from Pervin, Capstick, and Roberts [28] is used to describe the Λ_b^0 baryon decays in this measurement.

2.4.1 Heavy Quark Effective Theory

HQET is developed around the fact that, since $m_q \ll \Lambda_{QCD}$ and $m_Q \gg \Lambda_{QCD}$, the heavy degrees of freedom can be integrated out of the QCD Lagrangian. Non-perturbative corrections lead to a typical scale of momentum transfer between the quarks in hadrons with one heavy quark of order Λ_{QCD}. Hence, the velocity v of the heavy quark is nearly unchanged by strong interaction effects, although the momentum is changed by an amount of the order Λ_{QCD}, since $\Delta v = \Delta p/m_Q$. As $m_Q \to \infty$ the heavy quark can be described by a four velocity, v, which is constant in time. In this limit the interaction of heavy quarks within heavy hadrons is identical; gluons provide the only source of strong interaction with heavy quarks, since the quark-quark interactions have been integrated out of the Lagrangian. A useful relation in the decays of $\bar{B}$ hadrons into charm hadrons is $q^2 = (p - p')^2$, where p is the parent four momentum and p' is the daughter four momentum. In heavy quark effective theory, the momentum transfer is typically described in terms of four velocities $w = v \cdot v'$, where the four velocity $v^\mu \equiv p^\mu/m$ is related to the classical momentum. In the rest frame of the $\bar{B}$ hadron $v = (1, 0, 0, 0)$, so that $w = \left(\frac{E_C}{m_C}, 0, 0, 0\right)$. More generally, w can be related to q^2 in any reference frame,

$$w = \frac{m_B^2 + m_C^2 - q^2}{2m_B m_C}. \tag{2.14}$$

In the effective theory the velocity of the parent (m_{Q_i}) and daughter (m_{Q_j}) heavy hadrons are essentially fixed, so that p^μ/m_Q is constant even as $m_Q \to \infty$. Thus, the effective theory relates hadrons with the same velocities, although their masses and momenta may be quite different. The weak currents in the effective theory

$$\mathcal{V}_\mu \equiv \bar{\mathcal{Q}}_j \gamma_\mu \mathcal{Q}_i \tag{2.15}$$

$$\mathcal{A}_\mu \equiv \bar{\mathcal{Q}}_j \gamma_\mu \gamma_5 \mathcal{Q}_i, \tag{2.16}$$

Hadron	Mass [MeV/c^2]	Lifetime [ps]	Quark Content	J^P	s_ℓ
B^-	5279.0±0.5	1.671±0.018	$b\bar{u}$	0^-	1/2
$\bar{B}^0$	5279.4±0.5	1.536±0.014	$b\bar{d}$	0^-	1/2
$\bar{B}_s^0$	5396.6±2.4	1.461±0.057	$b\bar{s}$	0^-	1/2
Λ_b^0	5624±9	1.229±0.080	bud	$1/2^+$	0
D^+	1869.4±0.5	1.040±0.007	$c\bar{d}$	0^-	1/2
D^0	1864.6±0.5	0.4103±0.0015	$c\bar{u}$	0^-	1/2
D_s^+	1968.3±0.5	0.490±0.009	$c\bar{s}$	0^-	1/2
Λ_c^+	2284.9±0.6	0.200±0.006	cud	$1/2^+$	0
D^{*+}	2010.0±0.5		$c\bar{d}$	1^-	1/2
D^{*0}	2006.7±0.5		$c\bar{u}$	1^-	1/2
D_s^{*+}	2112.1±0.7		$c\bar{s}$	1^-	1/2
D_0^{*+}	2400±???		$c\bar{d}$	0^+	1/2
$D_1^{'+}$	2461±???		$c\bar{d}$	1^+	1/2
D_1^+	2427±???		$c\bar{d}$	1^+	1/2
D_2^{*+}	2459±4		$c\bar{d}$	2^+	3/2
D_0^{*0}	2400±???		$c\bar{d}$	0^+	1/2
$D_1^{'0}$	2461±???		$c\bar{d}$	1^+	1/2
D_1^0	2422.2±1.8		$c\bar{d}$	1^+	1/2
D_2^{*0}	2458.9±2.0		$c\bar{d}$	2^+	3/2
D_{s0}^{*+}	2317.4±0.9		$c\bar{s}$	0^+	1/2
$D_{s1}^{'+}$	2459.3±1.3		$c\bar{s}$	1^+	1/2
D_{s1}^+	2535.35±0.60		$c\bar{s}$	1^+	1/2
D_{s2}^{*+}	2572.4±1.5		$c\bar{s}$	2^+	3/2
$\Lambda_c^+(2593)$	2593.9±0.8		cud	$1/2^-$	0
$\Lambda_c^+(2625)$	2626.6±0.8		cud	$3/2^+$	0
$\Sigma_c(2455)^{++}$	2452.5±0.6		cuu	$1/2^+$	1
$\Sigma_c(2455)^+$	2451.3±0.7		cud	$1/2^+$	1
$\Sigma_c(2455)^0$	2452.2±0.6		cdd	$1/2^+$	1

Table 2.3: Masses, lifetimes, and quantum numbers of bottom and charm hadrons considered, where $\mathbf{S}_\ell \equiv \mathbf{J} - \mathbf{S}_Q$ and $P = (-1)^{L+1}$. All numbers have been taken from the PDG, except those without uncertainties assigned to the mass, which are taken from the `EvtGen` table.

can be related to the weak currents in the complete theory, $V_\mu \equiv \bar{Q}_j \gamma_\mu Q_i$ and $A_\mu \equiv \bar{Q}_j \gamma_\mu \gamma_5 Q_i$, by a coefficient function

$$J_\mu = C_{ji} \mathcal{J}_\mu + ..., \tag{2.17}$$

where $J_\mu = V_\mu$ or A_μ and $\mathcal{J}_\mu = \mathcal{V}_\mu$ or $\mathcal{A}_\mu$ [27], which can be calculated in the leading-logarithmic approximation [29, 30],

$$C_{ji}(w) = \left[\frac{\alpha_s(m_{Q_i})}{\alpha_s(m_{Q_j})}\right]^{a_I} \left[\frac{\alpha_s(m_{Q_j})}{\alpha_s(\mu)}\right]^{a_L}, \tag{2.18}$$

where

$$a_I = -\frac{6}{25} \tag{2.19}$$

for $b \to c$ and

$$a_L = \frac{8[wr(w) - 1]}{27}, \tag{2.20}$$

for

$$r(w) = \frac{1}{\sqrt{w^2 - 1}} \ln(w + \sqrt{w^2 - 1}). \tag{2.21}$$

Although these relations pertain to generic heavy quark decays, discussions of matrix elements and form factors in the following sections are given for $\bar{B}$ decays.

2.4.2 Matrix Elements of Semileptonic $\bar{B}$ Decays

Semileptonic $\bar{B} \to \ell^- \bar{\nu} D X$ decays can be generically described by the amplitude

$$T = \frac{G_f}{\sqrt{2}} V_{cb} \bar{u}_\ell \gamma^\mu (1 - \gamma^5) v_{\bar{\nu}} \langle X_c(p', s') | \bar{c} \gamma_\mu (1 - \gamma_5) b | X_b(p, s) \rangle. \tag{2.22}$$

While the leptonic current $L^\mu = \bar{u}_\ell \gamma^\mu (1 - \gamma^5) v_{\bar{\nu}}$ can be calculated explicitly, the hadronic current $J_\mu = \bar{c} \gamma_\mu (1 - \gamma_5) b$ has not been calculated from first principles. Instead, the hadronic current is typically expanded in form factors, which are model dependent. Since the hadronic current must transform as a four vector, the form factors can only depend on the Lorentz invariants, namely p^2, p'^2, and $p \cdot p'$, which can be expressed through q^2. This is straightforward to see since the four momenta of the parent and daughter hadron are the only four vectors involved in the decays. The form factors used in the generation of the Monte Carlo will be discussed further in Chapter 4.

The complete theory vector $V_\mu = \bar{c} \gamma_\mu b$ and axial vector $A_\mu = \bar{c} \gamma_\mu \gamma_5 b$ currents can be phenomenologically related to the Lorentz invariants for the $\bar{B} \to D$ meson decays by [22]

$$\langle D(p') | V_\mu | \bar{B}(p) \rangle = f_+(q^2)(p + p')_\mu + f_-(q^2)(p - p')_\mu, \tag{2.23}$$

while for the $\bar{B} \to D^*$ meson decays

$$\langle D^*(p', \varepsilon) | V_\mu | \bar{B}(p) \rangle = g(q^2) \varepsilon_{\mu\nu\alpha\beta} \varepsilon^{*\nu} (p + p')^\alpha (p - p')^\beta, \tag{2.24}$$

$$\langle D^*(p', \varepsilon) | A_\mu | \bar{B}(p) \rangle = -if(q^2) \varepsilon^*_\mu - i\varepsilon^* \cdot p [a_+(q^2)(p + p')_\mu + a_-(q^2)(p - p')_\mu], \tag{2.25}$$

where ε is the polarization vector of the D^* which satisfies $p' \cdot \varepsilon = 0$ and all quantities which depend on q^2 (*e.g* $f_\pm(q^2)$, $g(q^2)$, $a_\pm(q^2)$, etc.) are form factors in the decays. The matrix element for decays to D^{**} with quantum numbers 1^+ are similar to those for the D^* decays, which have quantum numbers 1^-, except for an extra factor of γ_5 in both the vector and axial vector currents, which is needed for the difference in parity between the parent and daughter meson. The $\bar{B} \to D_2$ matrix elements are [27]

$$\begin{aligned}
\langle D_2(p',\varepsilon)|V_\mu|\bar{B}(p)\rangle &= ih(q^2)\varepsilon_{\mu\nu\lambda\rho}\varepsilon^{*\nu\alpha}p_\alpha(p+p')^\lambda(p-p')^\rho, && (2.26)\\
\langle D_2(p',\varepsilon)|A_\mu|\bar{B}(p)\rangle &= k(q^2)\varepsilon^*_{\mu\nu}p^\nu + \varepsilon^*_{\alpha\beta}p^\alpha p^\beta[b_+(q^2)(p+p')_\mu \\
&\qquad + b_-(q^2)(p-p')_\mu]. && (2.27)
\end{aligned}$$

The vector and axial vector baryon currents are related to the Lorentz invariants by [28]

$$\begin{aligned}
\langle \Lambda_c^+|V_\mu|\Lambda_b^0\rangle &= \bar{u}(p',s')\left(F_1\gamma_\mu + F_2\frac{p_\mu}{m_{\Lambda_b}} + F_3\frac{p'_\mu}{m_{\Lambda_c}}\right)u(p,s), && (2.28)\\
\langle \Lambda_c^+|A_\mu|\Lambda_b^0\rangle &= \bar{u}(p',s')\left(G_1\gamma_\mu + G_2\frac{p_\mu}{m_{\Lambda_b}} + G_3\frac{p'_\mu}{m_{\Lambda_c}}\right)\gamma_5 u(p,s), && (2.29)
\end{aligned}$$

$$\begin{aligned}
\langle \Lambda_c(2593)^+|V_\mu|\Lambda_b^0\rangle &= \bar{u}(p',s')\left(F_1\gamma_\mu + F_2\frac{p_\mu}{m_{\Lambda_b}} + F_3\frac{p'_\mu}{m_{\Lambda_c}}\right)\gamma_5 u(p,s), && (2.30)\\
\langle \Lambda_c(2593)^+|A_\mu|\Lambda_b^0\rangle &= \bar{u}(p',s')\left(G_1\gamma_\mu + G_2\frac{p_\mu}{m_{\Lambda_b}} + G_3\frac{p'_\mu}{m_{\Lambda_c}}\right)u(p,s), && (2.31)
\end{aligned}$$

and

$$\begin{aligned}
\langle \Lambda_c(2625)^+|V_\mu|\Lambda_b^0\rangle &= \bar{u}^\alpha(p',s')\left[\frac{p_\alpha}{m_{\Lambda_b}}\left(F_1\gamma_\mu + F_2\frac{p_\mu}{m_{\Lambda_b}} + F_3\frac{p'_\mu}{m_{\Lambda_c}}\right)\right. \\
&\qquad \left. + F_4 g_{\alpha\mu}\right]u(p,s), && (2.32)\\
\langle \Lambda_c(2625)^+|A_\mu|\Lambda_b^0\rangle &= \bar{u}^\alpha(p',s')\left[\frac{p_\alpha}{m_{\Lambda_b}}\left(G_1\gamma_\mu + G_2\frac{p_\mu}{m_{\Lambda_b}} + G_3\frac{p'_\mu}{m_{\Lambda_c}}\right)\right. \\
&\qquad \left. + G_4 g_{\alpha\mu}\right]\gamma_5 u(p,s), && (2.33)
\end{aligned}$$

where $F_i \equiv F_i(q^2)$ and $G_i \equiv G_i(q^2)$ are distinct for each of the three decays and $u(p,s)$ and $\bar{u}(p',s') = u^\dagger(p',s')\gamma^0$ are Dirac spinors. $\bar{u}^\alpha(p',s')$ is the Rarita-Schwinger spinor [31], which is needed for spin-$\frac{3}{2}$ fermions. The Rarita-Schwinger spinor can be decomposed into a spin-$\frac{1}{2}$ Dirac spinor and polarization vector ε^α, which corresponds to the spin-1 part,

$$\bar{u}^\alpha(p',s') = \varepsilon^\alpha \bar{u}(p',s'). \tag{2.34}$$

The polarization vector again satisfies $p' \cdot \varepsilon = 0$, so that the Rarita-Schwinger spinor satisfies $p'_\alpha \bar{u}^\alpha(p',s') = p'_\alpha \varepsilon^\alpha \bar{u}(p',s') = 0$.

In the Λ_b^0 rest frame, the polarization vector can be written as $\varepsilon^\alpha(\vec{0}, M) = (0, \vec{e}(M))$, where $M = \pm 1$ corresponds to transverse polarization and $M = 0$ implies longitudinal polarization, such that [32]

$$\vec{e}(\pm 1) = \frac{1}{\sqrt{2}}(\mp 1, -i, 0), \tag{2.35}$$

$$\vec{e}(0) = (0, 0, 1). \tag{2.36}$$

The four spin states of the Rarita-Schwinger spinor can then be written as

$$\bar{u}^\alpha(\pm\frac{3}{2}) = \varepsilon^\alpha(\pm 1)u(\pm\frac{1}{2}), \tag{2.37}$$

$$\bar{u}^\alpha(\pm\frac{3}{2}) = \sqrt{\frac{1}{3}}\varepsilon^\alpha(\pm 1)u(\mp\frac{1}{2}) + \sqrt{\frac{2}{3}}\varepsilon^\alpha(0)u(\pm\frac{1}{2}). \tag{2.38}$$

2.4.3 Spectator Model

In the spectator model, the light quark degrees of freedom are treated as "spectators", wholly unaffected by the transition of the b quark. This assumption simplifies the number of predictions for $\bar{B}$ decay rates, so that the transition rate is the same regardless of the flavor of the spectator quark. This is believed to be a reasonably good description of $\bar{B}$ mesons, but it is not as reliable for the Λ_b^0 baryons.

In order to determine the semileptonic branching ratios of the $\bar{B}$ meson decays, this measurement makes use of the spectator model prediction assuming the partial width of the semileptonic decays of $\bar{B}$ mesons are equal,

$$\Gamma(\bar{B}^0 \to \ell^- \bar{\nu}_\ell X) = \Gamma(B^- \to \ell^- \bar{\nu}_\ell X) = \Gamma(\bar{B}_s^0 \to \ell^- \bar{\nu}_\ell X), \tag{2.39}$$

where

$$\Gamma(B \to \ell\bar{\nu}X) = \frac{1}{\tau(B)}\mathcal{BR}(B \to \ell\bar{\nu}X). \tag{2.40}$$

This assumption greatly simplifies the measurement, since the direct measurements of the semileptonic branching ratios are generally dependent on the fragmentation fractions.

From the spectator model, the partial widths of the semileptonic $\bar{B}$ meson decays into the pseudoscalar D mesons are also expected to be equal,

$$\Gamma(\bar{B}^0 \to \ell^- \bar{\nu}_\ell D^+) = \Gamma(B^- \to \ell^- \bar{\nu}_\ell D^0) = \Gamma(\bar{B}_s^0 \to \ell^- \bar{\nu}_\ell D_s^+) \equiv \Gamma, \tag{2.41}$$

$$\Gamma(\bar{B}^0 \to \ell^- \bar{\nu}_\ell D^{*+}) = \Gamma(B^- \to \ell^- \bar{\nu}_\ell D^{*0}) = \Gamma(\bar{B}_s^0 \to \ell^- \bar{\nu}_\ell D_s^{*+}) \equiv \Gamma^*, \tag{2.42}$$

$$\Gamma(\bar{B}^0 \to \ell^- \bar{\nu}_\ell D^{**+}) = \Gamma(B^- \to \ell^- \bar{\nu}_\ell D^{**0}) = \Gamma(\bar{B}_s^0 \to \ell^- \bar{\nu}_\ell D_s^{**+}) \equiv \Gamma^{**}. \tag{2.43}$$

$$\tag{2.44}$$

The additional constraint that

$$\Gamma(\bar{B} \to \ell\bar{\nu}_\ell D) + \Gamma^*(\bar{B} \to \ell\bar{\nu}_\ell D^*) + \Gamma^{**}(\bar{B} \to \ell\bar{\nu}_\ell D^{**}) = \Gamma(\bar{B} \to \ell\bar{\nu}_\ell X) \tag{2.45}$$

can also applied to use the well-measured $\bar{B} \to \ell^-\bar{\nu}D$ and $\bar{B} \to \ell^-\bar{\nu}D^*$ branching ratios to constrain the poorly measured $\bar{B} \to \ell^-\bar{\nu}D^{**}$ branching ratios. This constraint makes the D^{**}

partial width essentially an "everything else" parameter and includes non-resonant decays in addition to actual D^{**} decays. The right hand side of Eq. (2.45) includes the $b \to u\ell^-\bar{\nu}X$ transition as well as the $b \to c\ell^-\bar{\nu}X$. This additional part of the total width is ignored in this measurement, as it is suppressed by $\left|\frac{V_{ub}}{V_{cb}}\right|^2 \sim 0.002 - 0.017$ [9].

The Λ_b^0 baryon is not necessarily well-described by the spectator model, since the presence of the two additional quarks may affect the decay rates to the excited Λ_c^+ states relative to the excited D mesons. Instead, fixed branching ratios are used for the Λ_b^0 semileptonic branching ratios (see Chapter 6).

Chapter 3

Experimental Apparatus

The CDF experiment sits at site B0 of the Tevatron collider in the Fermilab accelerator complex, shown in Figure 3.1. The Tevatron ring collides thirty-six anti-circulating bunches of protons and anti-protons every 396 ns at a center-of-mass energy of 1,960 GeV in two interaction regions along the ring: B0, which is the site of the CDF experiment, and D0, where the D0 experiment [33] is located. Each proton bunch contains approximately two hundred billion protons, while each anti-proton bunch contains approximately twenty billion anti-protons. The stages in the production and acceleration of the particle and anti-particle beams are described below, followed by a description of the CDF experiment, with a focus on the parts of the detector which are relevant for the reconstruction of semileptonic $\bar{B}$ decays in this measurement.

3.1 Fermilab Accelerator Complex

The Fermilab accelerator complex was first established in 1969. Robert Wilson served as the charismatic first director of the lab and took an interest in the aesthetic development of the Fermilab site. The physics program began in 1972 with proton beam energies of 200 GeV accelerated in the main ring, now known as the Tevatron, and transported to the fixed target experimental areas. The colliding beam program, which collided protons and anti-protons, commenced in 1986 under the direction of Leon Lederman after a seven year development period. Initially a center-of-mass energy of 625 GeV was achieved, which was later increased to nearly 1 TeV. In order to facilitate the colliding beam program, the Main Injector was built adjacent to the main ring to act as a storage and accelerating device. Some of the machines in the accelerator complex, like the Cockcroft-Walton and the linear accelerator, are still in use more than thirty five years after their development. The current colliding beam program has six stages of acceleration for protons, which are described below. The anti-protons have a different sequence of production and acceleration, which is described after the acceleration sequence of the protons.

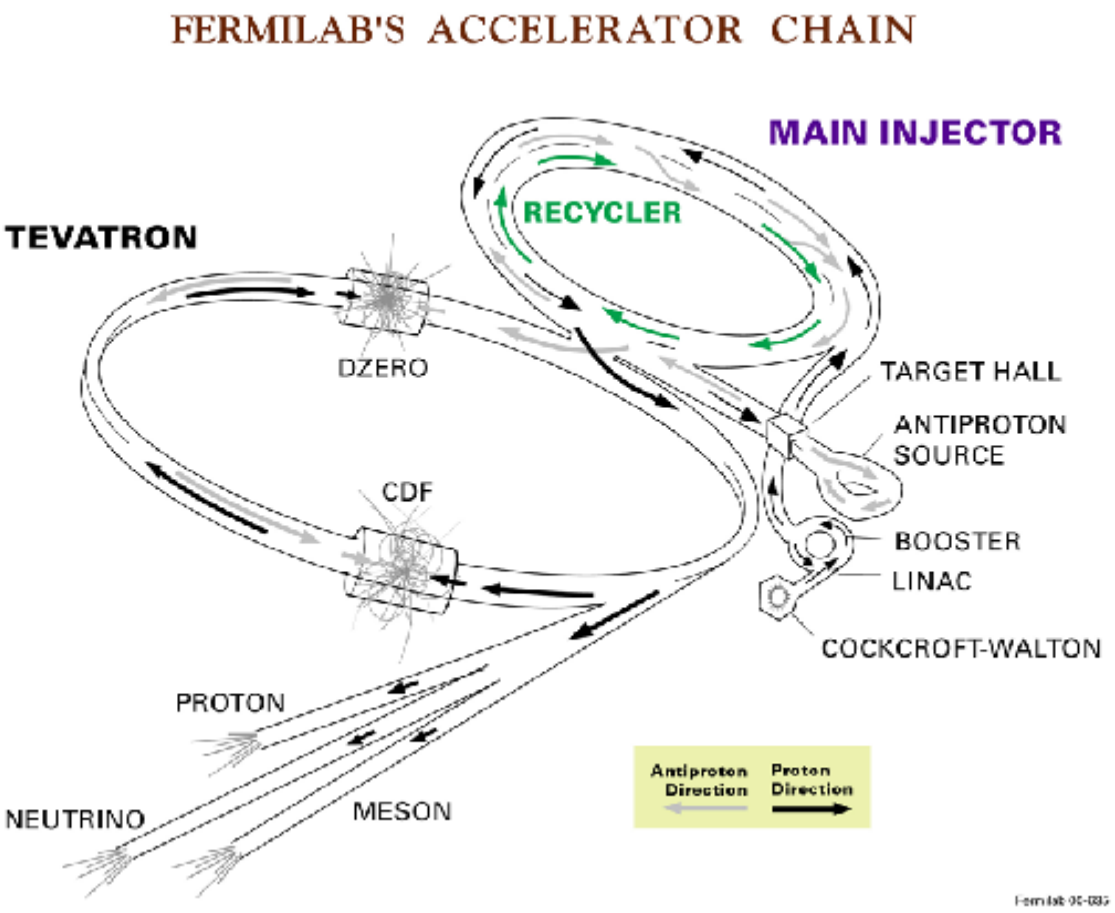

Figure 3.1: Fermilab accelerator complex.

3.1.1 Cockcroft-Walton Pre-Accelerator

The Cockcroft-Walton pre-accelerator is the first stage in the acceleration of protons. The pre-accelerator produces negatively charged hydrogen ions, H^-, from hydrogen gas, and accelerates the negatively charged ions to an energy of 750 keV. This beam of H^- is passed through a transfer line to the linear accelerator.

3.1.2 Linear Accelerator

The linear accelerator ("Linac") accelerates the hydrogen ions from 750 keV to 400 MeV. The Linac is made up of two types of RF stations, which are electromagnetically resonant cavities with naturally resonant frequencies that lie within the radio frequencies (RF) of the electromagnetic spectrum. The two stages of the Linac are a low energy drift tube Linac (DTL), which consists of the first five RF stations, and a higher energy side coupled cavity Linac (SCL), which are used in the last seven RF stations. Bunching is a natural feature of RF cavities, since the oscillating electric field pushes back the slow ions which do not enter the drift tube before the field becomes negative, while those ions which entered the drift tube while the field was still positive are accelerated. After accelerating the hydrogen ions to 400 MeV, the H^- are transferred to the Booster. The Linac is the only part of the accelerator which does not match the RF frequencies to the other accelerators.

3.1.3 Booster

The Booster accepts 400 MeV H^- ions from the Linac, strips the two electrons off, and accelerates the protons to an energy of 8 GeV. The Booster is a circular synchrotron with 18 RF cavities distributed about a ring with a 75 m radius. The 201 MHz frequencies of the bunches from the Linac do not match the 37.8 MHz frequencies of the RF cavities in the Booster. Consequently, the bunches must first be de-phased through a process called para-phasing. Since the bunches arriving from the Linac are out of phase with the Booster RF cavities, the bunch structure from the Linac begins to disappear and the beam becomes like a constant line of charge. After all of the beam has been injected, the cavities eventually come into phase with each other, and a new 37.8 MHz bunch structure is formed, which in turn is passed to the Main Injector once the beam has been accelerated to 8 GeV.

3.1.4 Main Injector

The Main Injector is the second to last stage of proton acceleration, bringing protons up to an energy of 150 GeV for transfer to the Tevatron, or to an energy of 120 GeV for transfer to the Anti-proton Source. The Main Injector is a circular synchrotron with 18 accelerating RF cavities and a circumference of almost two miles, which is approximately half the circumference of the Tevatron. The Main Injector can also accept 8 GeV anti-protons from the Anti-Proton Source and accelerate them for transfer to the Tevatron.

3.1.5 Tevatron

The Tevatron, 6.28 km in circumference, is the ring on which the collider experiments are located. The Tevatron accelerates both protons and anti-protons from 150 GeV to 980 GeV and intersects the two anti-circulating beams at the two interaction points on the ring. The beams are kept in the machine for nearly 24 hours at a time, and instantaneous luminosities of nearly 2×10^{32} cm^{-2}s^{-1} are presently recorded. During the period of data taking for data used in this analysis, initial instantaneous luminosities ranged from 20×10^{30} cm^{-2}s^{-1} to 1.5×10^{32} cm^{-2}s^{-1}. A plot of the initial instantaneous luminosities versus time is shown in Figure 3.2.

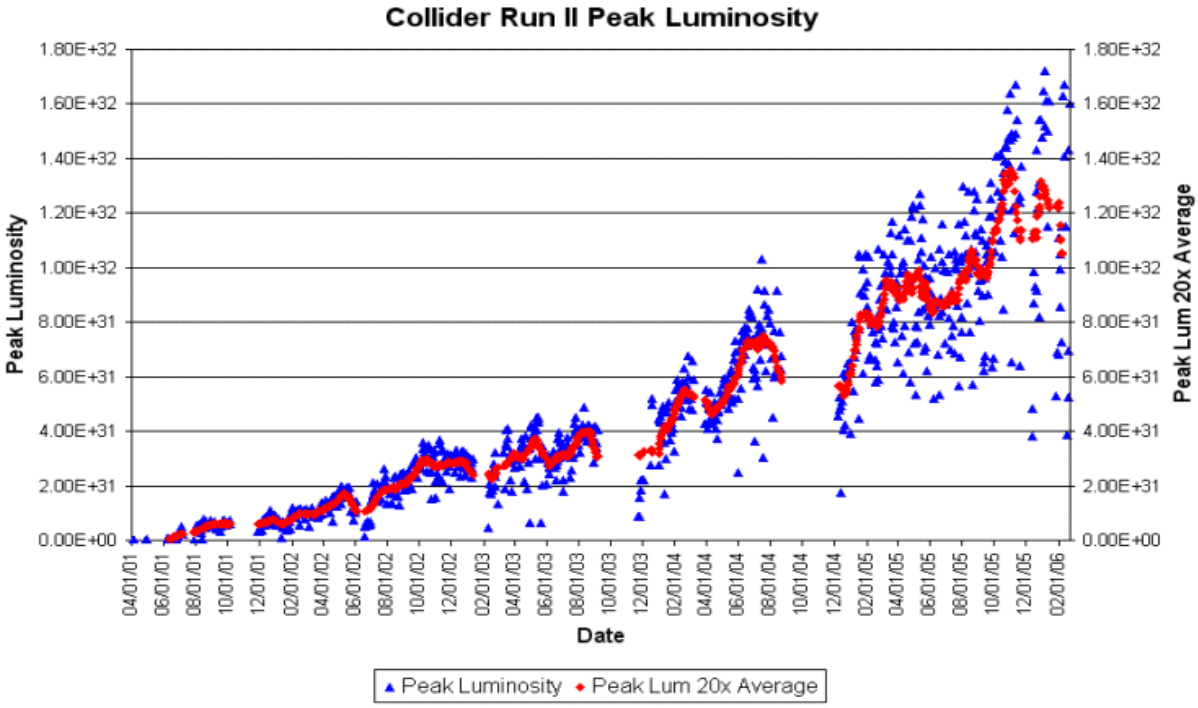

Figure 3.2: Initial instantaneous luminosities as a function of time.

3.1.6 Anti-Proton Source

Far more effort is devoted to cooling the anti-protons than the protons. Since anti-protons with outlying momentum and energies are still precious, they can't be readily discarded. The Anti-Proton Source is actually comprised of several steps by which anti-protons are produced and cooled before they are ready to be injected into the Tevatron.

Anti-protons are produced by colliding 120 GeV bunches of protons with a nickel target. Magnets are used to select 8 GeV anti-protons from the spray of particles produced. These anti-protons are transferred to the Debuncher, which cools the anti-proton beam. Before colliding with the nickel target, the proton bunches are rotated by 90° in phase space, so

that they have a large spread in energy but a small lag in arrival time at the target. Normally the bunches are designed to have a small spread in energy and a larger spread in phase. This rotation allows the anti-protons produced in the collisions with the target to be collected at nearly the same time, and the spread in the proton energies is insignificant compared to the spread in energies of the secondary particles produced in the collision. Constant effort must be expended to cool the anti-protons so that the energy of the bunches is nearly uniform. To that end, a variety of methods is used, including stochastic cooling of the beam. The Debuncher is a triangular-shaped synchrotron and a mean radius of 90 m. It captures the anti-protons coming off of the target by rotating the bunches in phase space opposite to the rotation of the protons before striking the target. The beam is stochastically cooled by picking up signal from anti-protons circulating at one side of the ring, amplifying the signal, and sending it to the opposite side of the ring. This signal is then applied to cool the anti-protons when they reach the opposite side of the ring. After cooling the anti-protons are then transferred to the Accumulator, which is another triangular-shaped synchrotron with a mean radius of 75 m. The Accumulator is a storage ring for the anti-protons, where they are stored at 8 GeV and cooled until they are needed for acceleration in the Main Injector. A third storage ring for anti-protons is the Recycler, which is a circular synchrotron located along the ceiling of the Main Injector. The Recycler stores and cools 8 GeV anti-protons with a stochastic cooling process and, in the future, with an electron cooling process.

3.2 CDF Detector

A full description of the CDF detector can be found in the CDF technical design report [34]. The detector consists of several main components, namely a tracking system inside a magnetic field, electromagnetic and hadronic calorimeters outside of the tracking system, and muon chambers beyond the calorimeter systems. A schematic of the passage of different particles through the CDF detector is shown in Figure 3.3, while a cut-away view of the CDF detector is shown in Figure 3.4. The parts of the detector which are relevant to the detection of semileptonic $\bar{B}$ decays include the tracking systems, which are used to vertex the charm hadron with the lepton, the electromagnetic calorimeters and muon chambers, used for the lepton identification, and the trigger system, which includes a lepton plus displaced track trigger. This trigger preselects likely semileptonic $\bar{B}$ candidates before writing data to tape (see Section 3.2.4).

The most natural coordinate system for the detector geometry is cylindrical. The tracking coordinates are defined with the z-direction along the proton direction through the detector, while the x-direction is defined as the horizontal pointing away from the Tevatron ring. The polar angle θ is defined from the positive z-axis, while the azimuthal angle ϕ is defined from the positive x-axis. A commonly used track and detector parameter is the pseudo-rapidity, $\eta \equiv -\ln(\tan(\frac{\theta}{2}))$, which is an alternate measure of the "forwardness" of a track or detector system. The transverse momentum of a particle is expressed in terms of the azimuthal angle, $p_T \equiv p \sin\theta$.

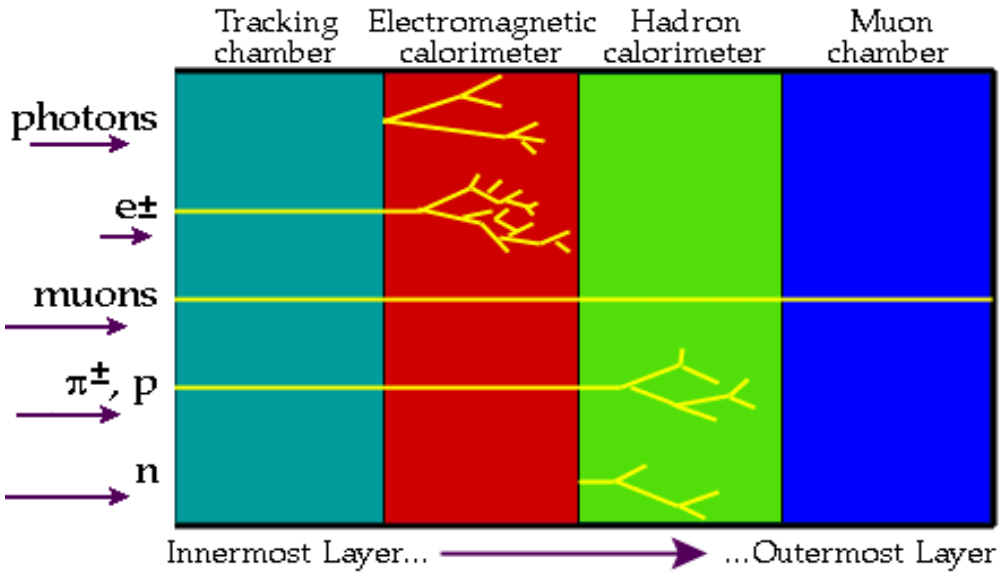

Figure 3.3: The passage of particles through the CDF detector.

3.2.1 Tracking

The tracking system, shown in Figure 3.5, forms the innermost part of the detector and lies inside the 1.4 Tesla superconducting solenoid magnet. The inner half of the tracking system consists of a silicon micro-strip detector, shown in Figure 3.6, with one layer of single-sided silicon micro-strips mounted on the beam pipe (L00), five double-sided layers of silicon arranged in three 29 cm long barrels known as the Silicon VerteX system (SVX II), and two forward layers of silicon arranged outside of the SVX II called the Intermediate Silicon Layers (ISL). The radial extent of the silicon system is from 1.5 cm $\leq r \leq$ 28 cm, while the detector extends $\sim$90 cm along the z-axis. One side of the double sided silicon micro-strips measures the axial position of the track, while the other side determines the z-position with an orientation of either 90° relative to the z-direction for the first, second, and fourth layers of the SVX II or a small, 1.2° stereo angle relative to the z-direction for the other two SVX II layers. The SVX II is divided into 12 azimuthal wedges and each wedge is divided into two electrically independent ladders. The silicon system has a measured impact parameter resolution of $\sim$50 μm precision for $p_T > 4$ GeV/c, which includes the resolution on the $p\bar{p}$ interaction width of approximately 30 μm. The impact parameter resolution is higher at lower p_T and depends on whether L00 silicon hits are used, as can be seen in Figure 3.7. L00 hits are not added to tracks used in this analysis. Since $\bar{B}$ hadrons travel a distance of roughly $L = c\tau_B \sim 450$ μm before decaying, this resolution is adequate for detection of $\bar{B}$ hadrons.

Outside of the silicon system, an open cell drift chamber called the Central Outer Tracker (COT), extends radially between 44 cm and 132 cm and 310 cm along the z-direction. It is divided into eight super-layers (SL). Each super-layer is composed of twelve cells, a diagram of which is shown for SL2 in Figure 3.8. Each cell is defined as one sense plane and two adjacent, grounded field sheets. Each sense plane consists of twelve gold-plated tungsten

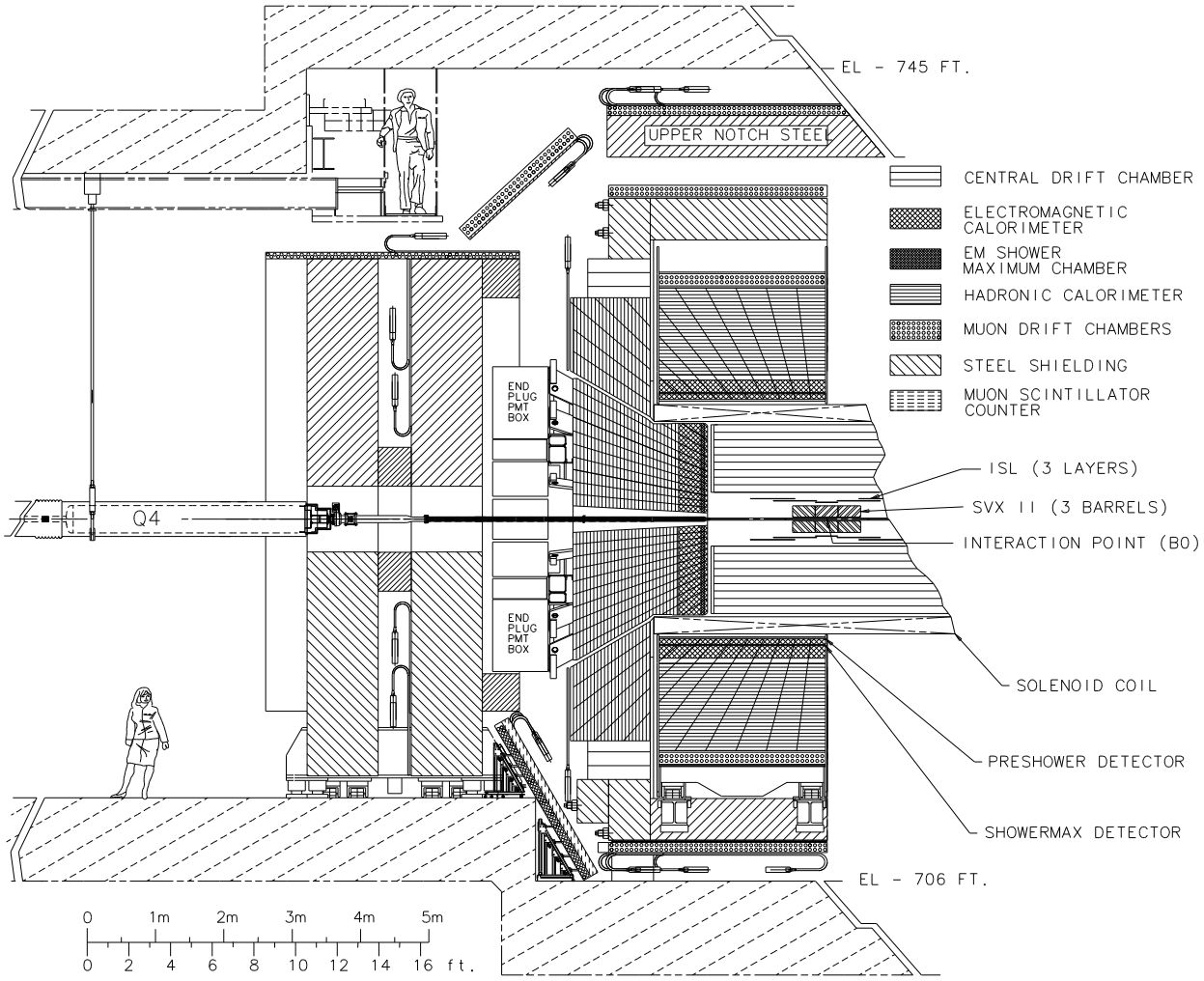

Figure 3.4: Cut-away schematic of half of the CDF Run II detector.

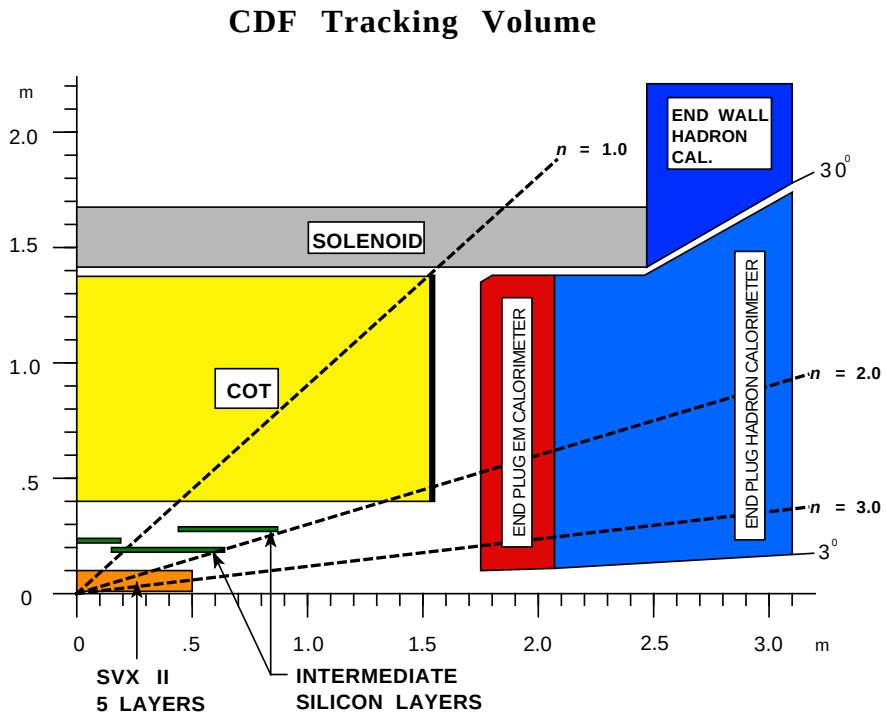

Figure 3.5: Diagram of the CDF Run II tracking system.

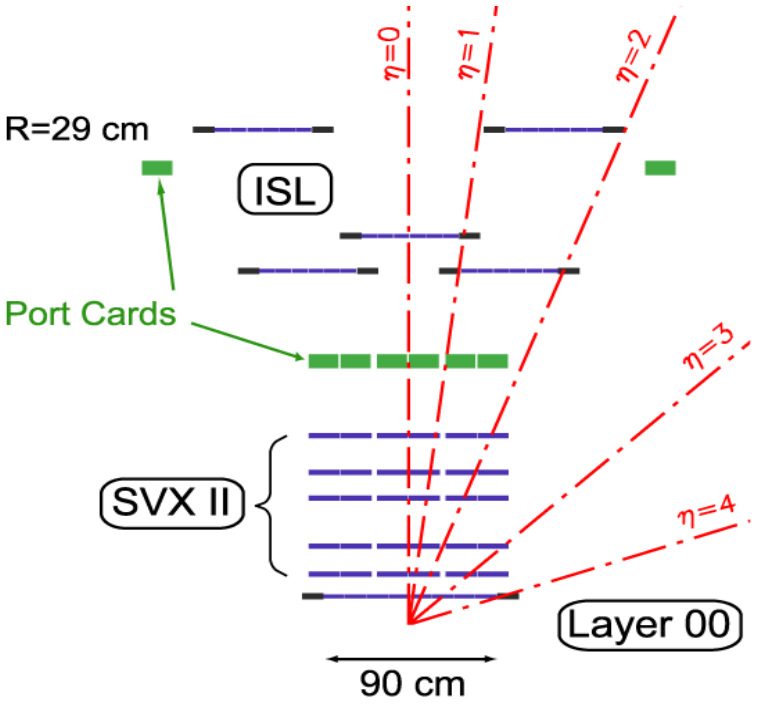

Figure 3.6: Schematic of the CDF Run II silicon detector.

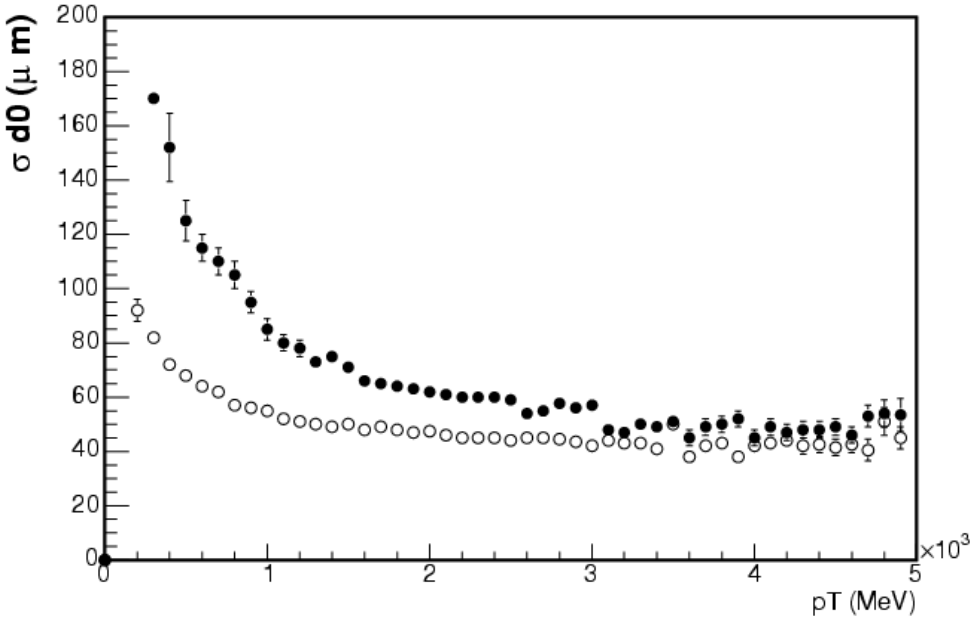

Figure 3.7: Impact parameter resolution of a track as a function of p_T for tracks with L00 (open circles) and without L00 (filled circles).

sense wires alternating with an equal number of potential wires every 3.8 mm. The field sheets are made of 10 μm thick gold-coated mylar. The chamber is filled with a nearly equal mixture of Argon and Ethane gases. A very small amount of oxygen is allowed to circulate in the chamber to reduce the buildup of hydrocarbons on the sense wires. Half of the super-layers measure the axial position of a track, with wire planes arranged parallel to the z-direction, while the alternate half are arranged with a $\pm 3^\circ$ angle from the perpendicular of the radial direction to make stereo measurements of the z-position of a track. The innermost super-layer is a stereo layer. Cosmic ray events are used to determine the transverse momentum resolution of the COT, which is measured to be:

$$\frac{\sigma_{p_T}}{p_T^2} = 0.00015 \text{ [GeV/c]}^{-1}. \tag{3.1}$$

The five parameters used to describe the trajectory of a charged particle through a magnetic field are transverse momentum (p_T), the z position of the track (z_0), the distance of closest approach of the track to the origin or primary vertex of the event (d_0), the azimuthal angle of the track (ϕ_0) at the point of minimum approach with the origin, and the cotangent of the polar angle ($\cot\theta$).

An additional feature of the drift chamber which is utilized in this analysis is the use of species-dependent energy loss through material (dE/dx) for particle identification. The energy loss for relativistic charged particles other than electrons is given by the Bethe-Bloch equation:

$$\frac{dE}{dx} = 4\pi N_A r_e^2 m_e c^2 z e \frac{Z}{A}\frac{1}{\beta}\left[\frac{1}{2}\ln\frac{2m_e c^2\beta^2\gamma^2 T_{max}}{I^2} - \beta^2 - \frac{\delta}{2}\right], \tag{3.2}$$

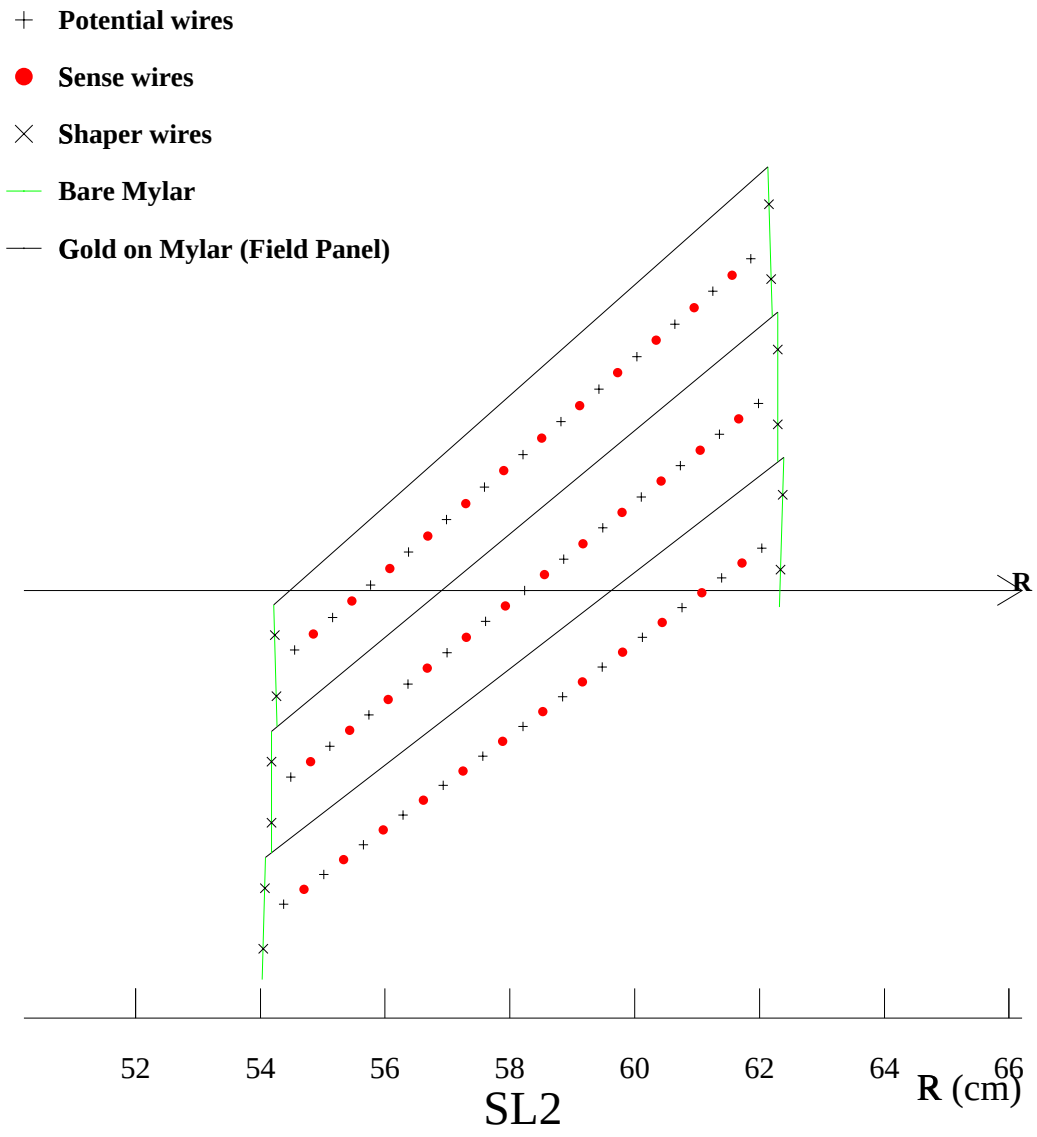

Figure 3.8: Schematic of the cells in the second super-layer of the CDF Run II drift chamber.

where T_{max} is the maximum kinetic energy that can be imparted to a free electron in a single collision, N_A is Avogadro's number, m_e is the mass of the electron, ze is the charge of the incident particle, $r_e \equiv \frac{e^2}{4\pi\epsilon_0 m_e c^2}$ is the classical Bohr radius of the electron, Z and A are the atomic number and mass of the absorber respectively, I is the mean excitation energy, δ is the density effect correction to the ionization energy loss, $\beta \equiv v/c$, and $\gamma \equiv \frac{1}{\sqrt{1-\beta^2}}$. The energy loss for different particle species at CDF is shown as a function of the particle momentum in Figure 3.9. Knowledge of the specific energy loss of pions and protons for transverse momenta above 2 GeV/c is used to reduce background in the semileptonic baryon signal, which is discussed in Section 5.2.1.

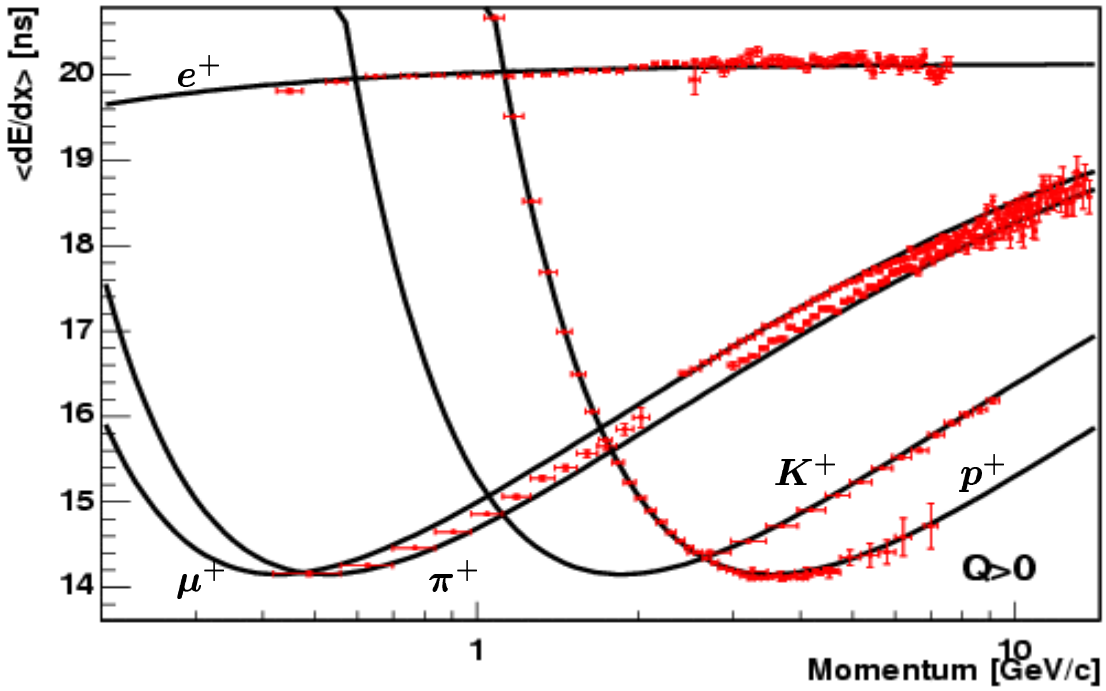

Figure 3.9: Mean dE/dx for different particles species in the CDF RunII drift chamber.

3.2.2 Electron Identification

Electron identification centers around the electromagnetic and hadronic sampling calorimeter systems, shown in Figure 3.10, which lie outside of the tracking systems and the solenoid magnet. The Central ElectroMagnetic (CEM) calorimeter consists of 23 alternating layers of 4.5 mm thick lead and 4 mm thick polystyrene scintillator segmented into twenty towers which cover $|\eta| < 1.1$ and 24 wedges which cover $0 \leq \phi < 2\pi$. The CEM has an energy resolution of $\frac{0.13}{\sqrt{E_T}} \pm 0.03$ [35], which is determined under test beam conditions. The Central HAdronic (CHA) calorimeter is made up of 23 alternating layers of 2" thick steel absorber and 6 mm thick acrylic scintillator, segmented into 18 towers covering $|\eta| < 1.0$

and 24 wedges which cover $0 \leq \phi < 2\pi$. The test beam energy resolution in the CHA is $\frac{0.75}{\sqrt{E_T}} \pm 0.03$ [36]. Electrons are identified both by minimum cuts on energy deposited in the CEM and by maximum cuts on energy deposited in the CHA. In addition to the electromagnetic calorimeter system, several electron shower detection systems exist. These include the Central Pre-Radiator (CPR), which is located between the solenoid and the CEM, and the Central Electromagnetic Shower (CES) detector, a multi-wire proportional chamber which is located roughly six radiation lengths inside the CEM. The CES has a set of anode wires which measure the z-position and a set of cathode strips which measure the transverse ("x-") direction. Beyond the central calorimetry, the forward calorimeters systems, including the plug electromagnetic (PEM) and hadronic (PHA) calorimeters and the wall hadronic calorimeter (WHA). These systems are not used in electron identification in this measurement.

One of the best ways to identify electrons and distinguish them from hadrons is with a cut on energy deposited in the CEM relative to the CHA (E_{Had}/E_{EM}). Other means of electron identification is by use of the lateral shower profile determined from the energy response of the CES and CPR. The extrapolated track trajectory can be matched to energy deposited in the calorimeters in both the transverse (ΔX) and longitudinal (ΔZ) directions. χ^2 quality matching quantities in ΔX and ΔZ are also used to determine a clean candidate sample of trigger electrons. The Lateral Shower profile (LShr) is another quantity used in electron selection. LShr is defined as,

$$LShr = 0.14 \frac{\sum_i (M_i - P_i)}{\sqrt{(0.14\sqrt{E_{EM}})^2 + \sum_i (\Delta P_i)^2}}, \tag{3.3}$$

where towers adjacent to the central tower in a default 3 tower by 1 wedge electromagnetic cluster are summed over. The 3 tower by 1 wedge electromagnetic clustering algorithm is used for all CEM quantities in this measurement. M_i is the energy measured in an adjacent tower, while P_i is the predicted energy deposited in the adjacent tower. E_{EM} is the total electromagnetic energy in a cluster and ΔP_i is the estimated uncertainty on P_i. The CES detector provides the z-position for the cluster in the LShr algorithm. Electrons or photons do not generally share energy between towers, allowing an upper bound on LShr to be used for electron selection.

3.2.3 Muon Identification

Four scintillator and proportional chamber systems, shown in Figure 3.11, are available for muon identification at CDF. The two central muon systems are used for muon identification in this measurement. The inner Central MUuon (CMU) chamber covers $|\eta| < 0.6$ with a four layer deep planar drift chamber, while the Central Muon uPgrade (CMP) muon chamber lies beyond the CMU and is separated from the CMU chambers by 60 cm of steel. The CMP adds four more layers of planar drift chambers arranged in a rectangular configuration and has a similar extent in η. The CMU is made up of 144 "modules", each containing 16 rectangular cells. The CMP detector includes a layer of scintillation counters on the outer surface of the wall drift chambers. Muons which are detected in both the CMU and CMP detectors are referred to as CMUP muons. All muons used in this measurement are

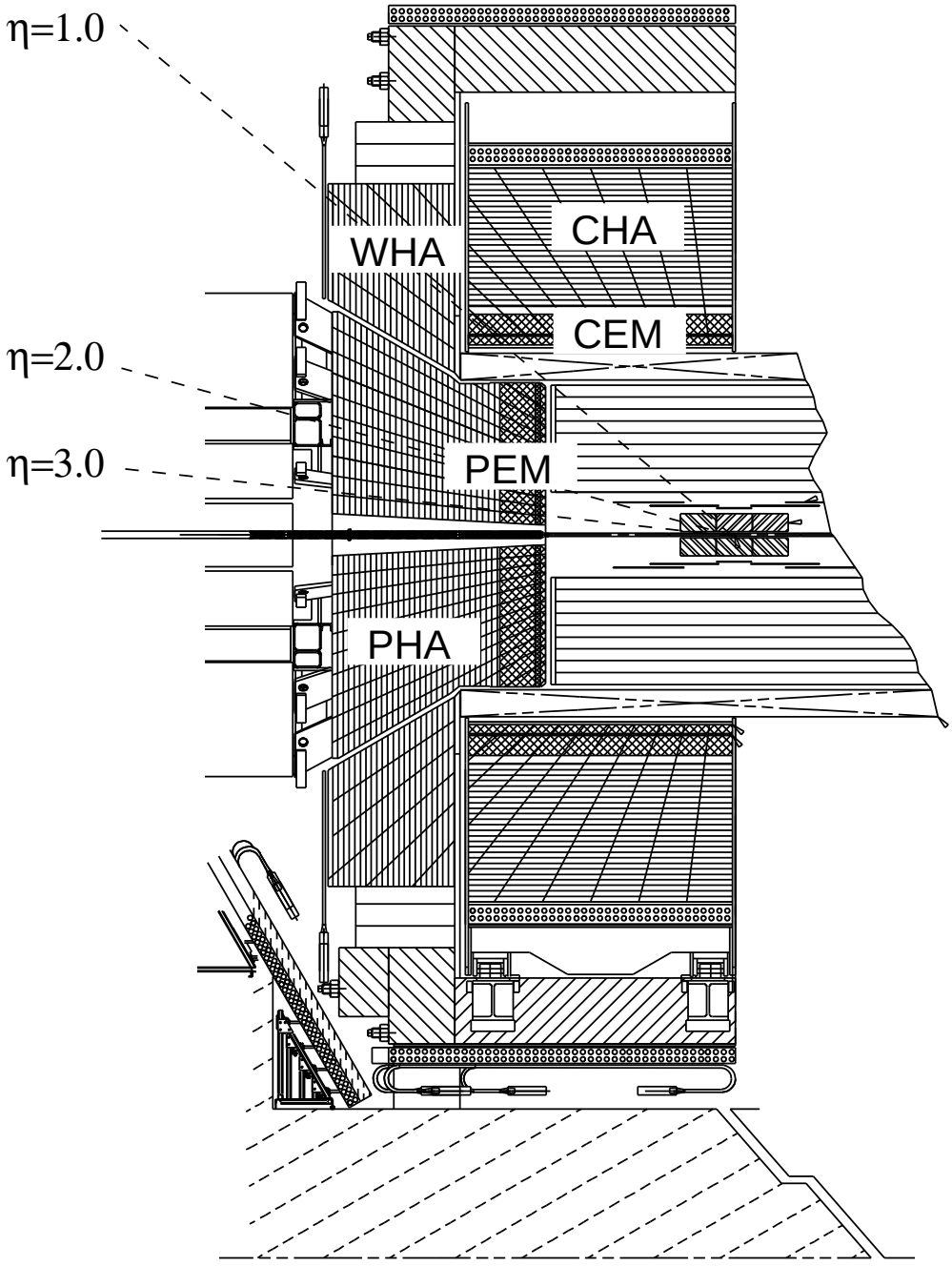

Figure 3.10: The CDF Run II calorimetry systems.

required to be CMUP muons. Additional outer muon chambers, known as the Central Muon eXtension (CMX) and the Intermediate MUon chamber (IMU) are also available for more forward muon detection.

Several matching variables between the track trajectory and hits in the muon chambers are available, including ΔX, which is the distance between the extrapolated track and the hit in the muon detector in the azimuthal direction, and ΔZ, the distance between the extrapolated track and the hit in the muon detector in the z-direction. Both of these variables are cut upon offline to eliminate candidate muons with low probability of being the trigger muon.

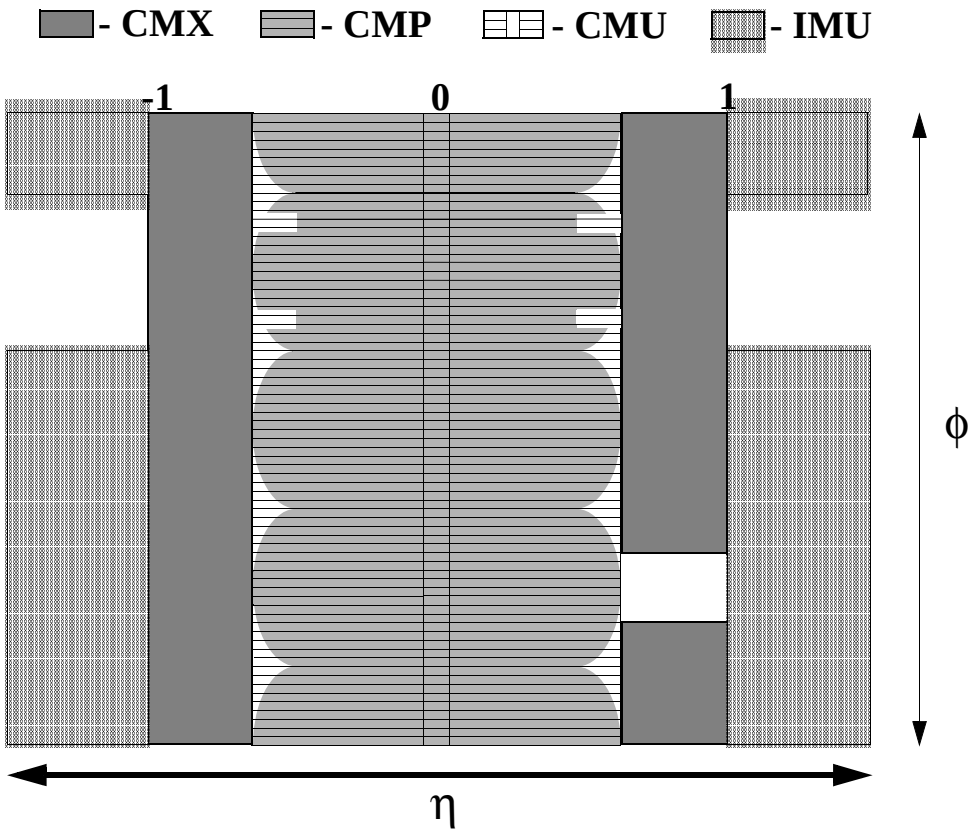

Figure 3.11: CDF Run II muon chamber coverage.

3.2.4 Trigger

The trigger system at CDF is essential for efficient data taking. The interaction rate is too high ($\sim 1.7\times10^6$ $p\bar{p}$ collisions per second) to record all events observed with the CDF Run II detector. In order to handle the large volume of data passing though the detector every second, a three level trigger system is used to select the most interesting events. The first two levels, Level-1 (L1) and Level-2 (L2) respectively, of the trigger system are hardware triggers, with accept rates of $\sim$20 kHz and $\sim$300 Hz respectively for the period of data

taking used in this measurement. The third level, Level-3 (L3), of the trigger system is a computer farm which assembles the pieces of the event from different detector subsystems and cuts on high-level quantities such as the combined mass of pairs of tracks. The average trigger accept rate of the L3 is ~ 60 Hz. Eighty percent of the candidate events are rejected at L3. The limiting rate for L3 is the rate at which data can be transferred to tape to be processed by the Production farms.

In addition to triggering on calorimeter quantities, the trigger system has the ability to trigger on tracks and track pairs in the first and second level of the trigger system, shown schematically in Figure 3.12. The eXtremely Fast Trigger (XFT) is a L1 trigger which uses track measurements from the COT for trigger decisions. The track segments from the XFT are linked with the eXTRaPolator (XTRP) and are passed to both the L1 trigger decision and to the Secondary Vertex trigger (SVT), which uses the track information from the XFT to make trigger decisions on tracks which are displaced some distance from the primary interaction point, also called the primary vertex. Displaced tracks are a distinguishing feature of $\bar{B}$ hadrons, making the SVT trigger particularly well-suited to the detection of $\bar{B}$ decays. There are several schemes of triggering on $\bar{B}$ events, for instance by triggering two leptons above a certain p_T threshold which are likely to originate from a J/ψ or by triggering on two displaced SVT tracks. The triggers of interest for semileptonic $\bar{B}$ decays include triggers designed to select events with a lepton and displaced track (ℓ+SVT). These triggers require a lepton with $p_T(\ell) > 4$ GeV/c, a displaced track with 120 μm $\leq |d_0| \leq 1$ mm and p_T(SVT) > 2 GeV/c, and an invariant mass cut $m(\ell + SVT) < 5$ GeV/c^2 on the lepton and SVT track. The trigger requirements for events used in this measurement are given in Section 5.1.

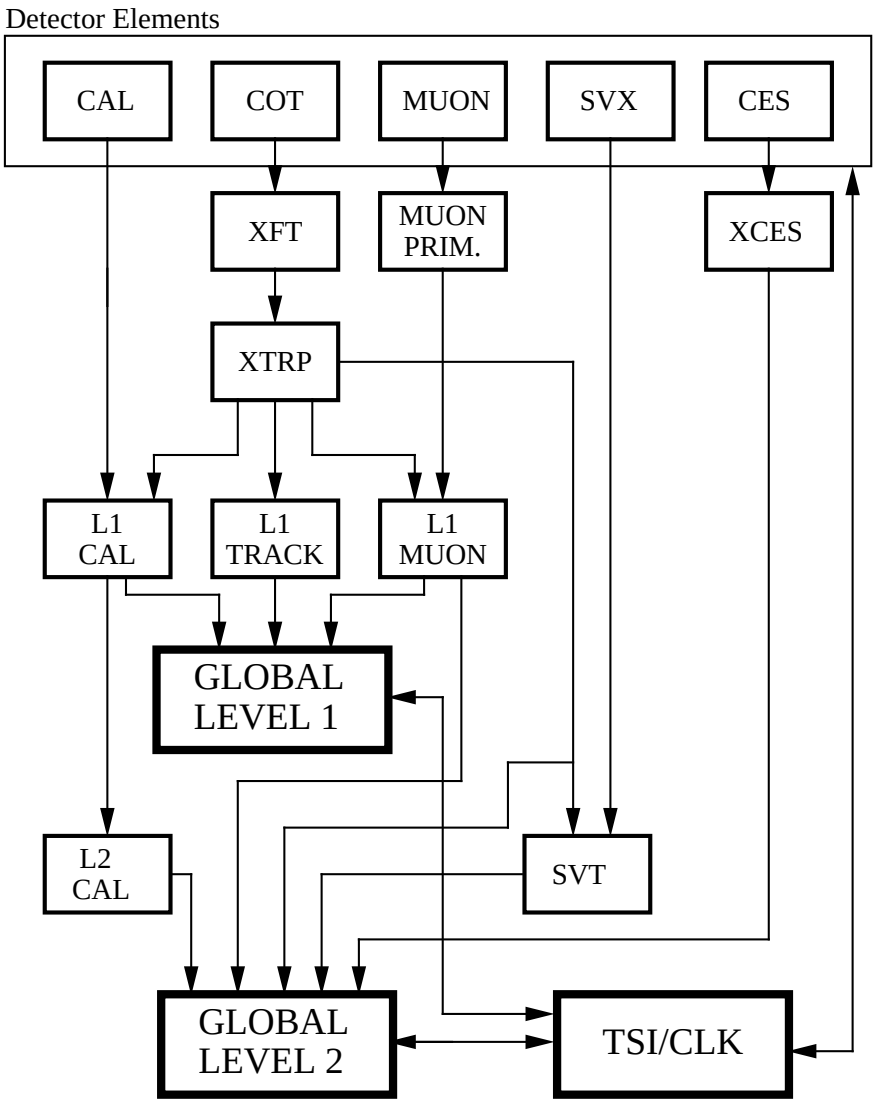

Figure 3.12: Hardware trigger system for CDF Run II data taking.

Chapter 4

Monte Carlo

Monte Carlo simulation is used at various points throughout the measurement. Although some of the Monte Carlo is generated for exclusive $\bar{B}$ decays while other Monte Carlo is generated for inclusive $\bar{B}$ semileptonic decays, all of the Monte Carlo used in the measurement have the same settings for generation.

The $\bar{B}$ hadron is generated with the `HeavyQuarkGenerator` software package [37], which generates a single $\bar{B}$ hadron according to an input transverse momentum and rapidity spectrum. Generally, a b quark is generated and fragmented according to the Petersen function (see Section 2.3). The Monte Carlo generated for this measurement uses an input transverse momentum spectrum which has been measured from data; the measurement does not rely on the validity of the Petersen fragmentation model. In this case the $\bar{B}$ hadron is generated directly according to the input spectrum. The generated $\bar{B}$ hadron is then passed to the `EvtGen` decay package [38], which decays the particle according to a specified decay chain. GEANT3 [39] simulates the passage of the long-lived particles through the material of the detector and includes multiple scattering effects.

The Monte Carlo are generated with a "realistic", as opposed to parametric, simulation, in which trigger paths are created and all detector bits are set just as they are for a given run in the real data. A tuned magnetic field and GEANT material description is applied in order to correct for regions of the detector where the material is under-represented in the default simulation. One hundred and five runs representing data taken between May 17, 2002 and April 16, 2004, spanning the period of data used in the measurement, are simulated. Twenty million events are generated for the inclusive $\bar{B}$ hadron decays, and ten million events are generated for each exclusive $\bar{B}$ meson decay listed in Table 6.1 in Chapter 6.

The p_T spectrum measured in the inclusive J/ψ cross-section [40] is used as the input $\bar{B}$ meson spectrum, while a Λ_b^0 spectrum tuned from the $\ell^-\Lambda_c^+$ data presented in this measurement is used as the input Λ_b^0 baryon spectrum (see Chapter 8). All of the Monte Carlo are generated with an input p_T threshold of $p_T(\bar{B}) > 5$ GeV/c.

4.1 Form Factors of Semileptonic $\bar{B}$ Decays

The $\bar{B}$ meson form factors included in the generation of the Monte Carlo used for this analysis are taken from HQET models. The ISGW2 [27] model implemented in `EvtGen` is used to

govern the $\bar{B}$ meson semileptonic decays to ground state and double excited charm mesons, while the HQET decay model implemented in `EvtGen` is used for the $\bar{B}$ meson semileptonic decays to excited charm states. Non-resonant D^{**} meson decays are described by the model developed by Goity and Roberts [41]. These decay models have been used by the BaBar experiment [42] for a number of years. The Λ_b^0 baryon semileptonic decay used is newly implemented for this measurement, thus the focus of this discussion is the treatment of the semileptonic baryon decays.

The baryon form factors for the primary $\Lambda_b^0 \to \Lambda_c^{+(*,**)}$ decays are taken from constituent quark model calculations made by Pervin *et al.* [28]. To order $\mathcal{O}(\frac{1}{m_Q})$ these results agree with the large N_c predictions by Leibovich and Stewart [43], although the constituent quark model form factors do not obey the relations among form factors predicted by HQET at higher orders of $\frac{1}{m_Q}$. Non-resonant Λ_b^0 decays are described by phase space.

A distinguishing characteristic of the HQET form factors is their dependence on a single form factor, expressed in terms of the product of four velocities $w = v \cdot v'$ (see Section 2.4.1). The most common HQET form factor in $\bar{B}$ meson decays, known as the Isgur-Wise function, is $\xi(w)$. Heavy quark flavor symmetry implies the normalization

$$\xi(1) \equiv 1. \tag{4.1}$$

The Isgur-Wise function is commonly expanded about $w = 1$

$$\xi(w) = 1 - \rho^2(w-1) + ... \tag{4.2}$$

The $\bar{B}$ meson matrix elements can then be written [22] in terms of the four velocities $v_\mu = p_\mu/m_B$ and $v'_\mu = p'_\mu/m_{D^{(*)}}$

$$\langle D(p')|V_\mu|\bar{B}(p)\rangle = \xi(w)[v_\mu + v'_\mu], \tag{4.3}$$

$$\langle D^*(p',\varepsilon)|V_\mu|\bar{B}(p)\rangle = \xi(w)\varepsilon_{\mu\nu\alpha\beta}\varepsilon^{*\nu}v'^{\alpha}v^{\beta} \tag{4.4}$$

$$\langle D^*(p',\varepsilon)|A_\mu|\bar{B}(p)\rangle = -i\xi(w)[(1+w)\varepsilon^*_\mu - (\varepsilon^* \cdot v)v'_\mu], \tag{4.5}$$

which can be compared with the general expressions for these matrix elements in Eqs. (2.23)-(2.25). The baryon form factors calculated by Pervin *et al.* also depend on a common form factor, which is determined for a harmonic oscillator potential. The analogous Isgur-Wise function determined by Pervin *et al.* is

$$\xi(w) \approx \exp\left[\frac{3m_\sigma^2}{\alpha^2}(w-1)\right] \tag{4.6}$$

which, following the exponential expansion in Eq. (4.2), implies that

$$\rho^2 = \frac{3m_\sigma^2}{\alpha^2}. \tag{4.7}$$

The common form factor, $I_H(w)$, from the Pervin calculation used in the Monte Carlo for the ground state $\Lambda_b^0 \to \ell^-\bar{\nu}\Lambda_c^+$ decay is

$$I_H(w) = \left(\frac{\alpha_\lambda \alpha_{\lambda'}}{\alpha^2_{\lambda\lambda'}}\right)^{3/2} e^{-\rho^2(w-1)}. \tag{4.8}$$

where $\alpha^2 \equiv \alpha^2_{\lambda\lambda'} = \frac{1}{2}(\alpha^2_\lambda + \alpha^2_{\lambda'})$ is a size parameter relating the parent and daughter baryons. The size parameters for the harmonic oscillator potential are $\alpha_\lambda = 0.59$ for Λ^0_b, $\alpha_{\lambda'} = 0.55$ for Λ^+_c and $\alpha_{\lambda'} = 0.47$ for $\Lambda_c(2593)^+$ and $\Lambda_c(2625)^+$. The constituent light quark mass m_σ has a value of 0.40 GeV/c^2 in the Pervin calculation and the slope of the Isgur-Wise function, $d\xi(w)/dw$, is -1.38 [28]. The dependence of the form factors on q^2, which can be related to w by Eq. (2.14), for the three $\Lambda^0_b \to \Lambda^{+(*,**)}_c$ semileptonic decays is shown in Figure 4.1.

4.2 Baryon Decay Model

Within the `EvtGen` framework, a new baryon decay model has been implemented for the Λ_b semileptonic decays: $\Lambda^0_b \to \ell^- \bar{\nu}_\ell \Lambda^+_c$, $\Lambda^0_b \to \ell^- \bar{\nu}_\ell \Lambda_c(2593)^+$, and $\Lambda^0_b \to \ell^- \bar{\nu}_\ell \Lambda_c(2625)^+$. This new model, based on the predictions of Pervin *et al.*, does not apply to non-resonant semileptonic baryon decays (listed in Table 6.5). Instead, a phase space model is used for the non-resonant semileptonic baryon decays. Previous measurements at CDF have used phase space for all Λ^0_b semileptonic decays.

In addition to the decay structure, the new decay model also permits the polarization of the Λ^0_b to be set at the time of generation. This feature is used for the systematic evaluation of the Λ^0_b polarization in Chapter 10. By default the Λ^0_b is generated unpolarized.

To check the results of the new decay model, 100,000 events are generated without cuts or trigger simulation for each of the three Λ^0_b decays considered. The differential decay rate relative to q^2 obtained from the new model is shown in Figure 4.2, where the areas for the $\Lambda_c(2593)^+$ and $\Lambda_c(2625)^+$ modes are normalized to the relative decay rates predicted by Pervin *et al.* For comparison, the $\bar{B}^0 \to \ell^- \bar{\nu} D^{+(*,**)}$ q^2 distributions, where the D^{**+} distribution includes non-resonant decays, are shown in Figure 4.3. The partial rate of the $\Lambda^{+(*,**)}_c$ relative to q^2 agrees very well with the theoretical predictions of Pervin, which is an important cross-check of the implementation of the new decay model. The Dalitz distribution of the μ^- and Λ^+_c for the three decay modes are shown in Figure 4.4.

Final state interactions and intermediate resonances are included in the ground state Λ^+_c decays, which is decayed with relative rates of intermediate and non-resonant states taken from the PDG [9], listed in Table 4.1. Note that the total $\Lambda^+_c \to pK^-\pi^+$ branching ratio used in the sample composition is $(5.0 \pm 1.3)\%$, also taken from the PDG.

Decay	$\mathcal{BR}$ (%)
$\Lambda^+_c \to \Delta^{++}K^-$	0.86±0.30
$p\bar{K}^*(892)^0$	1.6±0.5
$pK^-\pi^+$ (NR)	2.8±0.8

Table 4.1: Λ^+_c decay structure.

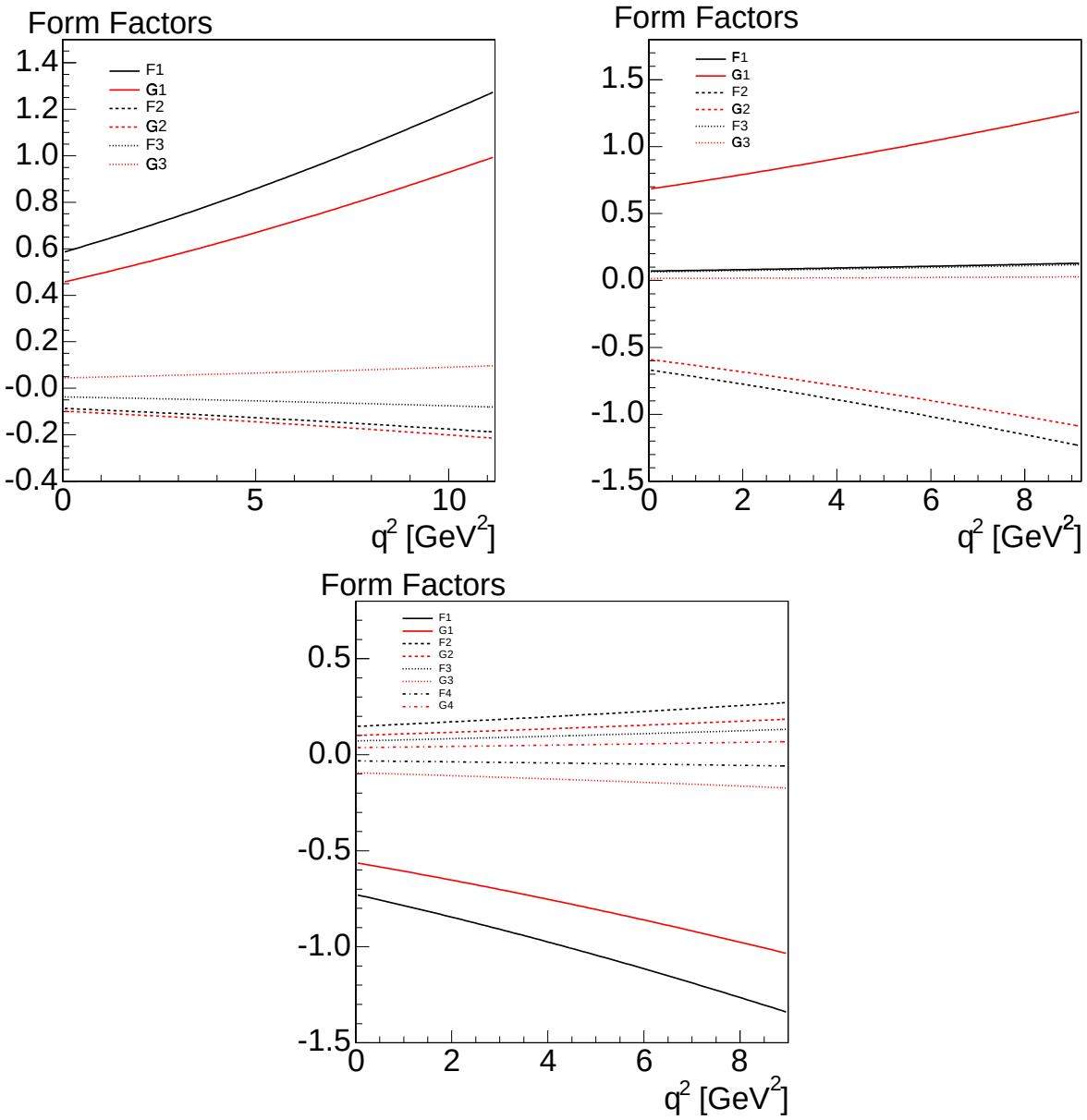

Figure 4.1: Form factor dependence on q^2 for semileptonic Λ_b^0 decays into Λ_c^+ (top left), $\Lambda_c(2593)^+$ (top right), and $\Lambda_c(2625)^-$ (bottom).

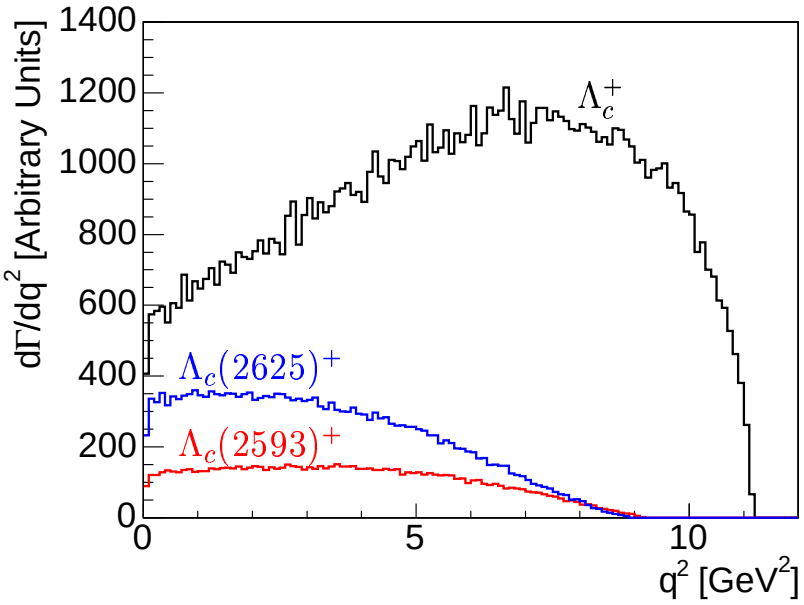

Figure 4.2: $d\Gamma/dq^2$ distributions for the Λ_c^+, $\Lambda_c(2593)^+$, and $\Lambda_c(2625)^+$ semileptonic decays of the Λ_b^0 baryon.

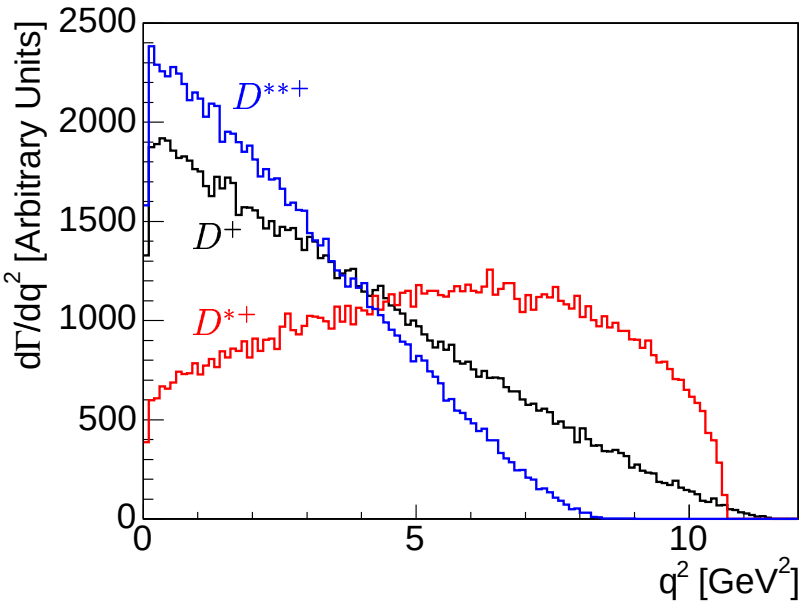

Figure 4.3: $d\Gamma/dq^2$ distributions for the D^+, D^{*+}, and D^{**+} semileptonic decays of the $\bar{B}^0$ meson. The D^{**+} contribution does not include non-resonant decays.

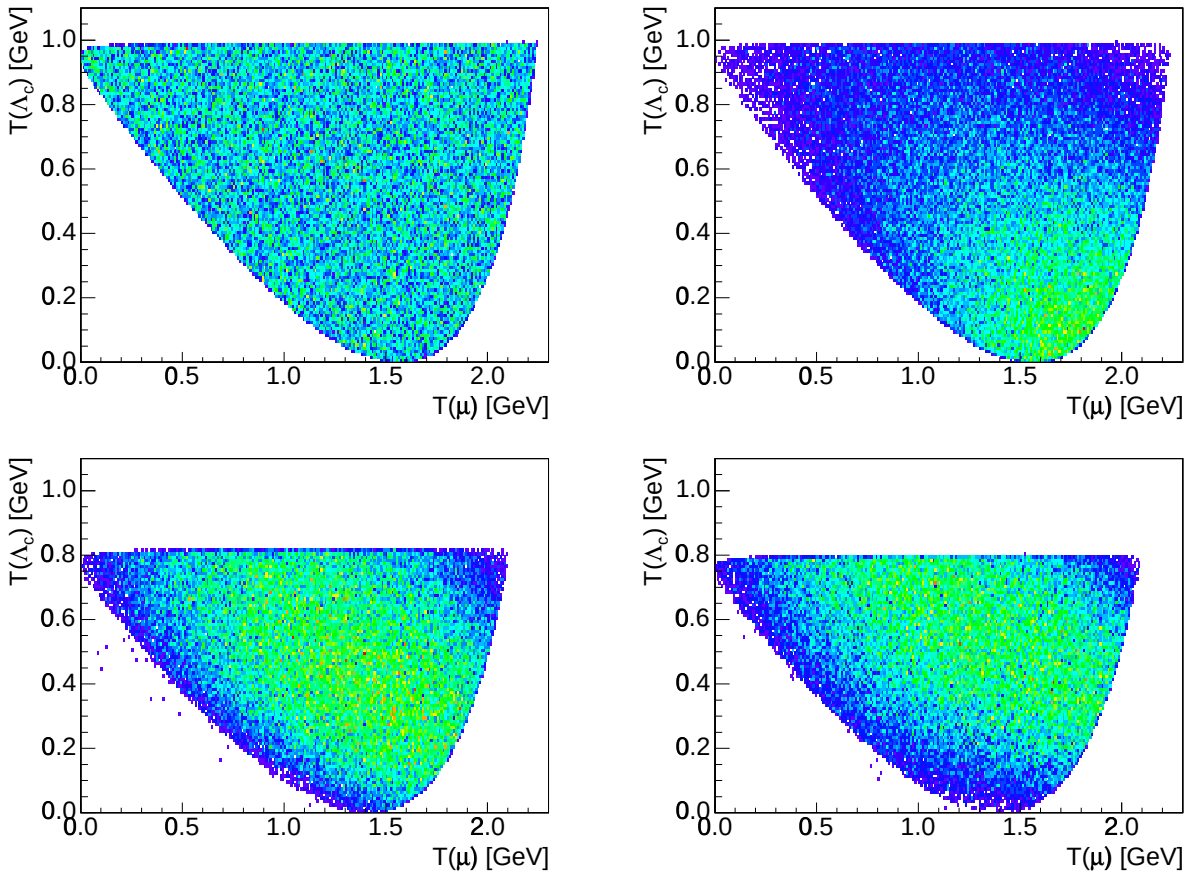

Figure 4.4: Dalitz distributions for phase space (top left) and the new decay model for the Λ_c^+ (top right), the $\Lambda_c(2593)^+$ (bottom left) and the $\Lambda_c(2625)^+$ (bottom right).

Chapter 5

Signal Reconstruction

The lepton-charm signals are obtained from the e+SVT and μ+SVT datasets. Only runs deemed suitable for B analyses are used. This requirement excludes runs for which the operation of the tracking chambers or central calorimeter or muon chambers are not optimal. In addition to isolated instances of non-optimal detector configurations, this also excludes the three month period of data taking in which COT aging effects, caused by a build-up of hydrocarbons on the sense wires which resulted in a reduction in efficiency of the COT. During this time, the voltages on the COT chamber were varied almost continuously, resulting in unstable tracking conditions. All tracks are refit with a Kalman fitter [44], using COT scaling parameters, missing detector material, and magnetic field which have been tuned to match control data samples.

A schematic diagram of the topology of semileptonic $\bar{B}$ decays used in this measurement is shown in Figure 5.1. A distinguishing feature of $\bar{B}$ decays is that they are comparatively long-lived, with average decay distances of $c\tau(\bar{B}) \approx 450$ μm. Consequently, one of the best ways to distinguish $\bar{B}$ decays from other decays is to select on lifetime-related quantities. Some of these discriminating quantities, such as the impact parameter of the tracks, are measured directly from the tracks. Other quantities, such as the distance, L, from the production and/or primary vertex to the point of decay (or "decay vertex") projected onto the momentum direction of the decaying hadron are inferred from the vertices constructed from the tracks. The decay vertices are reconstructed with the CTVMFT algorithm [45], using the charm daughter tracks with their assumed mass hypothesis to reconstruct the charm vertex and the additional lepton candidate to reconstruct the $\bar{B}$ candidate. The selection of candidates are based on a kinematic quantities appropriate for their reconstruction hypothesis, discussed in the following sections.

The proper decay time of the fully reconstructed charm hadron (*e.g.* $D^+ \to K^-\pi^+\pi^+$) using transverse measurement quantities, is

$$ct(D) = \frac{L_{xy}(\ell^- D \to D)}{p_T(D)} \times m(D), \tag{5.1}$$

where D corresponds to a generic, fully reconstructed charm hadron. The charm candidate proper decay time is reconstructed from the transverse decay distance of the reconstructed lepton-charm vertex to the reconstructed charm vertex, $L_{xy}(\ell^- D \to D)$. $m(D)$ is the mass of the charm hadron and $p_T(D)$ is the transverse momentum of the charm hadron.

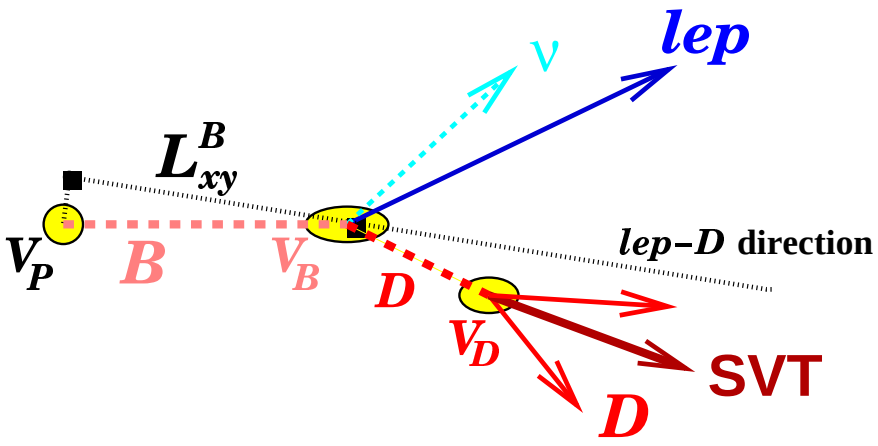

Figure 5.1: Semileptonic $\bar{B}$ decay.

Since the neutrino is not reconstructed in the semileptonic decay, it is not possible to know the true proper decay time of the $\bar{B}$ solely from the measured decay distance. Instead, a "pseudo"-proper decay time is constructed, based on information which is available from the reconstructed tracks,

$$ct^*(\ell^- D) \equiv \frac{L_{xy}(P.V. \rightarrow \ell^- D)}{p_T(\ell^- D)} \times m(B), \tag{5.2}$$

where $L_{xy}(P.V. \rightarrow \ell^- D)$ is the transverse distance from the primary interaction vertex to the reconstructed lepton-charm vertex, projected onto the transverse momentum of the lepton-charm system (highlighted in Figure 5.1). The other quantities are defined analogously to the quantities in Eq. (5.1). The "pseudo"-proper decay time reflects the missing neutrino information, since $p_T(\ell^- D) \leq p_T(\bar{B})$.

All quantities calculated relative to the primary vertex, such as $L_{xy}(P.V. \rightarrow D)$, are determined assuming that the axial position of the primary vertex is well described by the $p\bar{p}$ beam line. The $p\bar{p}$ beam line is determined from inclusive jet data, where long-lived tracks in the jets are "pruned" from the jet, using a χ^2 minimization of the vertex fit, to determine the position of the primary vertex in each event. These vertex positions are then averaged over 500,000 L2 trigger accepts to determine the $p\bar{p}$ beam line for a given run section. This method produces a "time-dependent" beam line, which is especially important for runs which last many hours (sometimes 20 hours or longer.) The z-position of the lepton-charm candidate is determined from the z-position of the lepton candidate track.

5.1 Trigger Requirements

The on-line ℓ+SVT trigger is confirmed off-line for both the trigger lepton and the SVT track. The CDF software package `LeptonSvtSel` is used to confirm the selection requirements on the trigger electron or muon and the SVT track in order to identify the trigger tracks.

1. Trigger electrons are confirmed by requiring that

- the electron be fiducial in the CEM,
- $E_T > 4$ GeV,
- $p_T > 4$ GeV/c,
- $\frac{E_{Had}}{E_{EM}} \in [0., 0.125)$,
- LShr < 0.2,
- χ^2_Z(CES) < 10,
- χ^2_X(CES) < 15,
- ΔX(CES) < 3 cm,
- ΔZ(CES) < 5 cm, and
- conversion electrons ($\gamma \rightarrow e^+e^-$) are removed by rejecting events in which
  - $\Delta\theta$(e,track) < 0.03, where the track is a generic track in the event,
  - Δ_{XY}(e,track) < 0.2 cm, and
  - the trigger electron and a track pass a CTVMFT vertex fit.

2. Trigger muons are confirmed by requiring that
   - the muon has hits in both the CMU and CMP muon chambers,
   - $p_T > 4$ GeV/c,
   - ΔX(CMU) < 15 cm, and
   - ΔX(CMP) < 20 cm.
3. The SVT track is matched to an offline track by
   - requiring that the offline track has 4 hits on 5 layers of the SVX II,
   - refitting the offline track, where additional requirements are made to
     - drop L00 hits and
     - drop 90^0 and stereo silicon z-hits,
   - using the time-dependent beam line determination,
   - $p_T > 2$ GeV/c,
   - $d_0 \in$ (0.012 cm, 0.100 cm) for both the on-line and off-line track,
   - requiring that the χ^2 matching distance, which relates the ϕ_0 and curvature of the on-line and offline tracks, is < 25, and
   - requiring that the SVT track has a $\chi^2 < 25$.
4. The final ℓ+SVT candidate is confirmed by requiring
   - $\Delta\phi(\ell, SVT) \in$ (0.035, 1.57) and
   - Invariant mass $m(\ell + SVT) < 5$ GeV/c^2.

5.2 Candidate Selection

In addition to trigger confirmation, several other selection cuts are applied to all channels, before requiring additional signal-dependent cuts.

1. All tracks in all candidates are required to have good track quality requirements including

   - a helix fit,
   - the errors on the track parameters are positive and real,
   - ≥ 3 silicon $r-\phi$ hits,
   - $p_T > 400$ MeV/c, and
   - $\eta < 2.0$.

   These cuts remove all tracks for which the Monte Carlo is unreliable (*e.g.* $p_T > 400$ MeV/c) or for which the data tracks itself is unreliable (*e.g.* $\eta < 2.0$).

2. All charm daughter tracks except the soft pion from the $D^{*+} \to D^0\pi^+$ are required to have

   - 2 axial and 2 stereo COT super-layers with ≥ 5 hits per super-layer.

   COT hit requirements are not made on the soft pion from the D^{*+} in an attempt to maximize the efficiency for reconstructing D^{*+} candidates. Since the pion generally has p_T less than $\sim$800 MeV/c, requiring COT hits would significantly reduce the number of D^{*+} candidates.

3. Tracks are made fiducial in the COT by requiring that

   - tracks that fall within $|z| \leq 1.5$ cm of the COT mid-plane and outside of the COT volume $|z| \geq 155$ cm are excluded,
   - all tracks pass through SL6 of the COT ($r_{SL6} = 106.0$ cm), and
   - trigger tracks and the lepton pass through SL8 of the COT ($r_{SL8} = 131.0$ cm).

   The COT fiducial cuts on tracks are designed to remove tracks which are unlikely to be well-described by the Monte Carlo. Since the Monte Carlo is used to determine most of the relative acceptance efficiencies between channels, good agreement between data and Monte Carlo is desired, even at the edge of the fiducial volume.

4. The electron is required to be isolated by demanding that

   - only one track is associated with a 1 wedge by 3 tower CEM hit cluster.

The electron isolation cut is applied to reduce potential discrepancies with the Monte Carlo, since nearby hadrons from the underlying event or $\bar{B}$ decay can obscure the electron shower. This behavior requires a full simulation of the underlying event and is not well described by the Monte Carlo simulation used in this measurement.

5. The charm candidates and the lepton-charm candidates are required to have

   - one charm daughter be the `LeptonSvtSel` matched SVT track,
   - $0.035 < \Delta\phi(\ell, charm) < 1.57$,
   - $\Delta\phi < 1.5$,
   - $\Delta\mathrm{R} < 1.5$, and
   - $\Delta\mathrm{Z} < 1.5$ cm.

   Requiring the charm daughter to match the triggered SVT track significantly reduces the background from random combination of tracks, called "combinatorial" background. The $\Delta\phi$, $\Delta\mathrm{R} \equiv \sqrt{\Delta\phi^2 + \Delta\eta^2}$, and $\Delta\mathrm{Z}$ cuts are very loose and remove only the most unlikely lepton-charm candidates.

These loose selections are used when skimming candidates from the dataset and are designed to confirm the ℓ+SVT trigger on each lepton-charm candidate. The soft pion from the D^{*+} is not vertexed with the D^0 to create the D^{*+} candidate. Instead, the D^0 candidate is flagged as a potential D^{*+} candidate if $\Delta m(D^{*+}, D^0) \in [0.0, 0.16]$ GeV/c^2 to create a loose D^{*+} candidate selection. This reduces the systematic uncertainty in the selection of the $\ell^- D^{*+}$ relative to the $\ell^- D^0$, since no additional vertex fit is performed. Consequently, the soft pion efficiency is better described by the Monte Carlo.

In order to determine the final analysis selection, kinematic selection criteria are first optimized for each lepton-charm channel. The figure of merit (FOM) used for optimization is $S/\sqrt{S+B}$. The signal, S, is taken from inclusive $\bar{B} \to \ell^- \bar{\nu} D X$ and $\Lambda_b^0 \to \ell^- \bar{\nu} \Lambda_c^+ X$ Monte Carlo. The background, B, is taken from the sidebands of the charm signal. In order for the FOM to accurately reflect the significance of the signals in data, S is scaled to the expected signal in data with a set of nominal cuts obtained by first optimizing each cut individually without applying any other cut. The cuts are then optimized a second time applying all optimal cuts from the prior optimization except the cut being optimized $(N-1)$. After two or three successive iterations, a stable optimal point is reached for all cuts. The optimization is performed twice; once without regard for non-combinatoric background reduction (*i.e.* prompt background removal), and a second time to account for additional, non-optimal cuts required to reduce the non-combinatoric backgrounds discussed in Section 5.2.1. Optimization plots and yields for the optimization with the $ct^*(\ell^- D/\Lambda_c^+)$ cut (see Section 5.2.1) are given in Appendix A.

Hoping to cancel as many differences in reconstruction as possible, the selection criteria are kept as similar as is feasible across channels. The optimized cuts designed to limit both the combinatoric and some non-combinatoric backgrounds are synthesized to minimize the differences in cut values between channels. The cuts are synthesized more easily in the meson channels, due to the different properties of baryon and meson decays. Cuts in which different

Cuts	$\ell^- D^0$	$\ell^- D^{*+}$	$\ell^- D^+$	$\ell^- D_s^+$	$\ell^- \Lambda_c^+$
$ct(D/\Lambda_c^+)$ [cm] >	-0.01	-0.01	-0.01	-0.01	-0.01
$ct(D/\Lambda_c^+)$ [cm] <	0.10	0.10	0.20	0.10	0.05
$ct^*(\ell^- D/\Lambda_c^+)$ [cm] >	0.02	0.02	0.02	0.02	0.02
$\sigma_{ct}(\ell^- D/\Lambda_c^+)$ [cm] <	0.04	0.04	0.04	0.04	0.04
$m(\ell^- D/\Lambda_c^+)$ [GeV/c^2] >	2.4	2.4	2.4	2.4	3.5
$m(\ell^- D/\Lambda_c^+)$ [GeV/c^2] <	5.1	5.1	5.1	5.1	5.4
$p_T(p)$ [GeV/c] >	N/A	N/A	N/A	N/A	2.0
$p_T(K)$ [GeV/c] >	0.6	0.6	0.6	0.6	0.6
$\chi^2_{2D}(D/\Lambda_c^+)$ <	10	10	10	10	5
vtx. prob.$(\ell^- D/\Lambda_c^+)$ >	10^{-7}	10^{-7}	10^{-7}	10^{-7}	10^{-4}
$L_{xy}/\sigma_{Lxy}(D/\Lambda_c^+)$ >	4.5	4.5	11	4.5	4.5
$\Delta m(D^*, D)$ [GeV/c^2] >	N/A	0.1440	N/A	N/A	N/A
$\Delta m(D^*, D)$ [GeV/c^2] <	N/A	0.1475	N/A	N/A	N/A
$\lvert m(\phi) - 1.019 \rvert$ [GeV/c^2] <	N/A	N/A	N/A	0.0095	N/A

Table 5.1: Synthesized signal selection.

optimal values are expected due to differences in the kinematics of the decay (*e.g.* the proper decay time of the D^+ and Λ_c^+) are not synthesized. The synthesized selection criteria are listed in Table 5.1. Additional cuts to reduce non-combinatoric backgrounds are discussed in the following section.

5.2.1 Non-Combinatoric Background Reduction

A notable aspect of semileptonic B decays is the sundry backgrounds and cross-talks via excited charm states that contribute to the lepton-charm signals. Some of these, such as the cross-talk between the B^- and $\bar{B}^0$ are, in principle, well-known and can be accounted for with an estimation of the pertinent branching ratios and reconstruction efficiencies. Other backgrounds, such as the so-called "prompt" background observed in the semileptonic signals, are not understood. Ways to reduce contamination to the semileptonic signals from these sources are discussed. Another non-combinatoric background arises from the misidentification of the charm daughters, leading to so-called reflection backgrounds. These backgrounds can be understood with Monte Carlo simulation and are also straightforward to take into account.

Prompt Background

One striking feature of the lepton-charm signals is an unknown prompt background, which can be seen most clearly in the "pseudo"-proper decay time of the $\ell^- D^+$ channels. A similar effect is observed in all of the meson signals, although no prompt background is observed in the $\ell^- \Lambda_c^+$ signals. The wrong sign (WS) lepton-charm combinations, which require an unphysical lepton and charm combination (*e.g.* $\ell^+ D^+$), are used to check the behavior of

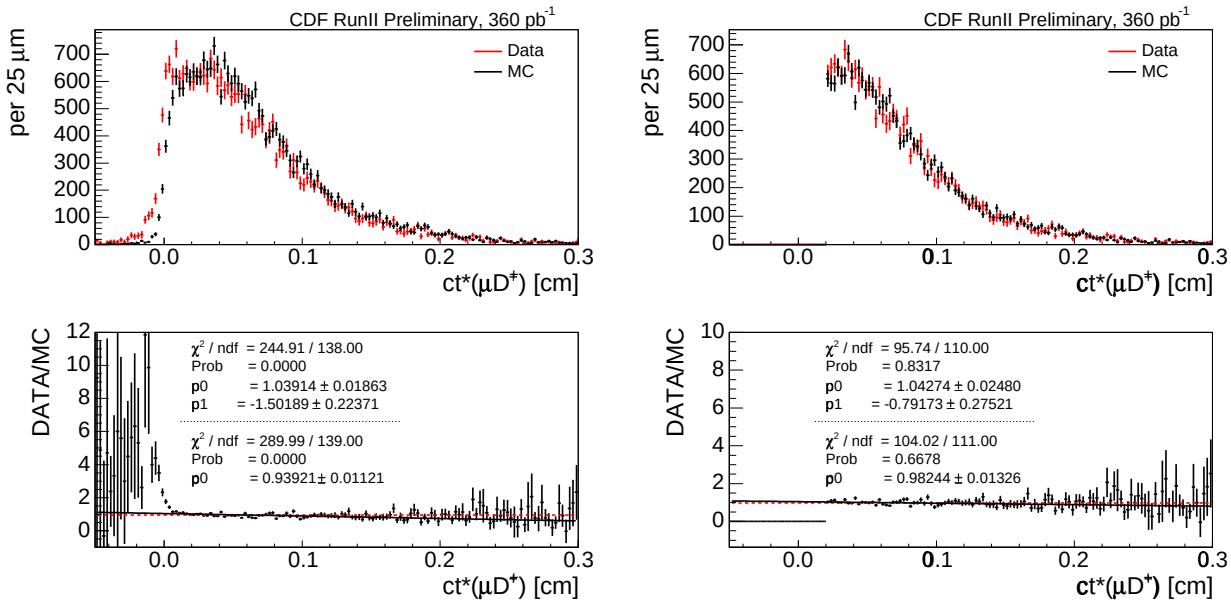

Figure 5.2: $ct^*(\mu^- D^+)$ comparisons for μ+SVT data and Monte Carlo before (left) and after (right) the $ct^*(\mu^- D^+) > 200$ μm cut. The lower plots show the ratio of data to Monte Carlo seen in the upper plots. Two fits are performed on the ratio of data to Monte Carlo: a linear fit, which is listed with its fit probability above the dashed line, and a zeroth order polynomial fit, which is listed with its fit probability below the dashed line.

combinatorial backgrounds, since no real semileptonic $\bar{B}$ signal is expected to be present. The physical, right sign (RS) lepton-charm combinations (*e.g.* $\ell^- D^+$) can have non-combinatorial backgrounds which are not present in the WS combinations.

While the sources of the prompt background are unknown, it is expected to have a significant false lepton contribution to both WS and RS lepton-charm signals. There are also possible contributions from $b\bar{b}$ gluon-splitting to both WS and RS lepton-charm combinations and $c\bar{c}$ gluon-splitting to RS lepton-charm combinations only. In an attempt to eliminate this background, the low ct^* region has been explicitly removed. Requiring $ct^*(\ell^- D/\Lambda_c^+) > 200$ μm is sufficient to bring the data and the Monte Carlo into reasonable agreement in all channels, shown in Figure 5.2 for the $\mu^- D^+$ before and after the $ct^*(\mu^- D^+)$ cut. This cut reduces the yield in the lepton-charm signals by approximately 20%.

The prompt background can also be observed in the impact parameter of the charm signal. The removal of the low ct^* region brings the data into good agreement with the Monte Carlo, as can be seen in Figure 5.3. For this comparison the impact parameter of the charm candidate is normalized above 150 μm in both the data and the Monte Carlo. Before the ct^* cut is applied, a significant prompt discrepancy between the two distributions is observed in the D^+ signal, while the data and the Monte Carlo agree well after the ct^* cut.

The effect of the $ct^*(\ell^- D/\Lambda_c^+)$ cut is cross-checked with the WS lepton-charm correlations. This is not a definitive measure of prompt background reduction, but it does give some indication of remaining contamination in the signals. WS distributions for both the e+SVT

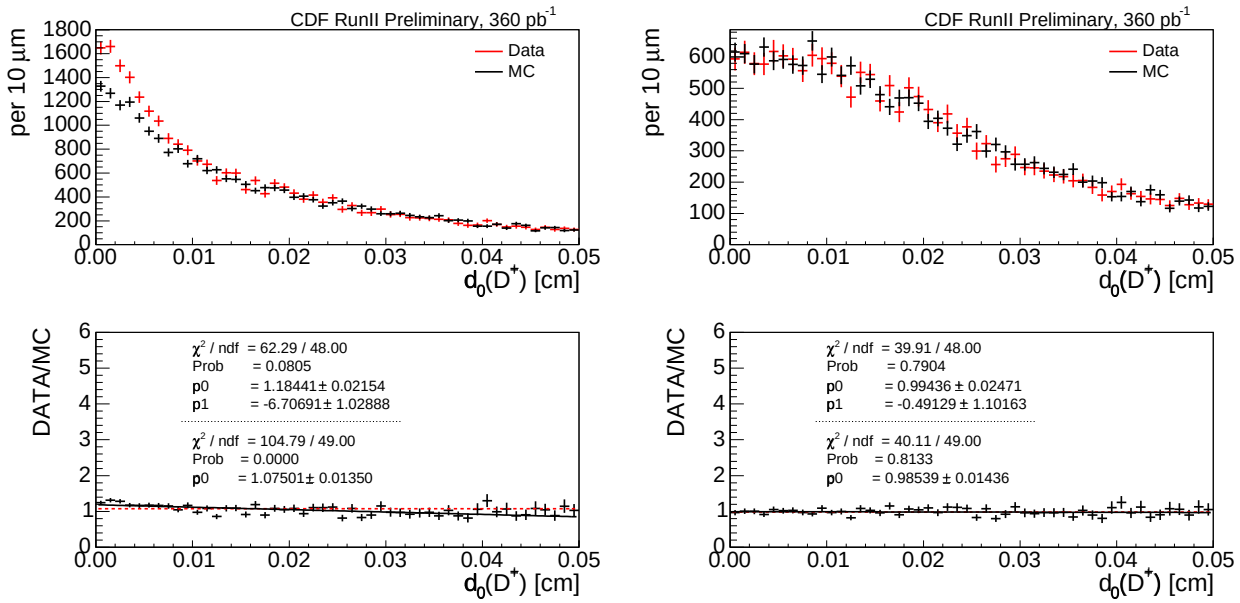

Figure 5.3: Impact parameter distributions of D^+ before the $ct^*(\mu^- D^+)$ cut (left) and after the $ct^*(\mu^- D^+)$ cut (right) in the μ+SVT data.

and μ+SVT samples are shown after the $ct^*(\ell^- D/\Lambda_c^+)$ cut is applied in Figs. 5.4 and 5.5. Yields in the WS distributions are determined by fixing all of the parameters of a double Gaussian signal function to the values determined for the RS signals (cf. Figures 5.12 and 5.13), allowing only the Gaussian normalization and the background shape to float in the fit. The $ct^*(\ell^- D/\Lambda_c^+)$ cut removes most of the WS signal in both the e+charm and μ+charm, although a persistent $2\,\sigma$ significant WS signal remains in all of the electron-charm signals except the D_s^+. Some WS signal remains in the D^0, D^{*+}, D^+, and D_s^+ muon-charm signals. There is no observable WS signal in the $\mu^+\Lambda_c^+$ combination. Significant WS signals are observed in the D^0 and D^{*+} signals, with 4-6 σ significant signals in both the e+SVT and μ+SVT data. The most likely contribution to the remaining WS signal is from real, irreducible conversion electrons and decay-in-flight muons ($K^-/\pi^- \to \mu^-$) combining with a real charm. The possibility of the K-π mis-identification can also contribute to a long-lived WS background in the D^0. The presence of these residual WS signals are treated as a source of systematic uncertainty in the measurement, discussed in Chapter 10.

Reflections

Another consideration in lepton-charm signal reconstruction arises from reflections of other charm states into the charm signal of interest. The Monte Carlo distributions of reflections into the various μ-charm signals are shown in Figure 5.6. The relative normalizations of the reflection shapes are scaled to their expected contribution in data, assuming $f_u : f_d : f_s : f_{\Lambda_b} = 0.4 : 0.4 : 0.1 : 0.1$ *for illustrative purposes only.* In instances where a quantitative estimate is required for the reflection contribution to a given charm signal, the relative contribution of the reflection to the charm signal is determined independent of the relative fragmentation fractions used for illustrating the relative scale of the reflections. Significant

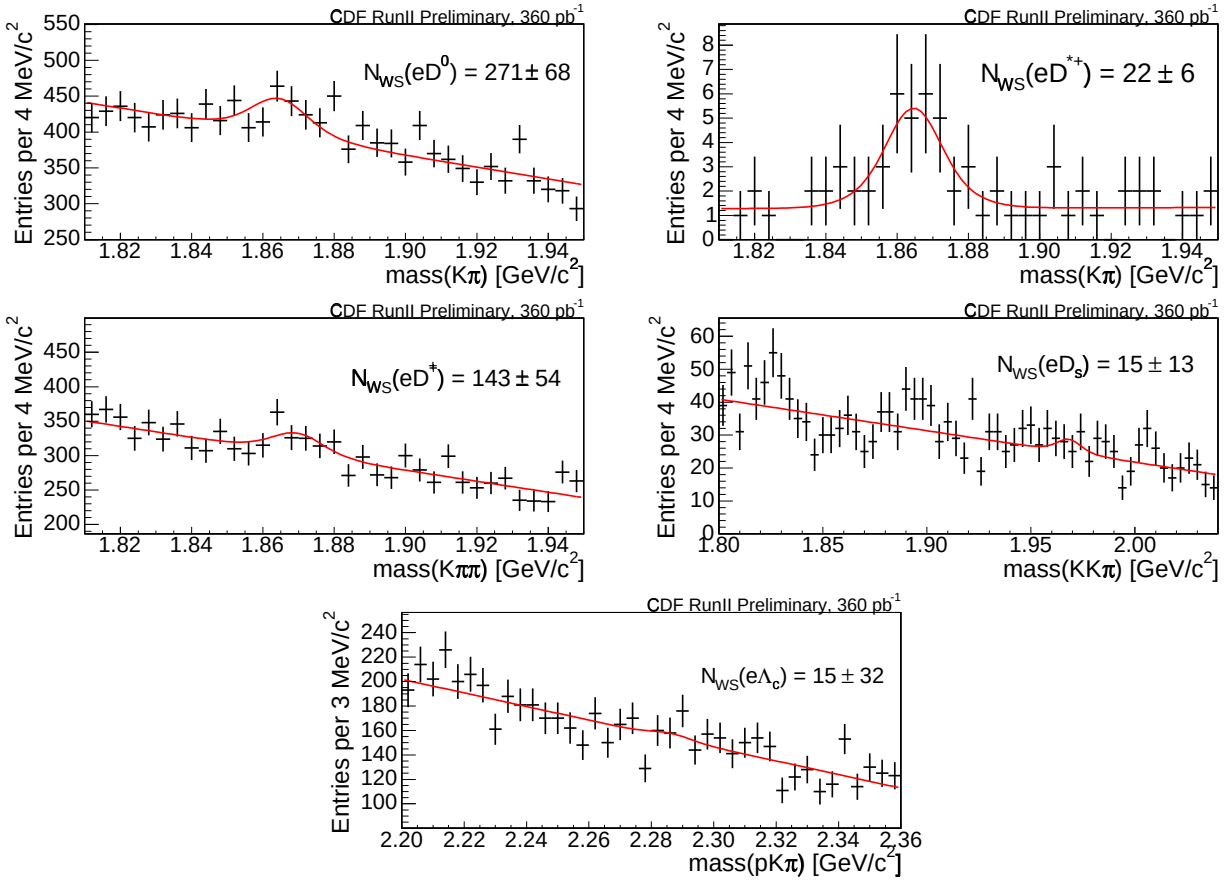

Figure 5.4: Invariant mass distributions of e+SVT wrong sign combinations for (top to bottom, left to right) D^0, D^{*+}, D^+, D_s^+, and Λ_c^+ after the $ct^*(e^- D/\Lambda_c^+)$ cut.

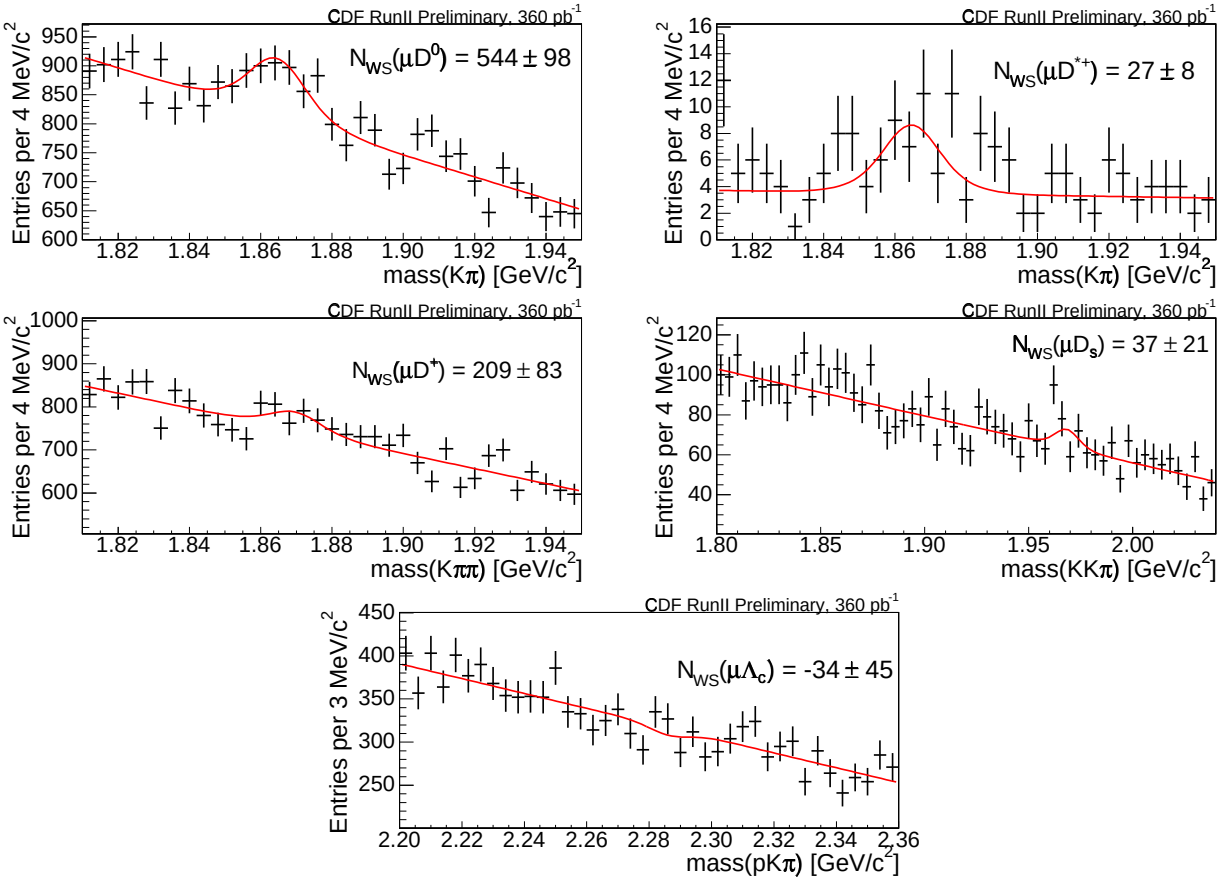

Figure 5.5: Invariant mass distributions of μ+SVT wrong sign combinations for (top to bottom, left to right) D^0, D^{*+}, D^+, D_s^+, and Λ_c^+ after the $ct^*(\mu^- D/\Lambda_c^+)$ cut.

reflections are clearly present beneath the Λ_c^+ and D^+ signals. Because of the kinematics of the decays, the reflections' contribution to the Λ_c^+ signal is relatively flat across the signal region, while the D_s^+ reflection into the D^+ "turns-on" directly beneath the signal. No significant reflections are observed in the D^{*+} or D_s^+ signals, partly due to the $\Delta m(D^{*+}, D^0)$ and ϕ mass cuts, respectively. While the possibility of a significant self-reflection due to $K-\pi$ swap in $D^0 \to K^-\pi^+$ is an issue in D^0 signals, knowledge of the $\ell^+ D^0$ WS signal fixes the normalization of the self-reflection. An estimate of the WS $\ell^+ D^0$ contamination into the RS $\ell^- D^0$ signal can be obtained using the yields shown in Figures 5.4 and 5.5, as well as in Table 5.5. A 15% cross-feed of WS into RS (and vice versa) would decrease the RS yield by 0.3% if the D^0 self-reflection were included. Hence the D^0 self-reflection in the D^0 yield is safely ignored.

One of the most significant reflections is the D_s^+ reflection into the D^+ signal. The $D_s^+ \to K^+K^-\pi^+$ decay cannot readily be vetoed, due to the turn-on of the reflection directly under the D^+ signal. In this case the D_s^+ reflection must be included in the fit to the D^+ signal. It is possible to determine the total number of $D_s^+ \to K^+K^-\pi^+$ which lie beneath the $D^+ \to K^-\pi^+\pi^+$ signal by reconstructing the number of $D_s^+ \to \phi\pi^+$, where $\phi \to K^+K^-$, in a large region around the D^+ signal, such that $1.78\ \mathrm{GeV/c^2} \leq m(K^+K^-\pi^+) \leq 1.95\ \mathrm{GeV/c^2}$ and $|m(K^+K^-) - 1.019\ \mathrm{GeV/c^2}| < 0.0095\ \mathrm{GeV/c^2}$. The reconstructed $D_s^+ \to \phi\pi^+$ events are shown in Figure 5.7.

An inclusive $\bar{B}_s^0 \to \ell^-\bar{\nu}D_s^+X$ Monte Carlo, where the D_s^+ decays completely inclusively according to the `EvtGen` table, is used to relate the number of $D_s^+ \to \phi\pi^+$ measured in data to the total number of $D_s^+ \to K^+K^-\pi^+$ expected to contribute to the D^+ signal. One hundred million fully inclusive events are generated. By reconstructing $N_{MC,D_s^+\to\phi\pi^+}$ and $N_{MC,D_s^+\to K^-K^+\pi^+}$ in a manner completely analogous to $N_{data,D_s^+\to\phi\pi^+}$, the number of D_s^+ mesons expected to contribute to the D^+ signal can be calculated by evaluating

$$N_{data,D_s^+\to K^+K^-\pi^+} = \frac{N_{data,D_s^+\to\phi\pi^-}}{R_{\phi\pi^+}}, \tag{5.3}$$

where

$$R_{\phi\pi} \equiv \frac{N_{MC}(D_s^+ \to \phi\pi^+)}{N_{MC}(D_s^+ \to K^+K^-\pi)}. \tag{5.4}$$

In order to improve statistics, the electron and muon Monte Carlo samples are combined to produce the D_s^+ reflection shape, shown in Figure 5.8. The reflection shape is fitted in the region $m(K^+K^-\pi^+) \in [1.70, 1.95]\ \mathrm{GeV/c^2}$ with an error function for $m(K^+K^-\pi^+) > 1.866$, $z = a \cdot erfc((x-b)*c) + f$, and damped with a linear term for $m(KK\pi) \leq 1.866$, $z = a \cdot erfc((x-b)*c) - e*(1/x - 1/d) + f$, where x is the mass of the D^+. The Monte Carlo scaling factor $R_{\phi\pi^+}$ is averaged between the electron and muon samples

$$\begin{aligned} R_{e,\phi\pi^+} &= 0.235 \pm 0.011 \\ R_{\mu,\phi\pi^+} &= 0.257 \pm 0.011 \end{aligned}$$

to give

$$R_{\phi\pi^+} = 0.246 \pm 0.008.$$

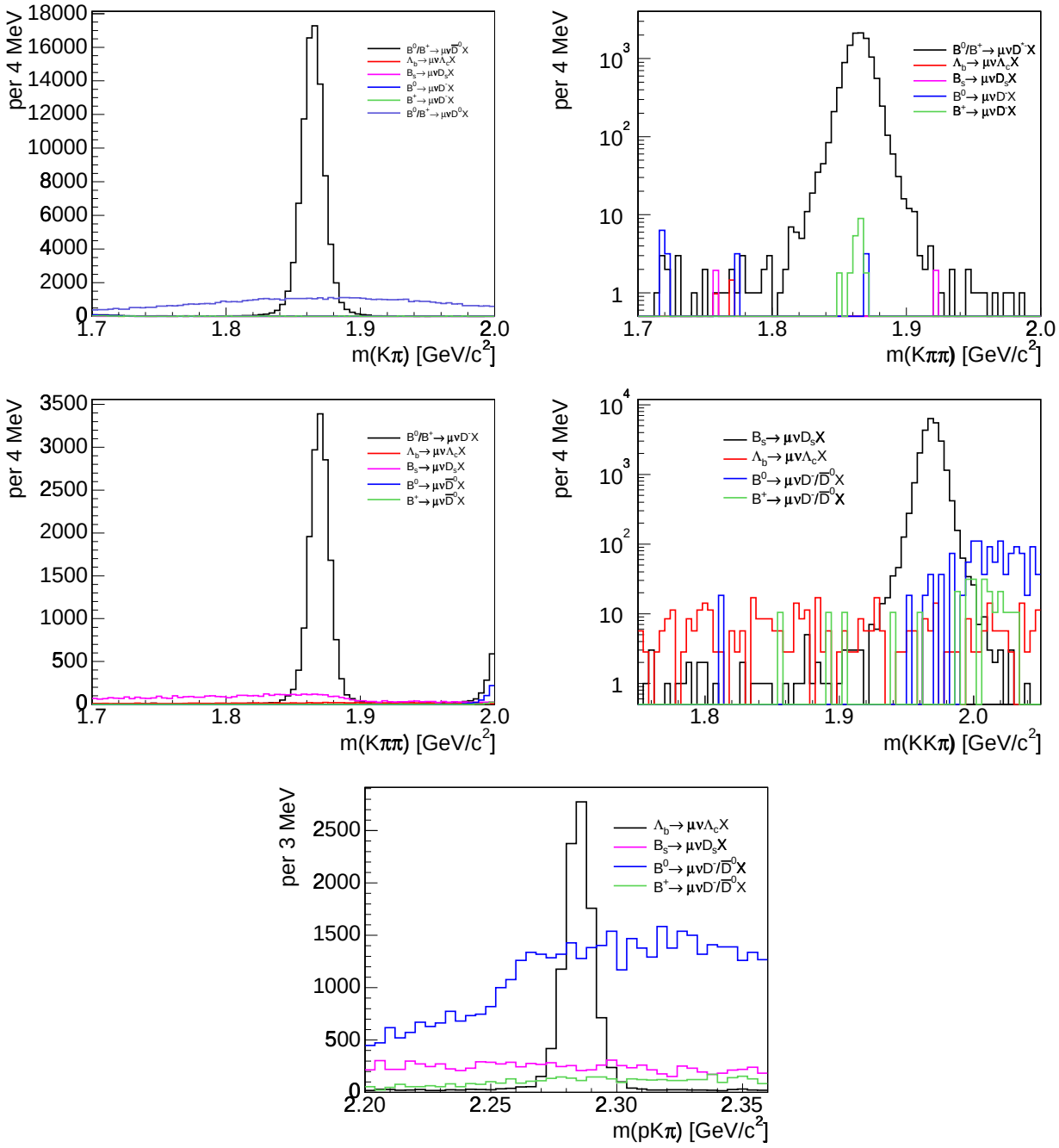

Figure 5.6: MC reflection shapes for D^0 (top left), D^{*+} (top right), D^+ (middle left), D_s^+ (middle right), and Λ_c^+ (bottom). The shapes are normalized to their expected contributions, assuming $f_u : f_d : f_s : f_{\Lambda_b} = 0.4 : 0.4 : 0.1 : 0.1$, used *for illustrative purposes only.*

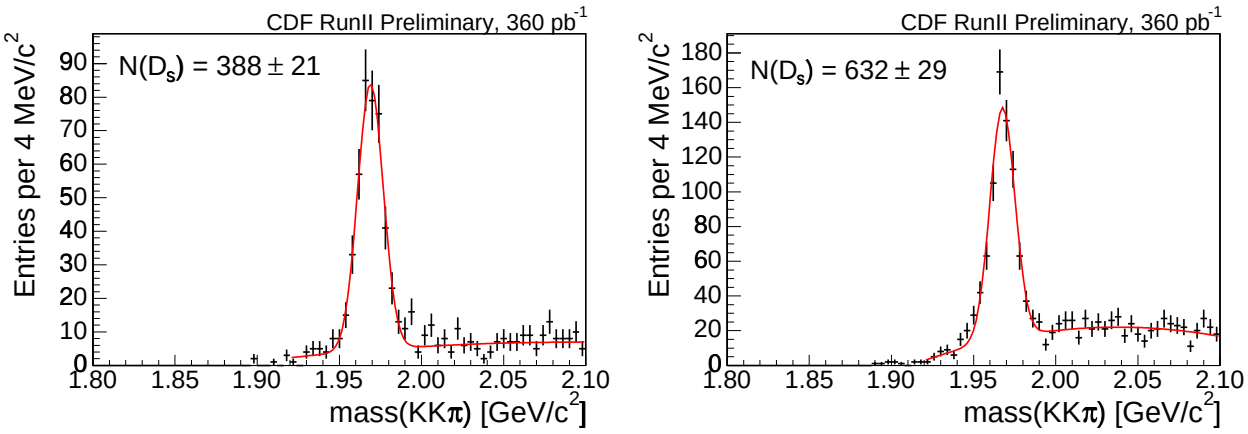

Figure 5.7: $N(D_s^+ \to \phi\pi^+)$ reconstructed in $m(K\pi\pi) \in [1.78, 1.95]$ in the e+SVT data (left) and the μ+SVT data (right).

	e+SVT		μ+SVT	
D_s^+ Reflection	$N(D_s^+)$	$N(e^-D^+)$	$N(D_s^+)$	$N(\mu^-D^+)$
Constrained	1,710±76	10,779±149	2,778±461	20,236±216
Fixed	1,577	10,797±149	2,570	20,267±247
Floating	3,267±1,097	10,575±201	5,054±1,665	19,906±336
None	—	11,015±157	—	20,643±258

Table 5.2: $\ell^- D^+$ yield with different D_s^+ reflection normalization configurations.

The numbers of D_s^+ candidates measured in the D^+ lepton-charm samples are

$$\begin{aligned} N_e(D_s^+ \to K^+K^-\pi^+) &= 1577 \pm 100 \\ N_\mu(D_s^+ \to K^+K^-\pi^+) &= 2570 \pm 144. \end{aligned}$$

The normalization of the reflection is constrained to the predicted number of D_s^+ reflection events within errors and combined with a double Gaussian and a linear background in a χ^2-fit to the D^+ signal. In order to keep the broad Gaussian and reflection shape reasonably independent, the double Gaussian parameters are determined before the reflection shape is added to the fit. When the combined fit is performed, the parameters of the double Gaussian are constrained within their errors. The changes in yield with different constraints on $N(D_s^+)$ are listed in Table 5.2. The normalization of the D_s^+ shape is allowed to float to cross-check the results of the scaling. The floating normalization is consistent with the measured normalization in both the e^-D^+ and μ^-D^+, although the error on this value is quite large. The number of $\ell^- D^+$ events, $N(D^+)$, when the D_s^+ reflection is included is consistent whether the $N(D_s^+)$ is constrained, fixed, or permitted to float in the fit. The $\ell^- D^+$ yield decreases by roughly 1.5% when the D_s^+ reflection is included in the fit.

The D^+ and D_s^+ reflections in the Λ_c^+ signal are relatively flat under the signal region and sideband subtraction is expected to remove their effect on signal distributions within

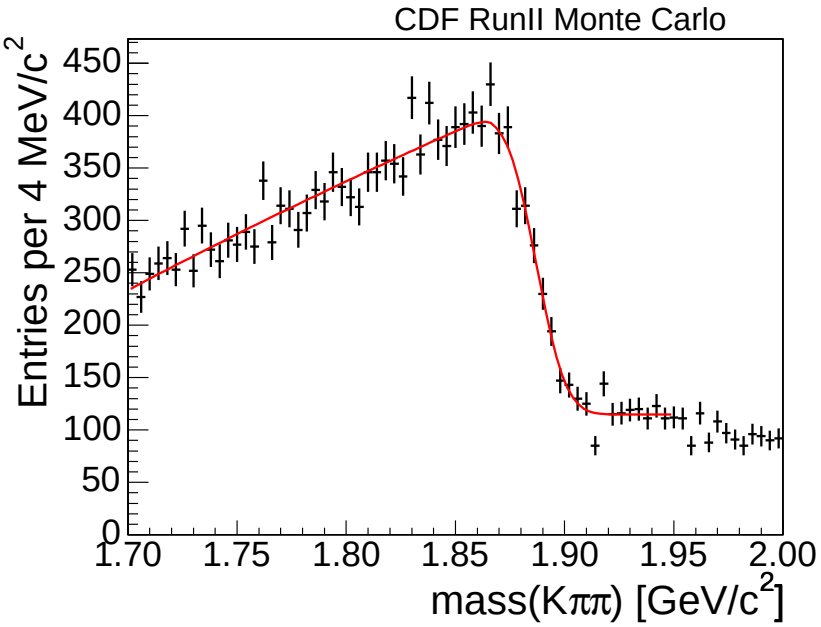

Figure 5.8: Combined e and μ D_s^+ reflection shape determined from inclusive $\bar{B}_s^0 \to e^-/\mu^-\bar{\nu}D_s^+X$ Monte Carlo, where the D_s^+ decays inclusively.

statistical uncertainty. Correspondingly, the event count obtained by fitting is not expected to be significantly influenced by the presence of these backgrounds. This can be checked in the Λ_c^+ mass distribution by vetoing on the D^+, D_s^+, and D^{*+} reflections and checking the change in yield in the data against that predicted by the Monte Carlo. These reflections into the Λ_c^+ signal are vetoed by reassigning the $pK\pi$ hypothesis to the other charm states and removing candidates which fall within the following mass windows:

- $|m(K\pi\pi)$ - 1.8694 GeV/c$^2|$ < 0.020 GeV/c^2,
- $|m(KK\pi)$ - 1.968 GeV/c$^2|$ < 0.020 GeV/c^2,
- 0.1430 GeV/c$^2 <$ $m(K\pi\pi) - m(K\pi)$ < 0.1490 GeV/c^2.

The effect of these vetoes is tabulated in Table 5.3. The D^+ and D^{*+} vetoes reduce the data yield by an amount consistent with the Monte Carlo prediction, while the effect of the D_s^+ veto appears to be under-estimated in the Monte Carlo. This difference is primarily responsible for the discrepancy in yield reduction between the data and the Monte Carlo when all three reflections are vetoed simultaneously. The inability of the Monte Carlo to accurately reproduce the effect of the vetoes in data is most likely a result of the non-linear shape of the reflections, particularly in the mass window below the Λ_c^+ signal, where the D^+ reflection falls off. For this reason, a dE/dx cut to reduce the D^+ reflection in the Λ_c^+ mode is preferred over direct vetoes.

	e+SVT		μ+SVT	
Veto	Data (%)	MC (%)	Data (%)	MC (%)
D^+	88.1 ± 4.3	86.9 ± 1.3	86.2 ± 3.1	86.9 ± 1.2
D^{*+}	98.1 ± 4.7	99.8 ± 1.4	95.7 ± 3.4	97.6 ± 1.3
D_s^+	81.2 ± 4.2	86.0 ± 1.3	81.5 ± 3.6	85.8 ± 1.2
all	66.9 ± 4.1	72.9 ± 1.1	64.1 ± 2.5	72.6 ± 1.1

Table 5.3: Effect of different charm vetoes on data and Monte Carlo in the Λ_c^+ signal.

dE/dx

The background beneath the Λ_c^+ signal can be reduced without vetoing on contributing reflections by instead applying a dE/dx likelihood ratio ($\mathcal{LR}$) cut on the proton. The likelihood ratio constructed is $\mathcal{LR}(p) \equiv \mathcal{L}(p)/[\mathcal{L}(p)+\mathcal{L}(K)+\mathcal{L}(\pi)+\mathcal{L}(e)+\mathcal{L}(\mu)]$, where $\mathcal{L} \propto \exp(-\frac{Z^2}{2\sigma_Z^2})$ and $Z \equiv \ln \frac{dE/dx(measured)}{dE/dx(predicted)}$. Figure 5.9 shows the $\mathcal{LR}$ distributions for protons from $\Lambda^0 \to p\pi^-$ and kaons and pions from $D^{*+} \to D^0\pi^+\pi K^-\pi^+$ with the proton hypothesis applied (see Appendix B for selection of the D^{*+} and Λ samples). A cut on the proton $\mathcal{LR}$ of 0.3, chosen from the control samples to reduce background while keeping the proton efficiency high, is applied to the data. This cut primarily removes contamination from pions, which contribute to the $D^+ \to K^-\pi^+\pi^+$ and $D^{*+} \to [K^-\pi^+]\pi^+$ reflections, and has little discriminating power between protons and kaons.

The dE/dx $\mathcal{LR}(p)$ cut flattens the background and reduces the overall background level by a factor of five, while it reduces the signal by ~35% in the μ+SVT data and ~28% in the e+SVT data. The efficiency of this dE/dx cut must be determined from data (see Section 7.1.3), because the Monte Carlo does not describe energy loss effects in the COT for an accurate prediction of the dE/dx in the Monte Carlo.

Discrepancies between Data and Monte Carlo

The final agreement between the data and the Monte Carlo will be discussed in Section 7.2. While agreement between the data and the Monte Carlo is generally good, the $\ell^- D^0$ signals, which show a significant disagreement in all quantities that depend on the charm candidate, are notable exceptions. The disagreement in the $p_T(D^0)$ is especially striking (see Figures 5.10 and 5.11). Since the $\ell^- D^0$ signals have twice the statistics of the next highest statistics lepton-charm signal, an additional cut is placed on the $p_T(D^0) > 5$ GeV/c, improving the probability of agreement between the data and the Monte Carlo. This cut eliminates any significant bias between the $p_T(D^0)$ and $p_T(K)$ distributions; in both distributions a first order polynomial does not fit the ratio of data to Monte Carlo significantly better than a zeroth order polynomial. This is sufficient to bring the other quantities which are cut upon into agreement comparable with the other lepton-charm channels, shown in Section 7.2, Figures 7.11-7.12 and in Appendix D, Figures D.4-D.5.

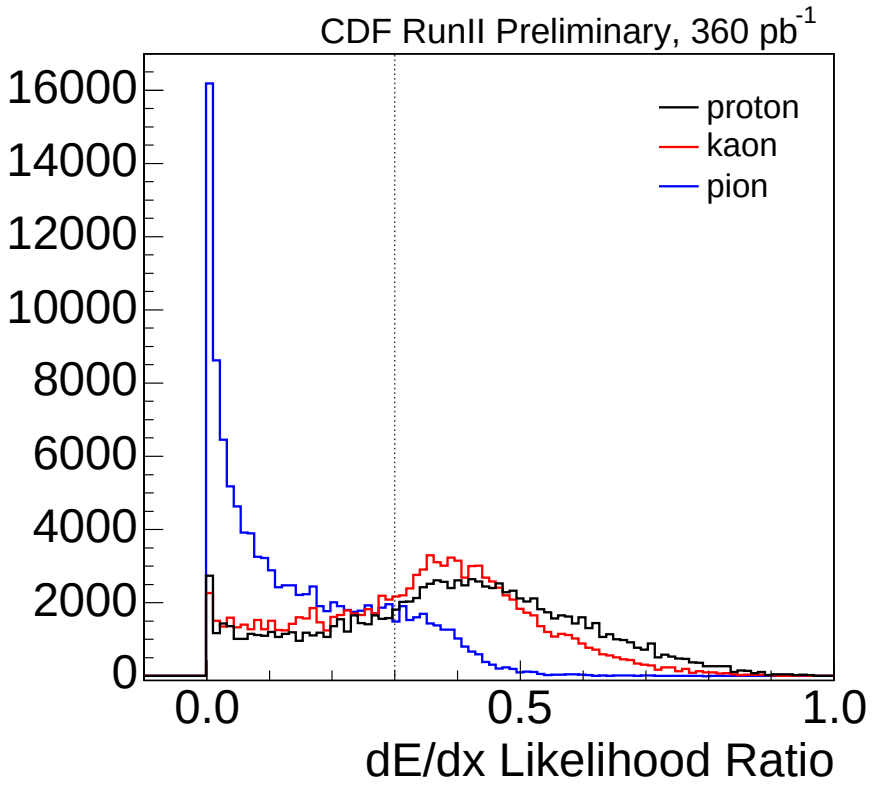

Figure 5.9: dE/dx $\mathcal{LR}$ distribution with the proton mass hypothesis. The proton comes from $\Lambda \to p\pi$, while the kaon and pion come from $D^{*+} \to [K\pi]\pi$. The cut value is shown with the dashed line.

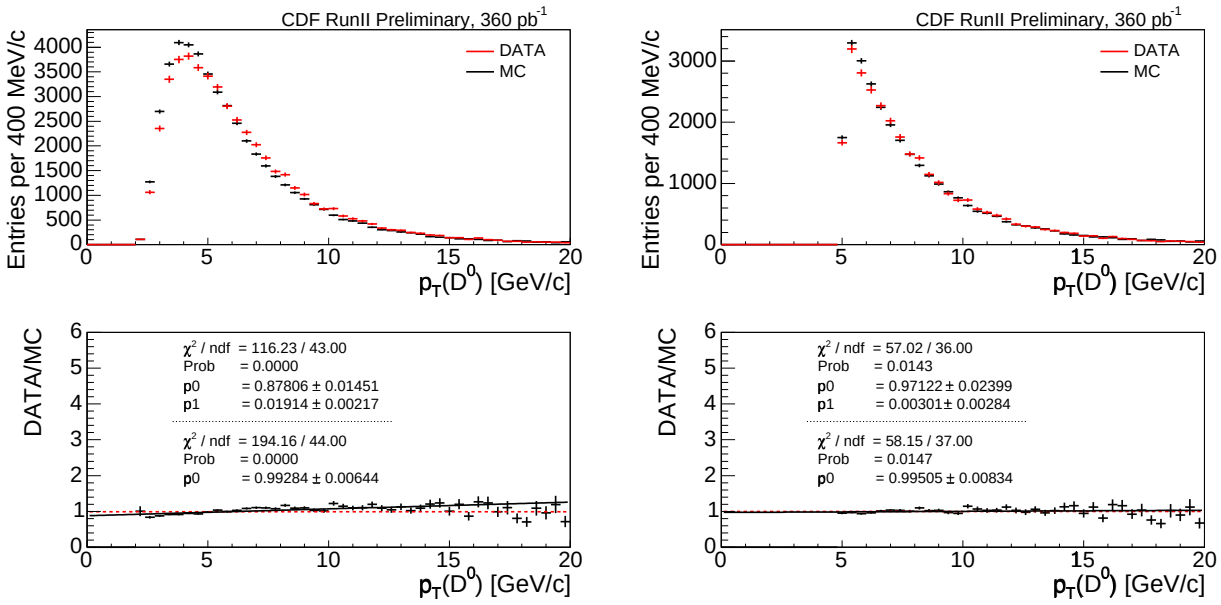

Figure 5.10: μ+SVT data and Monte Carlo comparisons of $p_T(D^0)$ before (left) and after (right) requiring $p_T(D^0) > 5$ GeV/c.

5.2.2 Final Signal Selection

Table 5.4 lists the final selection cuts for the lepton-charm signals, combining the synthesized signal selection with additional selection requirements to reduce sources of non-combinatoric background and improve agreement between the data and the Monte Carlo. All charm signals are fitted with a double Gaussian plus a linear background except the D^+, which includes a term in the fit for the D_s^+ reflection. The invariant mass distributions of the charm signals in the e+SVT sample are shown in Figure 5.12, while the μ+SVT charm signals are shown in Figure 5.13. The final charm yields are listed in Table 5.5.

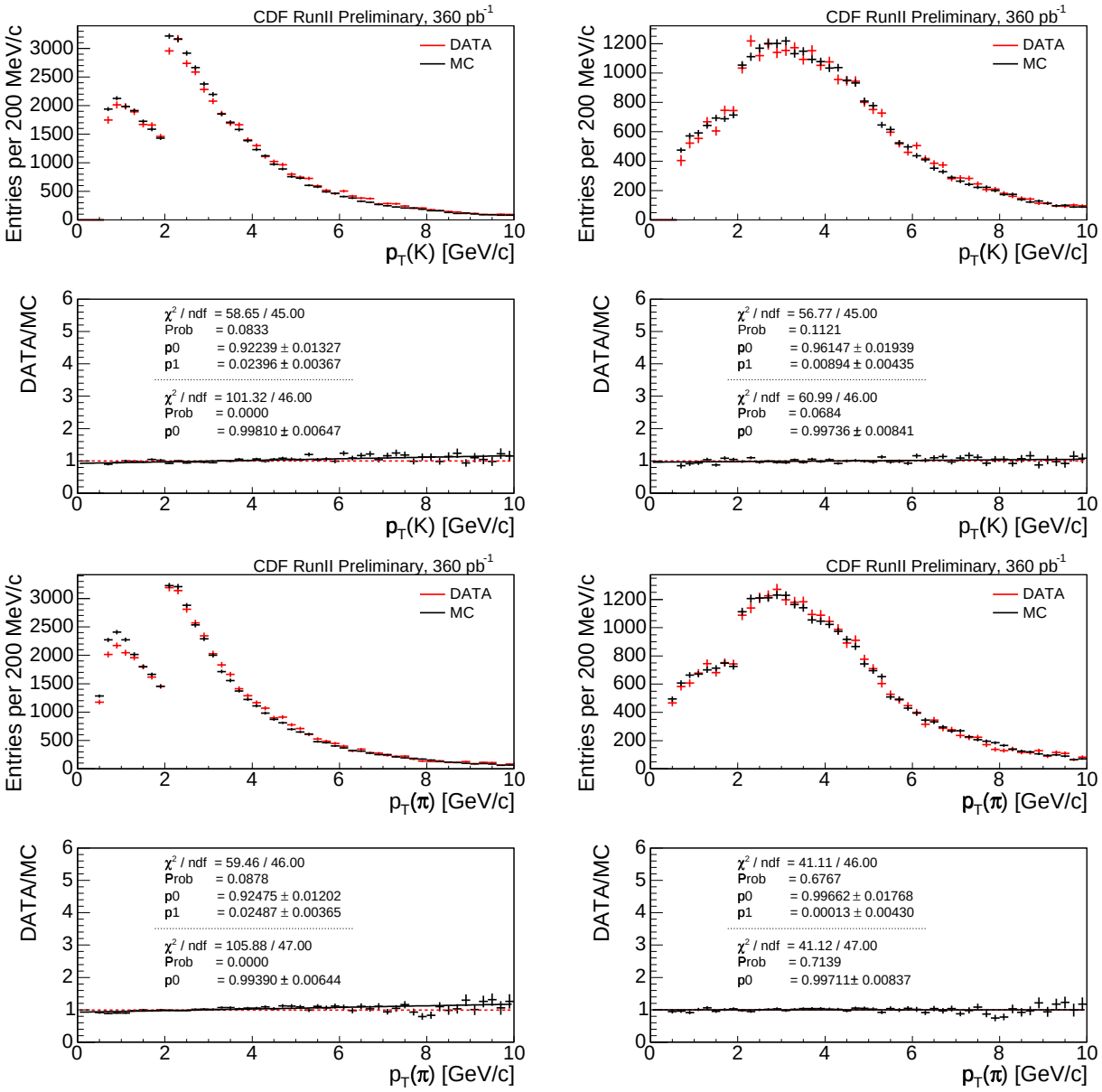

Figure 5.11: μ+SVT data and Monte Carlo comparisons of $p_T(K)$ (top) and $p_T(\pi)$ (bottom) before (left) and after (right) requiring $p_T(D^0) > 5$ GeV/c.

Cuts	$\ell^- D^0$	$\ell^- D^{*+}$	$\ell^- D^+$	$\ell^- D_s^+$	$\ell^- \Lambda_c^+$
$ct(D/\Lambda_c^+)$ [cm] >	-0.01	-0.01	-0.01	-0.01	-0.01
$ct(D/\Lambda_c^+)$ [cm] <	0.10	0.10	0.20	0.10	0.05
$ct^*(\ell^- D/\Lambda_c^+)$ [cm] >	0.02	0.02	0.02	0.02	0.02
$\sigma_{ct}(\ell^- D/\Lambda_c^+)$ [cm] <	0.04	0.04	0.04	0.04	0.04
$m(\ell^- D/\Lambda_c^+)$ [GeV/c^2] >	2.4	2.4	2.4	2.4	3.4
$m(\ell^- D/\Lambda_c^+)$ [GeV/c^2] <	5.1	5.1	5.1	5.1	5.5
$p_T(D/\Lambda_c^+)$ [GeV/c] >	5.0	5.0	N/A	N/A	N/A
$p_T(p)$ [GeV/c] >	N/A	N/A	N/A	N/A	2.0
$p_T(K)$ [GeV/c] >	0.6	0.6	0.6	0.6	0.6
$\chi^2_{2D}(D/\Lambda_c^+)$ <	10	10	10	10	5
vtx. prob.$(\ell^- D/\Lambda_c^+)$ >	10^{-7}	10^{-7}	10^{-7}	10^{-7}	10^{-4}
$L_{xy}/\sigma_{Lxy}(D/\Lambda_c^+)$ >	4.5	4.5	11	5	4.5
$\Delta m(D^*, D)$ [GeV/c^2] >	N/A	0.1440	N/A	N/A	N/A
$\Delta m(D^*, D)$ [GeV/c^2] <	N/A	0.1475	N/A	N/A	N/A
$\lvert m(\phi) - 1.019 \rvert$ [GeV/c^2] <	N/A	N/A	N/A	0.0095	N/A
dE/dx $\mathcal{LR}(p)$ >	N/A	N/A	N/A	N/A	0.3

Table 5.4: Final signal selection.

	e+SVT			μ+SVT		
Decay	Yield	FOM	Fit Prob(%)	Yield	FOM	Fit Prob(%)
$\ell^- D^0$	16,939±160	122	64.4	29,909±224	159	12.5
$\ell^- D^{*+}$	2,998±56	54.1	1.27	5,492±77	73.3	1.14
$\ell^- D^+$	10,779±149	90.2	9.43	20,236±216	114	50.7
$\ell^- D_s^+$	1,012±44	27.3	7.84	2,069±84	36.6	30.2
$\ell^- \Lambda_c^+$	1,755±106	32.8	33.9	2,984±130	40.9	40.9

Table 5.5: Lepton-charm signal yields after all cuts.

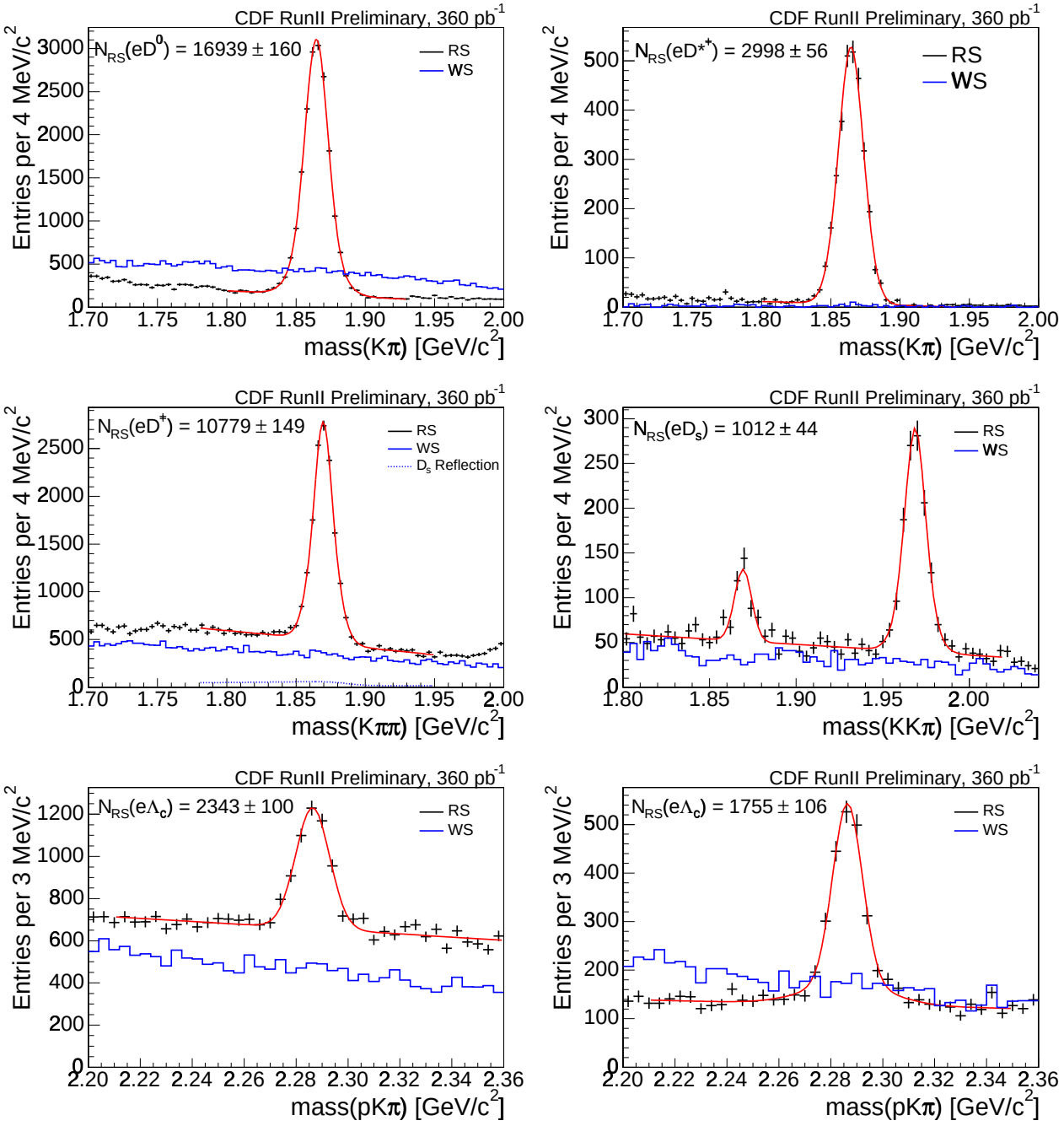

Figure 5.12: e+SVT right sign (black) and wrong sign (blue) invariant mass distributions of D^0 (top left), D^{*+} (top right), D^+ (middle left), D_s^+ (middle right), Λ_c^+ without the dE/dx cut (bottom left) and with the dE/dx cut (bottom right).

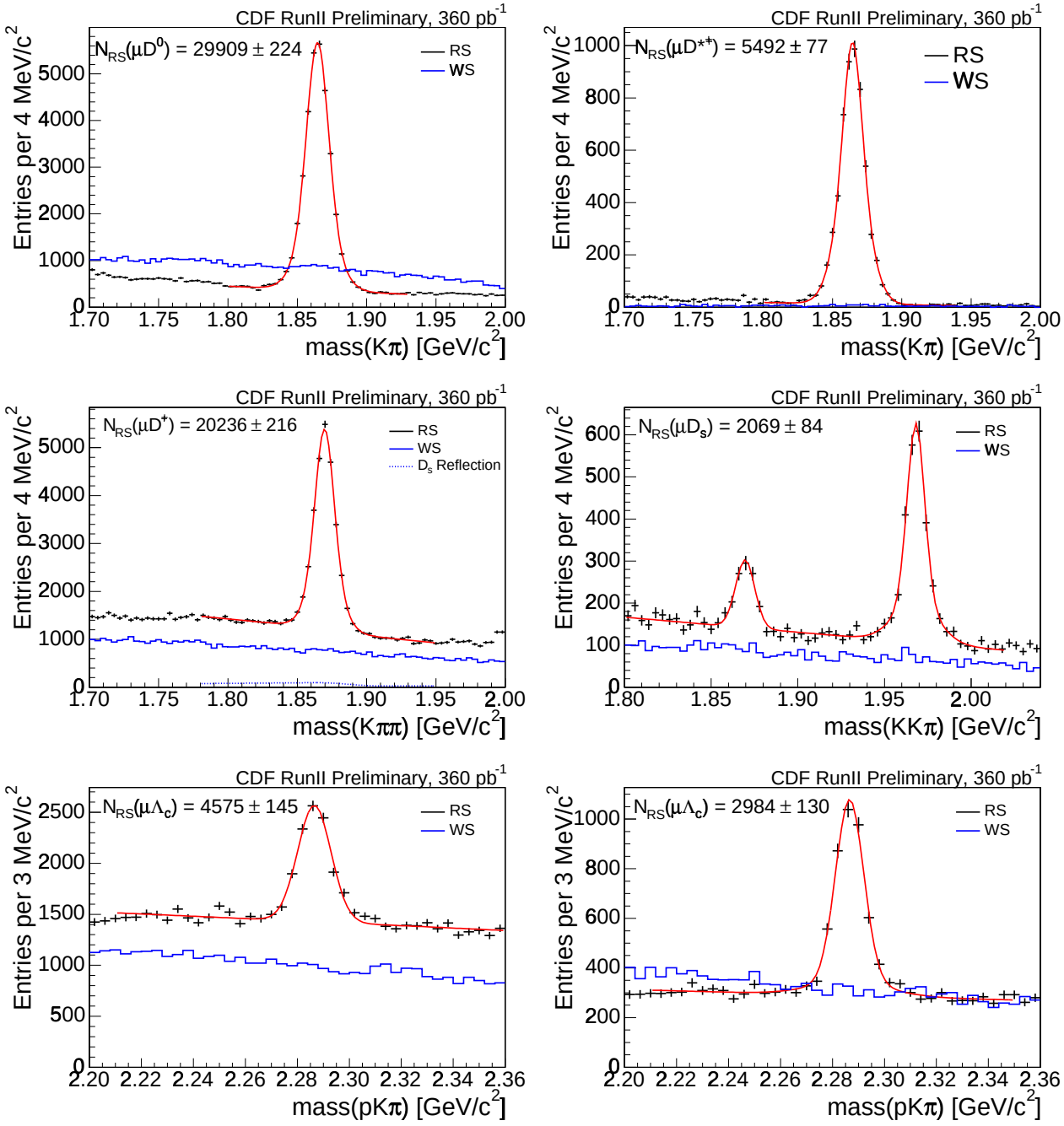

Figure 5.13: μ+SVT right sign (black) and wrong sign (blue) invariant mass distributions of D^0 (top left), D^{*+} (top right), D^+ (middle left), D_s^+ (middle right), Λ_c^+ without the dE/dx cut (bottom left) and with the dE/dx cut (bottom right).

Chapter 6

Sample Composition

Sundry unknown or poorly known pieces of information obscure the ability to disentangle the lepton-charm samples from their parent $\bar{B}$ hadrons. The primary source of uncertainty is the missing neutrino from the semileptonic decay, from which the need for a sample composition arises. Since the neutrino is not reconstructed, other excited charm states can feed into the ground state and cannot readily be distinguished from the ground state in the candidate selection quantities considered. The excited charm contribution to the final signal must instead be parameterized with their branching ratios and efficiencies to be detected, since additional missing energy is present. The excited charm states are primarily missing photons or neutral pions, but charged pions and kaons are also missed in cascade decays to the ground state charm candidates, since only the ground state daughter tracks, including the charged pion from the $D^{*+} \to D^0\pi^+$, are explicitly selected and stored. The decays included in the sample composition are listed in Table 6.1. Apart from uncertainties in the sample composition, many poorly known or unknown branching ratios also complicate the picture. The branching ratios of the bottom hadrons semileptonically decaying to charm hadrons have been parameterized with spectator model constraints.

6.1 Parameterization

Spectator model assumptions, discussed in Section 2.4.3, are applied to the relative rate at which $\bar{B}$ mesons decay to ground state and excited D mesons. These rates are assumed to be the same for B^-, $\bar{B}^0$, and $\bar{B}^0_s$ mesons. This assumption is held to be fairly good for $\bar{B}^0$ and B^-, but it is not known how accurately the spectator model characterizes $\bar{B}^0_s$ decays. While it is probably a good assumption for the $\bar{B}^0_s$ mesons as well, many of the $\bar{B}^0_s$ branching ratios are poorly measured or are simply not known. Certainly, the Λ^0_b is not necessarily well-described by spectator model arguments, since the two spectator quarks might have rather different effects in the baryon than the one light anti-quark present in the meson, particularly when describing the branching ratios to excited charm baryons.

If the only source of $\ell^- D^+$ combinations were from the direct decay $\bar{B}^0 \to \ell^-\bar{\nu}D^+$, the number of reconstructed $\ell^- D^+$ events are

$$N(\ell^- D^+) \;=\; N(\bar{B}^0) \times \mathcal{BR}(\bar{B}^0 \to \ell^-\bar{\nu}D^+) \times \mathcal{BR}(D^+ \to K^+\pi^-\pi^-)$$

$\bar{B}^0$	B^-	$\bar{B}_s^0$	Λ_b^0
$\ell^-\bar{\nu}D^+$	$\ell^-\bar{\nu}D^0$	$\ell^-\bar{\nu}D_s^+$	$\ell^-\bar{\nu}\Lambda_c^+$
$\ell^-\bar{\nu}D^{*+}$	$\ell^-\bar{\nu}D^{*0}$	$\ell^-\bar{\nu}D_s^{*+}$	$\ell^-\bar{\nu}\Lambda_c(2593)^+$
$\to D^0\pi^+$	$\to D^0\pi^0/\gamma$	$\to D_s^+\gamma$	$\to \Sigma_c(2455)^{++}\pi^-$
$D^+\pi^0/\gamma$			$\hookrightarrow \Lambda_c^+\pi^+$
			$\to \Sigma_c(2455)^0\pi^+$
$\ell^-\bar{\nu}D_1^+$	$\ell^-\bar{\nu}D_1^0$	$\ell^-\bar{\nu}D_{s1}^+(2460)$	$\hookrightarrow \Lambda_c^+\pi^-$
$\to D^{*0}\pi^+$	$\to D^{*0}\pi^0$	$\to D_{s0}^{*+}\pi^0$	$\to \Sigma_c(2455)^+\pi^0$
$\hookrightarrow D^0\pi^0/\gamma$	$\hookrightarrow D^0\pi^0/\gamma$	$\hookrightarrow D_s^+\pi^0$	$\hookrightarrow \Lambda_c^+\pi^0$
$\to D^{*+}\pi^0$	$\to D^{*+}\pi^-$	$\to D_s^+\gamma$	$\to \Lambda_c^+\pi^+\pi^-$
$\hookrightarrow D^0\pi^+$	$\hookrightarrow D^0\pi^+$		$\to \Lambda_c^+\pi^0\pi^0$
$D^+\pi^0/\gamma$	$D^+\pi^0/\gamma$		$\to \Lambda_c^+\gamma$
$\ell^-\bar{\nu}D_0^{*+}$	$\ell^-\bar{\nu}D_0^{*0}$	$\ell^-\bar{\nu}D_{s0}^{*+}(2317)$	$\ell^-\bar{\nu}\Lambda_c(2625)^+$
$\to D^0\pi^+$	$\to D^0\pi^0$	$\to D_s^+\pi^0$	$\to \Lambda_c^+\pi^+\pi^-$
$D^+\pi^0$	$D^+\pi^-$		$\to \Lambda_c^+\pi^0\pi^0$
			$\to \Lambda_c^+\gamma$
$\ell^-\bar{\nu}D_1^{'+}$	$\ell^-\bar{\nu}D_1^{'0}$	$\ell^-\bar{\nu}D_{s1}^{'+}(2535)$	
$\to D^{*0}\pi^+$	$\to D^{*0}\pi^0$	$\to D^{*+}K^0$	$\ell^-\bar{\nu}\Sigma_c(2455)^{++}\pi^-$
$\hookrightarrow D^0\pi^0/\gamma$	$\hookrightarrow D^0\pi^0/\gamma$	$\hookrightarrow D^0\pi^+$	$\to \Lambda_c^+\pi^+$
$\to D^{*+}\pi^0$	$\to D^{*+}\pi^-$	$D^+\pi^0/\gamma$	
$\hookrightarrow D^0\pi^+$	$\hookrightarrow D^0\pi^+$	$\to D^{*0}K^+$	$\ell^-\bar{\nu}\Sigma_c(2455)^0\pi^+$
$D^+\pi^0/\gamma$	$D^+\pi^0/\gamma$	$\hookrightarrow D^0\pi^0/\gamma$	$\to \Lambda_c^+\pi^-$
$\ell^-\bar{\nu}D_2^{*+}$	$\ell^-\bar{\nu}D_2^{*0}$	$\ell^-\bar{\nu}D_{s2}^{'+}(2573)$	$\ell^-\bar{\nu}\Sigma_c(2455)^+\pi^0$
$\to D^{*0}\pi^+$	$\to D^{*0}\pi^0$	$\to D^{*+}K^0$	$\to \Lambda_c^+\pi^0$
$\hookrightarrow D^0\pi^0/\gamma$	$\hookrightarrow D^0\pi^0/\gamma$	$\hookrightarrow D^0\pi^+$	
$\to D^{*+}\pi^0$	$\to D^{*+}\pi^-$	$D^+\pi^0/\gamma$	$\ell^-\bar{\nu}\Lambda_c^+ f_0$
$\hookrightarrow D^0\pi^+$	$\hookrightarrow D^0\pi^+$	$\to D^{*0}K^+$	
$D^+\pi^0/\gamma$	$D^+\pi^0/\gamma$	$\hookrightarrow D^0\pi^0/\gamma$	$\ell^-\bar{\nu}\Lambda_c^+\pi^+\pi^-(\mathrm{NR})$
$\to D^0\pi^0$	$\to D^0\pi^0$	$\to D^+K^0$	
$\to D^+\pi^-$	$\to D^+\pi^-$	$\to D^0K^+$	$\ell^-\bar{\nu}\Lambda_c^+\pi^0\pi^0(\mathrm{NR})$
$\ell^-\bar{\nu}D^{*+}\pi^0(\mathrm{NR})$	$\ell^-\bar{\nu}D^{*+}\pi^-(\mathrm{NR})$	$\ell^-\bar{\nu}D_s^{*+}\pi^0(\mathrm{NR})$	
$\to D^0\pi^+$	$\to D^0\pi^+$	$\to D_s^+\gamma$	
$D^+\pi^0/\gamma$	$D^+\pi^0/\gamma$		
		$\ell^-\bar{\nu}D_s^+\pi^0(\mathrm{NR})$	
$\ell^-\bar{\nu}D^{*0}\pi^+(\mathrm{NR})$	$\ell^-\bar{\nu}D^{*0}\pi^0(\mathrm{NR})$		
$\to D^0\pi^0/\gamma$	$\to D^0\pi^0/\gamma$		
$\ell^-\bar{\nu}D^+\pi^0(\mathrm{NR})$	$\ell^-\bar{\nu}D^+\pi^-(\mathrm{NR})$		
$\ell^-\bar{\nu}D^0\pi^+(\mathrm{NR})$	$\ell^-\bar{\nu}D^0\pi^0(\mathrm{NR})$		
$D^{(*)}\bar{D}^{(*)}K$	$D^{(*)}\bar{D}^{(*)}K$	$D^{(*)}\bar{D}^{(*)}K$	
$D^{(*)+}D^{(*)-}$			
$D_s^{(*)}D^{(*)}X$	$D_s^{(*)}D^{(*)}X$	$D_s^{(*)}D^{(*)}X$	$\tau^-\bar{\nu}\Lambda_c^+$
		$D_s^{(*)}D_s^{(*)}X$	$\tau^-\bar{\nu}\Lambda_c(2593)^+$
$\tau^-\bar{\nu}D^{+(*),(**)}$	$\tau^-\bar{\nu}D^{0(*),(**)}$	$\tau^-\bar{\nu}D_s^{+(*),(**)}$	$\tau^-\bar{\nu}\Lambda_c(2625)^+$

Table 6.1: $\bar{B}$ hadron sample composition.

$$
\begin{aligned}
& \times \varepsilon(\bar{B}^0 \to \ell^- \bar{\nu} D^+, D^+ \to K^+\pi^-\pi^-) \\
= \; & N(\bar{B}) f_d \times \tau(\bar{B}^0)\Gamma(\bar{B}^0 \to \ell^- \bar{\nu} D^+) \times \mathcal{BR}(D^+ \to K^+\pi^-\pi^-) \\
& \times \varepsilon(\bar{B}^0 \to \ell^- \bar{\nu} D^+, D^+ \to K^+\pi^-\pi^-), \qquad (6.1)
\end{aligned}
$$

where $N(\bar{B}^0)$ and $N(\bar{B})$ represent the numbers of produced $\bar{B}^0$ or generic $\bar{B}$ hadrons. Cross-talk between the various $\bar{B}$ hadrons into a specific lepton-charm final state complicates the picture. Taking this cross-talk into account, the individual decays which make up the sample composition are related to the predicted numbers of lepton-charm candidates by the relative fragmentation fractions, the number of $\bar{B}$ mesons, the lifetimes of the $\bar{B}$ mesons, and the individual charm branching ratios. The observed numbers of $\ell^- D$ candidates can generically be written as

$$
\begin{aligned}
N(\ell^- D_i) \; = \; & \sum_{j=d,u,s} N(\bar{B}) \times f_j \times \tau(\bar{B}_j) \sum_k \Gamma_k \times \mathcal{BR}_{ijk}(D_{jk} \to D_i)\mathcal{BR}(D_i) \\
& \times \varepsilon_{ijk}(\bar{B}_j \to \ell^- \bar{\nu} D_{jk} \to D_i), \qquad (6.2)
\end{aligned}
$$

where $D_i = D^+, D^0, D^{*+}, D_s^+$, $\Gamma_k = \Gamma, \Gamma^*, \Gamma^{**}$ and ε_{ijk} are the efficiencies of a particular decay chain.

The branching ratios used in the sample composition are listed in Tables 6.2-6.4 for the $\bar{B}$ mesons and in Table 6.5 for the Λ_b^0. Predictions from the `EvtGen` table are used to determine the $f_{D_{q,\alpha}} \equiv \mathcal{BR}(B_q \to D_{q,\alpha}) / \sum_{D_{q,\alpha}} \mathcal{BR}(B_q \to D_{q,\alpha})$ branching ratios of $\bar{B}$ to doubly excited charm states relative to $\mathcal{BR}(\bar{B}_q \to \ell^- \bar{\nu} D_q^{**})$ (cf. Table 6.6). Table 6.7 lists additional isospin factors used in the D_{s1}^+ and D_2^* decays. Other charm branching ratios and the $\bar{B}$ lifetimes used in the sample composition are listed in Appendix C. As previously mentioned, the Λ_b^0 semileptonic decays are parameterized by a fixed sample composition, which is independent of spectator model considerations. Since it is not clear how well the spectator model describes the excited baryon decays, this is a more reasonable approach. The uncertainties in the sample composition of the Λ_b^0 is considered separately in assigning systematic uncertainties in Chapter 10.

In addition to the primary decays which contribute to the semileptonic signal, indirect semileptonic decays (*e.g.* $B \to DD$) are also included in the sample composition (cf. Table 6.8). These decays feature a sequential decay to a muon or electron, either from a charm (semi)leptonic decay (*e.g.* $D \to \mu^+ \nu X$) or from a $\tau^- \to \mu^- \bar{\nu}_\mu \nu_\tau$. The PDG values for these branching ratios are used when available and the `EvtGen` values are used otherwise. The semileptonic decays of $D^+ \to \ell^+ \nu X$, $D^0 \to \ell^+ \nu X$, and $D_s^+ \to \ell^+ \nu X$ branching ratios are taken from the `EvtGen` table (see Appendix C), although measurements for the D^+ and D^0 semileptonic decays exist in the PDG. Since a number of the semileptonic charm branching ratios are not included in the PDG, the `EvtGen` table values are chosen for consistency. Some of the PDG branching ratios have large uncertainties and will be treated as a source of systematic uncertainty (discussed in Chapter 10).

$\bar{B}^0$ Decays	$\ell^- D^0/D^{*+}$	$\ell^- D^+$
$\ell^-\bar{\nu}D^+$		Γ
$\ell^-\bar{\nu}D^{*+}$		
$\to D^0\pi^+$	$\mathcal{BR}^*(D^0\pi^+)\Gamma^*$	
$D^+\pi^0/\gamma$		$\mathcal{BR}^*(D^+\pi^0/\gamma)\Gamma^*$
$\ell^-\bar{\nu}D_1^+$		
$\to D^{*0}\pi^+$		
$\hookrightarrow D^0\pi^0/\gamma$	$\frac{2}{3}f_{D_1^+}\mathcal{BR}^*(D^0\pi^0/\gamma)\Gamma^{**}$	
$\to D^{*+}\pi^0$		
$\hookrightarrow D^0\pi^+$	$\frac{1}{3}f_{D_1^+}\mathcal{BR}^*(D^0\pi^+)\Gamma^{**}$	
$D^+\pi^0/\gamma$		$\frac{1}{3}f_{D_1^+}\mathcal{BR}^*(D^+\pi^0/\gamma)\Gamma^{**}$
$\ell^-\bar{\nu}D_0^{*+}$		
$\to D^0\pi^+$	$\frac{2}{3}f_{D_0^{*+}}\Gamma^{**}$	
$D^+\pi^0$		$\frac{1}{3}f_{D_0^{*+}}\Gamma^{**}$
$\ell^-\bar{\nu}D_1'^+$		
$\to D^{*0}\pi^+$		
$\hookrightarrow D^0\pi^0/\gamma$	$\frac{2}{3}f_{D_1'^+}\mathcal{BR}^*(D^0\pi^0/\gamma)\Gamma^{**}$	
$\to D^{*+}\pi^0$		
$\hookrightarrow D^0\pi^+$	$\frac{1}{3}f_{D_1'^+}\mathcal{BR}^*(D^0\pi^+)\Gamma^{**}$	
$D^+\pi^0/\gamma$		$\frac{1}{3}f_{D_1'^+}\mathcal{BR}^*(D^+\pi^0/\gamma)\Gamma^{**}$
$\ell^-\bar{\nu}D_2^{*+}$		
$\to D^{*0}\pi^+$		
$\hookrightarrow D^0\pi^0/\gamma$	$a_2^{*+}f_{D_2^{*+}}\mathcal{BR}^*(D^0\pi^0/\gamma)\Gamma^{**}$	
$\to D^{*+}\pi^0$		
$\hookrightarrow D^0\pi^+$	$b_2^{*+}f_{D_2^{*+}}\mathcal{BR}^*(D^0\pi^+)\Gamma^{**}$	
$D^+\pi^0/\gamma$		$b_2^{*+}f_{D_2^{*+}}\mathcal{BR}^*(D^+\pi^0/\gamma)\Gamma^{**}$
$\to D^0\pi^0$	$c_2^{*+}f_{D_2^{*+}}\Gamma^{**}$	
$\to D^+\pi^-$		$d_2^{*+}f_{D_2^{*+}}\Gamma^{**}$
$\ell^-\bar{\nu}D^{*+}\pi^0$(NR)		
$\to D^0\pi^+$	$f_{D^{*+}\pi^0}\mathcal{BR}^*(D^0\pi^+)\Gamma^{**}$	
$D^+\pi^0/\gamma$		$f_{D^{*+}\pi^0}\mathcal{BR}^*(D^+\pi^0/\gamma)\Gamma^{**}$
$\ell^-\bar{\nu}D^{*0}\pi^+$(NR)		
$\to D^0\pi^0/\gamma$	$f_{D^{*0}\pi^+}\mathcal{BR}^*(D^0\pi^0/\gamma)\Gamma^{**}$	
$\ell^-\bar{\nu}D^+\pi^0$(NR)		$f_{D^+\pi^0}\Gamma^{**}$
$\ell^-\bar{\nu}D^0\pi^+$(NR)	$f_{D^0\pi^+}\Gamma^{**}$	

Table 6.2: Branching ratios used in the $\bar{B}^0$ meson sample composition.

B^- Decays	$\ell^- D^0/D^{*+}$	$\ell^- D^+$
$\ell^-\bar{\nu}D^0$	Γ	
$\ell^-\bar{\nu}D^{*0}$		
$\to D^0\pi^0/\gamma$	$\mathcal{BR}^*(D^0\pi^0/\gamma)\Gamma^*$	
$\ell^-\bar{\nu}D_1^0$		
$\to D^{*0}\pi^0$		
$\hookrightarrow D^0\pi^0/\gamma$	$\frac{1}{3}f_{D_1^0}\mathcal{BR}^*(D^0\pi^0/\gamma)\Gamma^{**}$	
$\to D^{*+}\pi^-$		
$\hookrightarrow D^0\pi^+$	$\frac{2}{3}f_{D_1^0}\mathcal{BR}^*(D^0\pi^+)\Gamma^{**}$	
$D^+\pi^0/\gamma$		$\frac{2}{3}f_{D_1^0}\mathcal{BR}^*(D^+\pi^0/\gamma)\Gamma^{**}$
$\ell^-\bar{\nu}D_0^{*0}$		
$\to D^0\pi^0$	$\frac{1}{3}f_{D_0^{*0}}\Gamma^{**}$	
$D^+\pi^-$		$\frac{2}{3}f_{D_0^{*0}}\Gamma^{**}$
$\ell^-\bar{\nu}D_1'^0$		
$\to D^{*0}\pi^0$		
$\hookrightarrow D^0\pi^0/\gamma$	$\frac{1}{3}f_{D_1'^0}\mathcal{BR}^*(D^0\pi^0/\gamma)\Gamma^{**}$	
$\to D^{*+}\pi^-$		
$\hookrightarrow D^0\pi^+$	$\frac{2}{3}f_{D_1'^0}\mathcal{BR}^*(D^0\pi^+)\Gamma^{**}$	
$D^+\pi^0/\gamma$		$\frac{2}{3}f_{D_1'^0}\mathcal{BR}^*(D^+\pi^0/\gamma)\Gamma^{**}$
$\ell^-\bar{\nu}D_2^{*0}$		
$\to D^{*0}\pi^0$		
$\hookrightarrow D^0\pi^0/\gamma$	$a_2^{*0}f_{D_2^{*0}}\mathcal{BR}^*(D^0\pi^0/\gamma)\Gamma^{**}$	
$\to D^{*+}\pi^-$		
$\hookrightarrow D^0\pi^+$	$b_2^{*0}f_{D_2^{*0}}\mathcal{BR}^*(D^0\pi^+)\Gamma^{**}$	
$D^+\pi^0/\gamma$		$b_2^{*0}f_{D_2^{*0}}\mathcal{BR}^*(D^+\pi^0/\gamma)\Gamma^{**}$
$\to D^0\pi^0$	$c_2^{*0}f_{D_2^{*0}}\Gamma^{**}$	
$\to D^+\pi^-$		$d_2^{*0}f_{D_2^{*0}}\Gamma^{**}$
$\ell^-\bar{\nu}D^{*+}\pi^-$(NR)		
$\to D^0\pi^+$	$f_{D^{*+}\pi^-}\mathcal{BR}^*(D^0\pi^+)\Gamma^{**}$	
$D^+\pi^0/\gamma$		$f_{D^{*+}\pi^-}\mathcal{BR}^*(D^+\pi^0/\gamma)\Gamma^{**}$
$\ell^-\bar{\nu}D^{*0}\pi^0$(NR)		
$\to D^0\pi^0/\gamma$	$f_{D^{*0}\pi^0}\mathcal{BR}^*(D^0\pi^0/\gamma)\Gamma^{**}$	
$\ell^-\bar{\nu}D^+\pi^-$(NR)		$f_{D^+\pi^-}\Gamma^{**}$
$\ell^-\bar{\nu}D^0\pi^0$(NR)	$f_{D^0\pi^0}\Gamma^{**}$	

Table 6.3: Branching ratios used in the B^- meson sample composition.

$\bar{B}_s^0$ Decays	$\ell^- D^0/D^{*+}$	$\ell^- D^+$	$\ell^- D_s^+$
$\ell^-\bar{\nu}D_s^+$			Γ
$\ell^-\bar{\nu}D_s^{*+}$			
$\to D_s^+\gamma$			Γ^*
$\ell^-\bar{\nu}D_{s0}^{*+}(2317)$			
$\to D_s^+\pi^0$			$f_{D_{s0}^{*+}}\Gamma^{**}$
$\ell^-\bar{\nu}D_{s1}^+(2460)$			
$\to D_{s0}^{*+}\pi^0$			
$\hookrightarrow D_s^+\pi^0$			$a_{s1}^+ f_{D_{s1}^+}\Gamma^{**}$
$\to D_s^+\gamma$			$b_{s1}^+ f_{D_{s1}^+}\Gamma^{**}$
$\ell^-\bar{\nu}D_{s1}^{'+}(2535)$			
$\to D^{*+}K^0$			
$\hookrightarrow D^0\pi^+$	$\frac{1}{2}f_{D_{s1}^{'+}}\mathcal{BR}^*(D^0\pi^+)\Gamma^{**}$		
$D^+\pi_g^0$		$\frac{1}{2}f_{D_{s1}^{'+}}\mathcal{BR}^*(D^+\pi_g^0)\Gamma^{**}$	
$\to D^{*0}K^+$			
$\hookrightarrow D^0\pi_g^0$	$\frac{1}{2}f_{D_{s1}^{'+}}\mathcal{BR}^*(D^0\pi_g^0)\Gamma^{**}$		
$\ell^-\bar{\nu}D_{s2}^{*+}(2573)$			
$\to D^{*+}K^0$			
$\hookrightarrow D^0\pi^+$	$a_{s2}^{*+} f_{D_{s2}^{*+}}\mathcal{BR}^*(D^0\pi^+)\Gamma^{**}$		
$D^+\pi_g^0$		$a_{s2}^{*+} f_{D_{s2}^{*+}}\mathcal{BR}^*(D^+\pi_g^0)\Gamma^{**}$	
$\to D^{*0}K^+$			
$\hookrightarrow D^0\pi_g^0$	$b_{s2}^{*+} f_{D_{s2}^{*+}}\mathcal{BR}^*(D^0\pi_g^0)\Gamma^{**}$		
$\to D^+K^0$		$c_{s2}^{*+} f_{D_{s2}^{*+}}\Gamma^{**}$	
$\to D^0K^+$	$d_{s2}^{*+} f_{D_{s2}^{*+}}\Gamma^{**}$		
$\ell^-\bar{\nu}D_s^{*+}\pi^0$(NR)			
$\to D_s^+\gamma$			$f_{D_s^{*+}\pi^0}\Gamma^{**}$
$\ell^-\bar{\nu}D_s^+\pi^0$(NR)			$f_{D_s^+\pi^0}\Gamma^{**}$

Table 6.4: Branching ratios used in the $\bar{B}_s^0$ meson sample composition; $\pi_g^0 \equiv \pi^0/\gamma$.

Λ_b^0 Decays	$\mathcal{BR}$
$\ell^- \bar{\nu}_\ell \Lambda_c^+ X$	$(9.2 \pm 2.1)\%$
$\ell^- \bar{\nu}_\ell \Lambda_c^+$	$(6.54 \pm 0.22)\%$
$\ell^- \bar{\nu}_\ell \Lambda_c(2593)^+$	$(3.07 \pm 1.02) \times 10^{-3}$
$\ell^- \bar{\nu}_\ell \Lambda_c(2625)^+$	$(5.14 \pm 0.99) \times 10^{-3}$
$\ell^- \bar{\nu}_\ell \Sigma_c(2455)^{++} \pi^-$	$(2.7 \pm 1.0) \times 10^{-3}$
$\ell^- \bar{\nu}_\ell \Sigma_c(2455)^{+} \pi^0$	$(2.7 \pm 1.0) \times 10^{-3}$
$\ell^- \bar{\nu}_\ell \Sigma_c(2455)^{0} \pi^+$	$(2.7 \pm 1.0) \times 10^{-3}$
$\ell^- \bar{\nu}_\ell \Lambda_c f_0$	$(2.6 \pm ??) \times 10^{-3}$
$\ell^- \bar{\nu}_\ell \Lambda_c \pi^+ \pi^-$ (NR)	$(5.2 \pm ??) \times 10^{-3}$
$\ell^- \bar{\nu}_\ell \Lambda_c \pi^0 \pi^0$ (NR)	$(2.6 \pm ??) \times 10^{-3}$

Table 6.5: Λ_b^0 baryon sample composition.

	D_α^+	D_α^0	$D_{s,\alpha}^+$
f_{D_1}	0.207	0.207	0.118
$f_{D_0^*}$	0.074	0.074	0.118
$f_{D_1'}$	0.137	0.137	0.206
$f_{D_2^*}$	0.137	0.137	0.206
$f_{D^*\pi}$	0.037	0.074	0.088
$f_{D\pi}$	0.111	0.222	0.265

Table 6.6: Branching ratios of $\bar{B}$ to doubly excited charm states relative to $\mathcal{BR}(B_q \to \ell^- \bar{\nu} D_q^{**})$.

	D_2^{*+}	D_2^{*0}	D_{s2}^{*+}	D_{s1}^+
a_2^*	-	-	-	0.7900
b_2^*	-	-	-	0.2100
a_2^*	0.1030	0.2090	0.0500	-
b_2^*	0.2090	0.1030	0.0500	-
c_2^*	0.2290	0.4590	0.4700	-
d_2^*	0.4590	0.2290	0.4300	-

Table 6.7: Isospin factors used to describe the D_{s1}^+ and D_2^* decays.

Decay	$\mathcal{BR}$
$\bar{B}^0 \to D^{(*)}\bar{D}^{(*)}K$	$(7.1^{+2.7}_{-1.7})\%$
$D^{(*)+}D^{(*)-}$	$(1.9\pm??)\times10^{-3}$
$D_s^{(*)-}D^{(*)+}X$	$(9^{+5}_{-4})\%$
$\tau^-\bar{\nu}D^{(*),(**)+}$	$(2.96\pm??)\%$
$B^- \to D^{(*)}\bar{D}^{(*)}K$	$(7.1^{+2.7}_{-1.7})\%$
$D_s^{(*)-}D^{(*)0}X$	$(9^{+5}_{-4})\%$
$\tau^-\bar{\nu}D^{(*),(**)+}$	$(2.96\pm??)\%$
$\bar{B}_s^0 \to D^{(*)}\bar{D}^{(*)}K$	$(6.8\pm??)\times10^{-3}$
$D_s^{(*)+}D^{(*)-}X$	$(15.4\pm??)\%$
$D_s^{(*)+}D_s^{(*)-}X$	$(23^{+21}_{-13})\%$
$\tau^-\bar{\nu}D_s^{(*),(**)+}$	$(2.92\pm??)\%$
$\Lambda_b^0 \to \tau^-\bar{\nu}\Lambda_c^+$	$(1.72\pm??)\%$
$\tau^-\bar{\nu}\Lambda_c(2593)^+$	$(4.3\pm??)\times10^{-3}$
$\tau^-\bar{\nu}\Lambda_c(2625)^+$	$(3.2\pm??)\times10^{-3}$

Table 6.8: Indirect decays contributing to the sample composition.

Chapter 7

Efficiencies

Since the $\bar{B}$ fragmentation fractions are measured relative to each other, most efficiencies in the measurement are expected to cancel. Many of the remaining relative efficiencies are determined from Monte Carlo realistic simulation. These efficiencies are discussed in Section 7.3. Comparisons between the data and the inclusive Monte Carlo samples, presented in Section 7.2, validate the use of Monte Carlo to estimate the relative efficiencies between $\bar{B}$ semileptonic decays and the lepton-charm signals. A few absolute efficiencies, such as the different XFT trigger efficiencies for K, π, and p are not properly described in the Monte Carlo. These efficiencies must be determined from data and are discussed first in Section 7.1.

7.1 Relative Efficiencies Determined from Data

Two significant efficiencies are not properly described by the Monte Carlo and must be adjusted to match the data. The relative XFT efficiencies between kaons, pions, and protons are not properly simulated by the Monte Carlo due to the incorrect energy loss modeling of the simulation in the COT. The single track efficiency, needed to adjust the Monte Carlo efficiency of the two-prong D^0 relative to the three-prong charm signals (*e.g.* D^+, D_s^+, Λ_c^+), must also be determined from the data. Both of these efficiencies have been measured relative to Monte Carlo in previous CDF analyses [46]-[48]. The basic method developed in these previous analyses for evaluating each of these efficiencies is followed. A third efficiency obtained from data is the efficiency of the proton dE/dx $\mathcal{LR}$ cut described in Section 5.2.1.

7.1.1 XFT Efficiencies

Previous determinations of the K, π, and proton XFT efficiencies corrections to the Monte Carlo have been applied to this measurement [46, 47]. The K and π XFT efficiencies are measured by reconstructing $D^+ \to K^-\pi^+\pi^+$ in two-track trigger (TTT) data, where two tracks are required to match to the SVT trigger. The track which is not matched to the trigger is treated as the unbiased track. The unbiased track is then examined to see whether it could have fired the XFT trigger. Tracks which could have passed the XFT trigger are included in the numerator of the efficiency, while all unbiased tracks are included in

Data period	K		π	
('02-'04)	a_0	a_1	a_0	a_1
2/09-10/09	0.9931±0.05	-0.0725±0.02	0.9772±0.03	0.00968±0.01
10/09-1/12	0.9584±0.02	-0.1952±0.007	1.0016±0.01	-0.1501±0.005
1/12-6/06	0.9359±0.02	-0.1919±0.007	0.9851±0.01	-0.1341±0.004
6/06-9/06	0.9282±0.01	-0.1897±0.005	0.9921±0.008	-0.1776±0.004
9/07-8/22	0.9643±0.01	-0.0907±0.004	0.9931±0.007	-0.0678±0.003
		proton		
('02-'03)	a_0	a_1	a_2	a_3
2/09-6/06	1.063±0.090	-1.326±0.963	3.198±3.218	-2.203±3.391

Table 7.1: XFT Monte Carlo corrections, parameterized as $\varepsilon_{XFT}(Data/MC) = \sum_i a_i p_T^{-i}$.

the denominator. A similar procedure is carried out for the proton XFT efficiency, using $\Lambda^0 \to p\pi^-$ events reconstructed in data collected with the TTT.

The K and π XFT efficiencies and the Monte Carlo corrections are shown in Figures 7.1 and 7.2. The corrections to the Monte Carlo are parameterized as $\varepsilon_{XFT} = \sum_{i=0}^{n} a_i p_T^{-i}$ for $p_T > 1.3$ GeV/c, where $n = 1$ for the K and π XFT efficiency corrections and $n = 3$ for the proton XFT efficiency correction. The fit parameters are listed in Table 7.1. The errors given for the K and π XFT corrections include an estimate of systematic effects. The most recent determination of the K and π XFT efficiencies over the full range of data used in the measurement are consistent with older determinations made for the first half of the data. This gives confidence that the proton XFT efficiency, which has been determined only for the first third of the data, can be applied to the entire data range considered. The lack of measurement of the proton XFT corrections for the later data are treated as a systematic uncertainty in Chapter 10.

7.1.2 Single Track Efficiency

The Monte Carlo is also unable to accurately estimate the efficiency with which an extra track is added to a decay. This efficiency is again measured from data relative to the Monte Carlo. In order to evaluate the efficiency of adding a single track to a decay vertex, the lepton plus four track $\mu^- D^0 \to \mu^- K^- \pi^+ \pi^- \pi^+$ state is reconstructed and normalized to $\mu^- D^0 \to \mu^- K^- \pi^+$ in both the data and Monte Carlo. This obtains the square of the efficiency to find a single track, ε^2_{trk}, in the data relative to the Monte Carlo, assuming that the third and fourth tracks in the $D^0 \to K^- \pi^+ \pi^- \pi^+$ are uncorrelated. This assumption will be treated as a systematic uncertainty in Chapter 10. The square of the efficiency to add a single track in data is determined as a function of $p_T(D^0)$ in both the data and in inclusive Monte Carlo samples to check for any potential p_T dependent effects. The selection applied to the $\mu^- D^0 \to \mu^- K^- \pi^+ \pi^- \pi^+$ signal, shown in Figure 7.3, is identical to the selection for $\mu^- D^0 \to \mu^- K^- \pi^+$ listed in Table 5.4, with the two additional pions required to have $p_T > 0.4$ GeV/c and to be fiducial in the COT. Two inclusive Monte Carlo samples, $\bar{B}^0/B^- \to \mu^- \bar{\nu} D^0 X \to \mu^- K^- \pi^+ \pi^- \pi^+$ and $\bar{B}^0/B^- \to \mu^- \bar{\nu} D^0 X \to \mu^- K^- \pi^+$, each generated

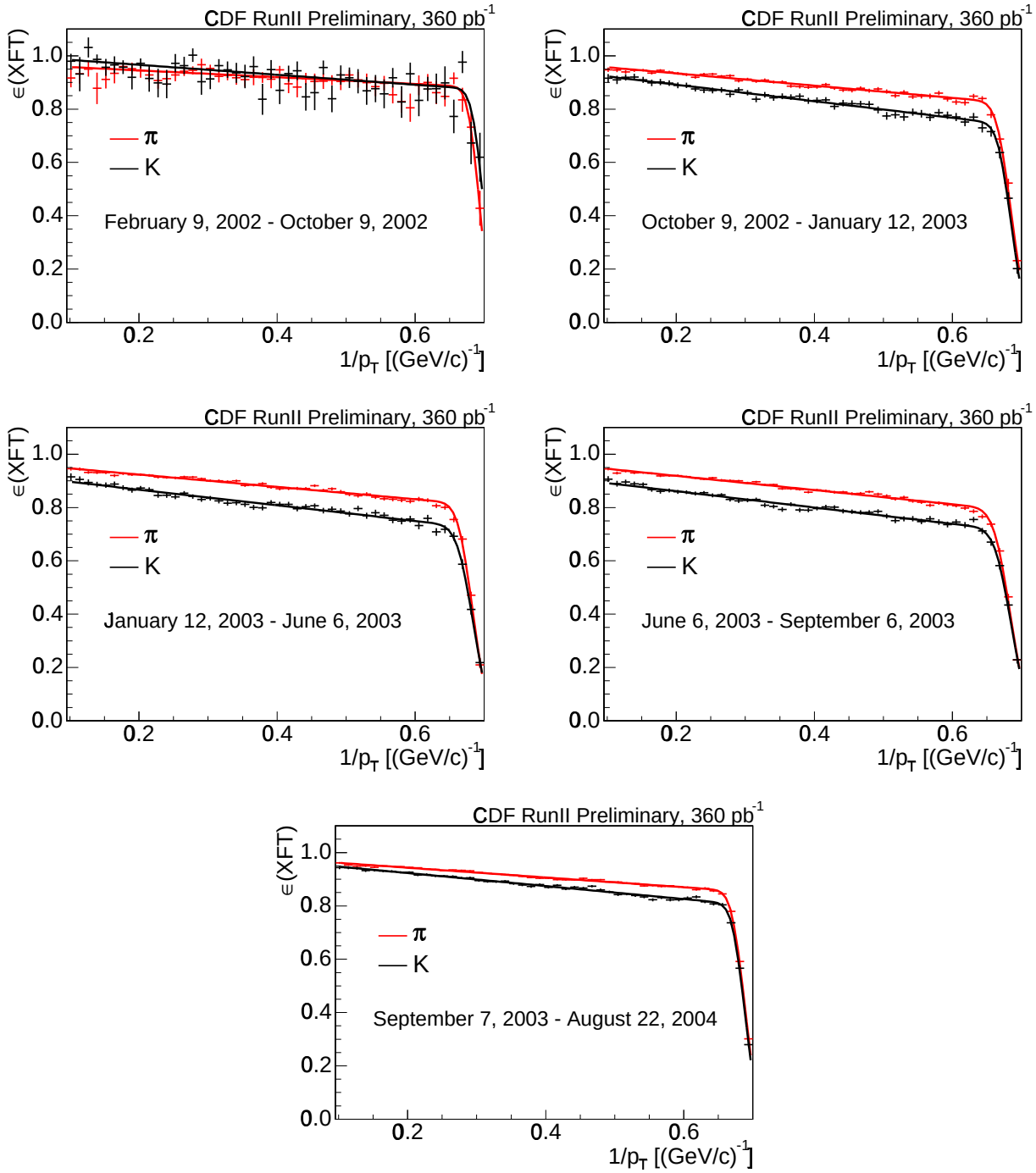

Figure 7.1: $\varepsilon_{XFT}(DATA)$ as a function of p_T^{-1} for pions (red) and kaons (black) for various run ranges indicated.

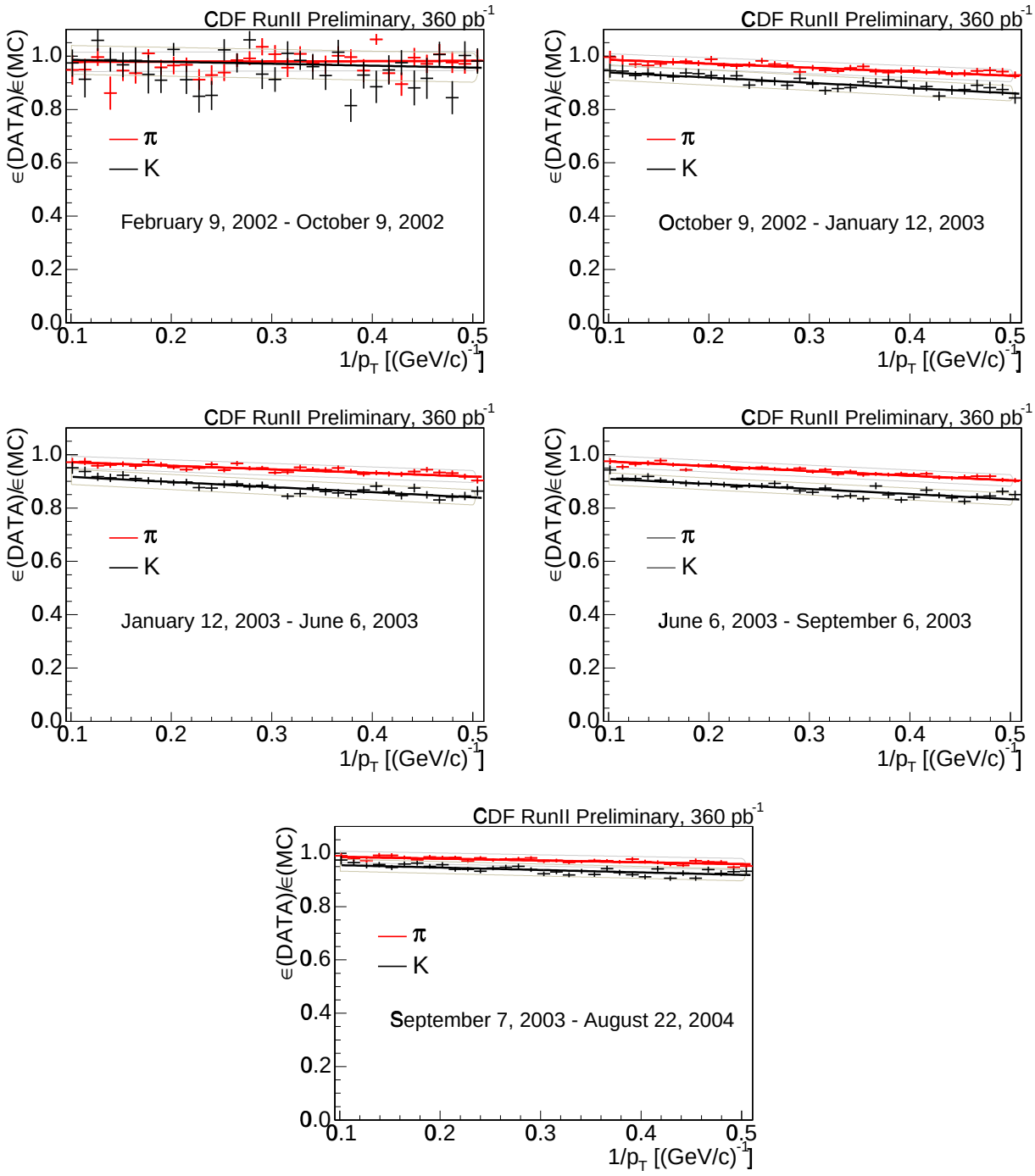

Figure 7.2: $\varepsilon_{XFT}(DATA)/\varepsilon_{XFT}(MC)$ as a function of p_T^{-1} for pions (red) and kaons (black).

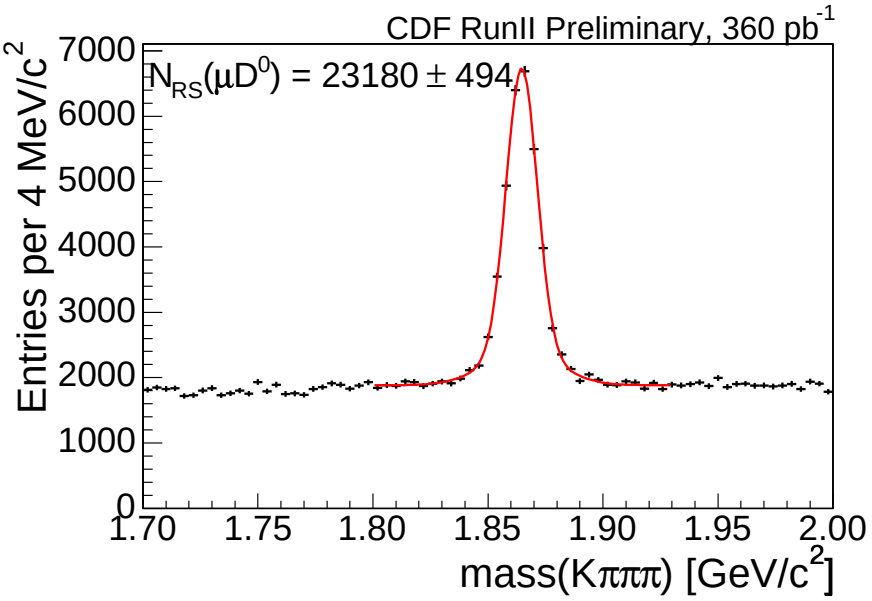

Figure 7.3: $\mu^- D^0$ signal, where $D^0 \to K^-\pi^+\pi^-\pi^+$.

with 20 million events, are used in this study to determine the single track efficiency in the Monte Carlo. All other efficiencies except the efficiency to add a single track are expected to cancel. Consequently, the Monte Carlo needs to be adjusted only by the relative branching ratios $\mathcal{BR}(D^0 \to K^-\pi^+\pi^-\pi^+)/\mathcal{BR}(D^0 \to K^-\pi^+) = 2.10 \pm 0.03 \pm 0.06$ [49].

The $p_T(D^0)$ distributions for $D^0 \to K^-\pi^+\pi^-\pi^+$ and $D^0 \to K^-\pi^+$ are shown for the data and for the Monte Carlo in Figure 7.4. The square of the single track efficiency in the data relative to the Monte Carlo (c.f. in Figure 7.5) is measured to be

$$\varepsilon^2_{trk} = 77.1 \pm 1.4\%.$$

This corresponds to a single track efficiency of

$$\varepsilon_{trk} = 87.8 \pm 0.8(stat)^{+1.9}_{-0.9}(\mathcal{BR})\%, \tag{7.1}$$

which is lower than the value determined in the previous analyses, due entirely to the different branching ratios used. Using the PDG branching ratios, the single track efficiency is consistent with the previous determination [48]. No $p_T(D^0)$ dependence in the single track efficiency is observed between the data and the Monte Carlo, as can be seen in Figure 7.5. The uncertainty in the $D^0 \to K^-\pi^+/K^-\pi^+\pi^-\pi^+$ branching fraction ratio contributes a significant uncertainty to the value of the single track efficiency, which is treated as a systematic uncertainty in the determination of the relative production of B^- to $\bar{B}^0$ (see Chapter 10).

The efficiency quoted in Eq. (7.1) approximately corresponds to the efficiency to add three silicon hits to a track (*i.e.* non-trigger tracks.) Some slight correction to this formula is required if differences in the rates at which one, two, or three tracks can be matched to the SVT track, thereby requiring four silicon hits, are taken into account. The adjustment

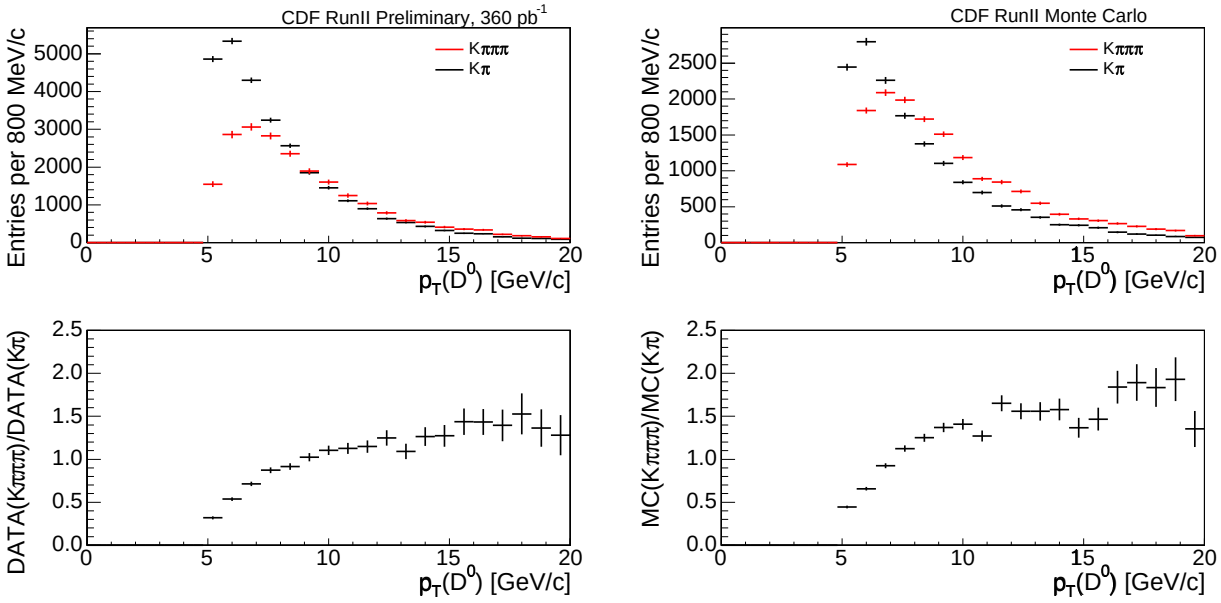

Figure 7.4: Single track efficiency binned in $p_T(D^0)$ measured in the data (left) and the Monte Carlo (right).

in the correction factor when taking account of trigger tracks is

$$f_{corr}(\ell D \to n\ trks) = \varepsilon_{trk}^{n-1} \sum_{i=1}^{n} k_i \cdot \varepsilon_{trig}^{i}, \tag{7.2}$$

where the number of trigger tracks is again assumed to be uncorrelated. The k_i's for the individual charm decays considered are listed in Table 7.2. In topologies with three or more tracks from the charm hadron, three tracks are matched to the SVT trigger track at approximately the same rate between the three track D^+, D_s^+, and Λ_c^+ decay modes and the four track $D^0 \to K3\pi$ decay. This means that most of the correction needed to account for additional trigger tracks in the three track modes is already taken into account in Eq. (7.1). The numbers of three matched tracks differ between channels by as much as 1.5% times the cube of the efficiency to add four silicon hits, which corresponds to a correction of less than half a percent assuming that $(0.878)^{4/3}$ gives a reasonable estimate of the efficiency to add four silicon hits to a track. This constitutes a negligible correction to the efficiency determined in Eq. (7.1), particularly when compared to the uncertainty introduced by the error on $\mathcal{BR}(D^0 \to K^-\pi^+\pi^-\pi^+)/\mathcal{BR}(D^0 \to K^-\pi^+)$ [49].

7.1.3 dE/dx Efficiency

The efficiency of the dE/dx $\mathcal{LR}$ cut applied to the proton, discussed in Section 5.2.1, also needs to be evaluated in data, as the COT simulation does not properly describe multiple scattering effects. The dE/dx efficiency is binned into data taken before run 179057 (February, 2004) and data taken afterward. Since the efficiency determination need only be self-consistent, the absolute change in dE/dx calibration does not affect the measurement as

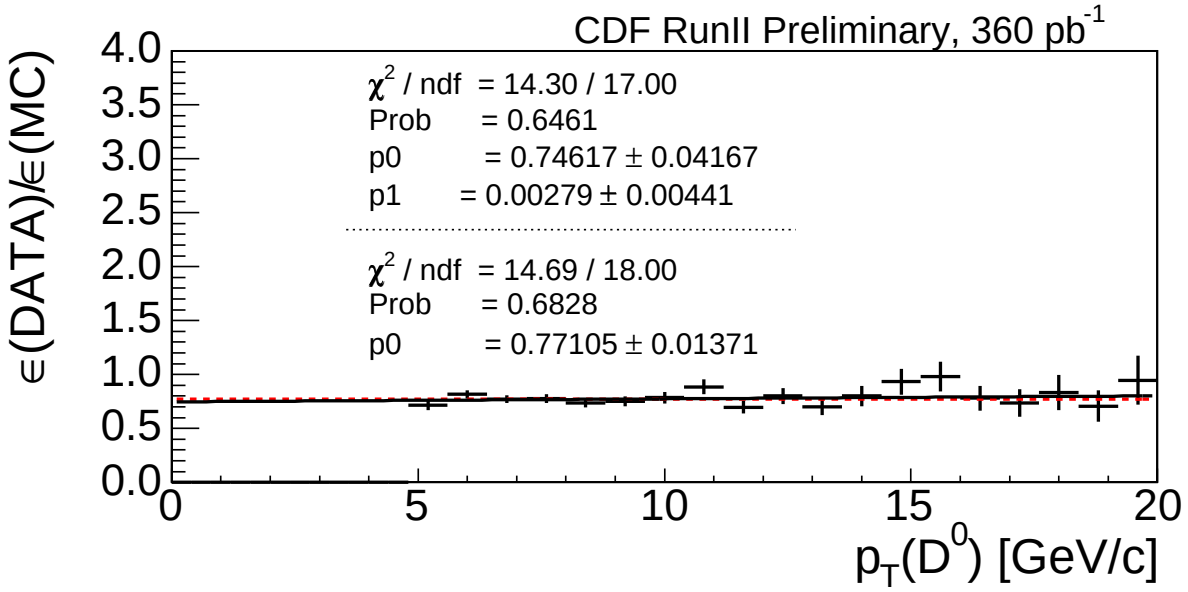

Figure 7.5: ε^2_{trk} binned in $p_T(D^0)$ for data relative to the Monte Carlo.

Decay	$k_1(\%)$	$k_2(\%)$	$k_3(\%)$	$k_4(\%)$
$\mu^- D^0(K^-\pi^+)$	80.0	20.0	-	-
$\mu^- D^0(K^-3\pi)$	74.8	22.0	3.2	0.1
$\mu^- D^+$	78.0	20.3	1.7	-
$\mu^- D_s^+$	76.4	20.4	3.2	-
$\mu^- \Lambda_c^+$	79.1	19.5	1.4	-
$e^- D^0(K^-\pi^+)$	81.6	18.2	-	-
$e^- D^0(K^-3\pi)$	77.2	20.1	2.6	0.1
$e^- D^+$	80.3	18.2	1.5	-
$e^- D_s^+$	76.7	20.1	3.2	-
$e^- \Lambda_c^+$	81.7	16.9	1.4	-

Table 7.2: Number of tracks matched to SVT tracks in the reconstructed charm states.

long as the Monte Carlo efficiency is adjusted accordingly. The $\Lambda^0 \to p\pi^-$ control sample described in Appendix B is used to evaluate the efficiency of the $\mathcal{LR}(p) > 0.3$ cut applied to the proton from the Λ_c^+ decay. Protons are not required to match to an XFT track, which might have different dE/dx efficiencies than non-XFT tracks. In the Λ control sample, 97.5±0.8% of protons are matched to XFT tracks, while 92.1±1.1% of the protons from Λ_c^+ are matched to an XFT track. The dE/dx efficiency is evaluated by dividing the number of protons which pass the dE/dx $\mathcal{LR}$ cut by all protons in bins of proton transverse momentum, shown in Figure 7.6. The shape of the efficiency is parameterized in two ways. In the first parameterization, the "wiggle" below 3.6 GeV/c is fit with a third order polynomial and a constant is used for $p_T(p) > 3.6$ GeV/c. In the second parameterization, the efficiency is fit with a constant for all p_T. Although both parameterizations fit the data well, the third order polynomial plus a constant fits the data better than fitting with only a constant. The former is used as the default parameterization in the measurement, while the second parameterization is used as a systematic uncertainty. In contrast, the efficiency determined for protons which are not matched to XFT tracks are well-described by a constant line, shown in Figure 7.7. The constant efficiency determined from the protons unmatched to XFT is consistent with the plateau of the matched tracks for $p_T(p)$ above 3.6 GeV/c.

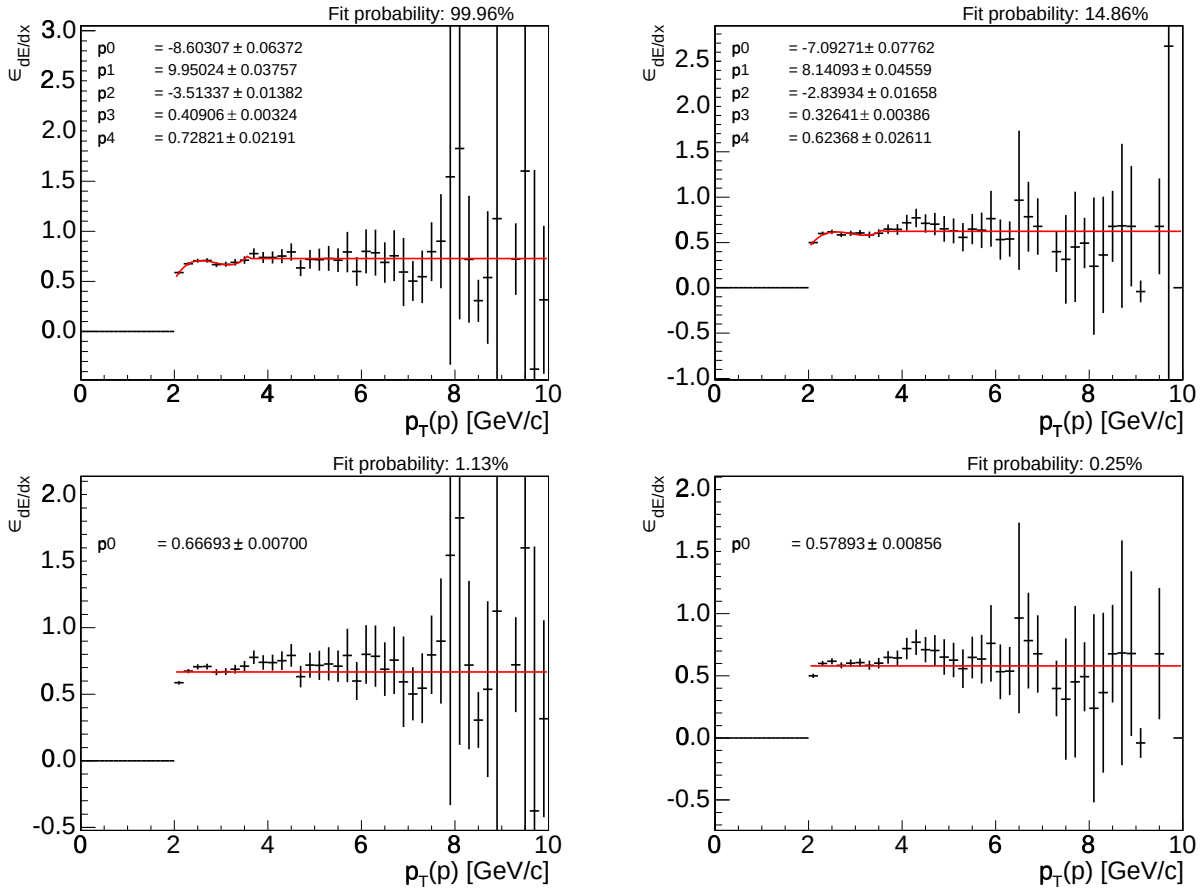

Figure 7.6: $\varepsilon_{dE/dx}$ measured in data as a function of $p_T(p)$ for protons matched to XFT tracks, fit with a third order polynomial plus constant (top row) and a constant (bottom row), for data taken before 179057 (left column) and after (right column).

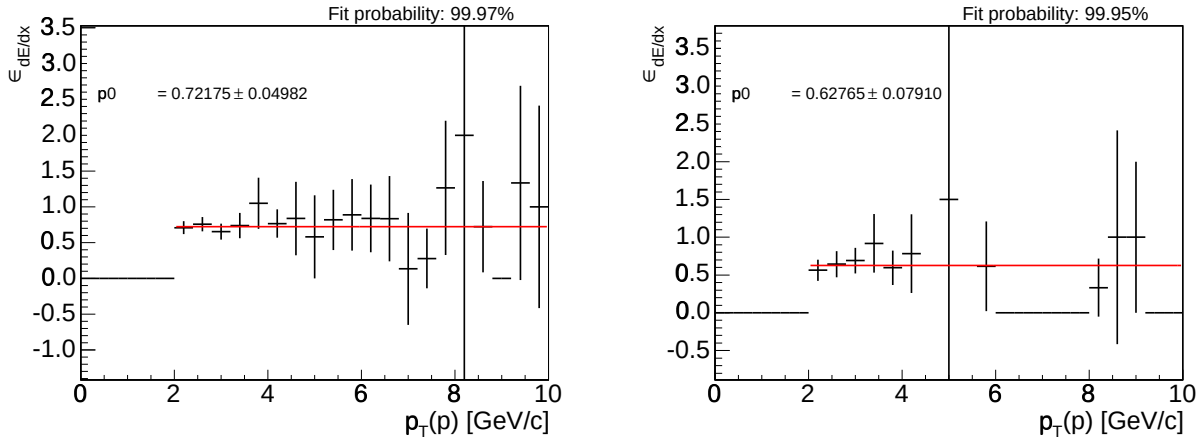

Figure 7.7: $\varepsilon_{dE/dx}$ measured in data as a function of $p_T(p)$ for protons which are not matched to XFT tracks, fit with a constant, for data taken before 179057 (left) and after (right).

7.2 Comparison of Data and Monte Carlo

Four inclusive Monte Carlo samples, $\bar{B}^0 \to \ell^- \bar{\nu} D^{0,+} X$, $B^- \to \ell^- \nu D^{0,+} X$, $\bar{B}^0_s \to \ell^- \nu D^+_s X$, and $\Lambda^0_b \to \ell^- \nu \Lambda^+_c X$ (described in Chapter 4) are used to validate the use of Monte Carlo to determine the kinematic efficiencies of the $\bar{B}$ semileptonic decays used in the measurement. Although exclusive Monte Carlo channels are used to extract relative efficiencies needed for the measurement of the relative fragmentation fractions, the quality of agreement between the data and the Monte Carlo is checked with the inclusive Monte Carlo samples. With the exception of a few distributions, such as the mass and, to a much lesser extent, the p_T of the lepton-charm vertex, the agreement between the data and the Monte Carlo should not be very sensitive to variations in the D^{**} branching ratios between the default EvtGen table and that which will be later determined in the fit for the fragmentation fractions.

Agreement between the data and the Monte Carlo are shown for distributions which are cut upon (*e.g.* $p_T(K)$), which are listed in Table 5.4. In general, agreement is better in the μ+SVT data than in the e+SVT. This is in part due to the inability of the Monte Carlo to correctly produce all radiative effects, to which electrons are more sensitive. Since the electron distributions are shifted uniformly across channels, this is not a concern. The comparisons for the μ+SVT data and Monte Carlo are shown in Figures 7.8-7.22. The e+SVT comparisons are included in Appendix D. In all cases the area of the Monte Carlo distribution is normalized to the corresponding area of the data distribution. The quality of the comparisons are quantified by fitting the ratio of data to the Monte Carlo by both a sloped and a constant line. The former indicates potential biases between the two distributions, while the latter gives a measure of overall agreement between the distributions. The Λ^0_b Monte Carlo has been re-weighted for the efficiency of the proton dE/dx cut discussed in Section 7.1.3 and is compared with the $\ell^- \Lambda^+_c$ data with the dE/dx cut applied. Agreement between the data and the Monte Carlo in the quantities examined is generally good except for quantities which depend on the errors of the charm or lepton-charm vertex, such as the $\sigma_{ct}(B)$ or the $\chi^2_{xy}(D)$.

Agreement between the data and the Monte Carlo in $p_T(\pi^*)$, the transverse momentum of the soft pion from the D^*, is very good in both the μ+SVT data and the e+SVT data (cf. Figures 7.16 and D.9), with an overall probability of agreement of 17.0% and 45.3% respectively and no observable bias in the ratio of the two distributions. Since the Monte Carlo agrees well with the data, no additional soft pion efficiency is determined beyond that which is predicted in the Monte Carlo.

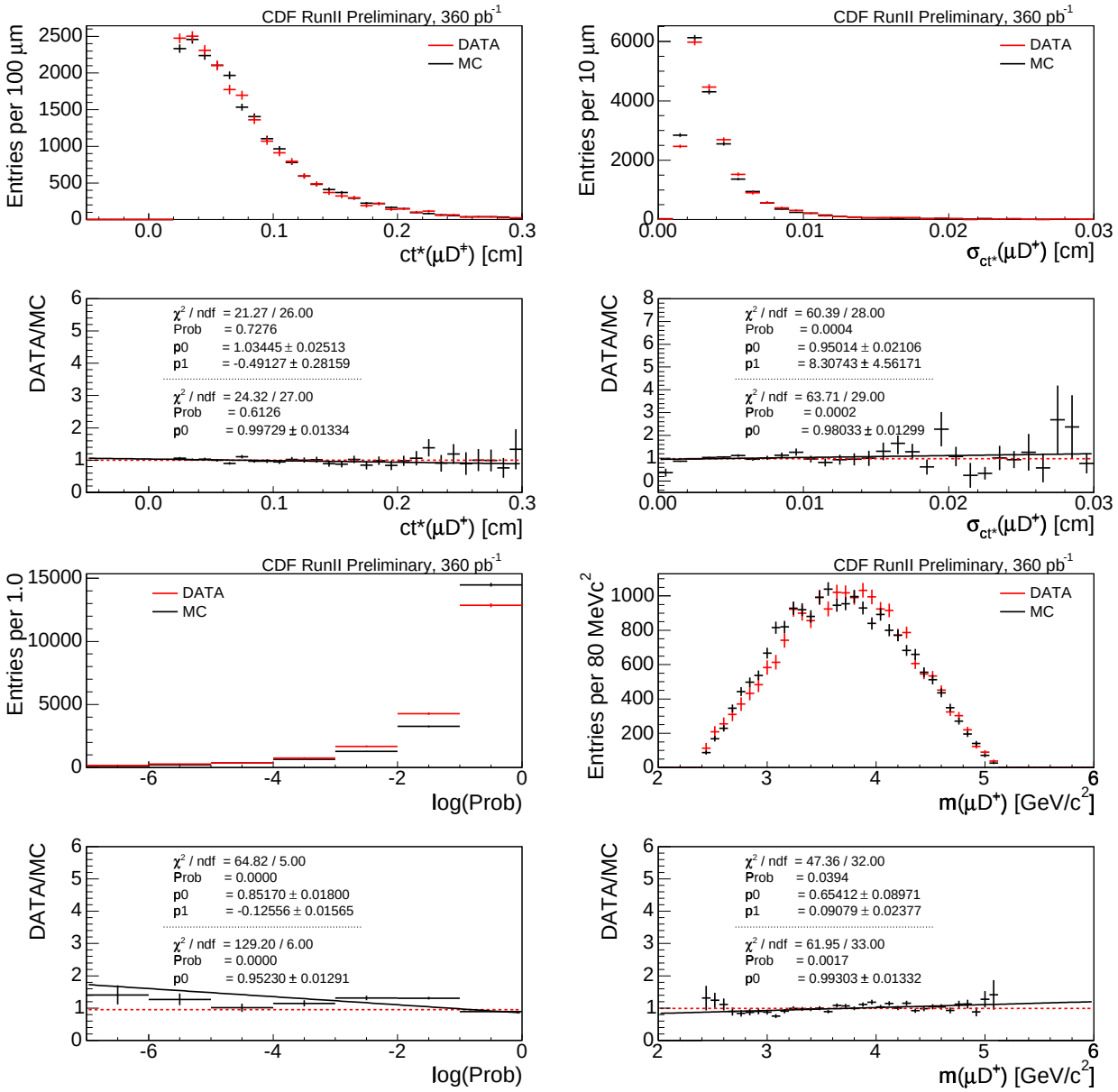

Figure 7.8: $\mu^- D^+$ data/MC comparisons of $ct^*(\mu^- D^+)$ (top left), $\sigma_{ct}(\mu^- D^+)$ (top right), $\mu^- D^+$ vertex probability (bottom left), and $m(\mu^- D^+)$ (bottom right).

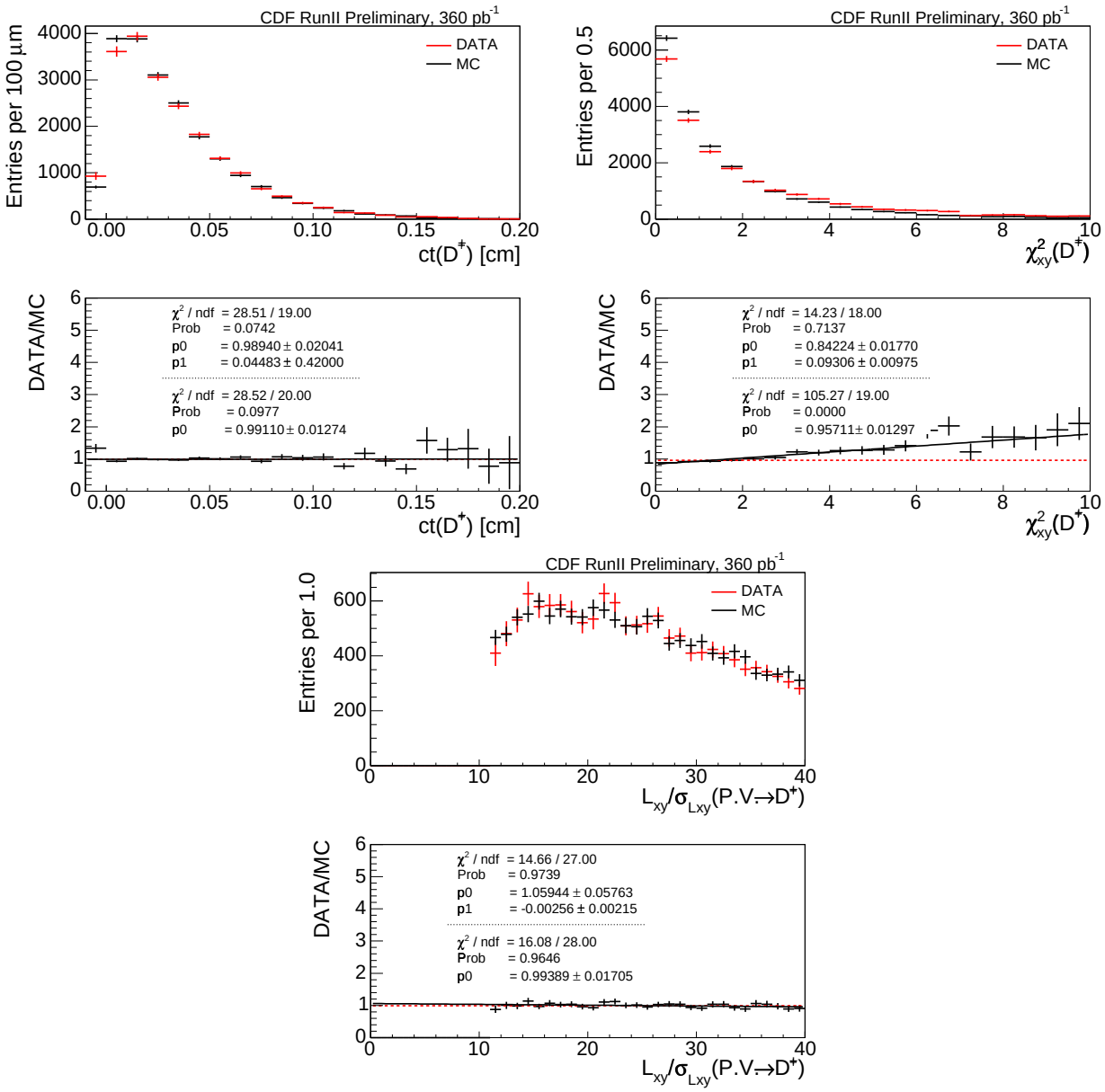

Figure 7.9: $\mu^- D^+$ data/MC comparisons of $ct(D^+)$ (top left), $\chi^2_{xy}(D^+)$ (top right), and $L_{xy}/\sigma_{L_{xy}}(P.V. \rightarrow D^+)$ (bottom).

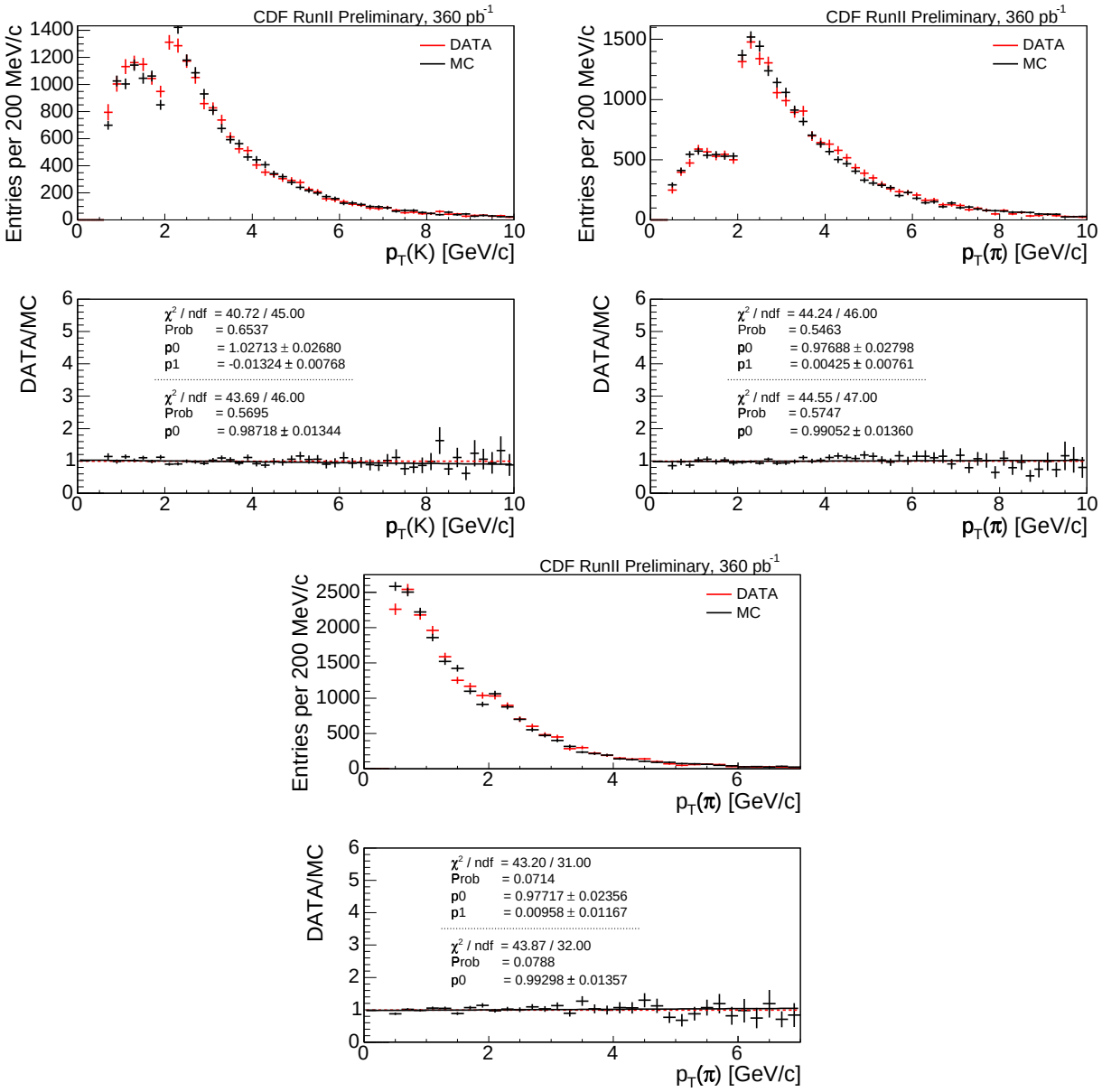

Figure 7.10: $\mu^- D^+$ data/MC comparisons of $p_T(K^-)$ (top right), $p_T(\pi^+(1))$ (top left), and $p_T(\pi^+(2))$ (bottom).

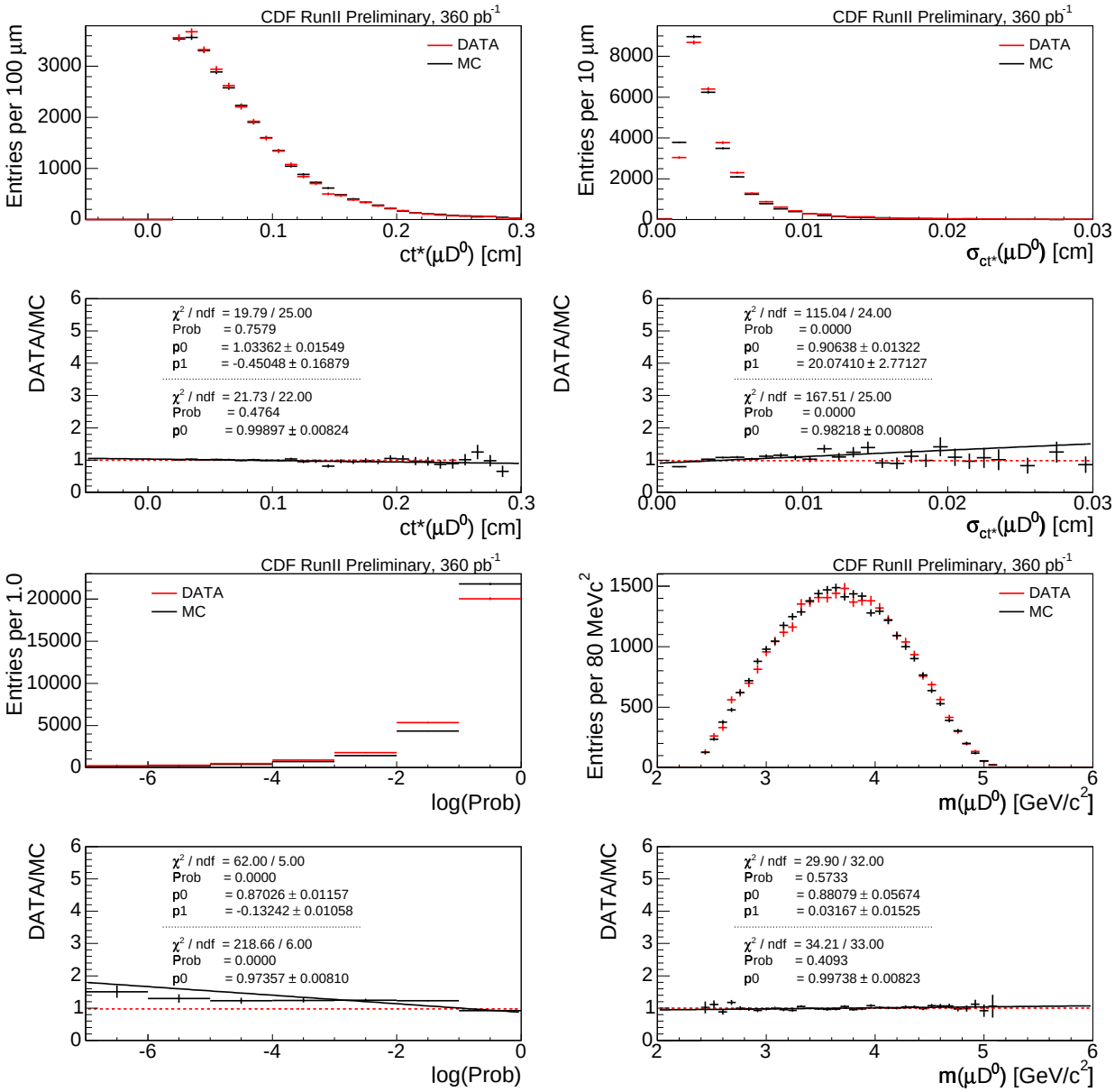

Figure 7.11: $\mu^- D^0$ data/MC comparisons of $ct^*(\mu^- D^0)$ (top left), $\sigma_{ct}(\mu^- D^0)$ (top right), $\mu^- D^0$ vertex probability (bottom left), and $m(\mu^- D^0)$ (bottom right).

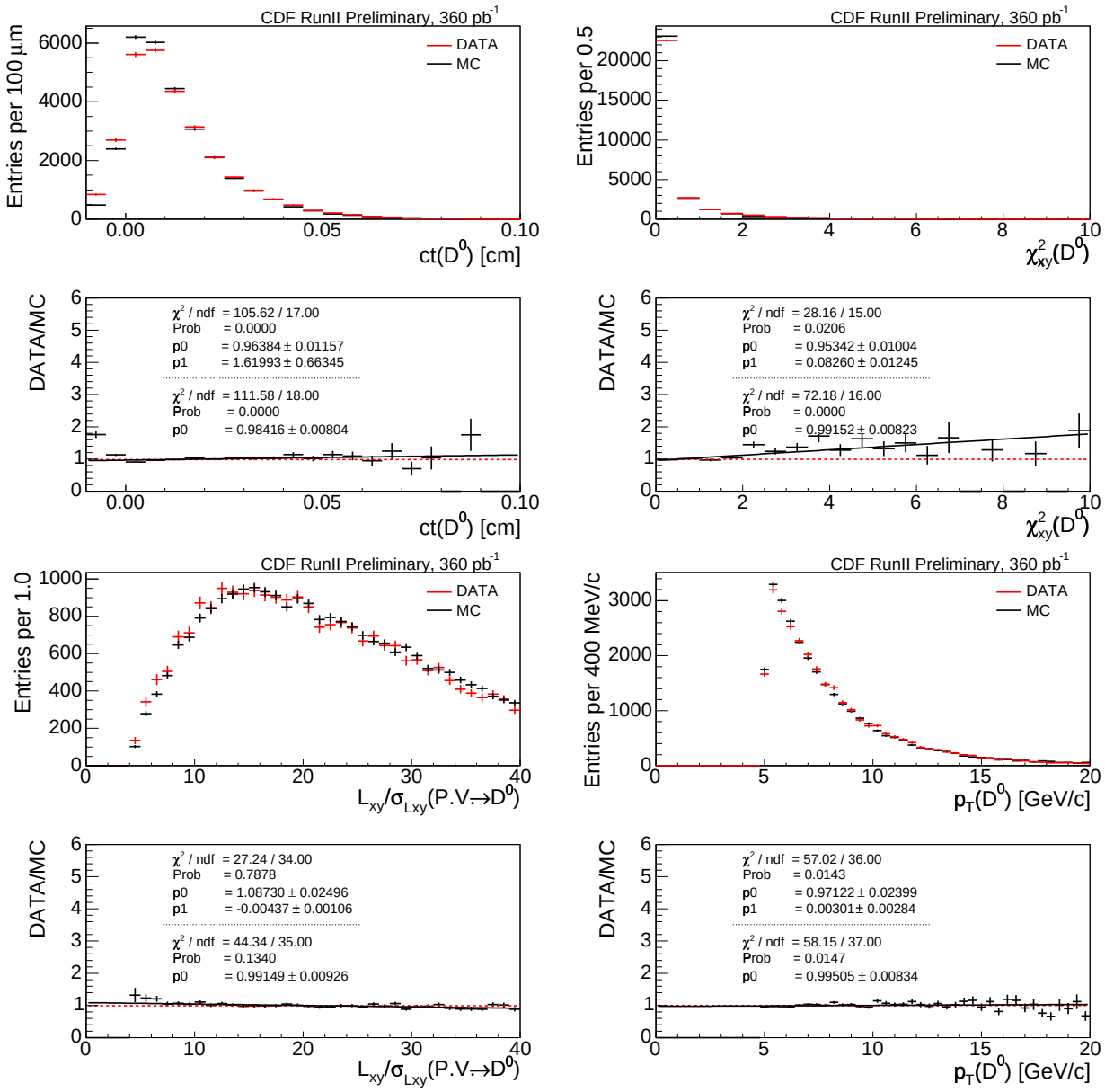

Figure 7.12: $\mu^- D^0$ data/MC comparisons of $ct(D^0)$ (top left), $\chi^2_{xy}(D^0)$ (top right), $L_{xy}/\sigma_{L_{xy}}(P.V. \to D^0)$ (bottom left), and $p_T(D^0)$ (bottom right).

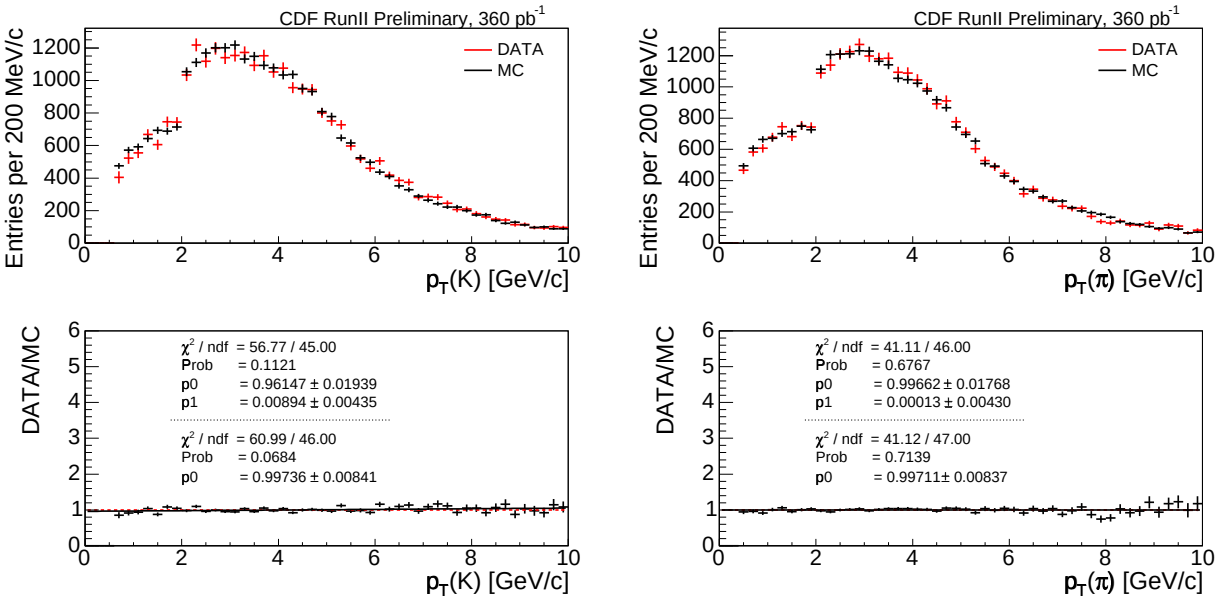

Figure 7.13: $\mu^- D^0$ data/MC comparisons of $p_T(K^-)$ (left) and $p_T(\pi^+)$ (right).

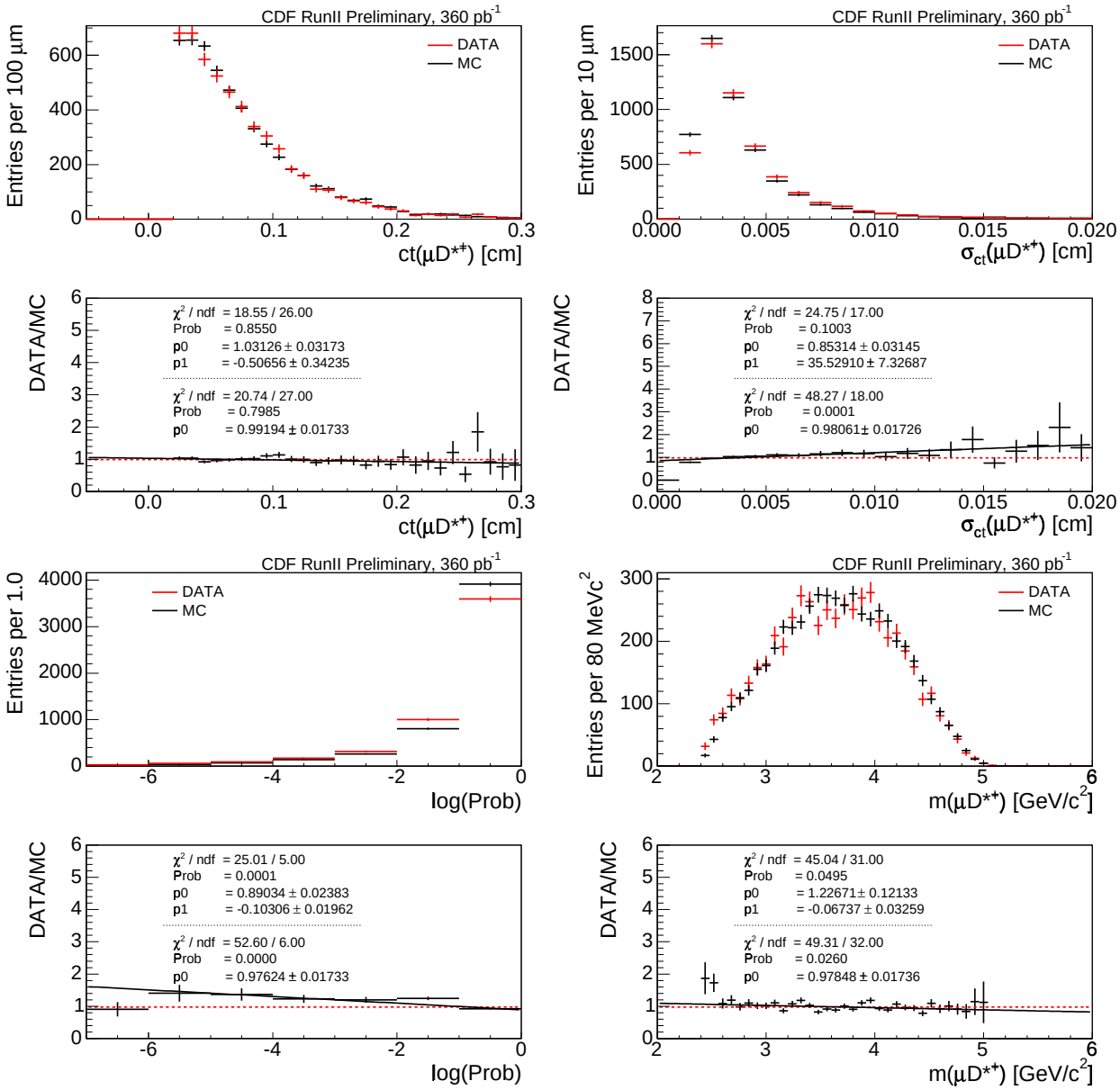

Figure 7.14: $\mu^- D^{*+}$ data/MC comparisons of $ct^*(\mu^- D^{*+})$ (top left), $\sigma_{ct}(\mu^- D^{*+})$ (top right), $\mu^- D^{*+}$ vertex probability (bottom left), and $m(\mu^- D^{*+})$ (bottom right).

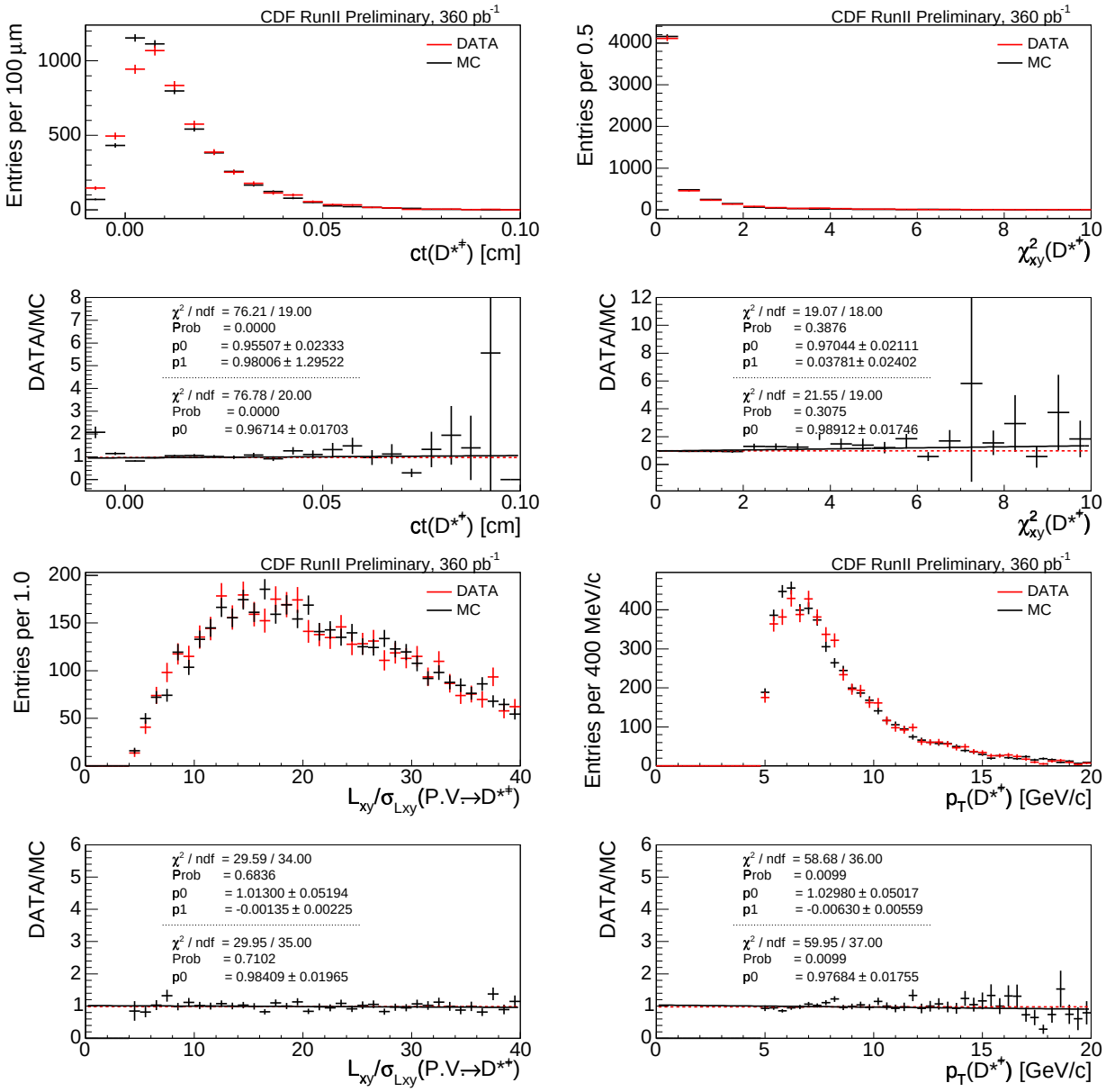

Figure 7.15:
$\mu^- D^{*+}$ data/MC comparisons of $ct(D^0)$ (top left), $\chi^2_{xy}(D^0)$ (top right), $L_{xy}/\sigma_{L_{xy}}(P.V. \rightarrow D^0)$ (bottom left), and $p_T(D^0)$ (bottom right) from the D^{*+} decay.

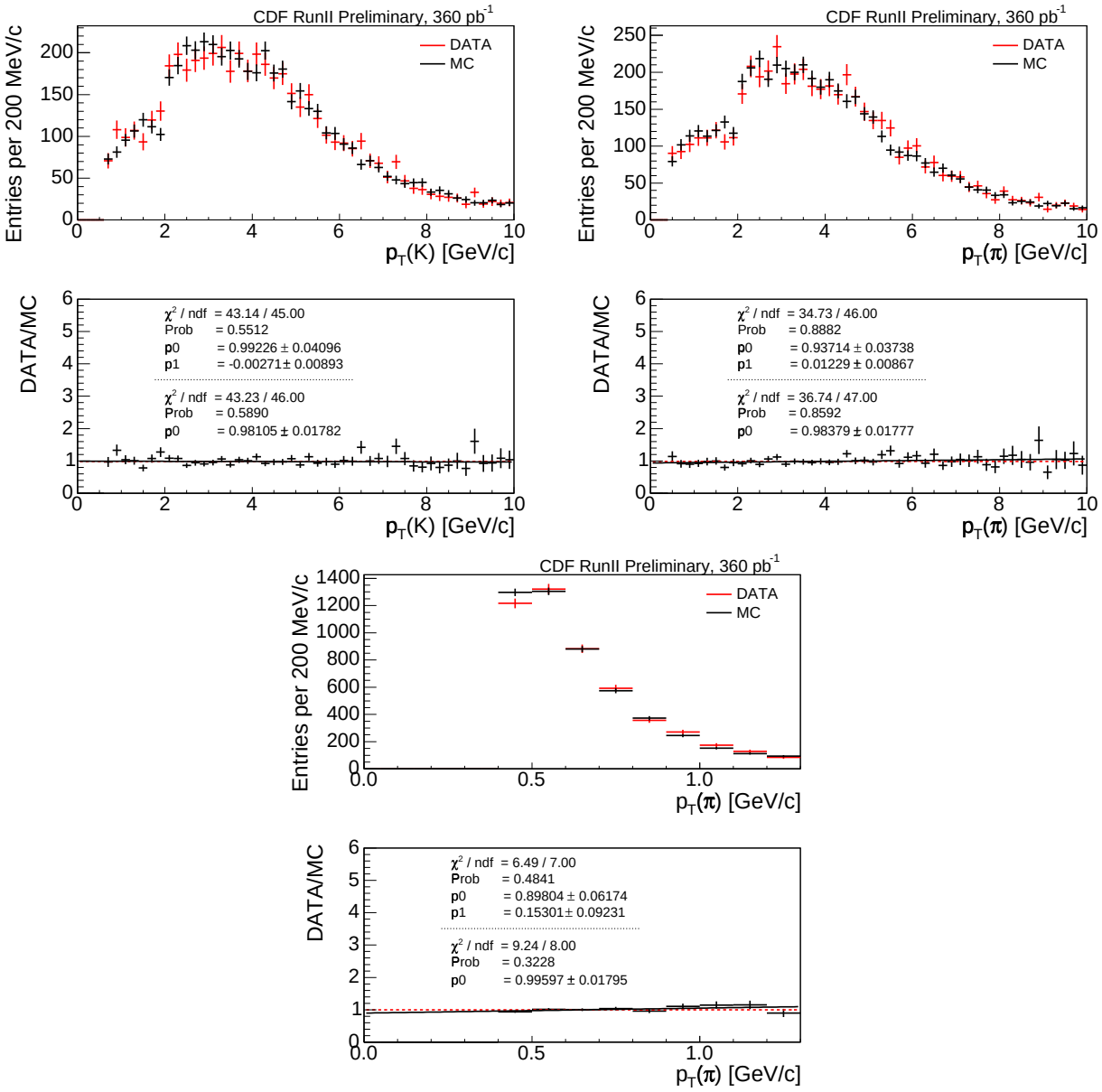

Figure 7.16: $\mu^- D^{*+}$ data/MC comparisons of $p_T(K^-)$ (top left), $p_T(\pi^+)$ (top right), and $p_T(\pi_*^+)$ (bottom), the soft pion from the D^{*+}.

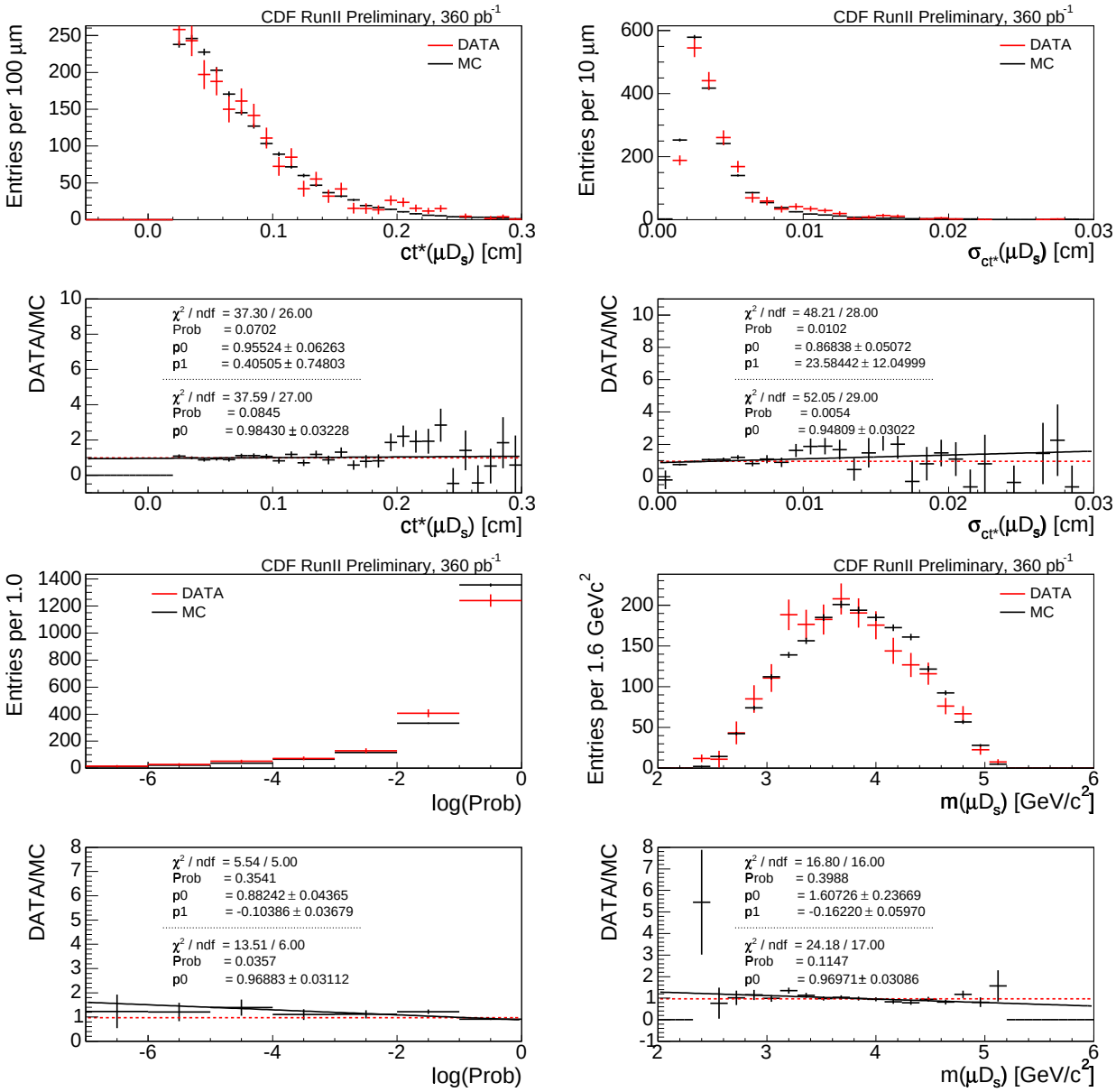

Figure 7.17: $\mu^- D_s^+$ data/MC comparisons of $ct^*(\mu^- D_s^+)$ (top left), $\sigma_{ct}(\mu^- D_s^+)$ (top right), $\mu^- D_s^+$ vertex probability (bottom left), and $m(\mu^- D_s^+)$ (bottom right).

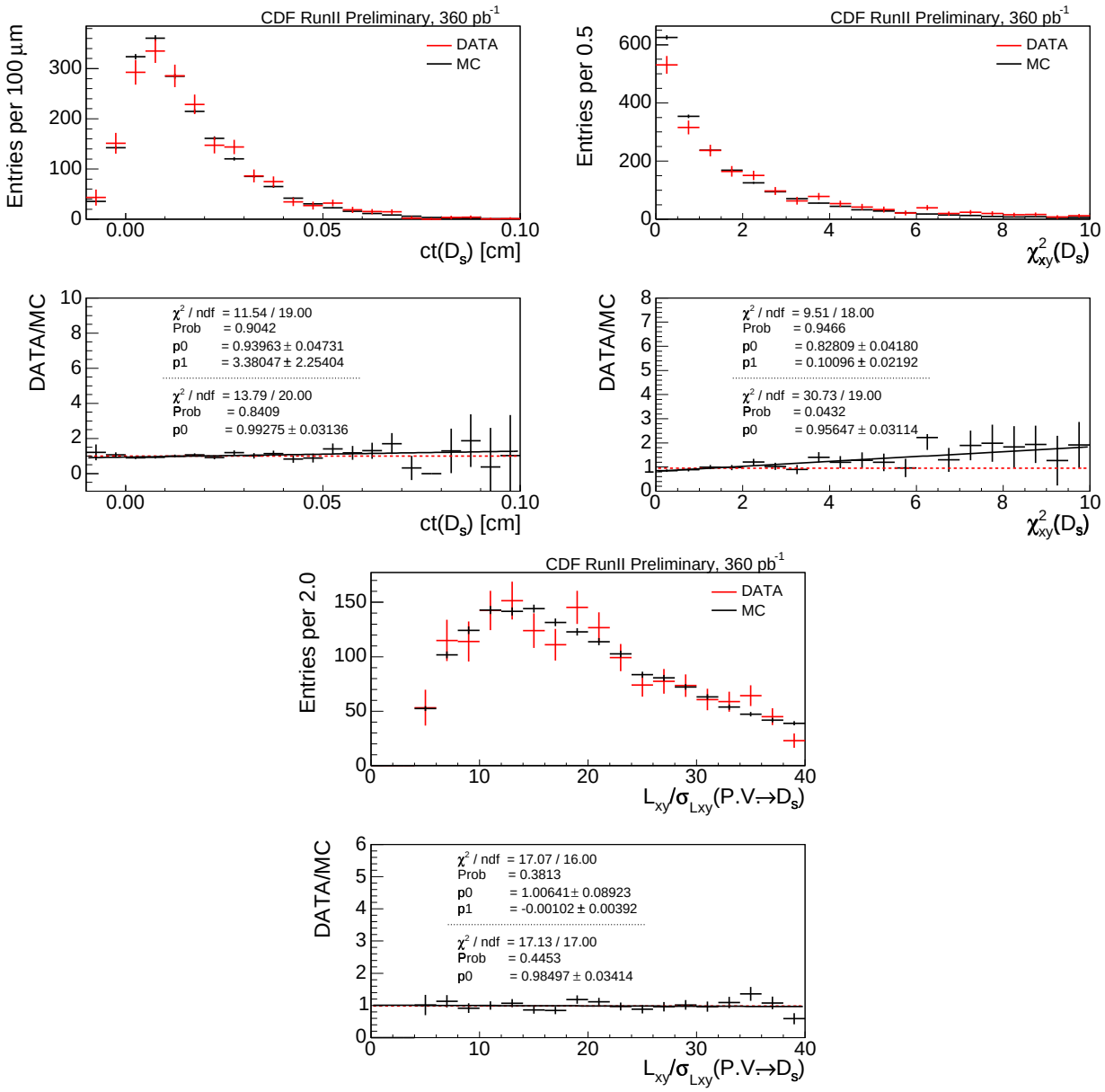

Figure 7.18: $\mu^- D_s^+$ data/MC comparisons of $ct(D_s^+)$ (top left), $\chi^2_{xy}(D_s^+)$ (top right), $L_{xy}/\sigma_{L_{xy}}(P.V. \to D_s^+)$ (bottom).

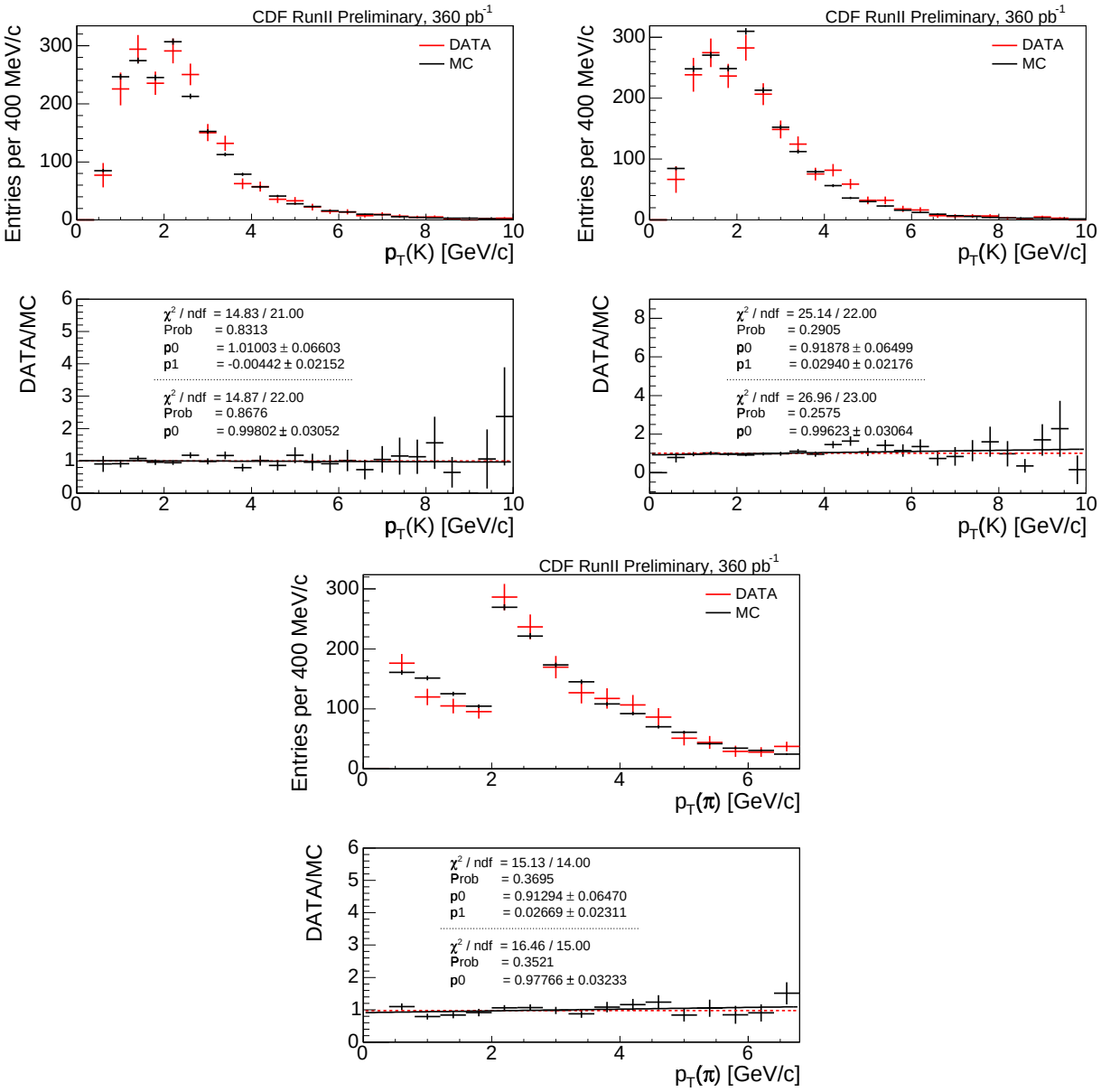

Figure 7.19: $\mu^- D_s^+$ data/MC comparisons of $p_T(K^+)$ (top left), $p_T(K^-)$ (top right), and $p_T(\pi^+)$ (bottom).

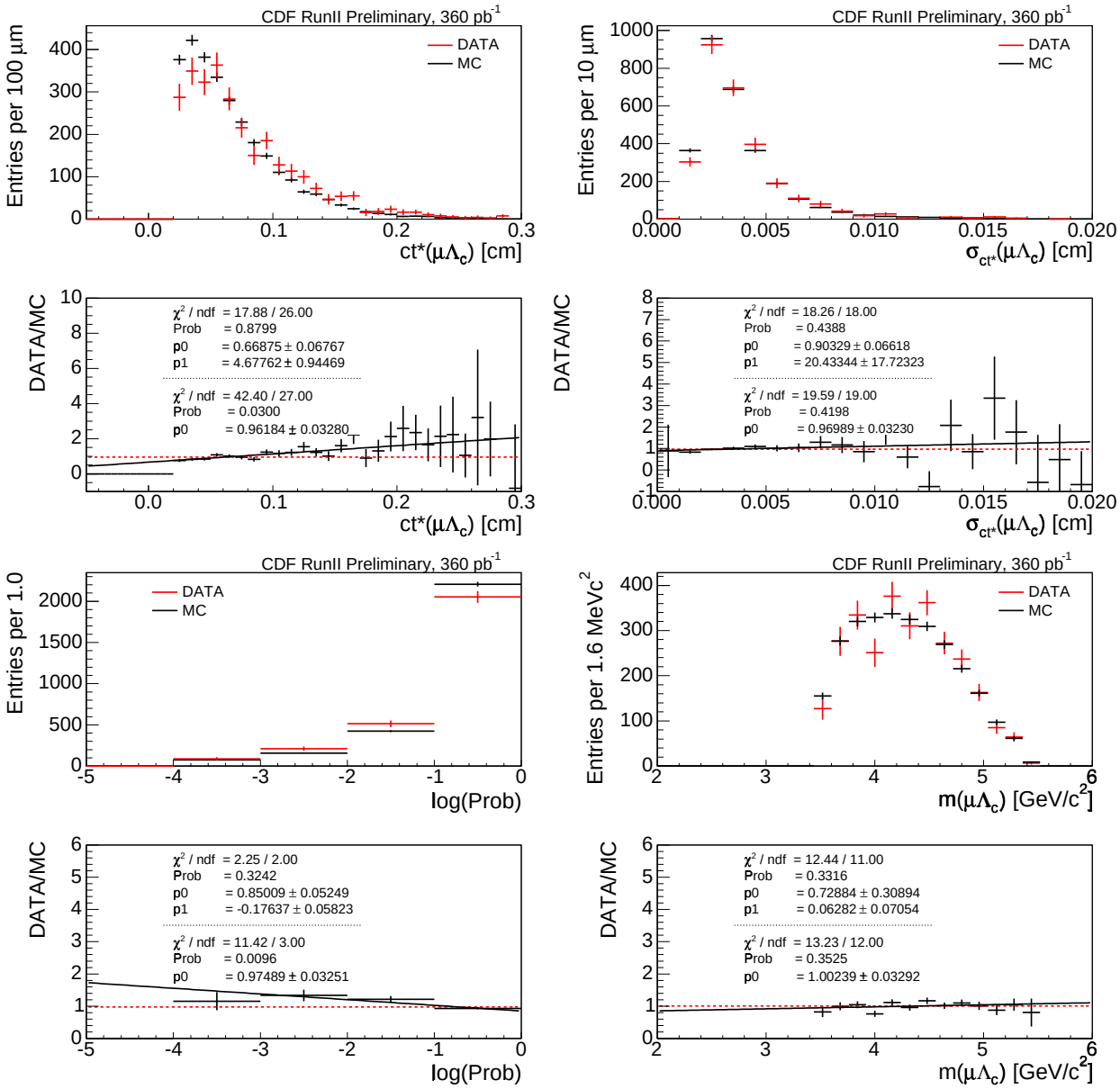

Figure 7.20: $\mu^-\Lambda_c^+$ data/MC comparisons of $ct^*(\mu^-\Lambda_c^+)$ (top left), $\sigma_{ct}(\mu^-\Lambda_c^+)$ (top right), $\mu^-\Lambda_c^+$ vertex probability (bottom left), and $m(\mu^-\Lambda_c^+)$ (bottom right).

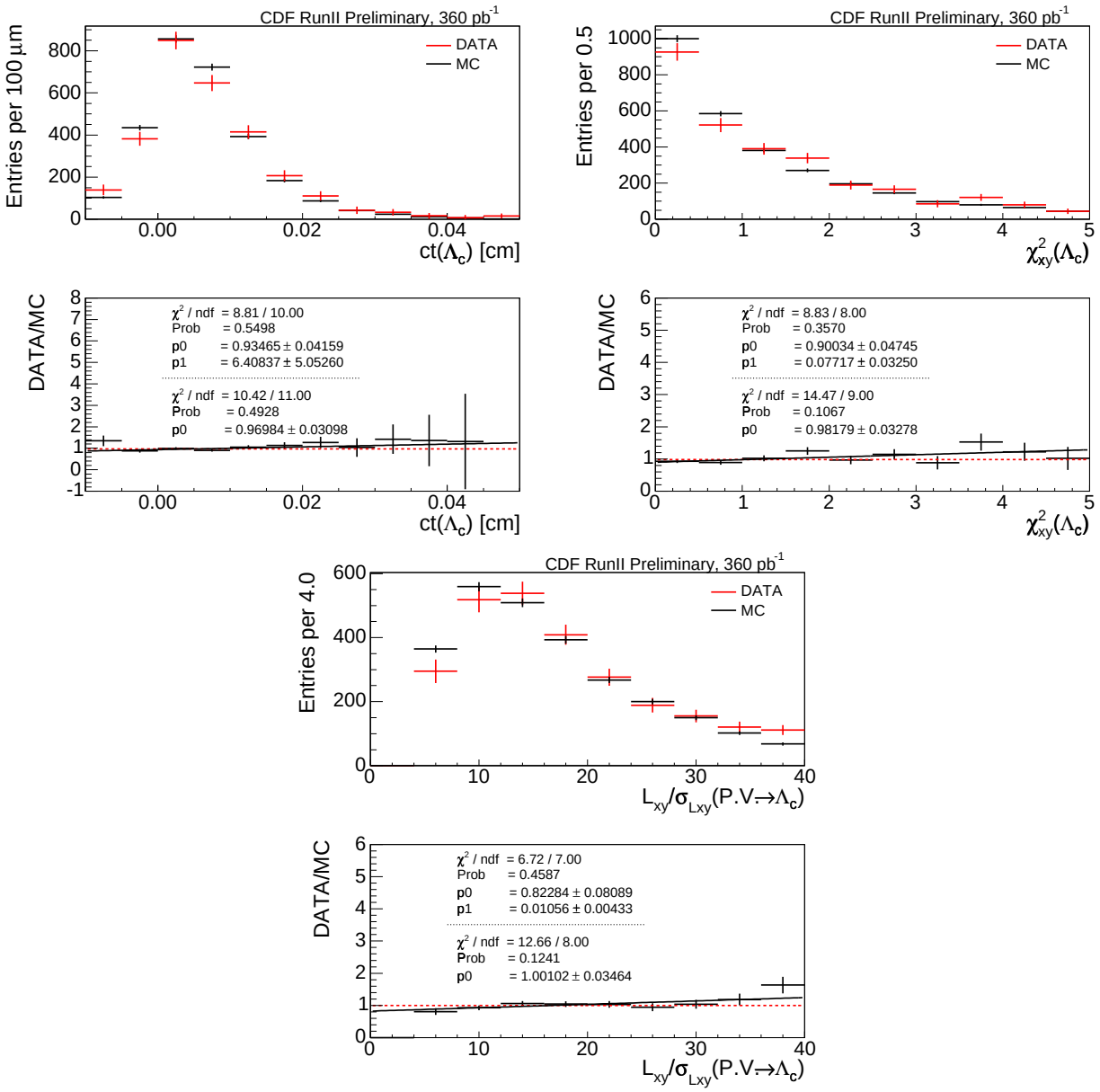

Figure 7.21: $\mu^-\Lambda_c$ data/MC comparisons of $ct(\Lambda_c^+)$ (top left), $\chi^2_{xy}(\Lambda_c^+)$ (top right), and $L_{xy}/\sigma_{L_{xy}}(P.V. \to \Lambda_c^+)$ (bottom left).

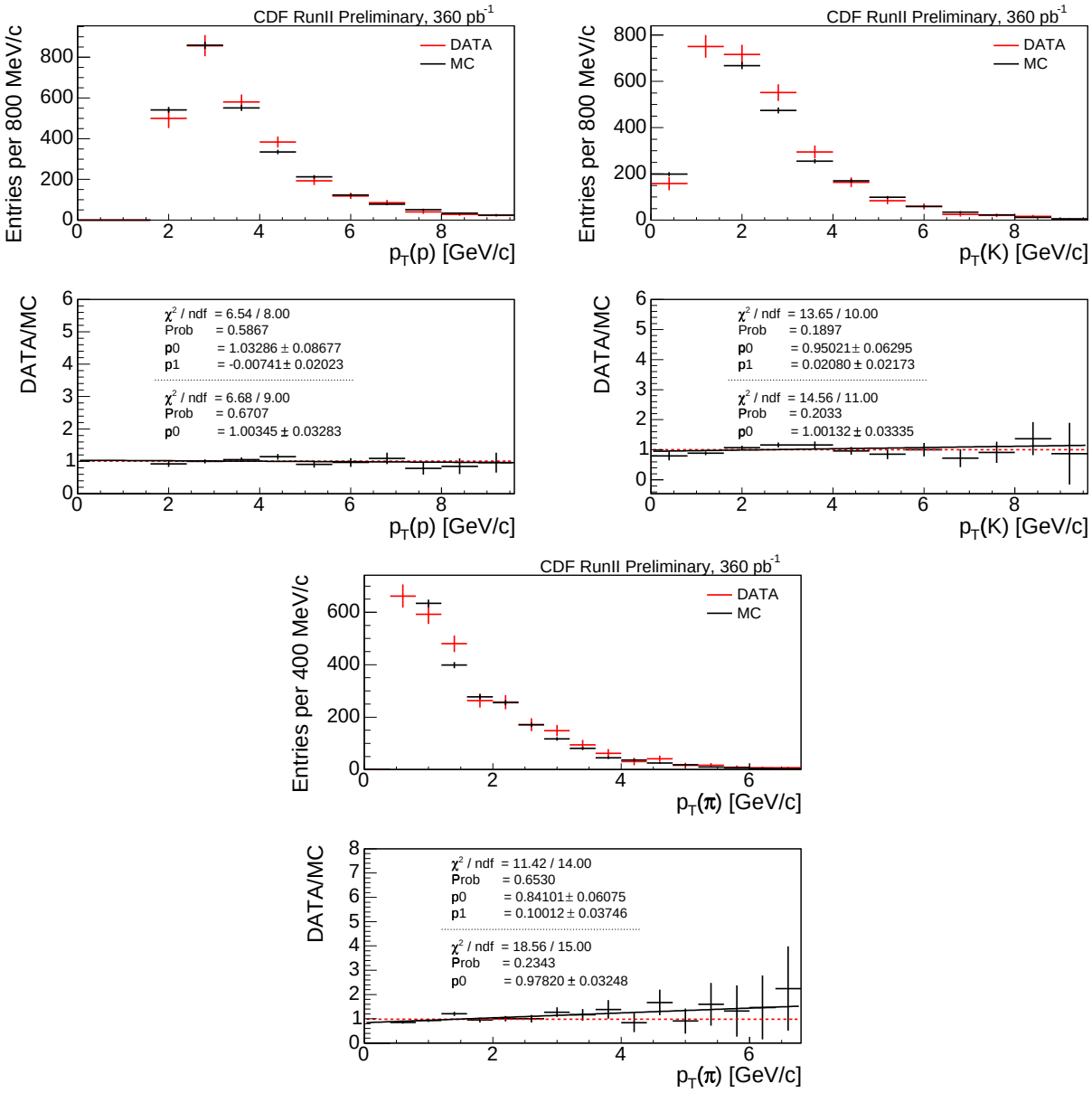

Figure 7.22: $\mu^- \Lambda_c^+$ data/MC comparisons of $p_T(p)$ (top left), $p_T(K^-)$ (top right), and $p_t(\pi^+)$ (bottom).

7.3 Total Relative Efficiencies

Monte Carlo simulations are generated for all exclusive meson decays included in the sample composition (see Chapter 6). Separate sets of Monte Carlo are generated for the e+SVT and μ+SVT data, since the efficiencies of electron decays is likely to be different than that of muon decays. The efficiency of each decay channel is quoted relative to the ground state decay mode in a particular lepton-charm channel in Tables 7.4-7.7. An inclusive $\Lambda_b^0 \to \ell^- \bar{\nu} \Lambda_c^+ X$ Monte Carlo, generated with the branching ratios listed in Table 6.5, is used to determine the efficiency of Λ_b^0 to contribute to the $\ell^- \Lambda_c^+$ signal. Only the $\Lambda_b^0 \to \tau^- \bar{\nu} \Lambda_c^+ X$ decays are generated separately from the inclusive $\ell^- \Lambda_c^+$ Monte Carlo.

The relative efficiencies included in the sample composition are the product of the acceptance, trigger, and analysis efficiencies,

$$\begin{aligned} \varepsilon_{rel}(\ell^- D^+) &= \varepsilon_{acceptance}(MC) \times \varepsilon_{trigger}(MC) \times \varepsilon_{analysis}(MC) \\ &\quad \times \varepsilon_{p/K/\pi\ trigger}(Data/MC). \end{aligned} \tag{7.3}$$

where the efficiencies are similar for the other lepton-charm signals. An extra factor of $\varepsilon_{trk}^{-1}(Data/MC)$ is needed for $\varepsilon_{rel}(\ell^- D^0)$ and $\varepsilon_{rel}(\ell^- D^{*+})$ to adjust the two track charm topology relative to the three track charm states, while the $\ell^- \Lambda_c^+$ relative efficiency requires an additional efficiency, $\varepsilon_{dE/dx}(Data)$, for the dE/dx cut on the proton.

Yields in each channel are determined by fitting the Monte Carlo signal with a double Gaussian, as is done in data. A single Gaussian is used to fit for the yield in the indirect lepton-charm decays, where the lepton originates from τ or another charm, because the yields are generally quite low in these channels and are poorly described by a double Gaussian. In cases where the fit fails, the number of events in the mass range is counted and the square root of the yield in that channel is taken as the error (which occurs primarily in very low efficiency "physics background" modes.) None of the branching ratios have been applied to the efficiencies listed in Tables 7.3-7.6. Since a fixed sample composition is used for the $\Lambda_b^0 \to \ell^- \bar{\nu}_\ell \Lambda_c^+$, the efficiencies quoted in Table 7.7 *do* have the branching ratios from Table 6.5 applied.

The indirect lepton-charm decays, the so-called "physics backgrounds", are not generated exclusively and are not readily comparable with the exclusive, primary decays without taking into account the branching ratios listed in Tables 6.2-6.5. The efficiencies for the indirect decays are listed with all excited charm and $\ell \to D$ branching ratios applied, although the efficiencies are not corrected for the ground state charm branching ratios. The $\tau^- \to \ell^- \bar{\nu}_\ell \nu_\tau$ branching ratios have also been applied to the indirect semileptonic decays where $\bar{B} \to \tau^- \bar{\nu} D X$ and $\Lambda_b^0 \to \tau^- \bar{\nu} \Lambda_c^+ X$. These efficiencies are also not corrected for the ground state charm branching ratios.

Decays	$e+SVT$	$\mu+SVT$
$\bar{B}^0 \to \ell^- \bar{\nu} D^+$	1.0 (10,887±108)	1.0 (13,067±116)
$\ell^- \bar{\nu} D^{*+} (D^+\pi^0/\gamma)$	1.061±0.015	1.100±0.013
$\ell^- \bar{\nu} D_1^+ (D^{*+}\pi^0 \to D^+\pi^0/\gamma)$	0.672±0.011	0.750±0.010
$\ell^- \bar{\nu} D_0^{*+} (D^+\pi^0)$	0.625±0.010	0.712±0.010
$\ell^- \bar{\nu} D_1^{'+} (D^{*+}\pi^0 \to D^+\pi^0/\gamma)$	0.680±0.010	0.748±0.010
$\ell^- \bar{\nu} D_2^{*+} (D^{*+}\pi^0 \to D^+\pi^0/\gamma)$	0.673±0.011	0.753±0.010
$\ell^- \bar{\nu} D_2^{*+} (D^+\pi^-)$	0.696±0.011	0.783±0.011
$\ell^- \bar{\nu} D^{*+}\pi^0 (D^+\pi^0/\gamma)$ (NR)	0.485±0.008	0.638±0.009
$\ell^- \bar{\nu} D^+\pi^0$ (NR)	0.544±0.009	0.764±0.010
$D^{(*)} \bar{D}^{(*)} K (\ell D^+ X)$	0.0012±0.0002	0.0044±0.0003
$D^{(*)+} D^{(*)-} (\ell D^+ X)$	0.0092±0.0004	0.0160±0.0005
$D_s^{(*)} D^{(*)} X (\ell D^+ X)$	0.0027±0.0002	0.0069±0.0003
$\tau^- \bar{\nu} D^{(*,**)X} (\ell D^+ X)$	0.0212±0.0005	0.0282±0.0007
$B^- \to \ell^- \bar{\nu} D_1^0 (D^{*+}\pi^- \to D^+\pi^0/\gamma)$	0.658±0.011	0.754±0.011
$\ell^- \bar{\nu} D_0^{*0} (D^+\pi^-)$	0.622±0.010	0.727±0.010
$\ell^- \bar{\nu} D_1^{'0} (D^{*+}\pi^- \to D^+\pi^0/\gamma)$	0.671±0.011	0.753±0.011
$\ell^- \bar{\nu} D_2^{*0} (D^{*+}\pi^- \to D^+\pi^0/\gamma)$	0.646±0.011	0.759±0.011
$\ell^- \bar{\nu} D_2^{*0} (D^+\pi^-)$	0.666±0.011	0.763±0.011
$\ell^- \bar{\nu} D^{*+}\pi^- (D^+\pi^0/\gamma)$ (NR)	0.491±0.010	0.626±0.009
$\ell^- \bar{\nu} D^+\pi^-$ (NR)	0.534±0.009	0.767±0.010
$D^{(*)} \bar{D}^{(*)} K (\ell D^+ X)$	0.0005±0.0001	0.0013±0.0001
$D_s^{(*)} D^{(*)} X (\ell D^+ X)$	0.0008±0.0001	0.0038±0.0002
$\tau^- \bar{\nu} D^{(*,**)} (\ell D^+ X)$	0.0031±0.0002	0.0045±0.0002
$\bar{B}_s^0 \to \ell^- \bar{\nu} D_{s1}^{'+}(2535) (D^{*+}K^0 \to D^+\pi^0/\gamma)$	0.612±0.010	0.695±0.010
$\ell^- \bar{\nu} D_{s2}^{*+}(2573) (D^{*+}K^0 \to D^+\pi^0/\gamma)$	0.575±0.009	0.665±0.009
$\ell^- \bar{\nu} D_{s2}^{*+}(2573) (D^+K^0)$	0.592±0.010	0.691±0.009
$D^{(*)} \bar{D}^{(*)} K (\ell D^+ X)$	0.0024±0.0002	0.0073±0.0003
$D_s^{(*)} D^{(*)} X (\ell D^+ X)$	0.0011±0.0001	0.0037±0.0002

Table 7.3: Relative efficiencies in $\ell^- D^+$ Monte Carlo. The yield (out of 10^7 generated events) is listed for the reference channel. $\ell \Rightarrow e, \mu$.

Decays	$e + SVT$	$\mu + SVT$
$\bar{B}^0 \to \ell^- \bar{\nu} D^{*+}(D^0\pi^+)$	0.970±0.012	1.028±0.012
$\ell^- \bar{\nu} D_1^+(D^{*+}\pi^0 \to D^0\pi^+)$	0.616±0.008	0.702±0.009
$\ell^- \bar{\nu} D_1^+(D^{*0}\pi^+ \to D^0\pi^0/\gamma)$	0.605±0.009	0.682±0.009
$\ell^- \bar{\nu} D_0^{*+}(D^0\pi^+)$	0.577±0.008	0.679±0.009
$\ell^- \bar{\nu} D_1^{'+}(D^{*+}\pi^0 \to D^0\pi^+)$	0.640±0.009	0.700±0.009
$\ell^- \bar{\nu} D_1^{'+}(D^{*0}\pi^+ \to D^0\pi^0/\gamma)$	0.557±0.008	0.631±0.008
$\ell^- \bar{\nu} D_2^{*+}(D^{*+}\pi^0 \to D^0\pi^+)$	0.613±0.009	0.707±0.009
$\ell^- \bar{\nu} D_2^{*+}(D^{*0}\pi^+ \to D^0\pi^0/\gamma)$	0.622±0.009	0.696±0.009
$\ell^- \bar{\nu} D_2^{*+}(D^0\pi^0)$	0.640±0.009	0.745±0.010
$\ell^- \bar{\nu} D^{*+}\pi^0(D^0\pi^+)$ (NR)	0.461±0.007	0.562±0.008
$\ell^- \bar{\nu} D^{*0}\pi^+(D^0\pi^0/\gamma)$ (NR)	0.451±0.007	0.578±0.008
$\ell^- \bar{\nu} D^0\pi^+$ (NR)	0.518±0.008	0.698±0.009
$D^{(*)}\bar{D}^{(*)}K(\ell D^0 X)$	0.0024±0.0002	0.0084±0.0003
$D^{(*)+}D^{(*)-}(\ell D^0 X)$	0.0033±0.0002	0.0074±0.0003
$D_s^{(*)}D^{(*)}X(\ell D^0 X)$	0.0026±0.0001	0.007±0.0002
$\tau^- \bar{\nu} D^{(*,**)}X(\ell D^0 X)$	0.0225±0.0005	0.0311±0.0007
$B^- \to \ell^- \bar{\nu} D^0$	1.0 (13,761±118)	1.0 (15,354±126)
$\ell^- \bar{\nu} D^{*0}(D^0\pi^0/\gamma)$	1.024±0.012	1.057±0.012
$\ell^- \bar{\nu} D_1^0(D^{*0}\pi^0 \to D^0\pi^0/\gamma)$	0.643±0.009	0.717±0.009
$\ell^- \bar{\nu} D_1^0(D^{*+}\pi^- \to D^0\pi^+)$	0.607±0.009	0.710±0.009
$\ell^- \bar{\nu} D_0^{*0}(D^0\pi^0)$	0.619±0.009	0.716±0.009
$\ell^- \bar{\nu} D_1^{'0}(D^{*0}\pi^0 \to D^0\pi^0/\gamma)$	0.648±0.009	0.742±0.009
$\ell^- \bar{\nu} D_1^{'0}(D^{*+}\pi^- \to D^0\pi^+)$	0.609±0.009	0.709±0.009
$\ell^- \bar{\nu} D_2^{*0}(D^{*0}\pi^0 \to D^0\pi^0/\gamma)$	0.638±0.009	0.726±0.009
$\ell^- \bar{\nu} D_2^{*0}(D^{*+}\pi^- \to D^0\pi^+)$	0.598±0.009	0.710±0.009
$\ell^- \bar{\nu} D_2^{*0}(D^0\pi^0)$	0.662±0.009	0.757±0.009
$\ell^- \bar{\nu} D^{*+}\pi^-(D^0\pi^+)$ (NR)	0.456±0.007	0.580±0.008
$\ell^- \bar{\nu} D^{*0}\pi^0(D^0\pi^0/\gamma)$ (NR)	0.474±0.007	0.597±0.008
$\ell^- \bar{\nu} D^0\pi^0$ (NR)	0.565±0.008	0.745±0.009
$D^{(*)}\bar{D}^{(*)}K(\ell D^0 X)$	0.0033±0.0002	0.0104±0.0004
$D_s^{(*)-}D^{(*)0}(\ell D^0 X)$	0.0044±0.0003	0.0109±0.0003
$\tau^- \bar{\nu} D^{(*,**)}X(\ell D^0 X)$	0.0403±0.0007	0.0523±0.0009
$\bar{B}_s^0 \to \ell^- \bar{\nu} D_{s1}^{'+}(2535)(D^{*+}K^0 \to D^0\pi^+)$	0.541±0.008	0.638±0.008
$\ell^- \bar{\nu} D_{s1}^{'+}(2535)(D^{*0}K^+ \to D^0\pi^0/\gamma)$	0.519±0.008	0.633±0.008
$\ell^- \bar{\nu} D_{s2}^{*+}(2573)(D^{*+}K^0 \to D^0\pi^+)$	0.513±0.008	0.614±0.008
$\ell^- \bar{\nu} D_{s2}^{*+}(2573)(D^{*0}K^+ \to D^0\pi^0/\gamma)$	0.501±0.008	0.621±0.008
$\ell^- \bar{\nu} D_{s2}^{*+}(2573)(D^0K^+)$	0.537±0.008	0.639±0.008
$D^{(*)}\bar{D}^{(*)}K(\ell D^0 X)$	0.0022±0.0002	0.0072±0.0003
$D_s^{(*)}D^{(*)}X(\ell D^0 X)$	0.0014±0.0001	0.0056±0.0002

Table 7.4: Relative efficiencies in $\ell^- D^0$ Monte Carlo. The yield (out of 10^7 generated events) is listed for the reference channel. $\ell \Rightarrow e, \mu$.

Decays	$e + SVT$	$\mu + SVT$
$\bar{B}^0 \to \ell^- \bar{\nu} D^{*+} (D^0 \pi^+)$	1.0 (8,876±96)	1.0 (10,677±104)
$\ell^- \bar{\nu} D_1^+ (D^{*+} \pi^0 \to D^0 \pi^+)$	0.642±0.011	0.696±0.010
$\ell^- \bar{\nu} D_1^{'+} (D^{*+} \pi^0 \to D^0 \pi^+)$	0.680±0.011	0.691±0.011
$\ell^- \bar{\nu} D_2^{*+} (D^{*+} \pi^0 \to D^0 \pi^+)$	0.642±0.011	0.698±0.011
$\ell^- \bar{\nu} D^{*+} \pi^0 (D^0 \pi^+)$ (NR)	0.484±0.009	0.552±0.009
$D^{(*)} \bar{D}^{(*)} K (\ell D^{*+} X \to D^0 \pi^+)$	0.0010±0.0003	0.0028±0.0002
$D^{(*)+} D^{(*)-} (\ell D^{*+} X \to D^0 \pi^+)$	0.0033±0.0003	0.0064±0.0004
$D_s^{(*)} D^{(*)} X (\ell D^{*+} X \to D^0 \pi^+)$	0.00105±0.00004	0.0023±0.0002
$\tau^- \bar{\nu} D^{(*,**)} (\ell D^{*+} X \to D^0 \pi^+)$	0.018±0.003	0.0235±0.0007
$B^- \to \ell^- \bar{\nu} D_1^0 (D^{*+} \pi^- \to D^0 \pi^+)$	0.646±0.011	0.696±0.011
$\ell^- \bar{\nu} D_1^{'0} (D^{*+} \pi^- \to D^0 \pi^+)$	0.640±0.011	0.701±0.011
$\ell^- \bar{\nu} D_2^{*0} (D^{*+} \pi^- \to D^0 \pi^+)$	0.620±0.011	0.688±0.011
$\ell^- \bar{\nu} D^{*+} \pi^- (D^0 \pi^+)$ (NR)	0.466±0.009	0.577±0.009
$D^{(*)} \bar{D}^{(*)} K (\ell D^{*+} X \to D^0 \pi^+)$	0.0006±0.0001	0.0013±0.0002
$D_s^{(*)} D^{(*)} X (\ell D^{*+} X \to D^0 \pi^+)$	0.00028±0.00006	0.00021±0.00007
$\tau^- \bar{\nu} D^{(*,**)} (\ell D^{*+} X \to D^0 \pi^+)$	0.002±0.001	0.0024±0.0009
$\bar{B}_s^0 \to \ell^- \bar{\nu} D_{s1}^{'+} (2535) (D^{*+} K^0 \to D^0 \pi^+)$	0.553±0.010	0.620±0.010
$\ell^- \bar{\nu} D_{s2}^{*+} (2573) (D^{*+} K^0 \to D^0 \pi^+)$	0.525±0.010	0.593±0.009
$D^{(*)} \bar{D}^{(*)} K (\ell D^{*+} X \to D^0 \pi^+)$	0.0007±0.0003	0.0022±0.0003
$D_s^{(*)} D^{(*)} X (\ell D^{*+} X \to D^0 \pi^+)$	0.00024±0.00008	0.0012±0.0002

Table 7.5: Relative efficiencies in $\ell^- D^{*+}$ Monte Carlo. The yield (out of 10^7 generated events) is listed for the reference channel. $\ell \Rightarrow e, \mu$.

Decays	$e + SVT$	$\mu + SVT$
$\bar{B}_s^0 \to \ell^- \bar{\nu} D_s^+$	1.0 (9,980±100)	1.0 (12,008±108)
$\ell^- \bar{\nu} D_s^{*+} (D_s^+ \gamma)$	1.035±0.014	1.11±0.014
$\ell^- \bar{\nu} D_{s0}^{*+} (2317) (D_s^+ \pi^0)$	0.684±0.011	0.773±0.011
$\ell^- \bar{\nu} D_{s1}^+ (2460) (D_{s0}^{*+} \pi^0 \to D_s^+ \pi^0)$	0.709±0.011	0.786±0.011
$\ell^- \bar{\nu} D_{s1}^+ (2460) (D_s^+ \gamma)$	0.710±0.011	0.781±0.011
$\ell^- \bar{\nu} D_s^{*+} \pi^0 (D_s^+ \gamma)$ (NR)	0.436±0.008	0.591±0.009
$\ell^- \bar{\nu} D_s^+ \pi^0$ (NR)	0.479±0.008	0.722±0.010
$D_s^{(*)} D^{(*)} X (\ell D_s^+ X)$	0.0023±0.0003	0.0086±0.0007
$D_s^{(*)+} D_s^{(*)-} (\ell D_s^+ X)$	0.0075±0.0003	0.0175±0.0005
$\tau^- \bar{\nu} D_s^{(*,**)+} (\ell D_s^+ X)$	0.034±0.005	0.052±0.001
$\bar{B}^0 \to D_s^{(*)+} D^{(*)-} (\ell D_s^+ X)$	0.0055±0.0003	0.0126±0.0005
$\bar{B}^+ \to D_s^{(*)+} D^{(*)-} (\ell D_s^+ X)$	0.0055±0.0003	0.0109±0.0005

Table 7.6: Relative efficiencies in $\ell^- D_s^+$ Monte Carlo. The yield (out of 10^7 generated events) is listed for the reference channel. $\ell \Rightarrow e, \mu$.

Decays	$e + SVT$	$\mu + SVT$
$\Lambda_b^0 \to \ell^- \bar{\nu} \Lambda_c^+ X$	1.0 (6,291±87)	1.0 (7,224±95)
$\tau^- \bar{\nu} \Lambda_c^+ X (\ell \Lambda_c^+ X)$	0.026±0.001	0.033±0.0007

Table 7.7: Relative efficiencies in $\ell^- \Lambda_c^+$ Monte Carlo. The yield (out of 10^7 generated events) is listed for the reference channel. $\ell \Rightarrow e, \mu$.

Chapter 8

Semileptonic $\bar{B}$ p_T Spectra

Differences between baryon and meson production momentum spectra could significantly affect the relative fragmentation fractions by enhancing or reducing the relative efficiency between the meson and baryon channels. The $\bar{B}$ p_T spectrum used to generate the Monte Carlo is especially important, since the relative efficiency between channels is in part determined by the p_T spectrum. The p_T spectrum determined in conjunction with the Run II measurement of the inclusive J/ψ cross-section [40] is used by default for all $\bar{B}$ meson Monte Carlo generation, but poor agreement is observed between the $\ell^-\Lambda_c^+$ data and the Monte Carlo generated with this spectrum. Instead, a p_T spectrum tuned from the $\ell^-\Lambda_c^+$ data is used to generate the Λ_b^0 Monte Carlo.

A fully hadronic Λ_b^0 branching ratio measurement at CDF Run II [50] compared the p_T spectra of $\bar{B}$ hadrons for $\bar{B}^0 \to D^+\pi^-$ and $\Lambda_b^0 \to \Lambda_c^+\pi^-$ and concluded that the Λ_b^0 p_T spectrum is significantly softer than the $\bar{B}^0$ spectrum. The semileptonic signals benefit from higher yields, but the origin of the charm signals is incompletely known due to the missing neutrino. Conversely, the fully reconstructed signals are in principle better understood, but these signals, which correspond to the first 360 pb^{-1}, are roughly a tenth of the semileptonic $\bar{B}$ signals. The semileptonic signals are sensitive to p_T effects above 7 GeV/c, which is harder than the fully reconstructed signals, with a $p_T(B)$ threshold of 4 GeV/c.

All of the semileptonic meson data are compared with the inclusive J/ψ cross-section spectrum, while the semileptonic baryon signal is compared with both the J/ψ spectrum and the fully hadronic Λ_b^0 spectrum. Only comparisons for the μ+SVT data and Monte Carlo are shown.

8.1 Semileptonic Meson Spectra

The comparisons between $\ell^- D$ meson data and the inclusive $\bar{B} \to \ell^-\bar{\nu}DX$ Monte Carlo are shown in Figure 8.1. The p_T spectrum determined in the inclusive J/ψ cross-section analysis is used as input for the Monte Carlo p_T spectrum. This spectrum has been measured well below 15 GeV/c, but measurements at higher p_T have large statistical uncertainty. Good agreement is observed between the data and the Monte Carlo for the $\mu^- D^+$ and $\mu^- D_s^+$ data. The agreement between the data and the Monte Carlo in the $\mu^- D^0$ and $\mu^- D^{*+}$ signals is not as good, although no statistically significant slope is observed in either case. The remaining

discrepancy between the data relative to the Monte Carlo in the $\mu^- D^0$, seen in the upper right set of plots in Figure 8.1, is covered by the variation of the total yield as part of the systematic uncertainty in the measurement (see Chapter 10).

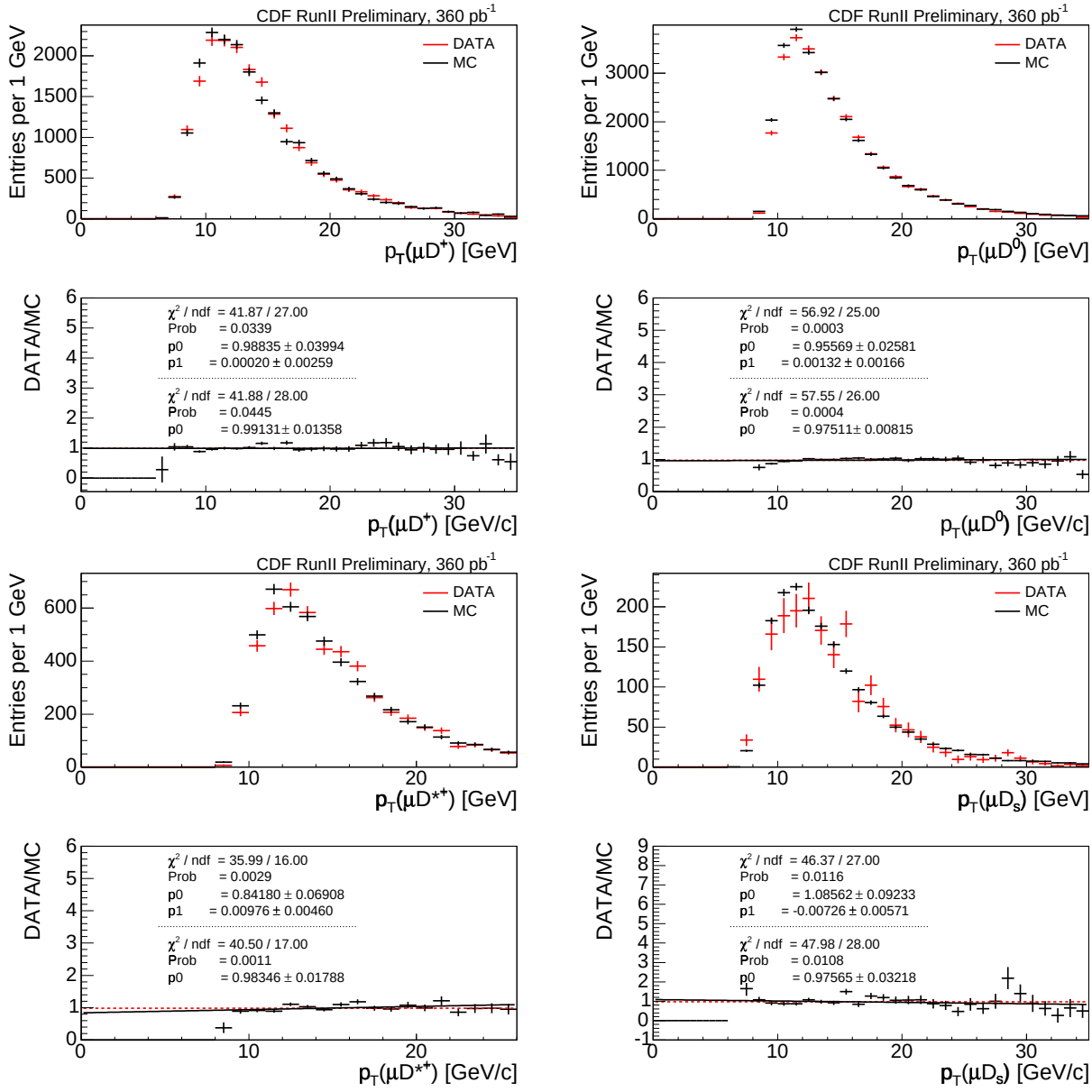

Figure 8.1: Comparison of $\mu^- D$ data and $\bar{B} \to \mu^- \bar{\nu} D X$ Monte Carlo for the $\mu^- D^+$ (top left), $\mu^- D^0$ (top right), $\mu^- D^{*+}$ (bottom left), and $\mu^- D_s^+$ (bottom right).

8.2 Semileptonic Baryon Spectrum

Two sets of $\Lambda_b^0 \to \ell^- \bar{\nu} \Lambda_c^+ X$ Monte Carlo, one generated with the hadronic Λ_b^0 spectrum and one generated with the J/ψ spectrum, are compared to the $\mu^- \Lambda_c^+$ data, shown in Figure 8.2.

While the hadronic Λ_b^0 spectrum is softer than the measured semileptonic spectrum, the J/ψ spectrum is harder than the data. Instead of using either spectrum, a p_T spectrum derived from the semileptonic $\ell^-\Lambda_c^+$ data is used, shown in Figure 8.3. The adjustment factor is determined using the disagreement between the weighted of the e+SVT and μ+SVT data and the J/ψ spectrum. The J/ψ spectrum is corrected by the function $w = b + m \cdot p_T$, where $b = 1.43 \pm 0.08$, and $m = -0.026 \pm 0.007$. The tuned spectrum is then varied by $\pm 2\,\sigma$ of the uncertainty on the slope (σ_m) to bound the uncertainty on this spectrum (see Chapter 10.) The generator level Λ_b^0 p_T spectrum is shown in Figure 8.4 for the semileptonic $\mu^-\Lambda_c^+$ spectrum, with $\pm 2\,\sigma$ variation, and compared with the generator-level J/ψ and hadronic Λ_b^0 spectra. The $\pm 2\,\sigma$ variation of the Λ_b^0 p_T spectrum is shown compared with data in Figure 8.5.

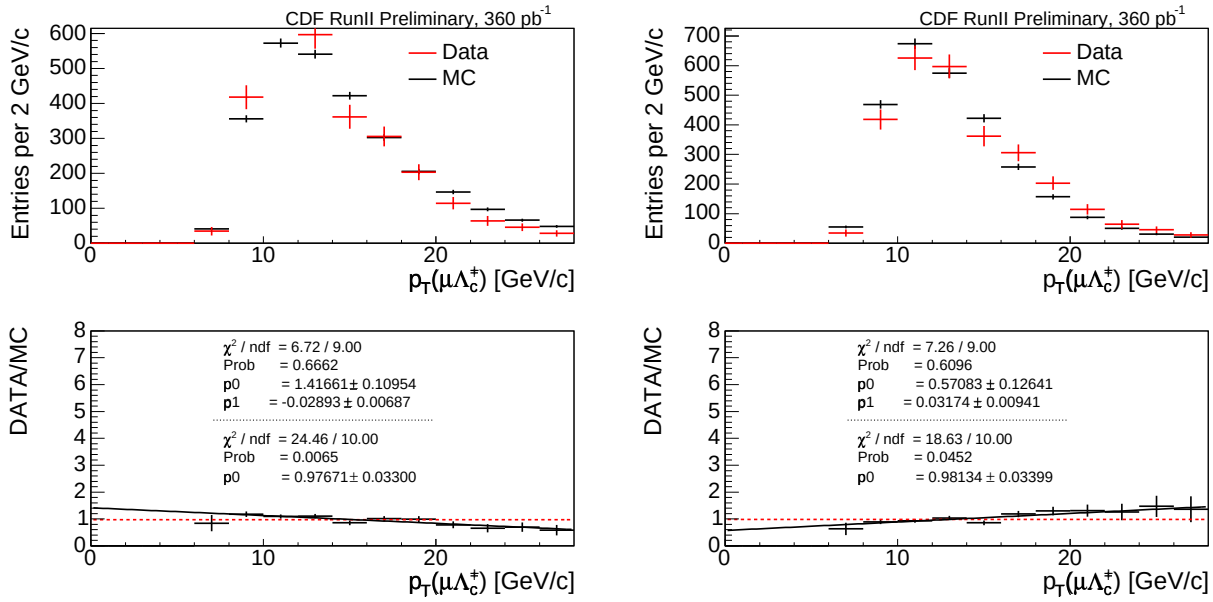

Figure 8.2: Comparisons of $\mu^-\Lambda_c^+$ data and Monte Carlo generated according to the J/ψ spectrum (left) and the hadronic Λ_b^0 spectrum (right).

8.3 Comparison of Meson and Baryon Spectra in Data

Reasonably good agreement between the $\mu^- D^+$ p_T spectrum and the $\mu^-\Lambda_c^+$ p_T spectrum is observed (cf. Figure 8.6). The semileptonic $\bar{B}^0$ and Λ_b^0 spectra are also compared using the $\mu^- D^{*+}$ signal, with all cuts except $p_T(D^0) > 5$ listed in Table 5.5 applied. The $\mu^- D^{*+}$ signal should be a cleaner source of $\bar{B}^0$'s than the $\mu^- D^+$ signal. The spectra obtained from the $\mu^- D^{*+}$ data is indeed observed to be harder than the $\mu^-\Lambda_c^+$ data. A $3\,\sigma$ significant shift is seen in the ratio and the lowest two bins of the $\mu^- D^{*+}$ p_T spectra are significantly shifted. However, it is not clear how readily the $\mu^- D^{*+}$ p_T spectra, which have an additional requirement on the soft pion, are expected to compare to the $\mu^-\Lambda_c^+$ spectra because of acceptance differences in the detection of the soft pion.

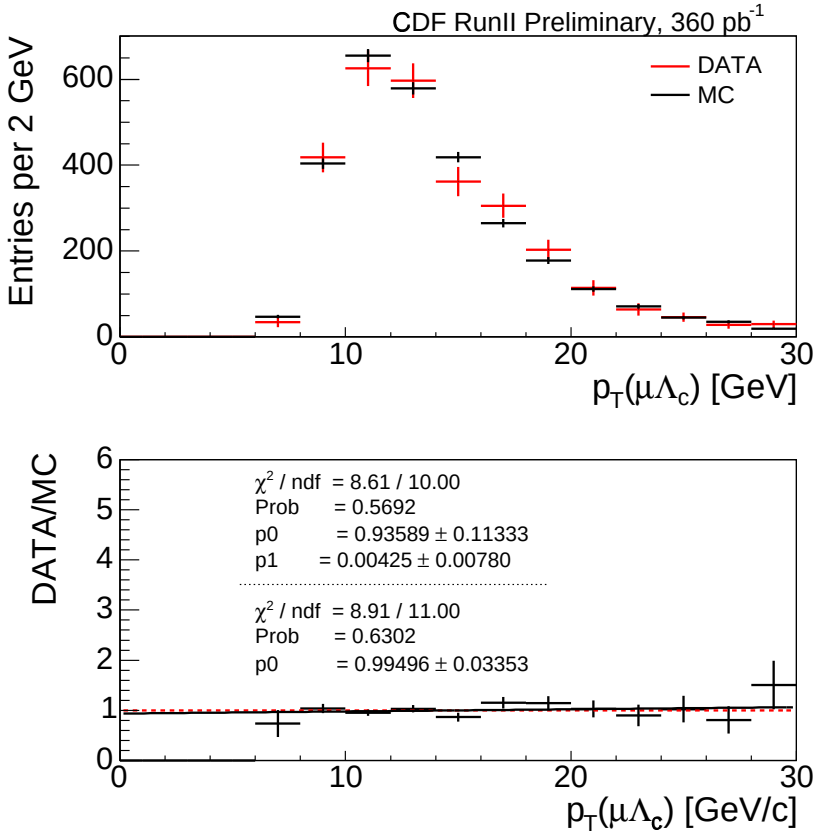

Figure 8.3: Comparison of $\mu^- \Lambda_c^+$ data and Monte Carlo generated according to the tuned semileptonic Λ_b^0 spectrum.

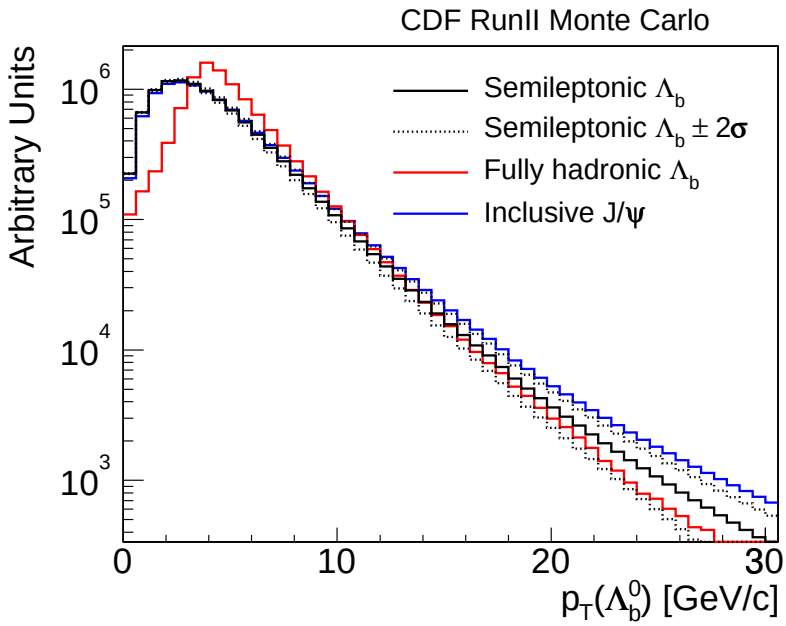

Figure 8.4: Generator-level comparisons of the J/ψ, semileptonic Λ_b^0, and hadronic Λ_b^0 p_T spectra.

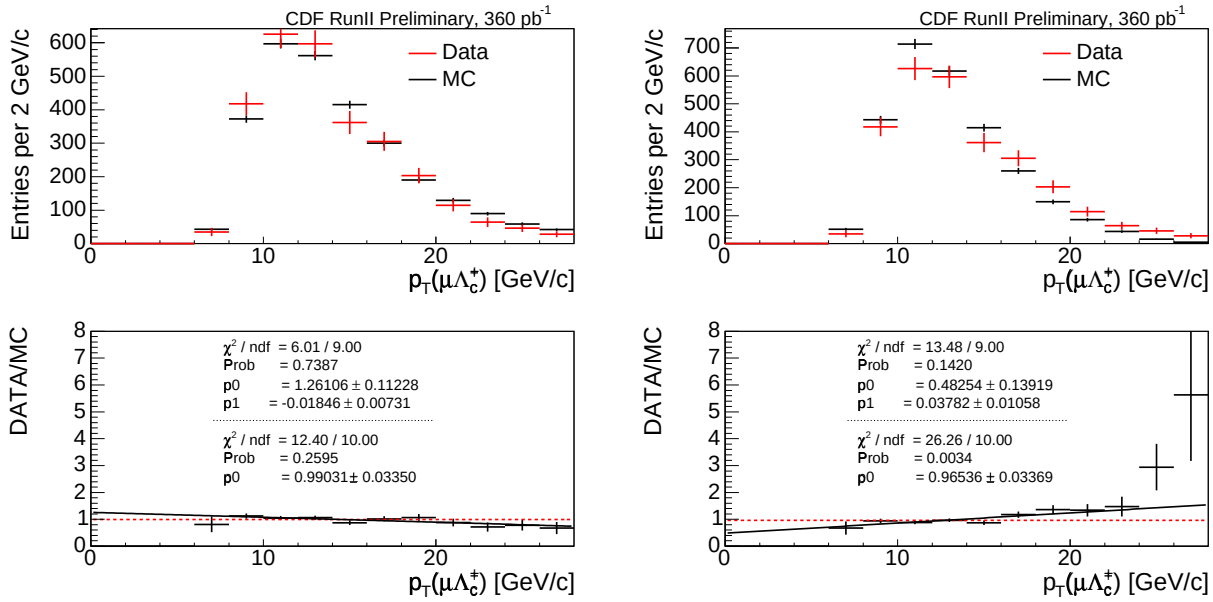

Figure 8.5: $\mu^-\Lambda_c^+$ data compared with the tuned semileptonic Λ_b^0 p_T spectrum shifted $+2\,\sigma$ (left) and $-2\,\sigma$ (right).

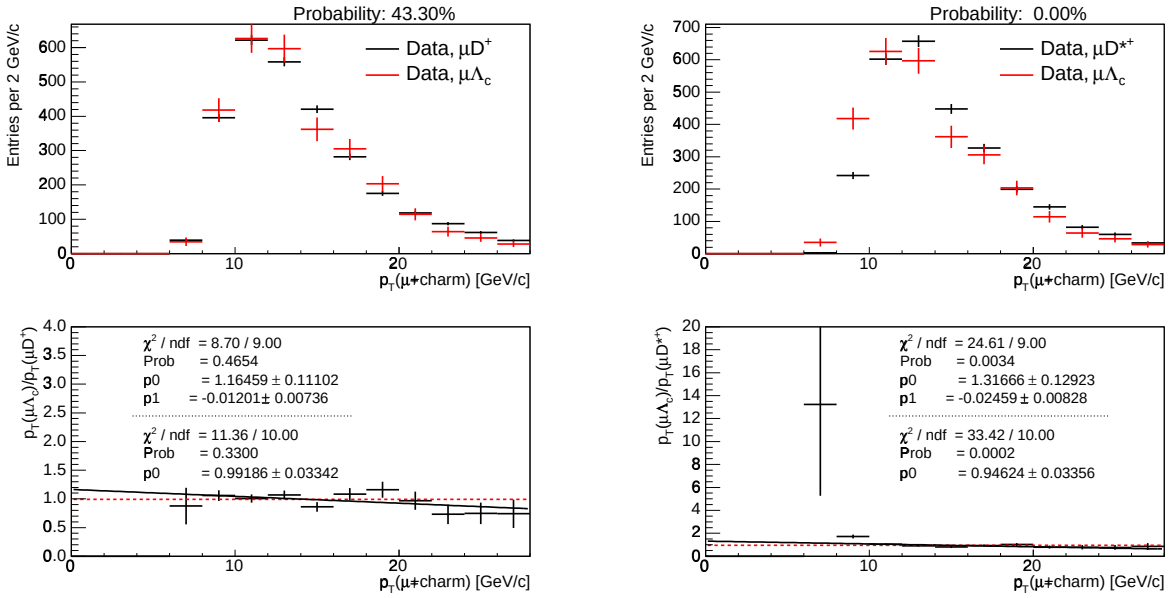

Figure 8.6: Comparisons of sideband subtracted $p_T(\mu^-\Lambda_c^+)$ data with $p_T(\mu^- D^+)$ data (left) and $p_T(\mu^-\Lambda_c^+)$ data with $p_T(\mu^- D^{*+})$ data (right).

8.4 Effective $\bar{B}$ p_T Threshold

In previous measurements of the fragmentation fractions, no dependence on the transverse momentum of the $\bar{B}$ hadron was taken into account. Due to the discrepancies in agreement between the semileptonic baryon spectrum and the inclusive J/ψ spectrum, a transverse momentum threshold is appropriate. Clearly, the values of the fragmentation fractions cannot be known below the reconstruction threshold of the semileptonic data. Generator-level effective $\bar{B}$ p_T spectra after all analysis level cuts applied are shown in Figure 8.7. A 7 GeV/c effective $p_T(\bar{B})$ threshold is observed, with 90% of events lying above 11.25 GeV/c for $p_T(\bar{B}^0)$ and $p_T(\bar{B}^0_s)$, above 11.0 GeV/c for $p_T(\bar{B}^0)$, and above 12.25 for $p_T(B^-)$, which is higher because of the additional $p_T(D^0) > 5$ GeV/c cut applied to the $\ell^- D^0$ signal.

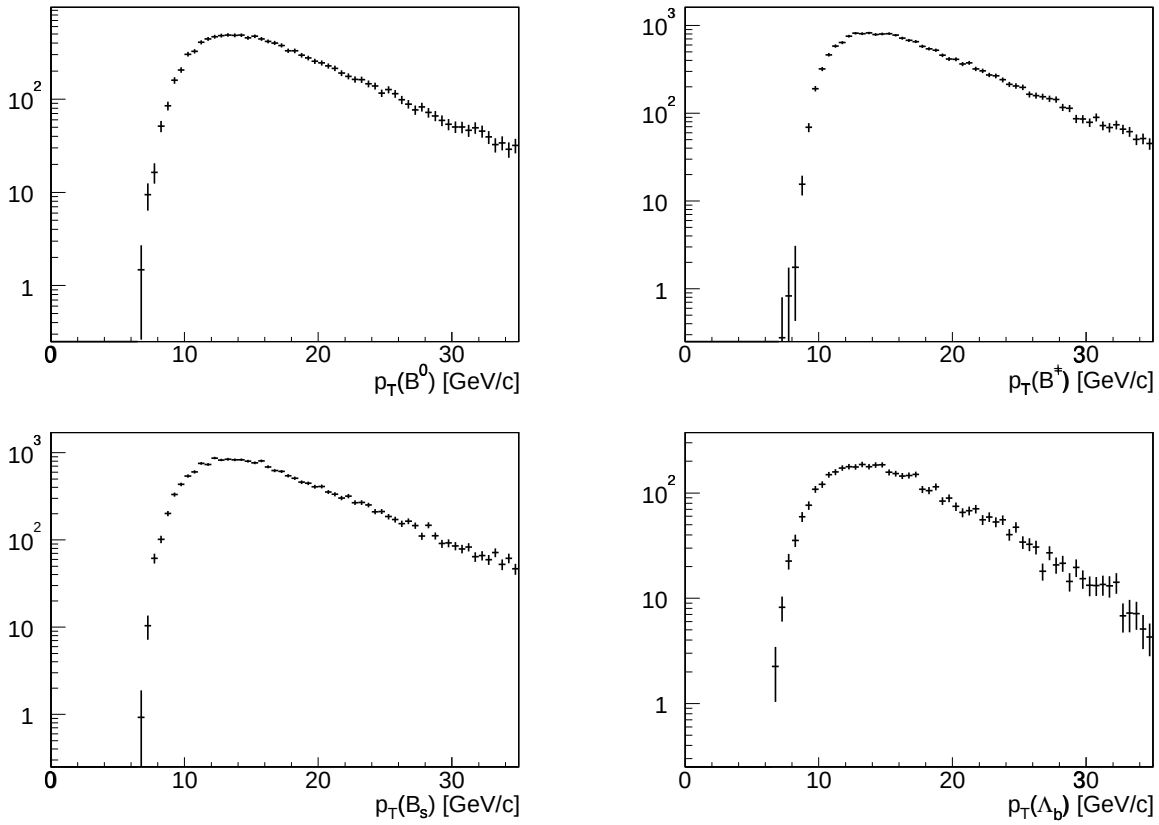

Figure 8.7: Effective $\bar{B}$ meson p_T threshold for $\bar{B}^0$ (top left), B^- (top right), $\bar{B}^0_s$ (bottom left), and Λ^0_b (bottom right).

Chapter 9

Fit of Relative Fragmentation Fractions

In order to fit for the relative fragmentation fractions, the sample composition discussed in Chapter 6 is implemented in a χ^2-fit. The measured yields in the five lepton-charm signals are fit to the yields predicted by the sample composition and the decay rates ($\Gamma^{(*,**)}$) of the B meson to the ground and excited states are constrained within their errors to the values predicted by the PDG. The χ^2 which is minimized is

$$\begin{aligned}\chi^2 &= \sum_{i=1}^{5}\left(\frac{N_i(\ell^- D/\Lambda_c^+)_{measured} - N_i(\ell^- D/\Lambda_c^+)_{predicted}}{\sigma_{N_{i,measured}}}\right)^2 \\ &\quad + \left(\frac{\Gamma - \Gamma_{PDG}}{\sigma_{\Gamma_{PDG}}}\right)^2 + \left(\frac{\Gamma^* - \Gamma^*_{PDG}}{\sigma_{\Gamma^*_{PDG}}}\right)^2 + \left(\frac{\Gamma^{**} - \Gamma^{**}_{PDG}}{\sigma_{\Gamma^{**}_{PDG}}}\right)^2, \end{aligned} \tag{9.1}$$

where $N(\ell^- D/\Lambda_c^+)_{predicted}$ is based on the semileptonic sample composition (described in Chapter 6). In order to simplify the sample composition in the fit and to fit in terms of better known quantities, the number of predicted lepton-charm events are expressed in terms of $N(\bar{B}^0)$, an overall normalization in the fit which is not indicative of the physical number of $\bar{B}^0$ mesons in the data. As a result the B meson lifetimes are included relative to the lifetime of the $\bar{B}^0$. This is preferable for the B^-, because the lifetime ratio $\tau(B^-)/\tau(\bar{B}^0)$ is better measured than $\tau(B^-)$ alone. The $\tau(\bar{B}^0_s)/\tau(\bar{B}^0)$ lifetime ratio is not better measured than the independent measurements of the $\tau(\bar{B}^0_s)$ and $\tau(\bar{B}^0)$ lifetimes. The predicted number of lepton-charm in the fit are expressed as

$$\begin{aligned} N(\ell^- D_i)_{predicted} &= \sum_{j=d,u,s} N(\bar{B}^0)\frac{f_j}{f_d} \times \tau(\bar{B}^0) \times \frac{\tau(\bar{B}_j)}{\tau(\bar{B}^0)} \\ &\quad \sum_k \Gamma_k \times \mathcal{BR}_{ijk}(D_{jk} \to D_i)\mathcal{BR}(D_i)\varepsilon_{ijk} \\ &= \sum_{j=d,u,s} N(\bar{B}^0)\frac{f_j}{f_u + f_d}\left(1 + \frac{f_u}{f_d}\right) \times \tau(\bar{B}^0) \times \frac{\tau(B_j)}{\tau(\bar{B}^0)} \\ &\quad \sum_k \Gamma_k \times \mathcal{BR}_{ijk}(D_{jk} \to D_i)\mathcal{BR}(D_i)\varepsilon_{ijk} \end{aligned} \tag{9.2}$$

where $D_i = D^+, D^0, D^{*+}, D_s^+$ and $\Gamma_k = \Gamma, \Gamma^*, \Gamma^{**}$ for the meson case, and

$$\begin{aligned} N(\ell^-\Lambda_c^+)_{predicted} &= N(\bar{B}^0)\frac{f_{\Lambda_b}}{f_u + f_d}\left(1 + \frac{f_u}{f_d}\right) \\ &\quad \times \mathcal{BR}(\Lambda_b^0 \to \ell^-\bar{\nu}\Lambda_c^+ X)\varepsilon(\Lambda_b^0 \to \ell^-\bar{\nu}\Lambda_c^+ X) \end{aligned} \tag{9.3}$$

for the baryon case. All of the Λ_b^0 and excited charm branching ratios in Eq. (9.3) are incorporated into the inclusive Monte Carlo and are implicitly included in the efficiency $\varepsilon(\Lambda_b^0 \to \ell^-\bar{\nu}\Lambda_c^+ X)$.

There are four free parameters in the χ^2 fit for the fragmentation fractions: three composition parameters f_u/f_d, $f_s/(f_u + f_d)$, $f_{\Lambda_b}/(f_u + f_d)$, termed $\{f_c\}$, and one normalization parameter $N(\bar{B}^0)$, and three constrained parameters: Γ, Γ^*, and Γ^{**}. The decision to fit for f_s and f_{Λ_b} relative to $f_u + f_d$ is made to minimize as many biases in the measurement as possible and to highlight the fact that the $\bar{B}_s^0$ is reconstructed relative to the $\bar{B}^0$ and B^- signals. Additionally, performing the fit relative to $f_u + f_d$ limits any possible inaccuracies in the separation of $\bar{B}^0$ and B^- through the sample composition into the $\ell^- D^0$ and $\ell^- D^+$ final states. The electron and muon samples are fit separately, since the relative lepton efficiencies between electrons and muons are not expected to readily cancel.

9.1 Toy Monte Carlo

Before performing the fit for the relative fragmentation fractions, the fitter is checked for biases with a toy Monte Carlo. Five toy yields are generated in each toy run by smearing the yields measured in the data by a random Gaussian times the measured error, $N_i(\ell D/\Lambda_c^+)_{toy} = N_i(\ell^- D/\Lambda_c^+)_{measured} + r_{Gaussian} \times \sigma_{N_{measured}}$.

To blind the toy analysis to the true sample composition parameters, the predicted number of events in each lepton-charm channel, Eqs. (9.2) and (9.3), for a reference set of composition parameters $\{f_c\}_{ref}$ is rescaled by S_{ref},

$$S_{ref,i} = \frac{N_i(\ell^- D/\Lambda_c^+)_{measured}}{N_i(\ell^- D/\Lambda_c^+; \{f_c\}_{ref}, N_{ref}(\bar{B}^0), ...)_{predicted}}. \tag{9.4}$$

A χ^2-fit to the sample composition parameters is then performed for each toy experiment, with $\chi^2 = (N_i(\ell D/\Lambda_c^+)_{toy} - S_{ref,i}N_i(\ell D/\Lambda_c^+, \{f_c\}_{ref})_{pred})^2/\sigma^2_{N_{meas}}$. The effect is to compare the best fit parameters $\{f_c\}_{toy}$ for each toy experiment to $\{f_c\}_{ref}$ with errors that represent the actual statistical errors in the data fit. The pull distributions of $\{f_c\}$ are checked to see if they are unit-width Gaussians.

The input parameters used to generate the toy are listed in Table 9.1 and the results of 10,000 toy experiments are given in Table 9.2. The fragmentation fraction fit parameters, errors, and pulls are shown for the e+SVT toy Monte Carlo in Figure 9.1. There are no significant biases in the means of any of the pulls. All of the pull widths are consistent with unity.

Fit Parameter	Toy Input
f_u/f_d	1.0
$f_s/(f_u+f_d)$	0.1
$f_{\Lambda_b}/(f_u+f_d)$	0.1
Γ [ps^{-1}]	0.0134
Γ^* [ps^{-1}]	0.0372
Γ^{**} [ps^{-1}]	0.0141
$N(\bar{B}^0)$ (10^9)	2.0

Table 9.1: Inputs used in the generation of the toy Monte Carlo.

	e+SVT		μ+SVT	
Fit Parameter	Pull mean	Pull sigma	Pull mean	Pull sigma
f_u/f_d	-0.006±0.010	1.005±0.007	-0.014±0.010	1.013±0.007
$f_s/(f_u+f_d)$	0.005±0.010	1.004±0.007	0.011±0.010	0.995±0.007
$f_{\Lambda_b}/(f_u+f_d)$	-0.007±0.010	1.000±0.007	-0.011±0.010	1.003±0.007
$N(\bar{B}^0)$ (10^9)	0.001±0.010	1.008±0.007	0.011±0.010	1.011±0.007

Table 9.2: Pull results of 10,000 toy runs.

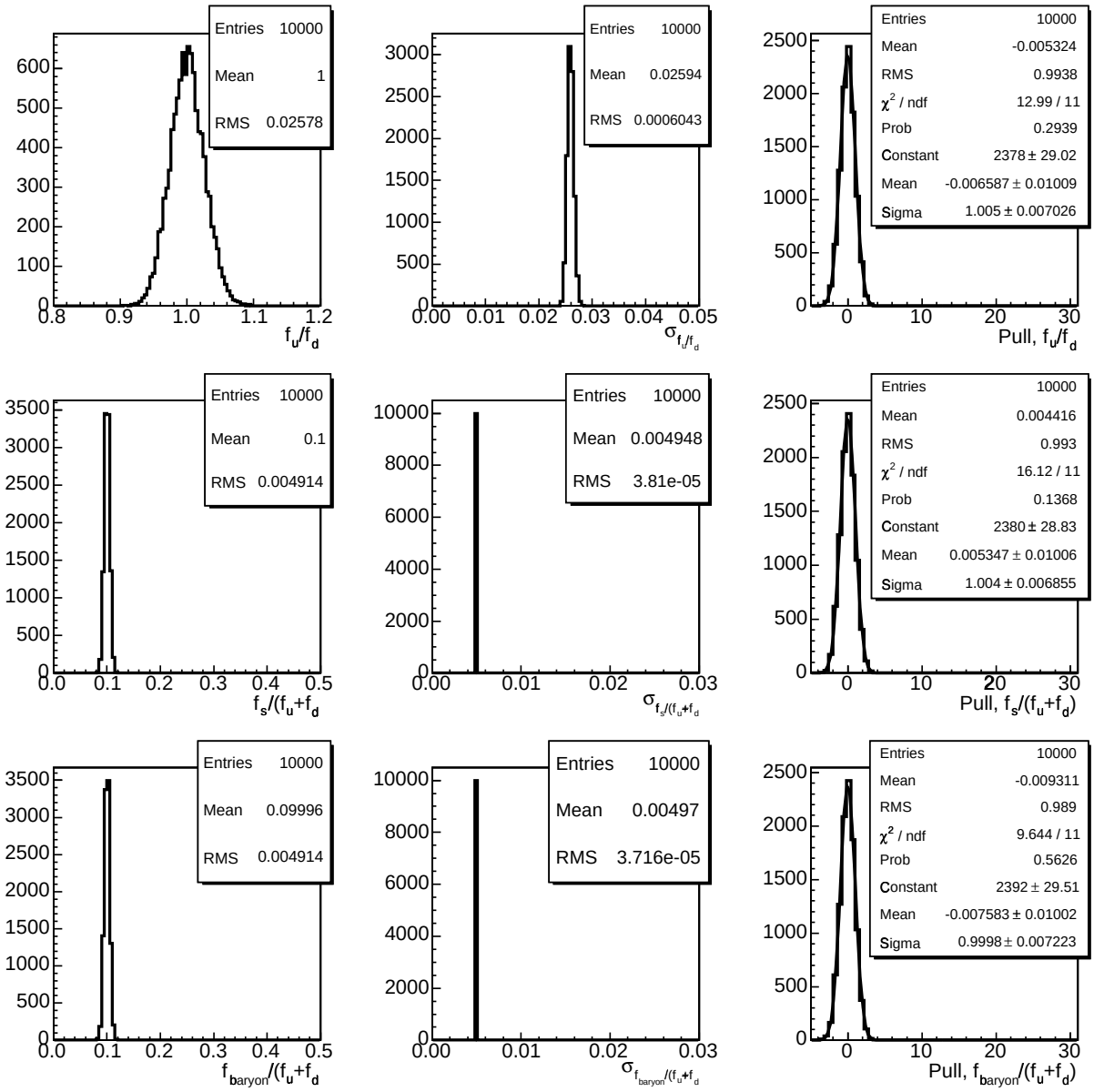

Figure 9.1: e+SVT fit value (left column), error (middle column), and pull (right column) of f_u/f_d (top row), $f_s/(f_u+f_d)$ (middle row), and $f_{\Lambda_b}/(f_u+f_d)$ (bottom row) for 10,000 toy fits where the Γ's are fixed to their PDG values in the fit.

9.2 Fit Results

The results of the fit are listed *with statistical errors only* in Table 9.3. The production of B^- relative to $\bar{B}^0$ is consistent with unity within $\sim 2\,\sigma$. The $\bar{B}_s^0$ production relative to the $\bar{B}^0$ and B^- production is higher than the LEP average measurement of 0.125 [9]. It is lower than the Run I result $f_s/(f_u + f_d) = 0.213 \pm 0.068$, although this result is consistent with the Run I measurement within $\sim 1\,\sigma$. However, $f_{\Lambda_b}/(f_u + f_d)$ is considerably higher than both the LEP results and the CDF Run I result. CDF measured $f_{\Lambda_b}/(f_u + f_d) = 0.118 \pm 0.042$ [7] in Run I and the world average for the measurement from the PDG is 0.128 ± 0.022 [9]. The increase in $f_{\Lambda_b}/(f_u + f_d)$ compared to the Run I and LEP results appears to be due, at least in part, to the softer Λ_b^0 p_T spectrum which has been determined from the lepton-charm semileptonic data. The Run I result used the default `BGenerator` spectrum for all meson and baryon channels, which is much too hard for the $\ell^- \Lambda_c^+$ p_T spectrum observed in the present data. The Run I result was based on a trigger with a $p_T(\ell) > 8$ GeV lepton trigger, which has a higher B p_T threshold than the Run II ℓ+SVT trigger data.

The results for $f_{\Lambda_b}/(f_u + f_d)$ using the three different Monte Carlo p_T spectra discussed in Chapter 8 for the determination of efficiencies are given in Table 9.4. Clearly, $f_{\Lambda_b}/(f_u + f_d)$ depends significantly on the choice of input spectrum used in the Monte Carlo, which determines the relative efficiency of the semileptonic baryon decay relative to the mesons. The best estimate of the spectrum from the data has been used, but since there is no way of knowing the true spectrum, the systematic uncertainty associated with $f_{\Lambda_b}/(f_u + f_d)$ has been estimated conservatively (see Chapter 10).

Fit results for the case when f_u is constrained to be equal to f_d are given in Table 9.5. The result of the fit is also considered when the B meson widths are not required to be equal, as predicted by the spectator model. In this case the rates for which a given B meson decays to a ground, excited, or doubly excited charm meson are individually constrained to the PDG predicted values through χ^2 constraints, as in the standard fit, but the Γ, Γ^*, and Γ^{**} decay widths are allowed to differ between B meson species. The fit results without the spectator model constraints applied are given in Table 9.6.

Using the values for the fragmentation fractions and the sample composition from Table 9.3, the contribution of the different B hadrons into the lepton-charm final states from direct semileptonic B decays are calculated relative to the contribution from the total direct contribution to the lepton-charm signal. The fraction of indirect lepton-charm decays relative to "primary" lepton-charm decays are also determined with the same fit results and both sets of numbers are listed in Table 9.7.

Fit Parameter	e+SVT	μ+SVT
f_u/f_d	1.044±0.028	1.062±0.024
$f_s/(f_u+f_d)$	0.162±0.008	0.158±0.006
$f_{\Lambda_b}/(f_u+f_d)$	0.292±0.020	0.275±0.015
Γ [ps^{-1}]	0.0157±0.0007	0.0154±0.0007
Γ^* [ps^{-1}]	0.0327±0.0014	0.0331±0.0013
Γ^{**} [ps^{-1}]	0.0145±0.0010	0.0146±0.0010
$N(\bar{B}^0)$ (10^9)	2.02±0.07	2.93±0.10

Table 9.3: Fit results *with statistical errors only.*

Fit Parameter	μ+SVT
$[f_{\Lambda_b}/(f_u+f_d)]_{default}$	0.28±0.02
$[f_{\Lambda_b}/(f_u+f_d)]_{hadronic\ \Lambda_b^0}$	0.36±0.02
$[f_{\Lambda_b}/(f_u+f_d)]_{inclusive\ J/\psi}$	0.21±0.01

Table 9.4: $f_{\Lambda_b}/(f_u+f_d)$ *with statistical errors only* for different input p_T spectra.

Fit Parameter	e+SVT	μ+SVT
f_u/f_d	1.0	1.0
$f_s/(f_u+f_d)$	0.163±0.008	0.158±0.006
$f_{\Lambda_b}/(f_u+f_d)$	0.294±0.020	0.277±0.015
Γ [ps^{-1}]	0.0156±0.0007	0.0153±0.0007
Γ^* [ps^{-1}]	0.0330±0.0014	0.0335±0.0013
Γ^{**} [ps^{-1}]	0.0144±0.0010	0.0143±0.0010
$N(\bar{B}^0)$ (10^9)	2.05±0.07	3.00±0.10

Table 9.5: Fit results *with statistical errors only* where $f_u/f_d = 1$.

Fit Parameter	e+SVT	μ+SVT
f_u/f_d	1.006±0.006	1.029±0.006
$f_s/(f_u+f_d)$	0.159±0.010	0.155±0.009
$f_{\Lambda_b}/(f_u+f_d)$	0.297±0.020	0.279±0.014
Γ_{B^0} [ps^{-1}]	0.0158±0.0007	0.0156±0.0007
Γ_{B^+} [ps^{-1}]	0.0133±0.0009	0.0133±0.0008
Γ_{B_s} [ps^{-1}]	0.0134±0.0009	0.0134±0.0009
$\Gamma^*_{B^0}$ [ps^{-1}]	0.0328±0.0014	0.0333±0.0014
$\Gamma^*_{B^+}$ [ps^{-1}]	0.0370±0.0017	0.0368±0.0015
$\Gamma^*_{B_s}$ [ps^{-1}]	0.0371±0.0017	0.0372±0.0017
$\Gamma^{**}_{B^0}$ [ps^{-1}]	0.0142±0.0010	0.0142±0.0009
$\Gamma^{**}_{B^+}$ [ps^{-1}]	0.0144±0.0010	0.0145±0.0010
$\Gamma^{**}_{B_s}$ [ps^{-1}]	0.0141±0.0010	0.0141±0.0010
$N(\bar{B}^0)$ (10^9)	2.03±0.08	3.00±0.10

Table 9.6: Fit results *with statistical errors only* with relaxed spectator model constraints.

Decays	e+SVT (%)	μ+SVT (%)
$\bar{B}^0 \to \ell^- \bar{\nu} D^{(*,**)+}(\ell^- D^+ X)/\sum \bar{B} \to \ell^- D^{(*,**)}(\ell^- D^+ X)$	86.2±1.3	83.1±0.9
$B^- \to \ell^- \bar{\nu} D^{*,**0}(\ell^- D^+ X)/\sum \bar{B} \to \ell^- D^{(*,**)}(\ell^- D^+ X)$	12.7±0.4	15.8±0.3
$\bar{B}^0_s \to \ell^- \bar{\nu} D^{**+}_s(\ell^- D^+ X)/\sum \bar{B} \to \ell^- D^{(*,**)}(\ell^- D^+ X)$	1.0 ±0.1	1.1±0.1
$N(\ell^- D^+)_{indirect}/N(\ell^- D^+)_{direct}$	2.4±0.2	4.8±0.2
$\bar{B}^0 \to \ell^- \bar{\nu} D^{*,**+}(\ell^- D^0 X)/\sum \bar{B} \to \ell^- D^{(*,**)}(\ell^- D^0 X)$	31.0±0.5	31.9±0.4
$B^- \to \ell^- \bar{\nu} D^{(*,**)0}(\ell^- D^0 X)/\sum \bar{B} \to \ell^- D^{(*,**)}(\ell^- D^0 X)$	68.4±0.8	67.2±0.6
$\bar{B}^0_s \to \ell^- \bar{\nu} D^{**+}_s(\ell^- D^0 X)/\sum \bar{B} \to \ell^- D^{(*,**)}(\ell^- D^0 X)$	0.8±0.1	0.9±0.1
$N(\ell^- D^0)_{indirect}/N(\ell^- D^0)_{direct}$	2.3±0.1	4.0±0.1
$B^0 \to \ell^- \bar{\nu} D^{*,**+}(\ell^- D^{*+} X)/\sum B \to \ell^- D^{*,**}(\ell^- D^{*+} X)$	90.5±2.4	89.5±1.8
$B^- \to \ell^- \bar{\nu} D^{**0}(\ell^- D^{*+} X)/\sum \bar{B} \to \ell^- D^{*,**}(\ell^- D^{*+} X)$	8.7±0.6	9.7±0.4
$\bar{B}^0_s \to \ell^- \bar{\nu} D^{**+}_s(\ell^- D^{*+} X)/\sum \bar{B} \to \ell^- D^{*,**}(\ell^- D^{*+} X)$	0.8±0.2	0.8±0.1
$N(\ell^- D^{*+})_{indirect}/N(\ell^- D^{*+})_{direct}$	1.5±0.2	2.3±0.3
$\bar{B}^0_s \to \ell^- \bar{\nu} D^{(*,**)+}_s(\ell^- D^+_s X)/\sum \bar{B} \to \ell^- D^{(*,**)}_s(\ell^- D^+_s X)$	100	100
$N(\ell^- D^+_s)_{indirect}/N(\ell^- D^+_s)_{direct}$	7.9±0.8	16.0±0.9
$\Lambda^0_b \to \ell^- \bar{\nu} \Lambda^{(*,**)+}_c(\ell^- \Lambda^+_c X)/\sum \bar{B} \to \ell^- \Lambda^{(*,**)}_c(\ell^- \Lambda^+_c X)$	100	100
$N(\ell^- \Lambda^+_c)_{indirect}/N(\ell^- \Lambda^+_c)_{direct}$	0.7±0.2	0.9±0.2

Table 9.7: Contributions from various $\bar{B}$ sources into the lepton-charm signals, using the fit results of the fragmentation fractions.

Chapter 10

Systematic Uncertainties

The main uncertainties in the measurement of the relative fragmentation fractions come from the uncertainties in the branching ratios of the charm mesons, which contribute both directly and indirectly to the measurement, and the uncertainty associated with the baryon p_T spectrum, which affects the Monte Carlo efficiency. The uncertainties in the measurement due to the XFT and dE/dx efficiencies are negligible in comparison. The complete list of systematic uncertainties assigned to the fragmentation fractions is given in Table 10.3. A weighted average between the e+SVT and μ+SVT samples is calculated before and after applying a particular systematic variation to determine the systematic uncertainty for a given quantity.

- Wrong Sign Background

  The wrong sign lepton-charm combinations represent several possible backgrounds which may be present in the right sign signals, with a significant contribution to the WS combinations expected to arise from false lepton candidates. Wrong sign signals are present in the data even after the prompt region is removed by requiring $ct^*(\ell^- D) > 200$ μm (see Section 5.2.1). Additionally, some discrepancy is still observed in the $ct^*(\ell^- D)$ comparisons between data and Monte Carlo, possibly indicating a residual background from false leptons. False leptons which originate from a "B"-like hadron (*i.e.* a relatively long-lived particle) are not necessarily represented equally between right sign and wrong sign combinations, as is the case with prompt false leptons. Since the false leptons of concern most likely come from a real $\bar{B}$ in which a hadronic track has been mis-identified as a lepton, they are enhanced in the right sign over the wrong sign lepton-charm combinations.

  This systematic uncertainty is studied by utilizing the large false lepton sample available from the two track trigger (TTT) semileptonic $\bar{B}$ decays, which has approximately five times more $\ell^- D^+$ and $\ell^- D^0$ events than the ℓ+SVT trigger sample. Since the statistics are much greater in the TTT sample and the lepton transverse momentum is lower, a larger sample of false leptons is available for study. This is accomplished by selecting low likelihood leptons [51, 52] in the semileptonic TTT events in which one of the charm daughters is one SVT track and the lepton is the other SVT trigger track [53]. This low-likelihood lepton sample is then used to estimate a scaling factor

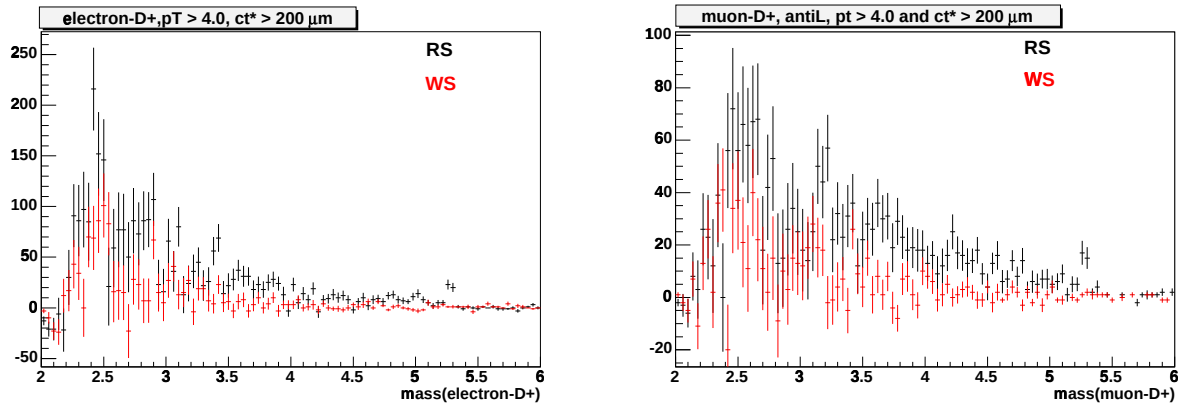

Figure 10.1: $m(\ell^- D^+)$ distributions for right and wrong sign $e^- D^+$ (left) and $\mu^- D^+$ (right) low lepton likelihood samples from the first 360 pb^{-1} of the TTT data.

required to translate the residual wrong sign "signals" in the ℓ+SVT data into an estimate of the false lepton contamination from $\bar{B}$ hadrons in the right sign signals. All of the selection requirements used in this analysis are applied and the number of right sign to wrong sign events are compared assuming that all of the wrong sign signal originates from false leptons of long-lived origin. The $m(\ell^- D^+)$ right sign and wrong sign distributions for false electrons and false muons can be seen in Figure 10.1. The scaling obtained for false leptons from long-lived "B"-like hadrons is $w_{ele} = 2.93 \pm 0.47$ and $w_\mu = 3.91 \pm 0.73$, assuming all of the wrong sign events originate from long-lived sources.

The right sign lepton-charm yields are decreased by the wrong sign yields scaled by the factor appropriate for the e+SVT and μ+SVT datasets. $f_s/(f_u + f_d)$ decreases by 0.001, while f_u/f_d decreases by 0.039 and $f_{\Lambda_b}/(f_u + f_d)$ increases by 0.018, since the $\ell^+ \Lambda_c^+$ has no observable WS signal.

- Variation of Selection Requirements

  The selection requirements have been chosen to be similar across the five lepton-charm channels, so as to cancel as many systematic uncertainties as possible while still respecting the different kinematic features of the decays. To check the dependence of the final result on these selection criteria, the signal selection has been varied such that the $p_T(D)$ cut is applied to all channels, while the $\chi^2_{xy}(D)$ and vertex probability requirements are the same. The varied cuts are given in Table 10.1. f_u/f_d decreases by 0.011, while $f_s/(f_u + f_d)$ increases by 0.0003 and $f_{\Lambda_b}/(f_u + f_d)$ increases by 0.019.

- D_s^+ Reflection in the D^+ Signal

  In addition to residual wrong sign backgrounds, another source of irreducible non-combinatoric background arises from the $D_s^+ \to K^+ K^- \pi^+$ reflection into the $D^+ \to K^- \pi^+ \pi^+$ signal. This has been measured from the data, using the Monte Carlo to scale the expected rates of generic $D_s^+ \to K^- \pi^+ \pi^+$ decays to the $D_s^+ \to \phi \pi^+$ decay (see Section 5.2.1). By default, the D_s^+ reflection is included in the fit to the D^+

Cuts	$\ell^- D^0$	$\ell^- D^{*+}$	$\ell^- D^+$	$\ell^- D_s^+$	$\ell^- \Lambda_c^+$
$ct(\ell^- D/\Lambda_c^+)$ [cm] >	-0.01	-0.01	-0.01	-0.01	-0.01
$ct(\ell^- D/\Lambda_c^+)$ [cm] >	0.10	0.10	0.20	0.10	0.05
$ct^*(\ell^- D/\Lambda_c^+)$ [cm] >	0.02	0.02	0.02	0.02	0.02
$\sigma_{ct}(\ell^- D/\Lambda_c^+)$ [cm] <	0.04	0.04	0.04	0.04	0.04
$m(\ell^- D/\Lambda_c^+)$ [GeV/c^2] >	2.4	2.4	2.4	2.4	3.4
$m(\ell^- D/\Lambda_c^+)$ [GeV/c^2] <	5.1	5.1	5.1	5.1	5.5
p_T(charm) [GeV/c] >	5.0	5.0	5.0	5.0	5.0
$p_T(p)$ [GeV/c] >	N/A	N/A	N/A	N/A	2.0
$p_T(K)$ [GeV/c] >	0.6	0.6	0.6	0.6	0.6
χ^2_{2D}(charm) <	10	10	10	10	10
vtx. prob.(ℓ+charm) >	10^{-7}	10^{-7}	10^{-7}	10^{-7}	10^{-7}
L_{xy}/σ_{Lxy}(charm) >	4.5	4.5	4.5	4.5	4.5
$\Delta m(D^*, D)$ [GeV/c^2] >	N/A	0.1440	N/A	N/A	N/A
$\Delta m(D^*, D)$ [GeV/c^2] <	N/A	0.1475	N/A	N/A	N/A
$\lvert m(\phi) - 1.019\rvert$ [GeV/c^2] <	N/A	N/A	N/A	0.0095	N/A
dE/dx $\mathcal{LR}(p)$ >	N/A	N/A	N/A	N/A	0.3

Table 10.1: Varied signal selection.

signal by constraining the normalization of the D_s^+ reflection within its uncertainty. In order to assign a systematic uncertainty on this method, the normalization of the reflection is allowed to vary both by fixing $N(D_s^+)$ to the number measured from data and also by allowing the $N(D_s^+)$ to float in the fit to the D^+ signal, listed for both scenarios in Table 5.2. The larger effect is observed when $N(D_s^+)$ is a free fit parameter: f_u/f_d increases by 0.0279, while $f_s/(f_u + f_d)$ increases by 0.013 and $f_{\Lambda_b}/(f_u + f_d)$ increases by 0.0046. Fixing the normalization produces a more moderate shift, with f_u/f_d increasing by 0.0014, $f_s/(f_u + f_d)$ increasing by 0.00002, and $f_{\Lambda_b}/(f_u + f_d)$ decreasing by 0.0001. Since the normalization procedure of the $N(D_s^+ \to \phi\pi^+)$ relative to $N(D_s^+ \to K^+K^-\pi^+)$ is, in principle, well-understood from the data and Monte Carlo, the variations obtained from fixing the normalization are taken as the systematic uncertainty associated with this method.

- XFT Efficiencies

  Knowledge of efficiencies which are different for the different particle species is essential for the proper determination of the relative efficiencies between lepton-charm channels. One of these sets of efficiencies are the XFT trigger efficiencies (described in Section 7.1.1), which are not expected to readily cancel in the relative efficiencies between the final state charm signals and cannot be accurately described by the Monte Carlo. The systematic uncertainty on this efficiency is determined by varied the default XFT efficiencies by $1\,\sigma$ of the fit parameters given in Table 7.1. To determine the systematic uncertainty of the shift in the K and π XFT efficiencies, the π efficiency, which has the larger uncertainty of the two, is shifted up or down by the uncertainties

in the XFT parameterizations, while the K efficiency is held constant. The shift in f_u/f_d is ± 0.003, while $f_s/(f_u + f_d)$ varies by ± 0.0004 and $f_{\Lambda_b}/(f_u + f_d)$ increases by 0.003. The systematic uncertainty associated with the proton efficiency is assigned by fitting the efficiency with a constant line [47]. This produces an increase in $f_{\Lambda_b}/(f_u + f_d)$ of 0.005. Since the proton XFT efficiency was evaluated for a previous version of the CDF software and only for data taken before the COT recovery period, the proton XFT efficiency is varied by correcting only data for which a measurement was taken, and applying no proton XFT correction to later data. This produces a decrease in $f_{\Lambda_b}/(f_u + f_d)$ of 0.0116. As this is known to be incorrect, this value does not reflect the proper systematic uncertainty, although it does provide a conservative estimate. In another attempt to quantify the uncertainty on the proton XFT efficiency, the proton parameterization was shifted by the full uncertainty on the fit parameters (all up or all down), which are quite large (often more than half of the central value.) The large uncertainties in the parameterization of the proton XFT efficiency should more than cover other uncertainties about the lack of a measurement for the later data and the use of the newer software release, both of which have little effect on the K and π efficiencies. In this case the variation in $f_{\Lambda_b}/(f_u + f_d)$ is $^{+0.006}_{-0.004}$, which is almost identical to the change from the constant fit to the proton efficiency. A systematic uncertainty of $\pm\sqrt{0.005^2 + 0.003^2} = 0.006$, where $^{+0.006}_{-0.004}$ has been symmetrized to ± 0.005, is assigned to $f_{\Lambda_b}/(f_u + f_d)$ for the uncertainty in the proton, pion, and kaon XFT efficiencies.

- Single Track Efficiency

  The efficiency to add a single track, needed to adjust the two track topology to the three track topology, is measured by reconstructing the $D^0 \to K^-\pi^+\pi^-\pi^+$ relative to the $D^0 \to K^-\pi^+$ (see Section 7.1.2). This method assumes that the two additional pions in the $D^0 \to K3\pi$ decay are uncorrelated. Since the two tracks are identified and pass through different parts of the detector, it is reasonable to make this assumption. The only way the determination of the single track efficiency might be biased by the correlation of the third and fourth tracks arises from vertexing effects. In order to assess the degree of bias that might occur in the vertexing of the $D^0 \to K3\pi$ due to the correlation between the two additional pions, a three track vertex is formed in the $\mu^- D^0 \to K^-\pi^+\pi^-\pi^+$ Monte Carlo and the impact parameter of the fourth track with respect to the three track vertex is determined. If the impact parameter of the fourth track lies outside of $1\,\sigma$ of the error on the vertex or $1\,\sigma$ of the error on the impact parameter, it is assumed that the fourth track could bias the position of the vertex. The distance of the fourth track with respect to the three-track vertex, normalized to the error, σ, on the impact parameter of the fourth track, is shown in Figure 10.2. From this distribution, the impact parameter of the fourth track is found outside $1\,\sigma$ of the three-track vertex $5.3 \pm 0.1\%$ of the time. It is assumed to correspond to good approximation to the degree of correlation in the efficiency of the third and fourth pions. With this estimate of the correlation, f_u/f_d decreases by 0.005, while $f_s/(f_u + f_d)$ and $f_{\Lambda_b}/(f_u + f_d)$ increase by 0.001.

  Another source of uncertainty in the determination of the single track efficiency is the error on the ratio of branching fractions of the two reconstructed D^0 decays, $\mathcal{BR}(D^0 \to$

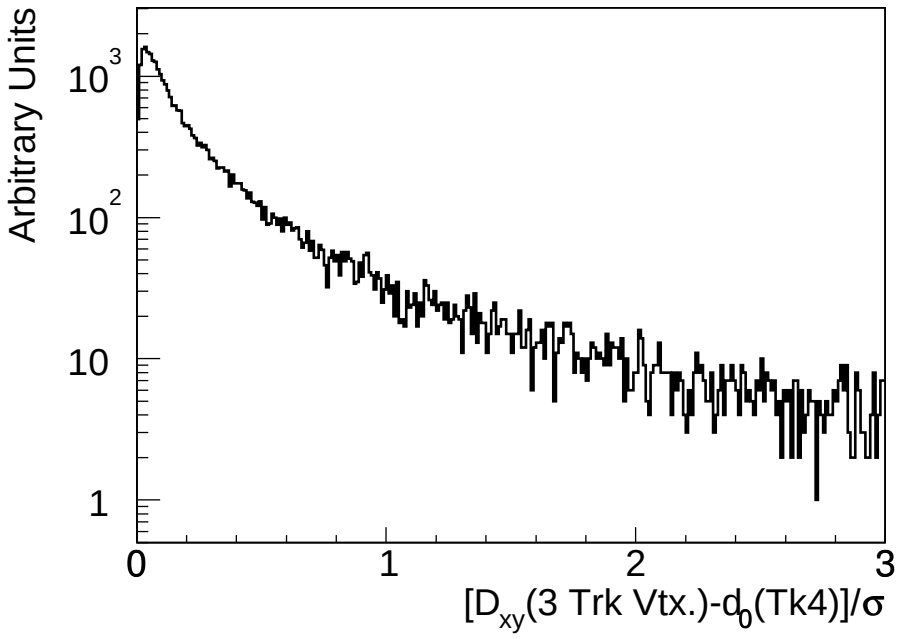

Figure 10.2: Distance between the fourth track in $D^0 \to K^-\pi^+\pi^-\pi^+$ with respect to vertex formed from the other three tracks, relative to larger of the uncertainty on the impact parameter of the fourth track w.r.t the vertex and the uncertainty on the vertex.

$K^-\pi^+\pi^-\pi^+)/\mathcal{BR}(D^0 \to K^-\pi^+) = 2.10 \pm 0.03 \pm 0.06$ [49]. Varying the branching ratio within the quoted uncertainty results in a shift of $^{+0.010}_{-0.016}$ in f_u/f_d. $f_s/(f_u + f_d)$ shifts by $^{+0.003}_{-0.001}$ and $f_{\Lambda_b}/(f_u + f_d)$ varies by ± 0.002.

- dE/dx Efficiency

  Accurate knowledge of the dE/dx cut on the proton in the $\Lambda_c^+ \to pK^-\pi^+$ decays is important for an accurate determination of the $\ell^-\Lambda_c^+$ efficiency relative to the semileptonic meson decays. The effect of the dE/dx efficiency parameterization is checked in three ways: (1) fit the efficiency curve with zeroth order polynomial for those events in which the proton is matched to an XFT track, (2) fit the efficiency curve with a zeroth order polynomial when the proton is not matched to an XFT track, and (3) fit for $f_{\Lambda_b}/(f_u + f_d)$ without applying the dE/dx cut to either the data or the Monte Carlo. Fitting protons matched to XFT tracks with the zeroth order polynomial increases $f_{\Lambda_b}/(f_u + f_d)$ by 0.0172, while fitting protons not matched to XFT tracks decreases $f_{\Lambda_b}/(f_u + f_d)$ by 0.0078. Fitting for $f_{\Lambda_b}/(f_u + f_d)$ without making the dE/dx cut on the proton decreases $f_{\Lambda_b}/(f_u + f_d)$ by 0.0117. The variation without any dE/dx cut applied is chosen as the systematic uncertainty assigned to the dE/dx cut. Variation of the dE/dx cut efficiency does not produce a significant change in either f_u/f_d or $f_s/(f_u + f_d)$.

- Λ_b^0 Polarization

  The polarization of the Λ_b^0 baryon in hadronic collisions is not known. By default, the

Λ_b^0 baryon is generated unpolarized for the Monte Carlo used in this measurement. In order to assign a systematic uncertainty to the possible polarizations of the Λ_b^0, the extreme cases are tested to bound the effect. A systematic uncertainty is assigned when it is fully polarized; when the Λ_b^0 is produced entirely spin up or entirely spin down. Fully polarizing the Λ_b^0 shifts the value of $f_{\Lambda_b}/(f_u+f_d)$ by $^{+0.008}_{-0.006}$, while the other fragmentation fractions are left unchanged.

- Sample Composition Lifetimes

  The $\bar{B}$ meson lifetimes are included in the sample composition relative to the $\bar{B}^0$ lifetime, which is needed to determine the predicted number of lepton-charm mesons (see Chapter 9). As there are uncertainties on the PDG values [9] of the lifetimes used in the fit (listed in Table C.3,) the lifetimes and lifetime ratios are varied in the sample composition within their PDG uncertainties. The central value of the lifetime ratio $\tau(B^-)/\tau(\bar{B}^0) = 1.086 \pm 0.017$ has changed several times in several years and different values are used in the sundry measurements of f_u/f_d. Although the lifetime ratio in the PDG is slightly higher than that used in other measurements of f_u/f_d, the uncertainty on the PDG value covers the central value of the other possible lifetime ratios. The shift in f_u/f_d due to the uncertainty in the lifetime ratio of B^- to $\bar{B}^0$ is $^{+0.018}_{-0.014}$, while the uncertainty in the lifetime ratio of $\tau(\bar{B}_s^0)/\tau(\bar{B}^0) = 0.9512 \pm 0.0381$ contributes a ± 0.006 shift to $f_s/(f_u+f_d)$. No lifetime is input in the fit for the baryon sample composition, although $f_{\Lambda_b}/(f_u+f_d)$ varies by ± 0.002 when $\tau(B^-)/\tau(\bar{B}^0)$ is varied within the PDG uncertainty because the Λ_b^0 fragmentation fraction is measured relative to the $\bar{B}^0$ and B^-.

- Monte Carlo Statistics

  Since a finite number of Monte Carlo events are generated for each exclusive decay in the sample composition (see Chapter 4,) the statistics of the generated Monte Carlo is checked to see whether the statistical uncertainties on the yields, which are used to determine the efficiencies, contribute a significant uncertainty to the measurement. The Monte Carlo yields in each decay are shifted by $\pm\ 1\,\sigma$ around their central values and the efficiencies are re-determined accordingly. All yields are shifted in the same direction, up or down, and then one half are randomly shifted up while the other half are shifted down. In all cases, the shift in all three relative fragmentation fractions is small compared to the other systematic uncertainties. The shift in which half are shifted up and half are shifted down contributes a ± 0.005 shift in f_u/f_d, ± 0.0007 in $f_s/(f_u+f_d)$, and a ± 0.0006 shift on $f_{\Lambda_b}/(f_u+f_d)$, all of which are negligible compared to other source of systematic error.

- Monte Carlo Lifetimes

  Knowledge of the $\bar{B}$ hadron lifetimes is also needed for the generation of the Monte Carlo. While the $\bar{B}^0$ and B^- lifetimes are well-measured, there are large uncertainties on the $\bar{B}_s^0$ and Λ_b^0 lifetimes in the PDG. In order to assign a systematic uncertainty to this effect, the Monte Carlo is re-generated with the $\bar{B}_s^0$ and Λ_b^0 lifetimes shifted by $1\,\sigma$ of the uncertainty on the PDG values: $\tau(\bar{B}_s^0)$=438$\pm$17 μm and $\tau(\Lambda_b^0)$=368$\pm$24 μm.

$f_s/(f_u+f_d)$ varies by $^{+0.005}_{-0.001}$ and $f_{\Lambda_b}/(f_u+f_d)$ varies by $^{+0.0077}_{-0.0136}$. The shift in $f_{\Lambda_b}/(f_u+f_d)$ is one of the largest uncertainties arising from a knowledge of the efficiency, but it is small compared to the uncertainties due to the imprecise knowledge of the baryon branching ratios.

- p_T Spectra

  The "true" $\bar{B}$ hadron p_T spectra are one of the least known aspects of the Monte Carlo generation. It's subsequent contribution to the knowledge of the relative efficiencies of the lepton-charm channels is significant in the determination of the fragmentation fractions. Consequently, the systematic uncertainties arising from the p_T spectra are estimated conservatively, since no definitive measurements for the $\bar{B}_s^0$ and Λ_b^0 are available. The systematic uncertainty assigned to the $\ell^-\Lambda_c^+$ p_T spectrum is taken from the $\pm 2\,\sigma$ variation of the tuned semileptonic Λ_b^0 p_T spectrum described in Section 8.2. This variation produces a $^{+0.039}_{-0.059}$ shift in $f_{\Lambda_b}/(f_u+f_d)$, while producing insignificant shifts in f_u/f_d and $f_s/(f_u+f_d)$. The weighted average of the shifts in the $\ell^-\Lambda_c^+$ data relative to the inclusive J/ψ spectrum is responsible for a larger negative shift than positive shift in this case. Since the p_T spectrum is not well understood, the uncertainty is assigned by averaging the shifts to obtain ± 0.049.

  Although the $\ell^- D_s^+$ spectra agrees well with the inclusive J/ψ spectrum, there is the possibility that the $\bar{B}_s^0$ meson p_T spectrum is also different from the $\bar{B}^0$ and B^- spectra, although the $\bar{B}_s^0$ spectrum is probably not as soft as the Λ_b^0 spectrum. The possibility of a $\bar{B}_s^0$ spectrum which is different from the $\bar{B}^0$ and B^- is accounted for by measuring $f_s/(f_u+f_d)$ with the default `HeavyQuarkGenerator` spectrum input while the B^0 and B^+ are generated with the inclusive J/ψ spectrum. This is a conservative assessment of the error since no significant discrepancy is observed between the $\ell^- D_s^+$ data and the inclusive J/ψ spectrum, as can be seen in Figure 10.3. This conservative variation results in an uncertainty on $f_s/(f_u+f_d)$ of -0.008.

- $\bar{B}$ Branching Ratios

  Systematic uncertainties due to the knowledge of the $\bar{B}$ branching ratios arise in the two places they occur in the sample composition: (1) the indirect contributions ("physics backgrounds") to the lepton-charm signals (*e.g.* $B \to DDX$), many of which are poorly determined experimentally, and (2) the uncertainty in the PDG semileptonic Λ_b^0 branching ratio, $\mathcal{BR}(\Lambda_b^0 \to \ell^-\bar{\nu}\Lambda_c^+ X) = (9.2 \pm 2.1)\%$ [9]. Since many of the measured "physics backgrounds" are poorly determined, the branching ratios predicted from `EvtGen` for the physics backgrounds are used in the sample composition to determine the systematic shift in the fragmentation fractions. Using the `EvtGen` predictions of the branching ratios for the physics backgrounds, which sometimes have very different central values than the PDG values, in the sample composition produces a shift of ± 0.001 in f_u/f_d, ± 0.002 in $f_s/(f_u+f_d)$, and ± 0.001 in $f_{\Lambda_b}/(f_u+f_d)$.

  To determine the systematic uncertainty associated with the inclusive semileptonic Λ_b^0 branching ratio, the PDG value is varied within its uncertainties, giving a $^{+0.076}_{-0.048}$ shift in $f_{\Lambda_b}/(f_u+f_d)$. This is one of the largest systematic uncertainties associated with this quantity.

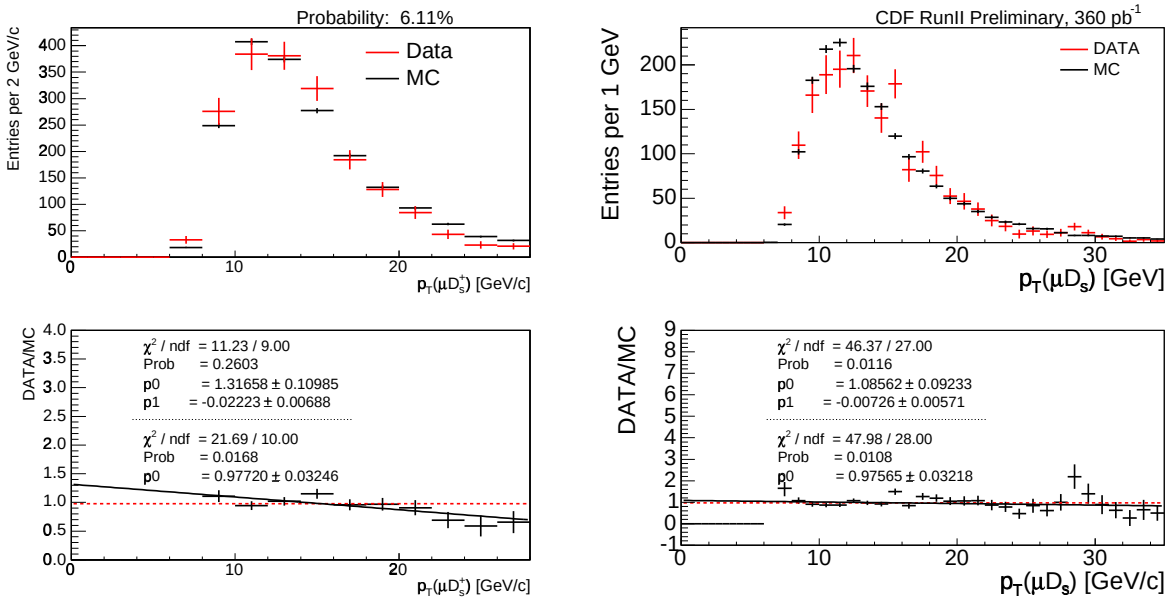

Figure 10.3: $\mu^- D_s^+$ data compared with the `HeavyQuarkGenerator` spectrum (left) and with the inclusive J/ψ p_T spectrum (right).

- Charm Branching Ratios

  Another source of systematic uncertainty due to branching ratios used in the sample composition arises from the often poor knowledge of the ground state charm branching ratios, which are taken from the PDG and listed in Table C.1. To determine the uncertainty in the fragmentation fractions, the central values of the ground state charm branching ratios included in the sample composition are varied, one by one, $\pm 1\,\sigma$ of the PDG uncertainty. The largest shift in f_u/f_d comes from $\mathcal{BR}(D^+ \to K^-\pi^+\pi^+)$, while the single largest uncertainty in $f_s/(f_u+f_d)$ is due to the large error on $\mathcal{BR}(D_s^+ \to \phi\pi^+)$. Poor knowledge of $\mathcal{BR}(\Lambda_c^+ \to pK^-\pi^+)$ also contributes the largest single systematic uncertainty to $f_{\Lambda_b}/(f_u+f_d)$.

  In addition to the poorly measured ground state charm branching ratios, many of the excited charm decays also have large uncertainties. To assess a systematic uncertainty for the limited knowledge of the excited charm decays, the excited charm branching ratios are varied within their error (if known) or by 30% if the branching ratios are unknown. Approximately half of the D^{**} branching ratios are randomly shifted up while the half is shifted down, and the pattern is reversed. f_u/f_d varies by ± 0.001, while $f_s/(f_u+f_d)$ changes by ± 0.003 and $f_{\Lambda_b}/(f_u+f_d)$ varies by ± 0.002. An alternate variation has been obtained by shifting all of the D^{**} branching ratios up or down by 30%, shifting f_u/f_d by ± 0.010, $f_s/(f_u+f_d)$ by ± 0.004, and $f_{\Lambda_b}/(f_u+f_d)$ by ± 0.011. Since most of these branching ratios are very poorly known, the latter shifts are chosen as the systematic uncertainties.

- Λ_b^0 Sample Composition

  A systematic uncertainty is assigned for the uncertain knowledge of the Λ_b^0 sample

Λ_b^0 Decays	$\mathcal{BR}$
$\ell^- \bar{\nu}_\ell \Lambda_c^+$	$(5.66 \pm 0.34)\%$
$\ell^- \bar{\nu}_\ell \Lambda_c(2593)^+$	$(5.53 \pm 0.33) \times 10^{-3}$
$\ell^- \bar{\nu}_\ell \Lambda_c(2625)^+$	$(1.17 \pm 0.07)\%$

Table 10.2: Λ_b^0 baryon sample composition predicted by Pervin *et al.* [28], assuming $\tau_{\Lambda_b^0} = (1.230 \pm 0.074) \times 10^{-12}$ s.

composition (see Chapter 6). By default, the semileptonic branching ratios to the excited $\Lambda_c(2593)^+$ and $\Lambda_c(2625)^+$ measured from CDF data [50] are used in the Λ_b^0 sample composition. The uncertainty on the b-baryon sample composition is estimated using the predictions of the semileptonic Λ_b^0 decay rates to the ground state and excited Λ_c^+'s made by Pervin *et al.* [28], which are listed in Table 10.2. In this variation, the non-resonant semileptonic Λ_b^0 decays are included with the same branching ratios used in the default sample composition. This variation increases $f_{\Lambda_b}/(f_u + f_d)$ by 0.003. A second source of uncertainty due to knowledge of the non-resonant decays has been explored by considering the sample composition without any of the non-resonant baryon modes included. The total semileptonic branching ratio in both cases is required to be $\mathcal{BR}(\Lambda_b^0 \to \ell^- \bar{\nu} \Lambda_c^+ X) = 9.2\%$. This second change decreases $f_{\Lambda_b}/(f_u + f_d)$ by 0.045 and is taken to be the systematic uncertainty on $f_{\Lambda_b}/(f_u + f_d)$.

The total systematic uncertainties due to the knowledge of the relative efficiencies, obtained by adding the individual systematic uncertainties related to the determination of the efficiencies used in the sample composition in quadrature, are $^{+0.025}_{-0.045}$ for f_u/f_d, $^{+0.011}_{-0.010}$ for $f_s/(f_u + f_d)$, and $^{+0.058}_{-0.056}$ for $f_{\Lambda_b}/(f_u + f_d)$. When uncertainties arising from branching ratios are included, the uncertainties increase to $^{+0.062}_{-0.074}$ for f_u/f_d, $^{+0.058}_{-0.035}$ for $f_s/(f_u + f_d)$, and $^{+0.141}_{-0.103}$ for $f_{\Lambda_b}/(f_u + f_d)$.

Systematic	f_u/f_d	$f_s/(f_u+f_d)$	$f_{\Lambda_b}/(f_u+f_d)$
False Leptons	-0.039	-0.001	$+0.018$
Variation of cuts	± 0.011	± 0.0003	± 0.019
D_s^+ reflection	$+0.001$	$+0.00002$	$+0.0001$
XFT eff.	± 0.003	± 0.0004	± 0.006
Single track	$^{+0.013}_{-0.014}$	± 0.002	± 0.002
Sample comp. lifetimes	$^{+0.018}_{-0.014}$	± 0.006	± 0.002
MC lifetimes	-	$^{+0.005}_{-0.001}$	$^{+0.0077}_{-0.0136}$
MC statistics	± 0.005	± 0.0007	± 0.0006
p_T spectra	-	± 0.008	± 0.049
dE/dx eff.	-	-	± 0.012
Λ_b^0 polarization	-	-	± 0.007
Total (eff)	$^{+0.025}_{-0.045}$	$^{+0.011}_{-0.010}$	$^{+0.058}_{-0.056}$
$\mathcal{BR}(\Lambda_b^0 \to \ell^- \bar{\nu} \Lambda_c^+ X)$	-	-	$^{+0.076}_{-0.048}$
Λ_b^0 sample composition	-	-	± 0.045
$\mathcal{BR}(D^{**})$	± 0.010	± 0.004	± 0.011
"physics bkgs"	± 0.001	± 0.002	± 0.001
$\mathcal{BR}(D^+ \to K^- \pi^+ \pi^+)$	± 0.054	± 0.003	± 0.010
$\mathcal{BR}(D^0 \to K^- \pi^+)$	± 0.020	± 0.003	± 0.003
$\mathcal{BR}(D_s^+ \to \phi \pi^+)$	± 0.0006	$^{+0.057}_{-0.034}$	± 0.001
$\mathcal{BR}(\Lambda_c^+ \to p K^- \pi^+)$	-	-	$^{+0.091}_{-0.053}$
Total ($\mathcal{BR}$)	± 0.058	$^{+0.057}_{-0.034}$	$^{+0.128}_{-0.086}$
Total	$^{+0.062}_{-0.074}$	$^{+0.058}_{-0.035}$	$^{+0.141}_{-0.103}$

Table 10.3: List of systematic uncertainties assigned.

Chapter 11

Final Result

The fragmentation fractions in the e+SVT data are measured to be

$$\frac{f_u}{f_d} = 1.044 \pm 0.028(stat) \quad (11.1)$$

$$\frac{f_s}{f_u + f_d} = 0.162 \pm 0.008(stat) \quad (11.2)$$

$$\frac{f_{\Lambda_b}}{f_u + f_d} = 0.292 \pm 0.020(stat), \quad (11.3)$$

and the fragmentation fractions in the μ+SVT data are measured to be

$$\frac{f_u}{f_d} = 1.062 \pm 0.024(stat) \quad (11.4)$$

$$\frac{f_s}{f_u + f_d} = 0.158 \pm 0.006(stat) \quad (11.5)$$

$$\frac{f_{\Lambda_b}}{f_u + f_d} = 0.275 \pm 0.015(stat). \quad (11.6)$$

Calculating the weighted average of the fragmentation fractions for e+SVT and μ+SVT gives,

$$\frac{f_u}{f_d} = 1.054 \pm 0.018(stat)^{+0.025}_{-0.045}(sys) \pm 0.058(\mathcal{BR}) \quad (11.7)$$

$$\frac{f_s}{f_u + f_d} = 0.160 \pm 0.005(stat)^{+0.011}_{-0.010}(sys)^{+0.057}_{-0.034}(\mathcal{BR}) \quad (11.8)$$

$$\frac{f_{\Lambda_b}}{f_u + f_d} = 0.281 \pm 0.012(stat)^{+0.058}_{-0.056}(sys)^{+0.128}_{-0.086}(\mathcal{BR}). \quad (11.9)$$

Since the semileptonic events measured have an effective $p_T(B) > 7.0$ threshold (see Section 8.4), f_q in this text indicates $f_q \equiv f_q(p_T(B) > 7.0$ GeV/c).

11.1 Comparison with Other Results

The $f_s/(f_u+f_d)$ and $f_{\Lambda_b}/(f_u+f_d)$ fragmentation fractions are also quoted without the ground state branching ratio, since the $\mathcal{BR}(D_s^+ \to \phi\pi^+)$ and $\mathcal{BR}(\Lambda_c^+ \to pK^-\pi^+)$ are the largest

sources of uncertainty arising from the knowledge of the branching ratios. Extracting the poorly measured $\mathcal{BR}(D_s^+ \to \phi\pi^+)$ and $\mathcal{BR}(\Lambda_c^+ \to pK^-\pi^+)$ from the results for comparison with the world averages gives

$$\frac{f_s}{f_u + f_d} \times \mathcal{BR}(D_s^+ \to \phi\pi^+) = (5.76 \pm 0.18(stat)^{+0.45}_{-0.42}(sys)) \times 10^{-3}, \quad (11.10)$$

$$\frac{f_{\Lambda_b}}{f_u + f_d} \times \mathcal{BR}(\Lambda_c^+ \to pK^-\pi^+) = (14.1 \pm 0.6(stat)^{+5.3}_{-4.4}(sys)) \times 10^{-3}. \quad (11.11)$$

In addition to the poorly measured charm branching ratio, the semileptonic $\Lambda_b^0 \to \ell^-\bar{\nu}\Lambda_c^+ X$ branching ratio can be factored out from Eq. (11.11),

$$\frac{f_{\Lambda_b}}{f_u + f_d} \times \mathcal{BR}(\Lambda_b^0 \to \ell^-\bar{\nu}\Lambda_c^+ X)\mathcal{BR}(\Lambda_c^+ \to pK^-\pi^+) = (12.9 \pm 0.6(stat) \pm 3.4(sys)) \times 10^{-4}. \quad (11.12)$$

This quantity can be compared more naturally with the LEP results, which quote $f_{\Lambda_b} \times \mathcal{BR}(\Lambda_b^0 \to \ell^-\bar{\nu}\Lambda_c^+) \times \mathcal{BR}(\Lambda_c^+ \to pK^-\pi^+)$ [54, 55]. When all branching ratios with large uncertainties are factored out, as in Eq. (11.12), $f_{\Lambda_b}/(f_u + f_d)$ is $2.3\,\sigma$ higher than the LEP results, assuming that $f_u = f_d = 39.7\%$ at LEP.

The result of this measurement is in agreement with the world averages of the fragmentation fraction of B^- relative to $\bar{B}^0$. The relative fragmentation fractions $f_s/(f_u + f_d)$ and $f_{\Lambda_b}/(f_u + f_d)$ differ from the world averages by $\sim 1\,\sigma$ and $\sim 2\,\sigma$, respectively. The central value of $f_{\Lambda_b}/(f_u + f_d)$ is higher than has previously been measured, either at the Tevatron or at LEP.

There is no particular indication that a higher rate of $\bar{B}_s^0$ production at the Tevatron could be contributing to the anomalous Run I values of $\bar{\chi}$. $f_s/(f_u + f_d)$ is quite compatible with the world averages [9]. The uncertainty on $f_s/(f_u + f_d)$ will significantly improve with an improved measurement of $\mathcal{BR}(D_s^+ \to \phi\pi^+)$, which is expected to be released from the CLEO-c experiment at Cornell in the next several months.

Knowledge of the $f_{\Lambda_b}/(f_u + f_d)$ result will be improved by better measurements of the $\Lambda_c^+ \to pK^-\pi^+$ branching ratio and also the semileptonic $\Lambda_b^0 \to \ell^-\bar{\nu}\Lambda_c^+ X$ branching ratio, in addition to proper measurements of the Λ_b^0 semileptonic sample composition, particularly the measurement of the $\Lambda_b^0 \to \ell^-\bar{\nu}\Lambda_c(2593)^+$ and $\Lambda_b^0 \to \ell^-\bar{\nu}\Lambda_c(2625)^+$ branching ratios. Additionally, a definitive measurement of the p_T spectrum of the Λ_b^0 and $\bar{B}^0$ in fully reconstructed modes will shed light on expected differences in the spectra and significantly reduce the systematic uncertainty.

The $f_{\Lambda_b}/(f_u + f_d)$ result is higher than both the Run I result and the LEP results. Differences between the Run I result include a lower transverse momentum trigger threshold, significantly higher statistics samples of lepton-charm events, consideration of excited Λ_c^+ states in the decay of the $\Lambda_b^0 \to \ell^-\bar{\nu}\Lambda_c^+ X$, a physical decay model for the $\ell^-\Lambda_c^+$ Monte Carlo, and a different p_T spectrum for the Λ_b^0. This measurement uses a trigger which requires a lepton with $p_T > 4$ GeV/c and a track with $p_T > 2$ GeV/c, while the Run I trigger required a lepton with $p_T > 8$ GeV/c. The Run I measurement reconstructed 79 ± 17 $e^-\Lambda_c^+$ events, while this measurement uses $1,755 \pm 106$ $e^-\Lambda_c^+$ events and $2,984 \pm 130$ $\mu^-\Lambda_c^+$ events. A physical decay model is now implemented in the Monte Carlo which is a much better description

of the data than phase space and a semileptonic Λ_b^0 sample composition is used, which was not considered in the Run I measurement. In Run I only the ground state $\Lambda_b^0 \to \ell^- \bar{\nu} \Lambda_c^+$ was included and spectator model assumptions were used to extract the branching ratio. The Run I measurement also did not consider differences in the baryon and meson p_T spectra, partly due to the low statistics in all lepton-charm channels. These appear to be the most salient differences between the two measurements. If the inclusive J/ψ cross-section is used for all p_T spectra including the $\ell^- \Lambda_c^+$ (see Table 9.4), $f_{\Lambda_b}/(f_u + f_d) = 0.21 \pm 0.01(stat)$ in the μ+SVT data, which is closer to the Run I result.

The difference between the $f_{\Lambda_b}/(f_u + f_d)$ result presented in this thesis and the LEP results may be explained by the gluonic environment in $p\bar{p}$ collisions. In addition to this effect, the transverse momenta of the $\bar{B}$ hadrons measured is significantly lower for the data used in this measurement than the $b\bar{b}$ data collected at the Z pole used in the LEP measurements. An interesting extension of the analysis would be to evaluate the behavior of the fragmentation fractions in bins of the lepton-charm p_T. This is difficult to accomplish with any precision at higher momenta for the present dataset, since the statistics are poor for $p_T(\ell^- D/\Lambda_c^+)$ above $\sim$15 GeV/c, but should be possible using a larger dataset of 1 fb^{-1} or more.

Bibliography

[1] S.W. Herb *et al.*, Phys. Rev. Lett. **39** 252 (1977).

[2] B. Andersson *et al.*, Phys. Rept. **97**, 31 (1983);
G.C. Fox, S. Wolfram, Nucl. Phys. **B168**, 285 (1980);
C. Marchesini, B.R. Webber, Nucl .Phys. **B238**, 1 (1984);
T.G. Gottschalk, Nucl. Phys. **B239**, 349 (1984);
R.D. Field, Phys. Lett. **B135**, 203 (1984);
R.D. Field, R.P. Feynman, Nucl. Phys. **B136**, 1 (1978).

[3] See I. Hinchliffe's "Quantum Chromodynamics" Review in [9] and references therein.

[4] H.D. Politzer, Phys. Rev. Lett. **30**, 1346 (1973).

[5] D.J. Gross and F. Wilczek, Phys. Rev. Lett. **30**, 1343 (1973).

[6] See http://www-cdf.fnal.gov/

[7] F. Abe *et al.*, The CDF Collaboration, Phys. Rev. **D54**, 6596 (1996);
F. Abe *et al.*, The CDF Collaboration, Phys. Rev. **D60**, 092005 (1999);
T. Affolder *et al.*, The CDF Collaboration, Phys. Rev. Lett. **84**, 1663 (2000).

[8] D. Buskulic *et al.*, ALEPH Collaboration, Phys. Lett. **B361**, 221 (1995);
P. Abreu *et al.*,DELPHI Collaboration, Phys. Lett. **B289**, 199 (1992);
P.D. Acton *et al.*,OPAL Collaboration, Phys Lett **B295**, 357 (1992).

[9] S. Eidelman *et al.*, Particle Data Group, Phys. Lett. **B592**, 1 (2004).

[10] F. Abe *et al.*, The CDF Collaboration, Phys. Rev. **D55**, 2546 (1997);
D. Acosta *et al.*, The CDF Collaboration, Phys. Rev. **D69**, 012002 (2004).

[11] The ALEPH, DELPHI, L3, OPAL, and SLD Collaborations,
LEP Electroweak Working Group, SLD Electroweak Group, and SLD Heavy Flavour Group; hep-ex/0509008 (2005).

[12] E. Berger *et al.*, Phys. Rev. Lett. **86**,4231 (2001).

[13] See for example J. Schwinger, Quantum Mechanics, Dover Publications Inc., New York (1958).

[14] S. Weinberg, Phys. Rev. Lett. **19**. 1264 (1967);
A. Salam, Elementary Particle Theory, ed. N. Svartholm, Almquist and Wilsells, Stockholm, p. 367 (1969);
S.L. Glashow, J. Iliopoulos, and L. Maiani, Phys. Rev. **D2**,1285 (1970).

[15] See B. Kayser's "Neutrino Mass, Mixing, and Flavor Change" Review in [9] and references therein.

[16] Peter W. Higgs, Phys. Rev. Lett. **13**, 508 (1964);.

[17] R. K. Ellis, W. J. Stirling, and B. R. Webber, QCD and Collider Physics, Cambridge University Press, Cambridge, UK (1996).

[18] M. Gell-Mann, Phys. Rev. Lett. **12**, 155 (1964).

[19] N. K. Nielsen, Am. J. Phys. **49**, 1171 (1981);
R. J. Hughes, Phys. Lett. **B97**, 246 (1980); Nucl. Phys. **B186**, 376 (1981);
K. Johnson, Asymptotic Realms of Physics, ed. by A. Guth, K. Huang, and R. L. Jaffe, MIT Press, Cambridge, MA (1983).

[20] M. Kobayashi and T. Maskawa, Prog. Theor. Phys. **49**, 652 (1973);
N. Cabibbo, Phys. Rev. Lett. **10**, 531 (1963).

[21] L. Wolfenstein, Phys. Rev. Lett. **51**, 1945 (1983).

[22] See for example Aneesh Manohar and Mark B. Wise, Heavy Quark Physics, Cambridge University Press, Cambridge, UK (2000).

[23] R.D. Field, Phys. Rev. **D65**, 094006 (2002).

[24] C. Peterson, D. Schlatter, I. Schmitt, Peter M. Zerwas (SLAC), Phys. Rev. **D27**, 105 (1983).

[25] Anthony Allen Affolder (UC, Berkeley). UMI-30-82087, UMI-30-82087-MC, FERMILAB-THESIS-2002-18, (2002).

[26] N. Isgur, D. Scora, B. Grinstein, and M.B. Wise, Phys. Rev. D**39**, 799 (1989).

[27] N. Isgur and M.B. Wise, Phys. Rev. **D43**, 819 (1991).

[28] M. Pervin, S. Capstick, and W. Roberts, Phys. Rev. C**72**, 035201 (2005).

[29] M.B. Voloshin and M.A. Shiffman, Yad. Fiz. **45**, 743 (1987) [Sov J. Nucl Phys. **45**, 463 (1987)];
H.D. Politzer and M.B. Wise, Phys. Lett. **B206**, 681 (1988); **208**. 504 (1988).

[30] A. Falk, H. Georgi, B. Grinstein, and M.B. Wise, Nucl. Phys. **B343** 1 (1990).

[31] W. Rarita and J.S. Schwinger, Phys. Rev. **60**, 60 (1941).

[32] Hartmut Pilkuhn, Relativistic Particle Physics, Springer Verlag, New York, NY (1979).

[33] See http://www-d0.fnal.gov/

[34] R. Blair *et al.*, CDF-II Collaboration, FERMILAB-PUB-96-390-E, (1996).

[35] L. Balka *et al.*, The CDF Collaboration, Nucl. Instrum. Meth. **A267** 272 (1988).

[36] S. Bertolucci *et al.*, The CDF Collaboration, Nucl. Instrum. Meth. **A267** 301 (1988).

[37] S. Gromoll, Ch. Paus, A Heavy Quark Generator, CDF internal note 5985, (2002).

[38] D.J. Lange, Nucl. Instrum. Meth. A**462**, 152 (2001).

[39] See http://wwwasdoc.web.cern.ch/wwwasdoc/geant_html3/geantall.html

[40] D. Acosta *et al.*, The CDF Collaboration, Phys. Rev. **D71**, 032001 (2005).

[41] J.L. Goity and W. Roberts, Phys. Rev. **D51** 3459 (1995).

[42] See http://www-public.slac.stanford.edu/babar/

[43] A.K. Leibovich and I.W. Stewart, Phys. Rev. **D57**, 5620 (1998).

[44] P. Billoir and S. Qian, Nucl. Instrum. Meth. A**294**, 219 (1990).

[45] See http://www-cdf.fnal.gov/cdfnotes/cdf1996_scanned.pdf

[46] D. Acosta *et al.*, The CDF Collaboration, Phys. Rev. Lett.**94**, 122001 (2005).

[47] A. Abulencia *et al.*, The CDF Collaboration, Submitted to Phys. Rev. Lett., [arXiv:hep-ex/0601003].

[48] A. Abulencia *et al.*, The CDF Collaboration, Phys. Rev. Lett. **96**, 191801 (2006).

[49] Q. He *et al.*, The CLEO Collaboration, Phys. Rev. Lett. **95**, 121801 (2005).

[50] Shin-shan Yu (Pennsylvania U.), FERMILAB-THESIS-2005-11, UMI-31-65771, UMI-31-65771-MC (2005).

[51] See http://www-cdf.fnal.gov/physics/new/bottom/072204.blessed-like-mu-tag/

[52] See http://www-cdf.fnal.gov/physics/new/bottom/081204.blessed-like-el-tag/

[53] See http://www-cdf.fnal.gov/physics/new/bottom/051020.semi_Bsmix/

[54] R. Barate *et al.*, ALEPH Collaboration, Eur. Phys. J. C**2**, 197 (1998);
P. Abreu *et al.*, DELPHI Collaboration, Z. Phys. C**68**, 375 (1995).

[55] Heavy Flavor Averaging Group (HFAG), www.slac.stanford.edu/xorg/hfag/.

Appendix A

Signal Optimization

The lepton-charm signals are optimized by using signal (S) distributions from inclusive $B \to \ell^- \bar{\nu} DX$ Monte Carlo samples and the background (B) distributions from the sidebands of the data. The figure of merit (FOM) used in the optimization is $S/\sqrt{S+B}$.

The electron and muon signals are optimized separately to allow for possible differences in electron and muon behavior in the detector, though very little difference in the optimal points is observed. Some cuts are applied without optimization. For instance, $ct(D/\Lambda_c^+)$ and $\sigma_{ct}(\ell^- D/\Lambda_c^+)$ cuts are determined from Monte Carlo before optimizing the other cuts. Two optimization passes have been made for both muons and electrons. In the first pass, the signals are optimized without removing the prompt background discussed in Section 5.2.1. This optimization is accomplished by first optimizing each cut individually to obtain a starting set of cuts, and then optimizing the N-1 set of optimal cuts. In order to obtain an accurate prediction of the significance of the cuts, the Monte Carlo signal yield is scaled to the yield obtained in data for this initial set of cuts. The optimized selections and yields without the $ct^*(\ell^- D/\Lambda_c^+)$ cut are given in Tables A.1-A.3. In the second optimization, the signals are re-optimized with the requirement that $ct^*(\ell^- D/\Lambda_c^+) > 200$ μm applied to all channels and the $p_T(D^0) > 5$ GeV/c cut applied *a priori* to check that the optimal values of the cuts are not considerably altered. In this case, the optimal values from the initial optimization are used as a starting point and only the N-1 optimization is performed. Optimization plots for the $\mu^- D/\Lambda_c^+$ signals requiring $ct^*(\mu D/\Lambda_c^+) > 200$ μm cut are shown in Figures A.1-A.4. The two sets of optimal cuts are quite similar, though a looser lepton-charm vertex probability cut is preferred when the prompt background is removed. Optimized selections and yields with the $ct^*(\ell^- D/\Lambda_c^+)$ cut are listed in Tables A.4-A.6. Several possible cuts were investigated (*e.g.* a helicity cut on the ϕ or $p_t(\ell D)$), but were not selected for the final optimal cuts as no value of the cut improved the significance.

Cuts	e^-D^0	e^-D^{*+}	e^-D^+	$e^-D_s^+$	$e^-\Lambda_c^+$
$ct(D/\Lambda_c^+)$ [cm] >	-0.01	-0.01	-0.01	-0.01	-0.01
$ct(D/\Lambda_c^+)$ [cm] <	0.10	0.10	0.20	0.10	0.05
$\sigma_{ct}(e^-D/\Lambda_c^+)$ [cm] <	0.04	0.04	0.04	0.04	0.04
$m(e^-D/\Lambda_c^+)$ [GeV] >	2.4	2.4	2.5	2.4	3.5
$m(e^-D/\Lambda_c^+)$ [GeV] <	5.0	5.0	5.1	5.1	5.3
$p_T(p)$ [GeV] >	N/A	N/A	N/A	N/A	1.8
$p_T(K)$ [GeV] >	0.5	0.5	0.7	0.6	0.6
$\chi^2_{2D}(D/\Lambda_c^+)$ <	10	10	8	10	5
vtx. prob.(e^-D/Λ_c^+) >	10^{-7}	10^{-7}	10^{-5}	10^{-7}	10^{-4}
$L_{xy}/\sigma_{Lxy}(D/\Lambda_c^+)$ >	5.5	5.5	10	5	5
$\lvert m(K^+K^-) - 1.019\rvert$ [GeV]>	N/A	N/A	N/A	0.0095	N/A
$\lvert cos(\zeta)\rvert$ >	N/A	N/A	N/A	0.25	N/A
$\Delta m(D^*, D)$ [GeV/c^2] >	N/A	0.1440	N/A	N/A	N/A
$\Delta m(D^*, D)$ [GeV/c^2] <	N/A	0.1475	N/A	N/A	N/A

Table A.1: e+SVT optimized signal selection without $ct^*(e^-D/\Lambda_c^+)$ cut applied. ζ is the helicity angle between the K^+ and D_s^+ in the ϕ rest frame.

Cuts	μ^-D^0	μ^-D^{*+}	μ^-D^+	$\mu^-D_s^+$	$\mu^-\Lambda_c^+$
$ct(D/\Lambda_c^+)$ [cm] >	-0.01	-0.01	-0.01	-0.01	-0.01
$ct(D/\Lambda_c^+)$ [cm] <	0.10	0.10	0.20	0.10	0.05
$\sigma_{ct}(\mu^-D/\Lambda_c^+)$ [cm] <	0.04	0.04	0.04	0.04	0.04
$m(\mu^-D/\Lambda_c^+)$ [GeV] >	2.4	2.4	2.6	2.6	3.5
$m(\mu^-D/\Lambda_c^+)$ [GeV] <	5.0	5.0	5.1	5.2	5.4
$p_T(p)$ [GeV] >	N/A	N/A	N/A	N/A	1.8
$p_T(K)$ [GeV] >	0.5	0.5	0.7	0.6	0.6
$\chi^2_{2D}(D/\Lambda_c^+)$ <	10	10	7	10	5
vtx. prob.(μ^-D/Λ_c^+) >	10^{-5}	10^{-5}	10^{-5}	10^{-7}	10^{-4}
$L_{xy}/\sigma_{Lxy}(D)$ >	5.5	5.5	10	5	4.5
$\lvert m(K^+K^-) - 1.019\rvert$ [GeV]>	N/A	N/A	N/A	0.0085	N/A
$\lvert cos(\zeta)\rvert$ >	N/A	N/A	N/A	0.25	N/A
$\Delta m(D^*, D)$ [GeV/c^2] >	N/A	0.1440	N/A	N/A	N/A
$\Delta m(D^*, D)$ [GeV/c^2] <	N/A	0.1475	N/A	N/A	N/A

Table A.2: μ+SVT optimized signal selection without $ct^*(\mu D/\Lambda_c^+)$ cut applied. ζ is the helicity angle between the K^+ and D_s^+ in the ϕ rest frame.

	e+SVT			μ+SVT		
Decay	Yield	FOM	S/B	Yield	FOM	S/B
$\ell^- D^0$	48,238±333	198	5.33	63,153±361	227	5.59
$\ell^- D^{*+}$	5,559±86	73.1	25.9	7,686±97	86.5	38.7
$\ell^- D^+$	19,955±228	120	2.62	27,071±272	138	2.41
$\ell^- D_s^+$	1,750±59	35.8	3.23	2,500±78	42.2	2.97
$\ell^- \Lambda_c^+$	4,088±161	27.6	0.23	5,651±187	33.2	0.24

Table A.3: Signal yields for optimized cuts without the $ct^*(\ell D/\Lambda_c^+)$ cut applied.

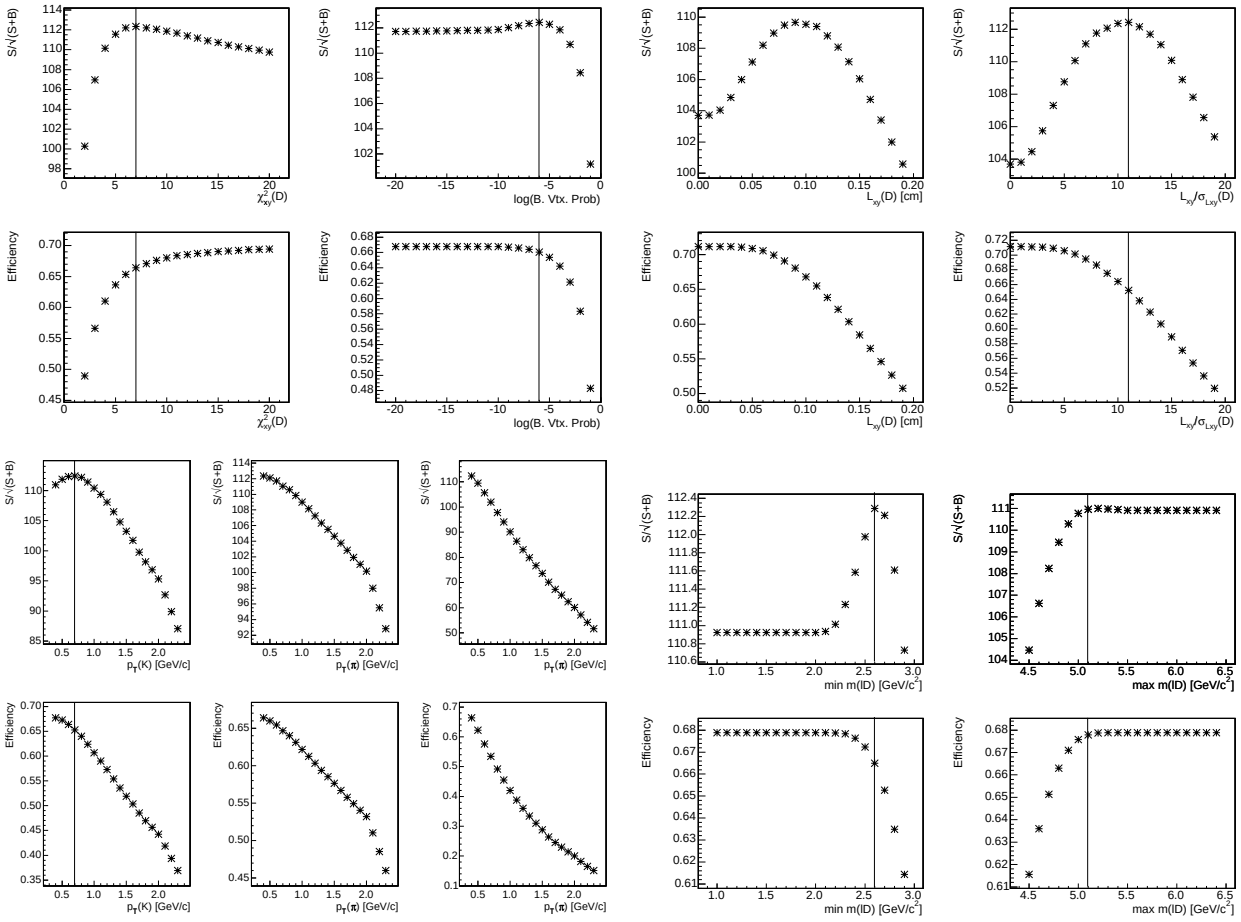

Figure A.1: $\mu^- D^+$ optimization and MC signal efficiency with $ct^*(\mu^- D^+) > 200$ μm for (top, left to right) $\chi^2(D^+)$, B vertex probability, $L_{xy}(P.V. \to D^+)$ and $L_{xy}(P.V. \to D^+)$ significance, (middle, left to right) $p_T(K^-)$, $p_T(\pi^+)$, $p_T(\pi^+)$, and lower and upper $m(\mu^- D^+)$ cuts.

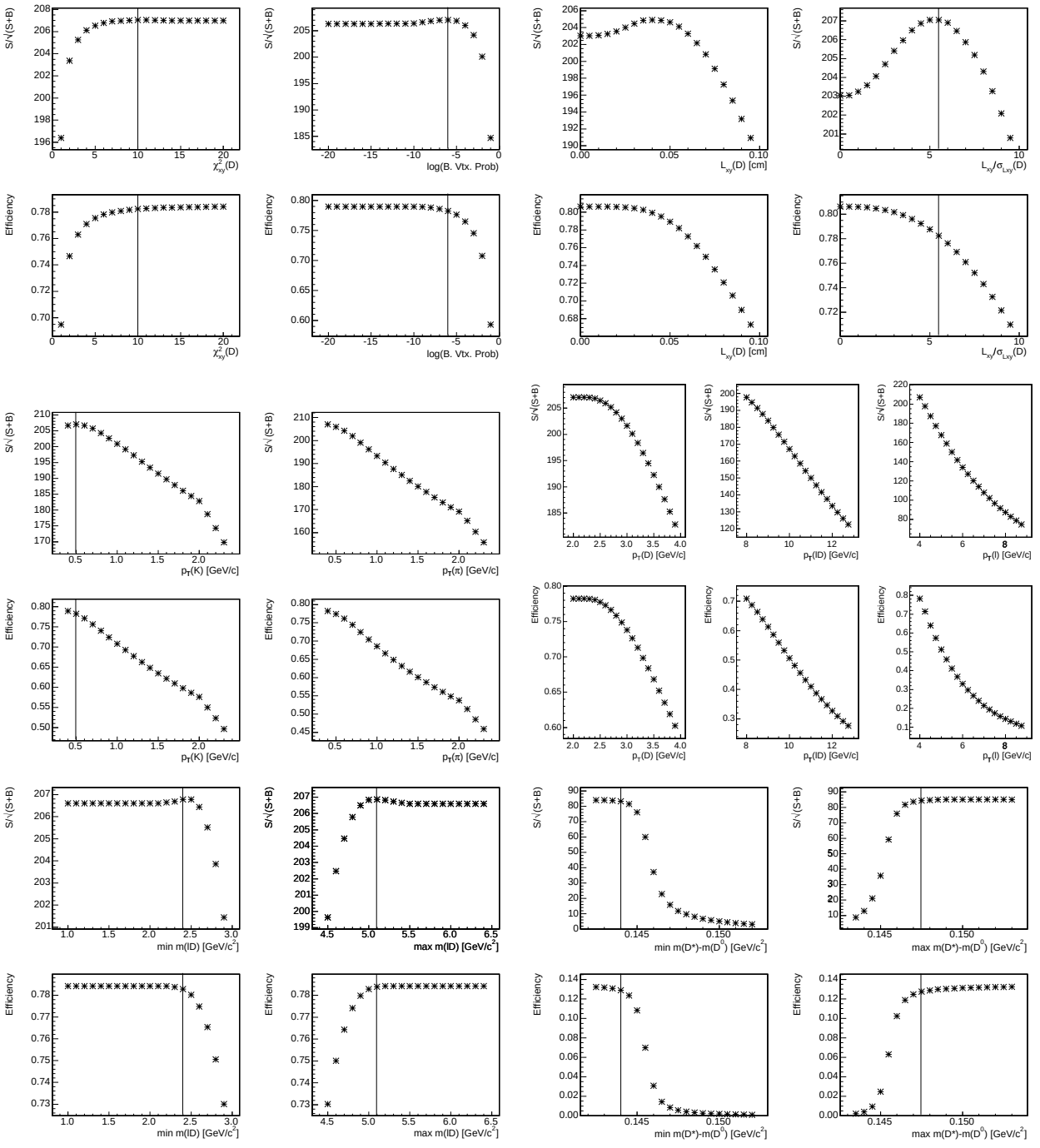

Figure A.2: $\mu^- D^0$ optimization and MC signal efficiency with $ct^*(\mu^- D^0) > 200$ μm for (top, left to right) $\chi^2(D^0)$, $\mu^- D^0$ vertex probability, $L_{xy}(P.V. \to D^0)$ and $L_{xy}(P.V. \to D^0)$ significance, (middle, left to right) $p_T(K^-)$, $p_T(\pi^+)$, $p_T(D^0)$, $p_T(\mu^- D^0)$, and $p_T(\mu^-)$, and (bottom, left to right) lower and upper $m(\mu^- D^0)$ cuts and $\Delta m(D^* - D^0)$ lower and upper cuts.

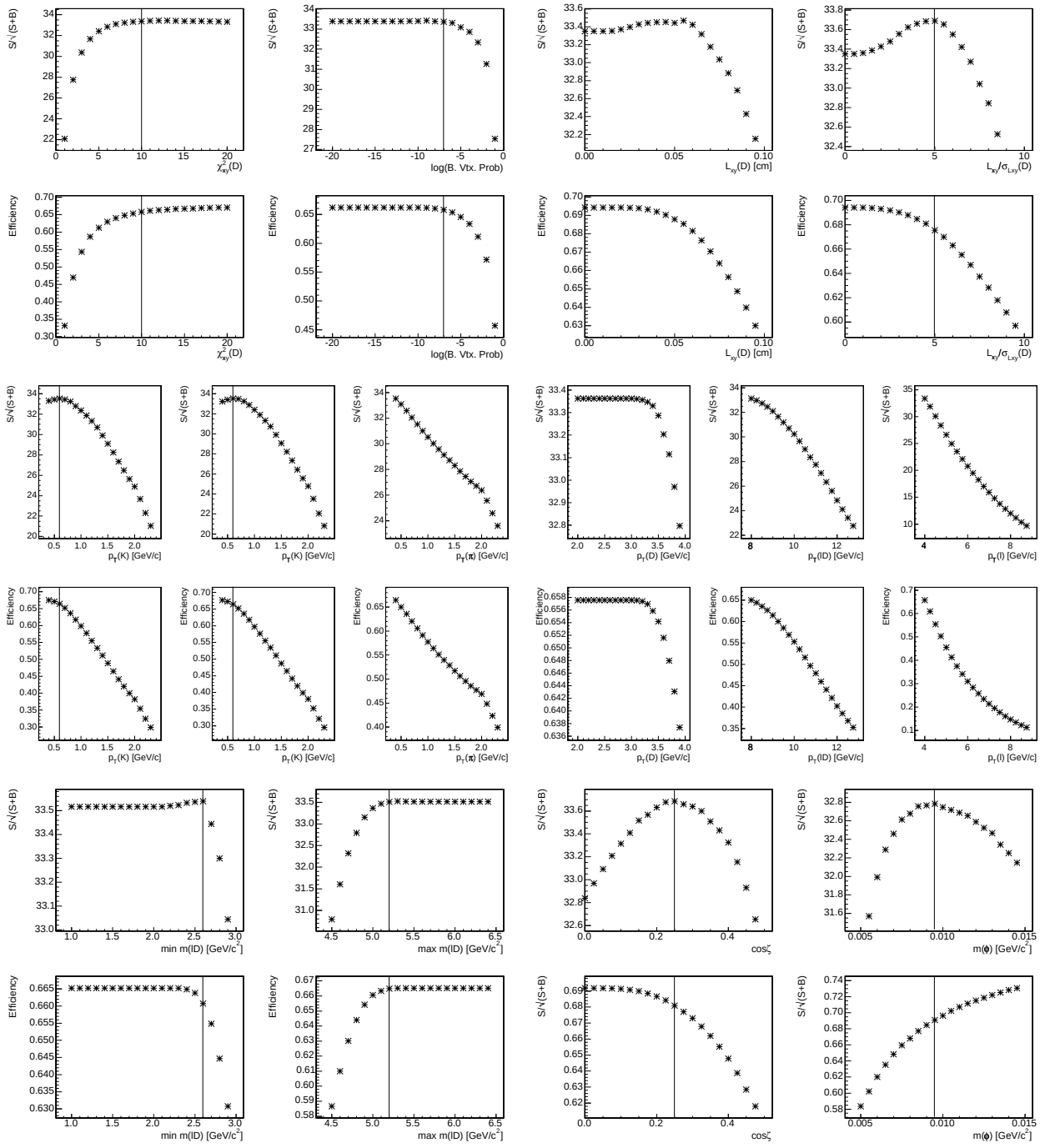

Figure A.3: $\mu^- D_s^+$ optimization and MC signal efficiency with $ct^*(\mu^- D_s^+) > 200$ μm for (top, left to right) $\chi^2(D_s^+)$, $\mu^- D_s^+$ vertex probability, $L_{xy}(P.V. \rightarrow D_s^+)$ and $L_{xy}(P.V. \rightarrow D_s^+)$ significance, (middle, left to right) $p_T(K^+)$,$p_T(K^-)$, $p_T(\pi^+)$, $p_T(D_s^+)$, $p_T(\mu^- D_s^+)$, and $p_T(\mu^-)$, and (bottom, left to right) $m(\mu^- D_s^+)$ lower and upper cuts, $|cos(\zeta)|$, where ζ is the helicity angle between the K^+ and D_s^+ in the ϕ rest frame, and $|m(\phi) - 1.019|$ cut.

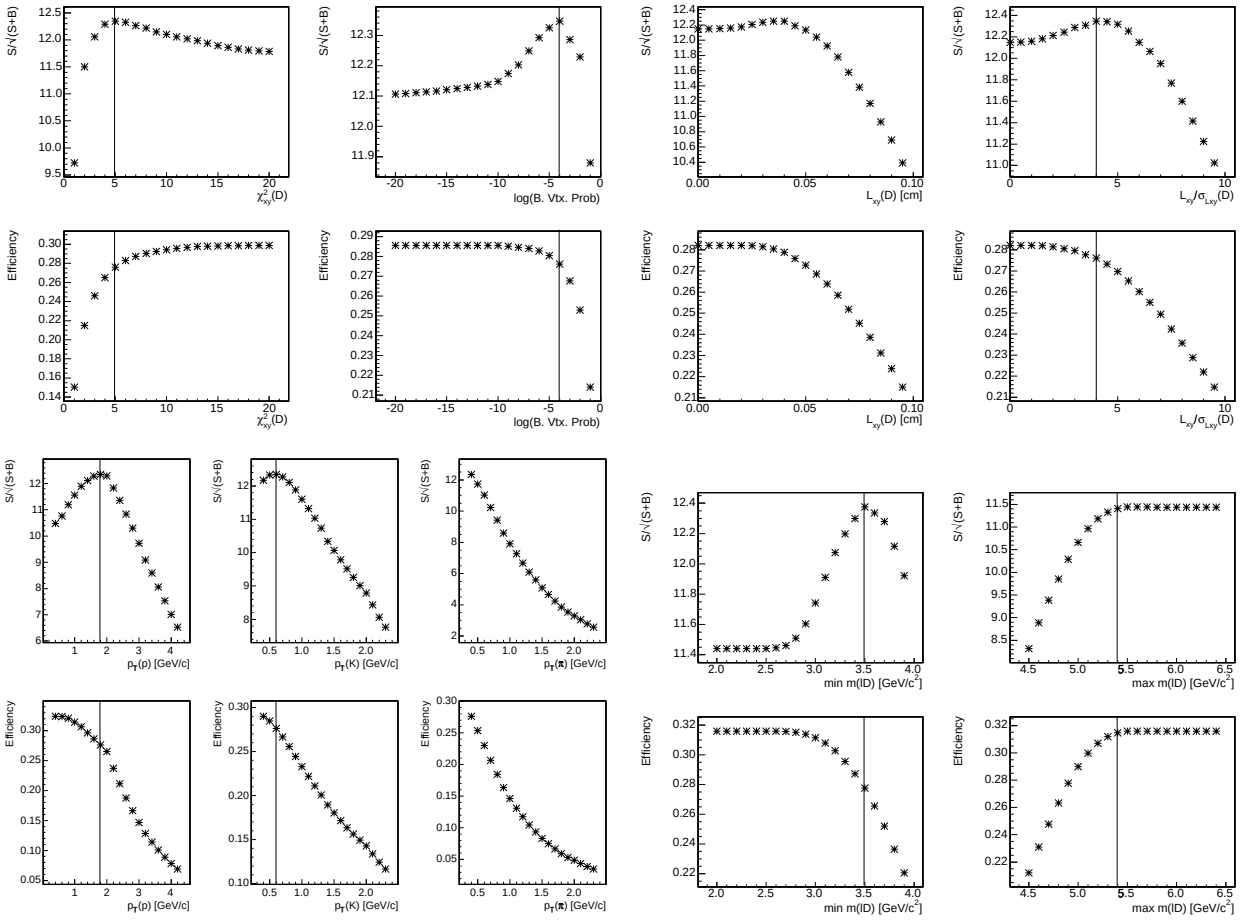

Figure A.4: $\mu^-\Lambda_c^+$ optimization and MC signal efficiency with $ct^*(\mu^-\Lambda_c^+) > 200$ μm for (top, left to right) $\chi^2(\Lambda_c^+)$, $\mu^-\Lambda_c^+$ vertex probability, $L_{xy}(P.V. \rightarrow \Lambda_c^+)$ and $L_{xy}(P.V. \rightarrow \Lambda_c^+)$ significance, (middle, left to right) $p_T(p)$, $p_T(K^-)$, $p_T(\pi^+)$, and lower and upper $m(\mu^-\Lambda_c^+)$ cuts.

Cuts	e^-D^0	e^-D^{*+}	e^-D^+	$e^-D_s^+$	$e^-\Lambda_c^+$
$ct(D/\Lambda_c^+)$ [cm] >	-0.01	-0.01	-0.01	-0.01	-0.01
$ct(D/\Lambda_c^+)$ [cm] <	0.10	0.10	0.20	0.10	0.05
$ct(e^-D/\Lambda_c^+)$ [cm] >	0.02	0.02	0.02	0.02	0.02
$\sigma_{ct}(e^-D/\Lambda_c^+)$ [cm] <	0.04	0.04	0.04	0.04	0.04
$m(e^-D/\Lambda_c^+)$ [GeV] >	2.4	2.4	2.5	2.4	3.4
$m(e^-D/\Lambda_c^+)$ [GeV] <	5.1	5.1	5.1	5.2	5.3
$p_T(D/\Lambda_c^+)$ [GeV] >	5	N/A	N/A	N/A	N/A
$p_T(p)$ [GeV] >	N/A	N/A	N/A	N/A	1.8
$p_T(K)$ [GeV] >	0.6	0.5	0.6	0.6	0.6
$\chi^2_{2D}(D/\Lambda_c^+)$ <	10	10	9	10	5
vtx. prob.(e^-D/Λ_c^+) >	10^{-7}	10^{-7}	10^{-6}	10^{-7}	10^{-5}
$L_{xy}/\sigma_{Lxy}(D)$ >	4	5.5	11	4.5	4
$\lvert m(K^+K^-) - 1.019\rvert$ [GeV]>	N/A	N/A	N/A	0.0095	N/A
$\lvert cos(\zeta)\rvert$ >	N/A	N/A	N/A	0.25	N/A
$\Delta m(D^*, D)$ [GeV/c^2] >	N/A	0.1440	N/A	N/A	N/A
$\Delta m(D^*, D)$ [GeV/c^2] <	N/A	0.1475	N/A	N/A	N/A

Table A.4: e+SVT optimized signal selection with $ct^*(e^-D/\Lambda_c^+)$ and $p_T(D^0)$ cuts applied. ζ is the helicity angle between the K^+ and D_s^+ in the ϕ rest frame.

Cuts	μD^0	μ^-D^{*+}	μ^-D^+	$\mu^-D_s^+$	$\mu^-\Lambda_c^+$
$ct(D/\Lambda_c^+)$ [cm] >	-0.01	-0.01	-0.01	-0.01	-0.01
$ct(D/\Lambda_c^+)$ [cm] <	0.10	0.10	0.20	0.10	0.05
$ct(\mu^-D/\Lambda_c^+)$ [cm] >	0.02	0.02	0.02	0.02	0.02
$\sigma_{ct}(\mu^-D/\Lambda_c^+)$ [cm] <	0.04	0.04	0.04	0.04	0.04
$m(\mu^-D/\Lambda_c^+)$ [GeV] >	2.4	2.4	2.6	2.6	3.5
$m(\mu^-D/\Lambda_c^+)$ [GeV] <	5.1	5.1	5.1	5.2	5.4
$p_T(D/\Lambda_c^+)$ [GeV] >	5	N/A	N/A	N/A	N/A
$p_T(p)$ [GeV] >	N/A	N/A	N/A	N/A	1.8
$p_T(K)$ [GeV] >	0.6	0.5	0.7	0.6	0.6
$\chi^2_{2D}(D/\Lambda_c^+)$ <	10	10	7	10	5
vtx. prob.(μ^-D/Λ_c^+) >	10^{-7}	10^{-6}	10^{-6}	10^{-7}	10^{-4}
$L_{xy}/\sigma_{Lxy}(D)$ >	5	5.5	11	5	4
$\lvert m(K^+K^-) - 1.019\rvert$ [GeV]>	N/A	N/A	N/A	0.0095	N/A
$\lvert cos(\zeta)\rvert$ >	N/A	N/A	N/A	0.25	N/A
$\Delta m(D^*, D)$ [GeV/c^2] >	N/A	0.1440	N/A	N/A	N/A
$\Delta m(D^*, D)$ [GeV/c^2] <	N/A	0.1475	N/A	N/A	N/A

Table A.5: μ+SVT optimized signal selection with $ct^*(\mu^-D/\Lambda_c^+)$ and $p_T(D^0)$ cuts applied. ζ is the helicity angle between the K^+ and D_s^+ in the ϕ rest frame.

	e+SVT			μ+SVT		
Decay	Yield	FOM	S/B	Yield	FOM	S/B
$\ell^- D^0$	23,640±251	143	8.21	31,483±266	163	7.12
$\ell^- D^{*+}$	4,589±79	66.5	27.2	6,320±88	78.5	40.5
$\ell^- D^+$	15,463±192	106	2.64	20,288±272	117	2.07
$\ell^- D_s^+$	1,434±53	32.5	3.16	2,079±71	38.0	2.97
$\ell^- \Lambda_c^+$	3,781±144	28.7	0.28	5,301±165	34.7	0.29

Table A.6: Signal yields for optimized cuts with the $ct^*(\ell^- D/\Lambda_c^+)$ and $p_T(D^0)$ cuts applied.

Appendix B

Selection of dE/dx Control Samples

$\mu^- D^{*+}$ and $\mu^-\Lambda$ control samples for the dE/dx distributions have been selected from the μ+SVT track dataset, required to pass `LeptonSvtSel`, and required to pass general candidate reconstruction requirements as described in Section 5.2. The selection criteria shown in Table B.1 were chosen to be as similar as possible to that of the μD^+ and $\mu\Lambda_c^+$, with the notable exception that "prompt" background is not removed with a cut on $ct^*(B)$. The D^{*+} candidate is flagged by selecting the candidate with the lowest mass difference $\Delta m(D^{*+}, D^0) \equiv m(D^0\pi^+) - m(D^0)$. The $\mu^- D^*$ and $\mu^-\Lambda$ signals after all selection requirements are shown in Figure B.1.

Cuts	$\mu^- D^{*+}$	$\mu^-\Lambda$
$m(D^{*+}/\Lambda)$ [GeV/c^2] $\in$	(1.4,2.0)	(1.0,1.16)
$ct(D^{*+}/\Lambda)$ [cm] $\in$	(-0.01, 0.10)	N/A
$\sigma_{ct}(B)$ [cm] $<$	0.04	N/A
$m(\mu^- D^{*+}/\Lambda)$ [GeV/c^2] $\in$	(2.5,5.0)	(2.0,5.0)
$p_T(p)$ [GeV/c] $>$	N/A	2.0
$p_T(K)$ [GeV/c] $>$	0.7	N/A
$\chi^2_{2D}(D^{*+}/\Lambda) <$	10	5
vtx. prob.$(\mu^- D^{*+}/\Lambda) >$	10^{-5}	10^{-5}
$L_{xy}(D^{*+}/\Lambda)$ [mm] $>$	N/A	4
$L_{xy}/\sigma_{Lxy}(D^{*+}/\Lambda) >$	5	5
$\Delta m(D^{*+}, D^0)$ [GeV/c^2] $\in$	(0.1440,0.1475)	N/A

Table B.1: D^{*+} and Λ control sample selection.

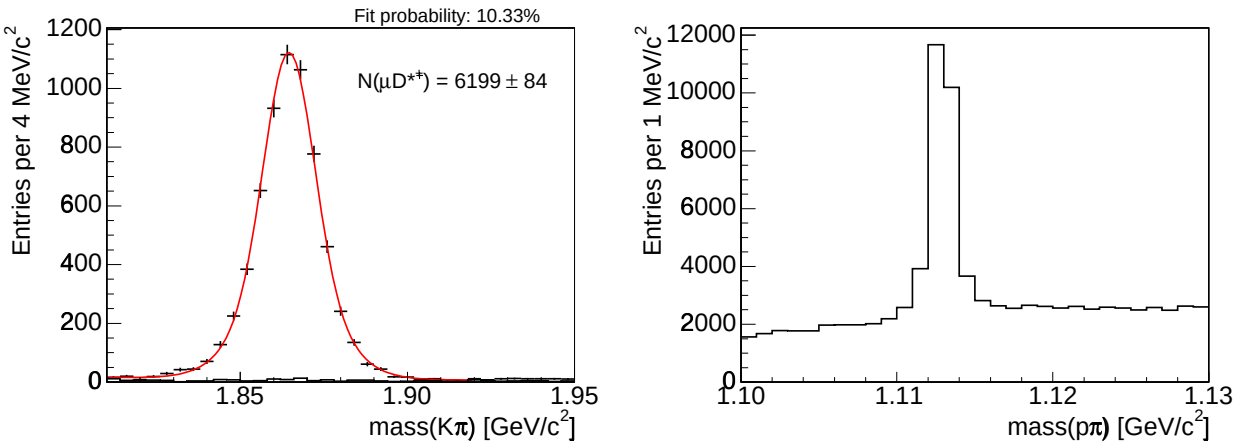

Figure B.1: D^* (left) and Λ (right) invariant mass distributions with all cuts applied.

Appendix C

Branching Ratios and Lifetimes

Charm Decay	$\mathcal{BR}(\%)$
$D^+ \to K^-\pi^+\pi^+$	8.8±0.6
$D^0 \to K^-\pi^+$	3.80±0.09
$D^{*+} \to D^0\pi^+$	67.7±0.5
$D_s^+ \to \phi\pi^+$	3.6±0.9
$\hookrightarrow K^+K^-$	49.1±0.6
$\Lambda_c^+ \to pK^+\pi^-$	5.0±1.3

Table C.1: Charm branching ratios.

B Decays	$\mathcal{BR}(\%)$
$\bar{B}^0 \to \ell^-\bar{\nu}X$	10.5 ± 0.8
$\ell^-\bar{\nu}D^+$	2.14 ± 0.20
$\ell^-\bar{\nu}D^*(2010)^+$	5.44 ± 0.23
$B^- \to \ell^-\bar{\nu}X$	10.2 ± 0.9
$\ell^-\bar{\nu}D^0$	2.15 ± 0.22
$\ell^-\bar{\nu}D^*(2007)^0$	6.5 ± 0.5

Table C.2: B branching ratios.

B	Lifetimes [ps]
$\tau(\bar{B}^{\,0})$	1.536±0.014
$\tau(B^-)$	1.671±0.018
$\tau(\bar{B}^{\,0}_s)$	1.461±0.057
$\tau(\Lambda^0_b)$	1.229±0.080
$\tau(B^-)/\tau(\bar{B}^0)$	1.086±0.017

Table C.3: B Lifetimes.

B Decay	Width ($\times 10^{-12}$ ps^{-1})
$\Gamma(\bar{B} \to \ell^- \bar{\nu} D)$	0.0134±0.0009
$\Gamma^*(\bar{B} \to \ell^- \bar{\nu} D^*)$	0.0372±0.0017
$\Gamma^{**}(\bar{B} \to \ell^- \bar{\nu} D^{**})$	0.0141±0.0010

Table C.4: Partial widths of the B mesons.

Decays	$\mathcal{BR}(\%)$
$D^+ \to e^+ \nu_e X$	13.94±??
$D^+ \to \mu^+ \nu_\mu X$	13.76±??
$D^0 \to e^+ \nu_e X$	6.61±??
$D^0 \to \mu^+ \nu_\mu X$	6.15±??
$D^+_s \to e^+ \nu_e X$	13.32±??
$D^+_s \to \mu^+ \nu_\mu X$	12.86±??
$\tau^- \to e^- \bar{\nu}_e \nu_\tau$	17.84±0.06
$\tau^- \to \mu^- \bar{\nu}_\mu \nu_\tau$	17.36±0.06

Table C.5: Other (semi)leptonic branching ratios. Branching ratios with unspecified uncertainties are taken from the `EvtGen` table.

Appendix D

Comparison of Data and Monte Carlo

Comparisons between the e+SVT data and the Monte Carlo for quantities which are cut upon are shown in Figures D.1-D.15. In all cases the area of the Monte Carlo distribution is normalized to the area of the data distribution. The quality of the comparisons are quantified by fitting the ratio of the data to the Monte Carlo by both a sloped and a constant line. The former indicates potential biases between the two distributions, while the latter gives a measure of overall agreement between the distributions.

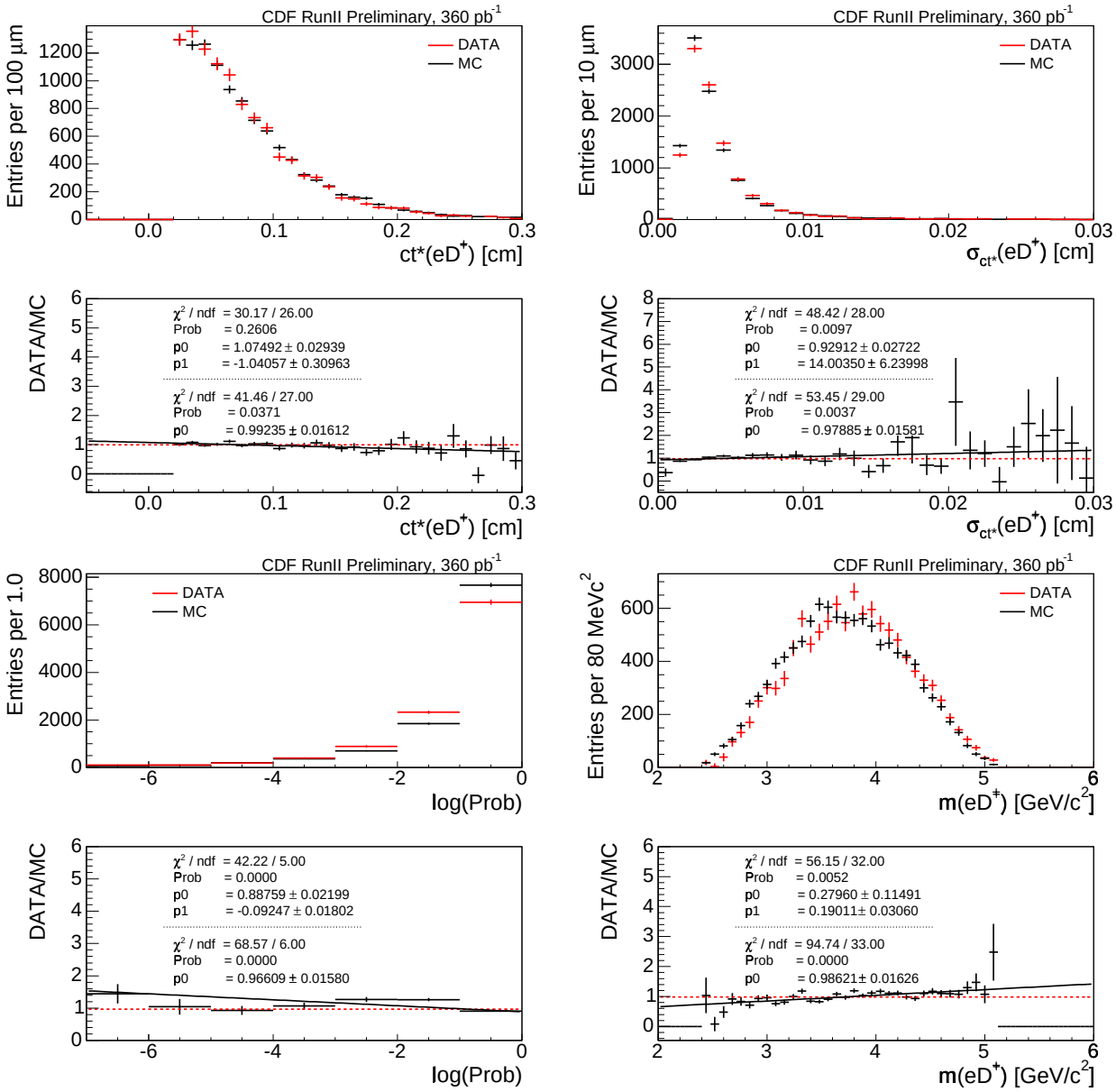

Figure D.1: e^-D^+ data/MC comparisons of $ct^*(e^-D^+)$ (top left), $\sigma_{ct}(e^-D^+)$ (top right), e^-D^+ vertex probability (bottom left), and $m(e^-D^+)$ (bottom right).

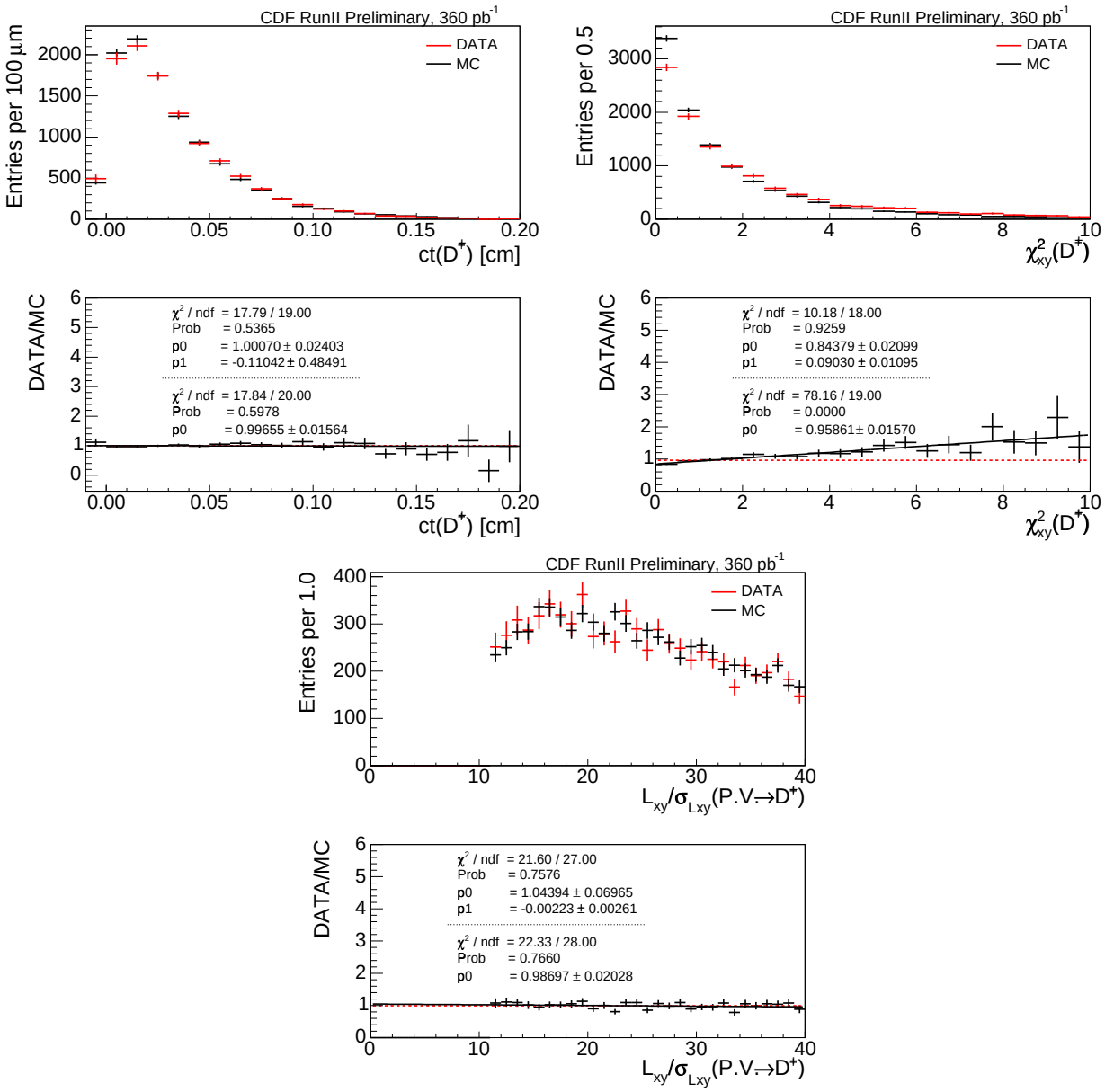

Figure D.2: $e^- D^+$ data/MC comparisons of $ct(D^+)$ (top left), $\chi^2_{xy}(D^+)$ (top right), and $L_{xy}/\sigma_{L_{xy}}(P.V. \to D^+)$ (bottom).

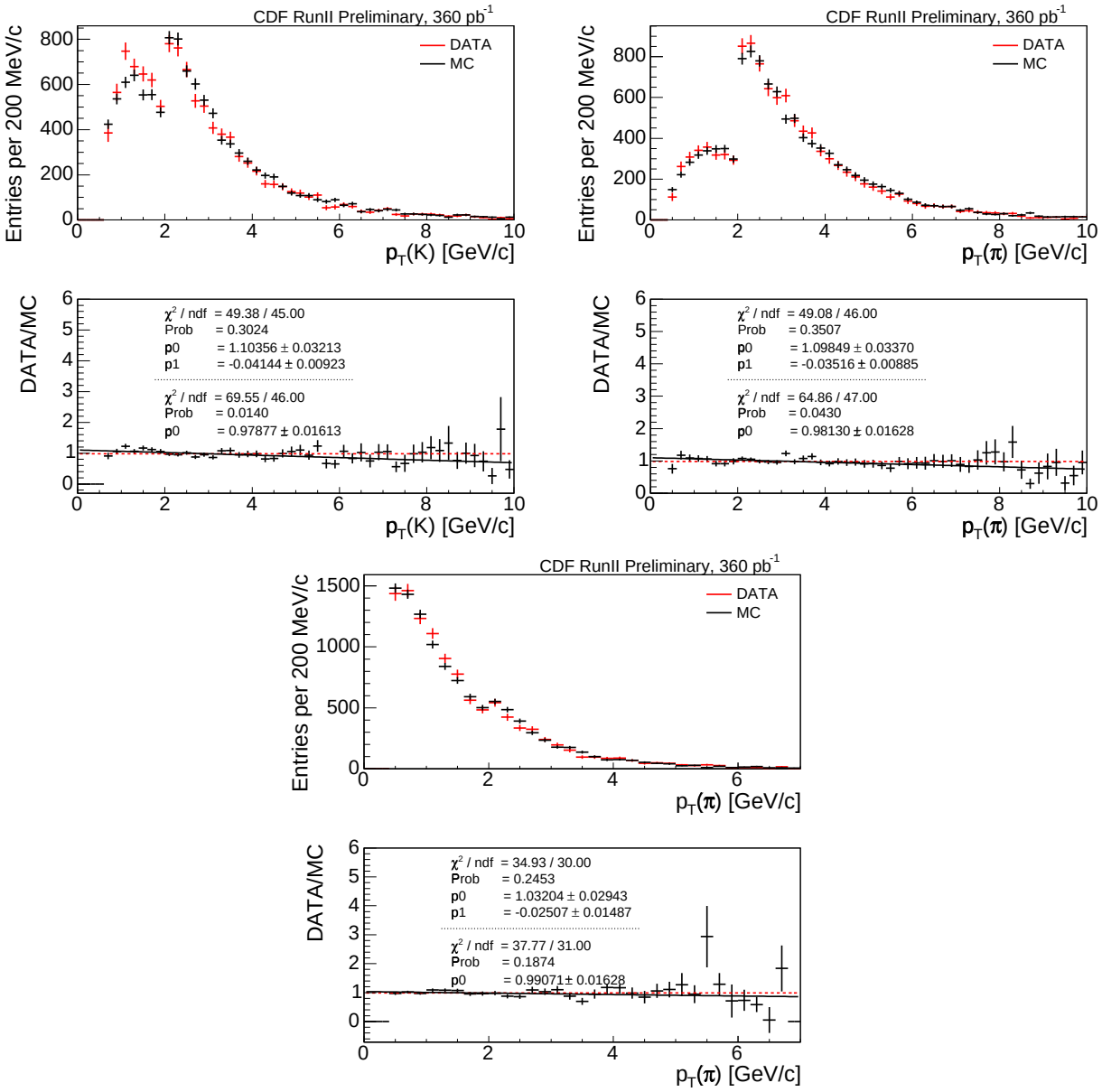

Figure D.3: eD^+ data/MC comparisons of $p_T(K^-)$ (top right), $p_T(\pi^+(1))$ (top left), and $p_T(\pi^+(2))$ (bottom).

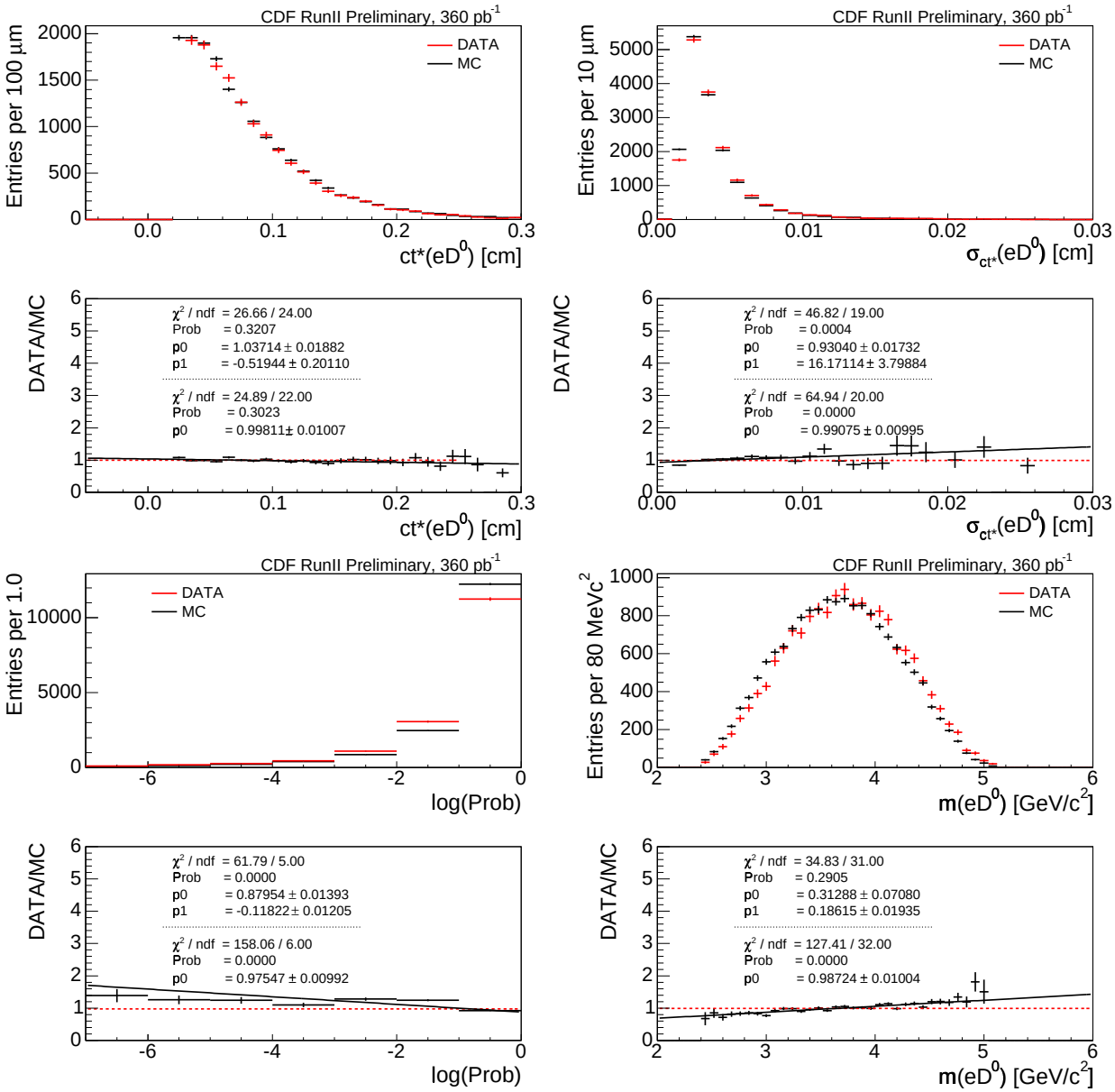

Figure D.4: $e^- D^0$ data/MC comparisons of $ct^*(e^- D^0)$ (top left), $\sigma_{ct}(e^- D^0)$ (top right), $e^- D^0$ vertex probability (bottom left), and $m(e^- D^0)$ (bottom right).

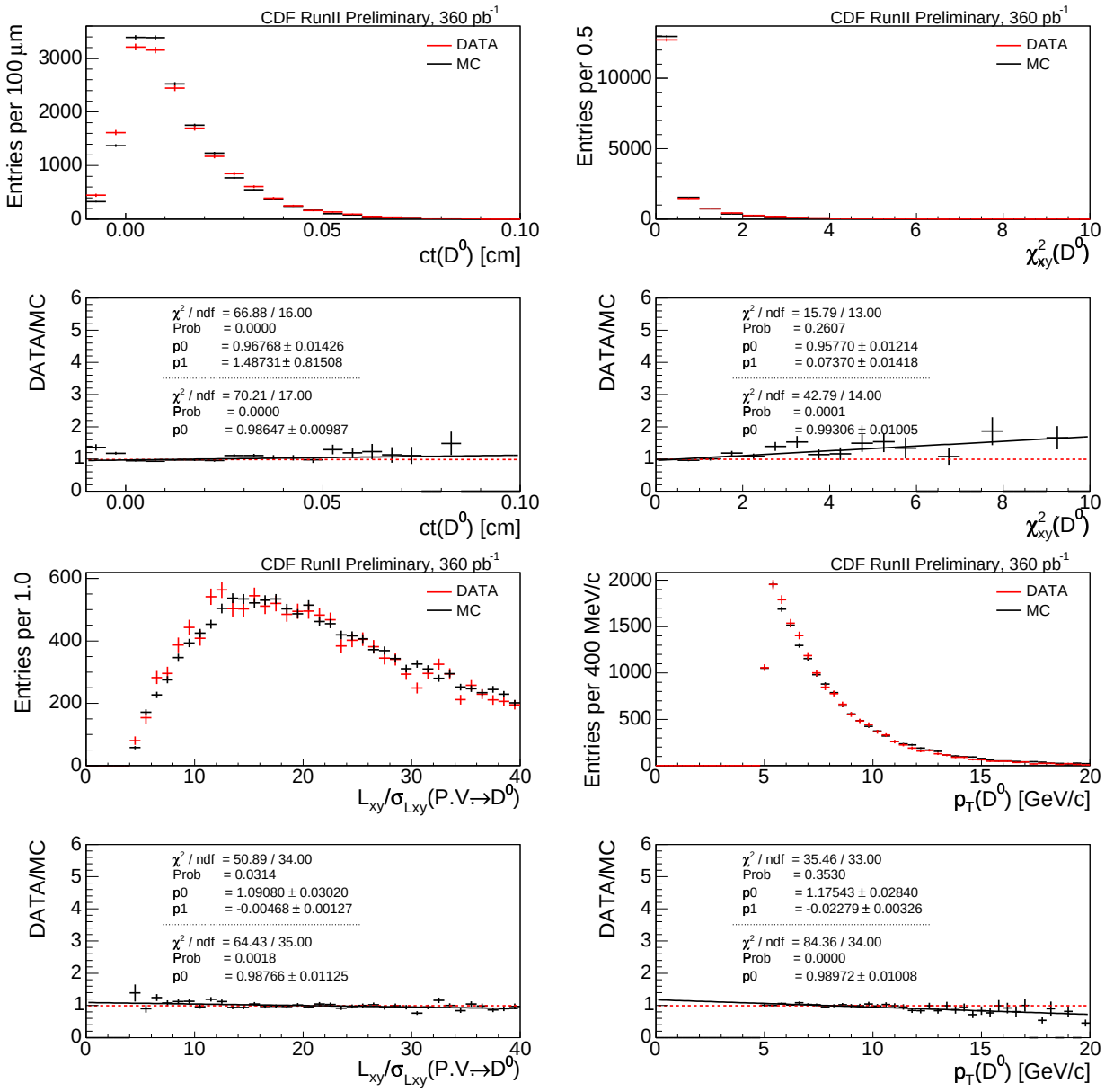

Figure D.5: $e^- D^0$ data/MC comparisons of $ct(D^0)$ (top left), $\chi^2_{xy}(D^0)$ (top right), $L_{xy}/\sigma_{L_{xy}}(P.V. \to D^0)$ (bottom left), and $p_T(D^0)$ (bottom right).

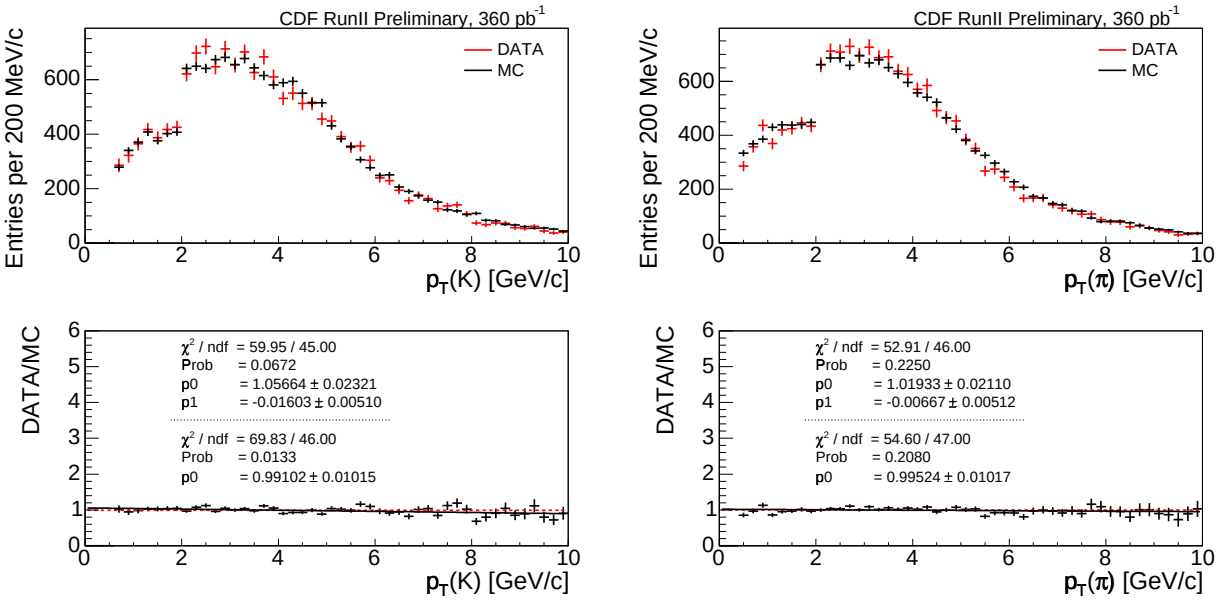

Figure D.6: $e^- D^0$ data/MC comparisons of $p_T(K^-)$ (left) and $p_T(\pi^+)$ (right).

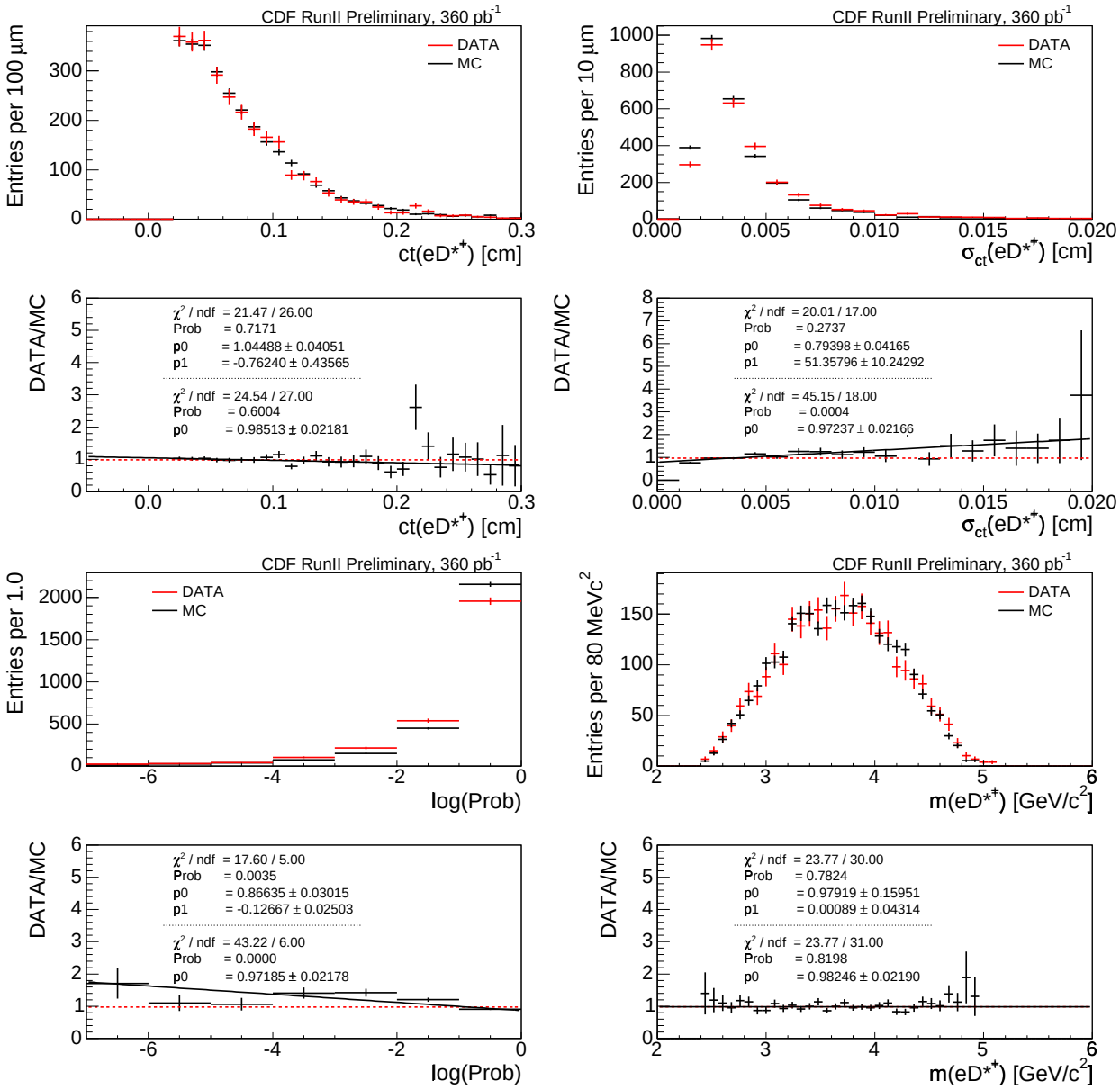

Figure D.7: $e^- D^{*+}$ data/MC comparisons of $ct^*(e^- D^{*+})$ (top left), $\sigma_{ct}(e^- D^{*+})$ (top right), $e^- D^{*+}$ vertex probability (bottom left), and $m(e^- D^{*+})$ (bottom right).

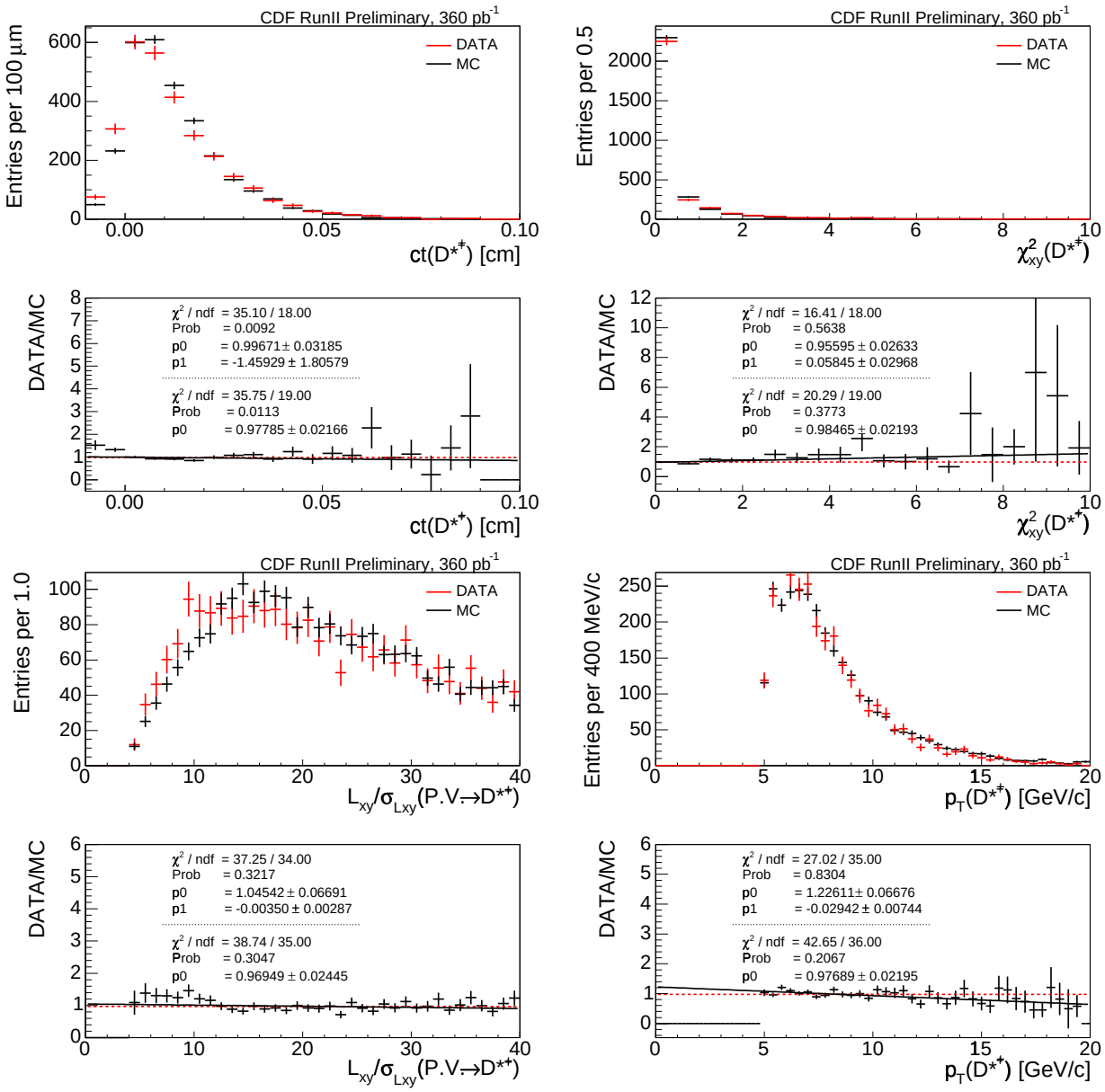

Figure D.8: $e^- D^{*+}$ data/MC comparisons of $ct(D^0)$ (top left), $\chi^2_{xy}(D^0)$ (top right), $L_{xy}/\sigma_{L_{xy}}(P.V. \to D^0)$ (bottom left), and $p_T(D^0)$ (bottom right) from the D^{*+} decay.

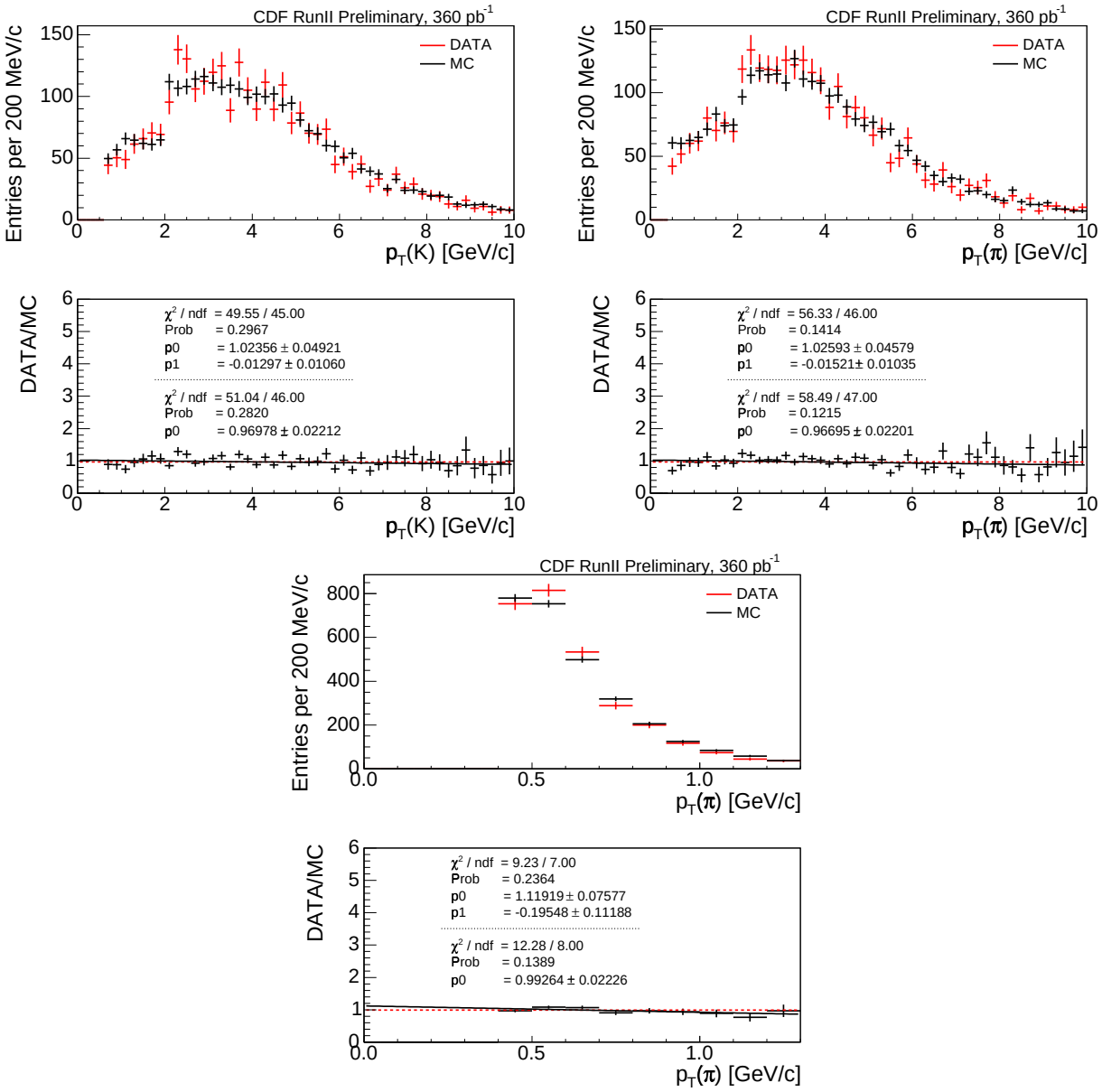

Figure D.9: $e^- D^{*+}$ data/MC comparisons of $p_T(K^-)$ (top left), $p_T(\pi^+)$ (top right), and $p_T(\pi_*^+)$ (bottom), the soft pion from the D^{*+} decay.

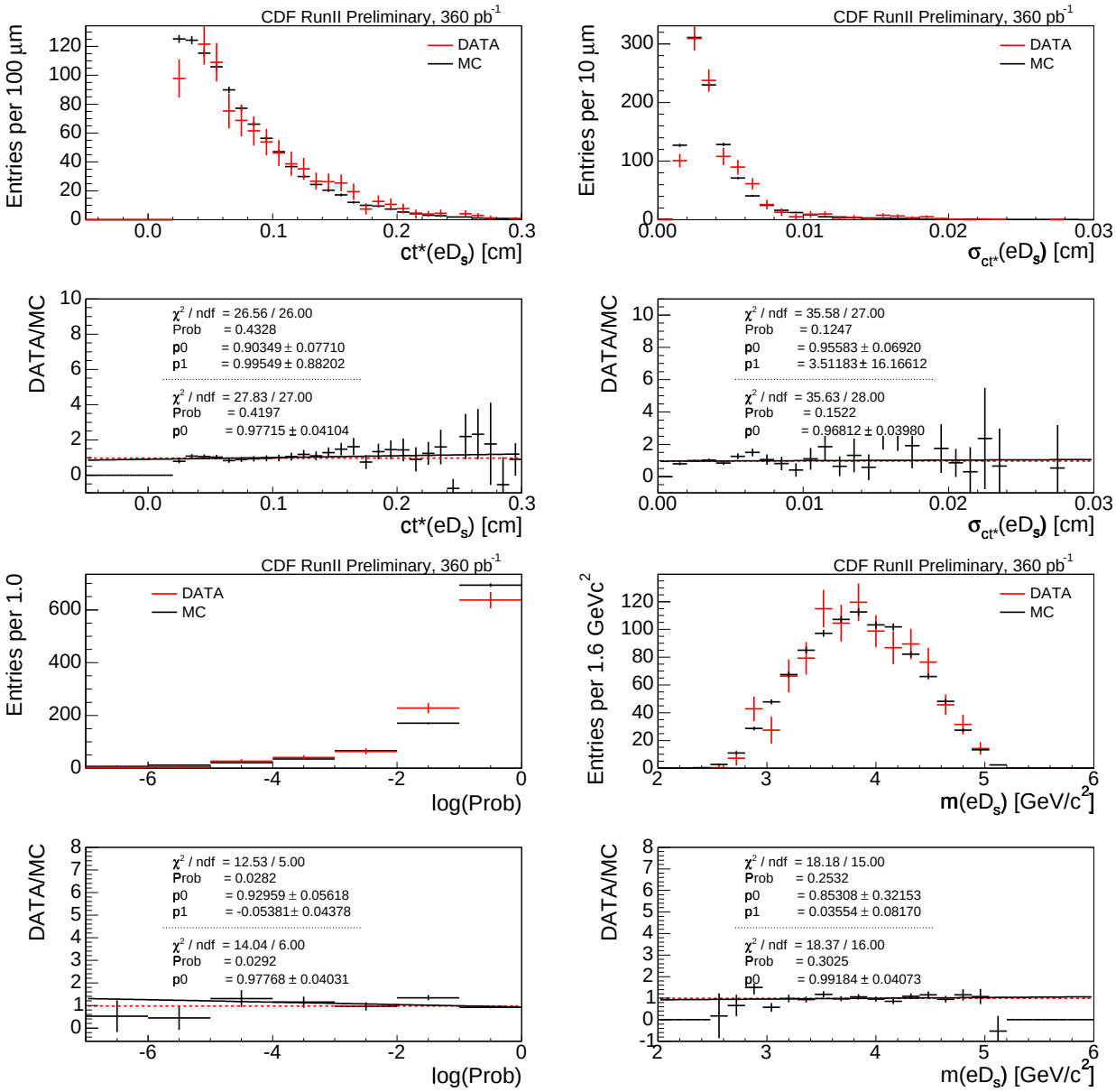

Figure D.10: $e^- D_s^+$ data/MC comparisons of $ct^*(e^- D_s^+)$ (top left), $\sigma_{ct}(e^- D_s^+)$ (top right), $e^- D_s^+$ vertex probability (bottom left), and $m(e^- D_s^+)$ (bottom right).

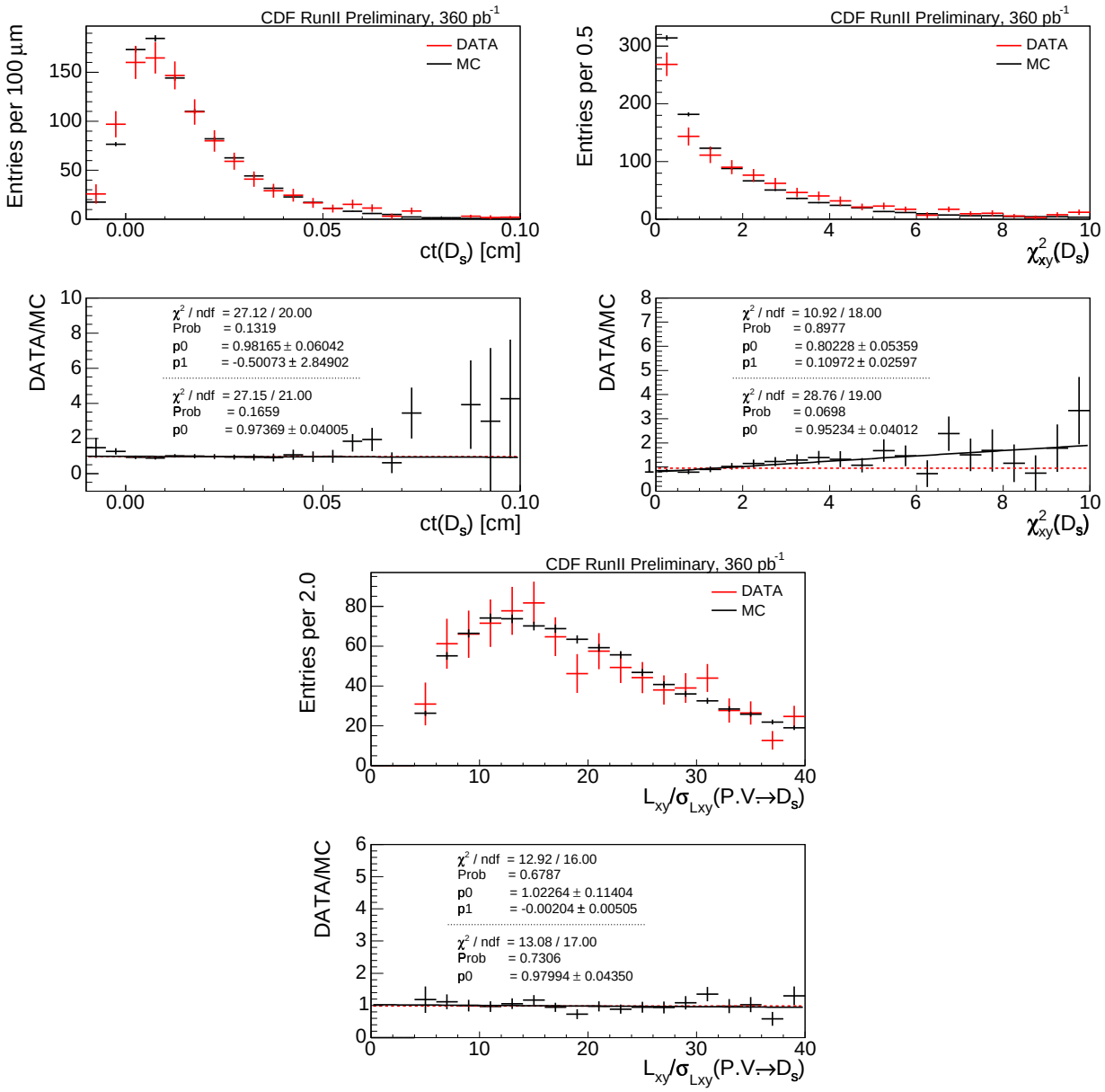

Figure D.11: $e^- D_s^+$ data/MC comparisons of $ct(D_s^+)$ (top left), $\chi^2_{xy}(D_s^+)$ (top right), $L_{xy}/\sigma_{L_{xy}}(P.V. \to D_s^+)$ (bottom).

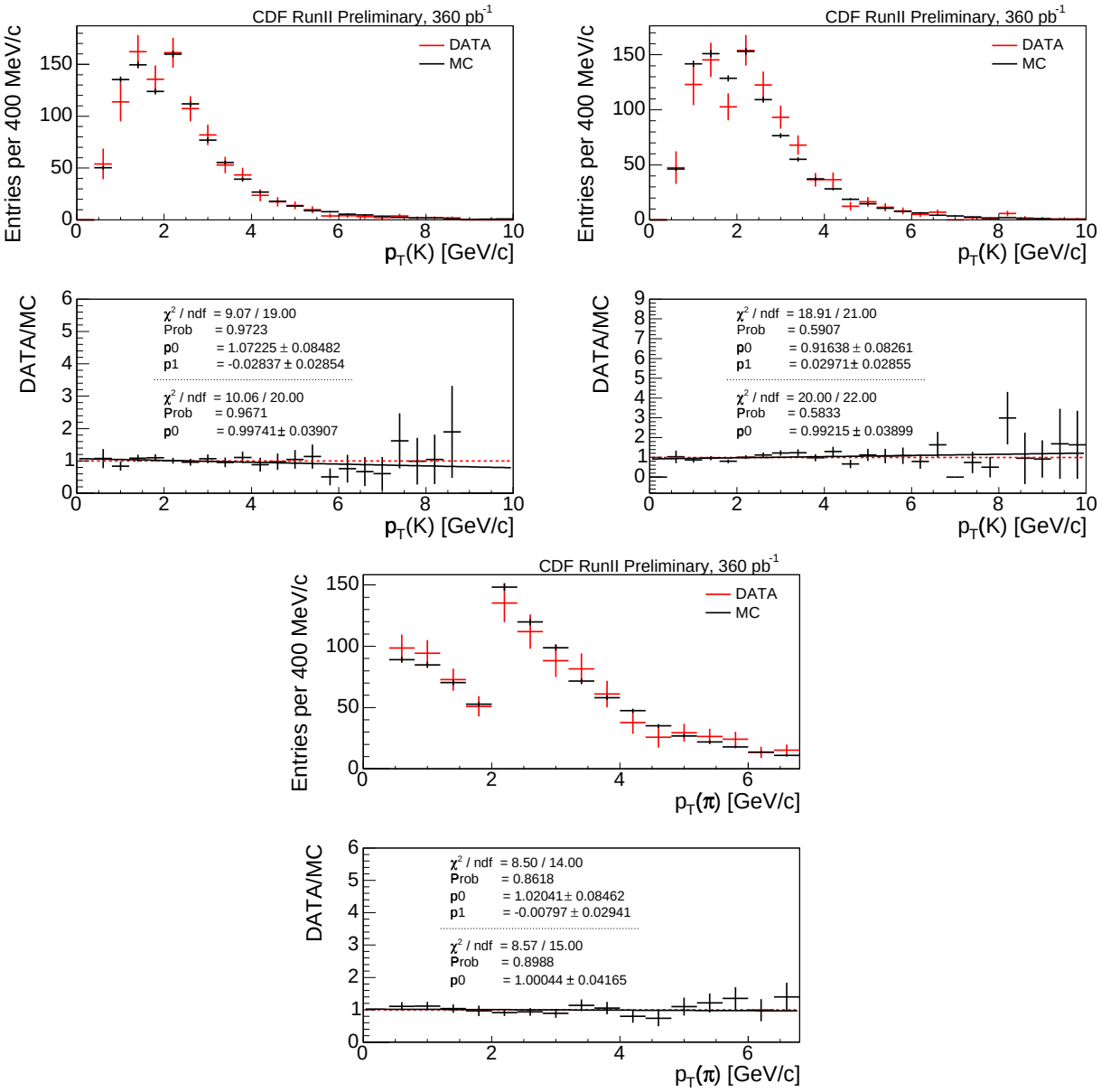

Figure D.12: $e^- D_s^+$ data/MC comparisons of $p_T(K^+)$ (top left), $p_T(K^-)$ (top right), and $p_T(\pi^+)$ (bottom).

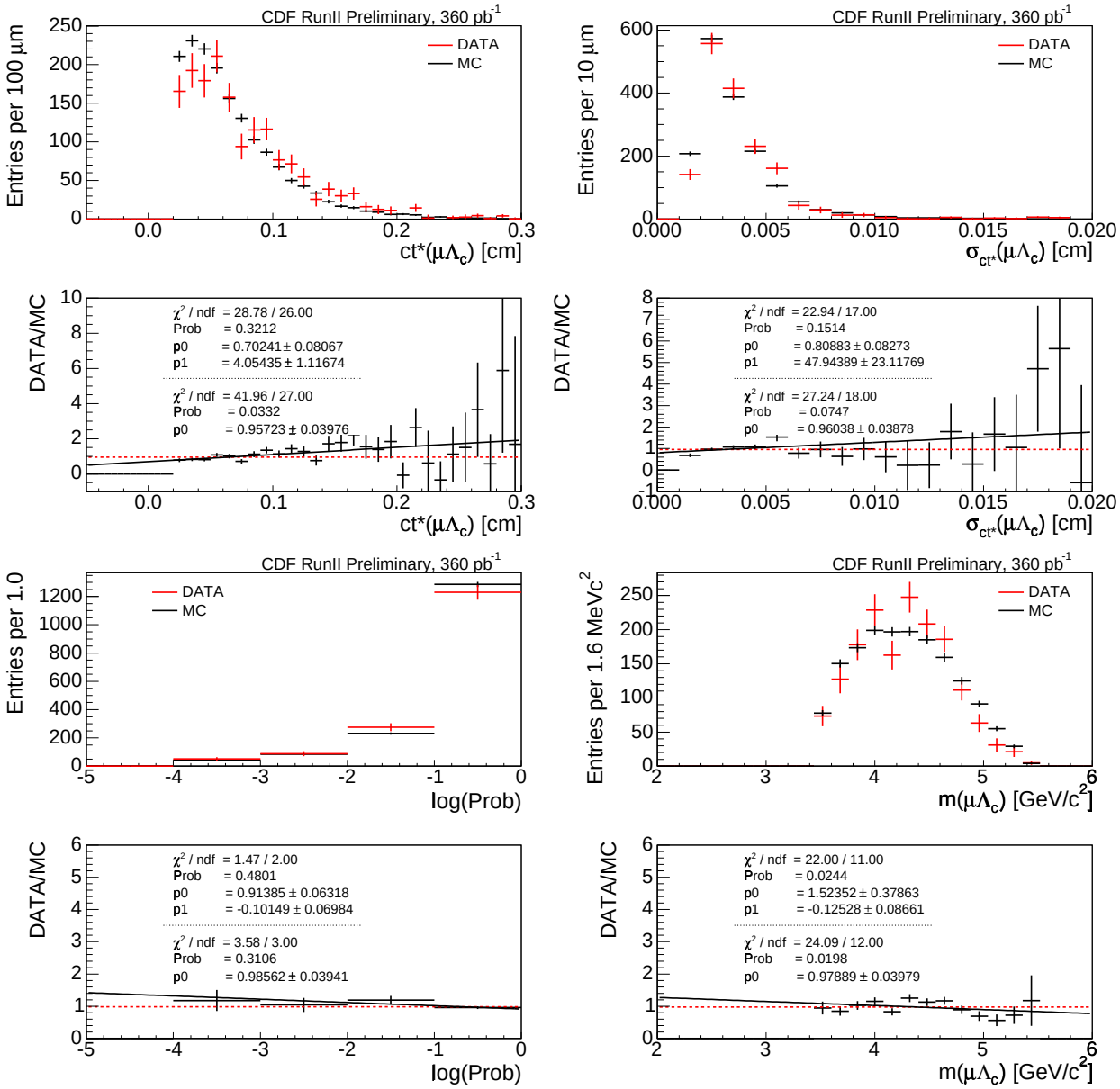

Figure D.13: $e^-\Lambda_c^+$ data/MC comparisons of $ct^*(e^-\Lambda_c^+)$ (top left), $\sigma_{ct}(e^-\Lambda_c^+)$ (top right), $e^-\Lambda_c^+$ vertex probability (bottom left), and $m(e^-\Lambda_c^+)$ (bottom right).

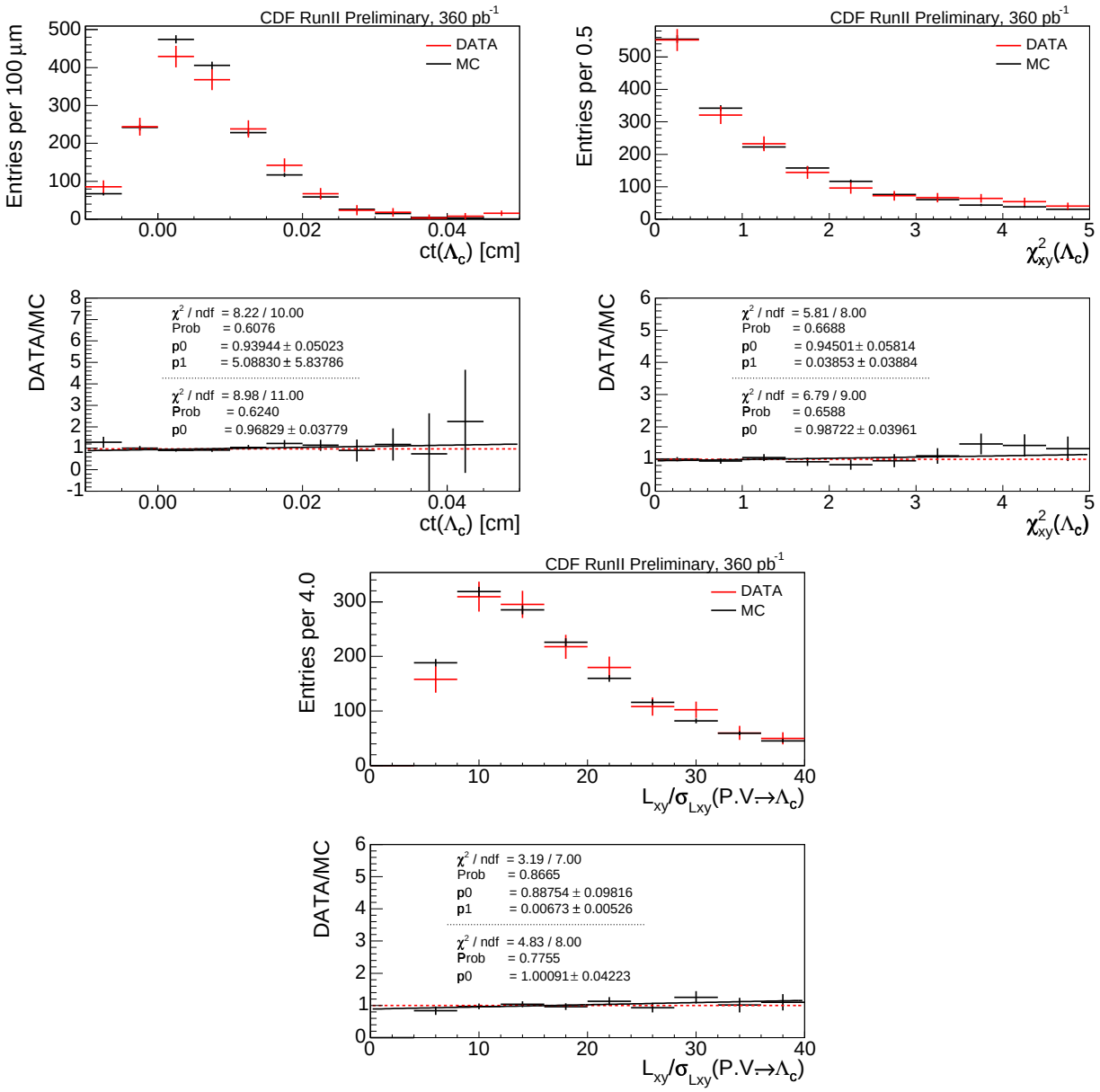

Figure D.14: $e^-\Lambda_c^+$ data/MC comparisons of $ct(\Lambda_c^+)$ (top left), $\chi^2_{xy}(\Lambda_c^+)$ (top right), and $L_{xy}/\sigma_{L_{xy}}(P.V. \to \Lambda_c^+)$ (bottom left).

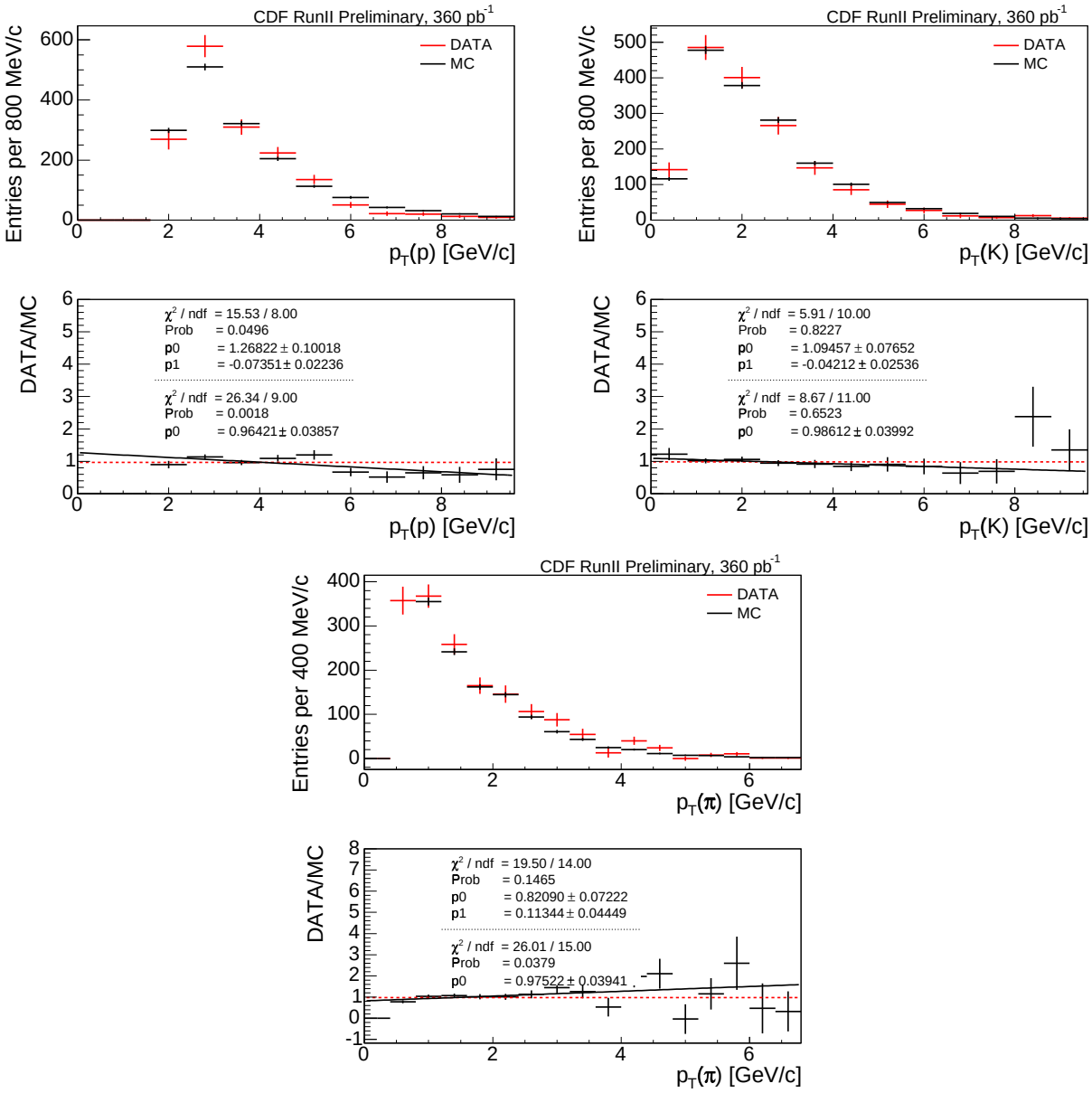

Figure D.15: $e^-\Lambda_c^+$ data/MC comparisons of $p_T(p)$ (top left), $p_T(K^-)$ (top right), and $p_T(\pi^+)$ (bottom).